Molecular Beam Scattering at Superthermal Energies

by

John Francis Reddington

Thesis presented for the Degree of Doctor of Philosophy

Faculty of Science

University of Edinburgh

1973

C O N T E N T S

Contents

SUMMARY

The work reported in this thesis concerns the study of atomic collision processes in the superthermal energy range by a molecular beams technique in order to gain information about the short range repulsive interactions existing between the colliding species.

Chapter one, and the references quoted therein, gives a short history of the subject of molecular beams, the aims of the experiments and the theories behind them.

In Chapter two, the phenomenon of "avoided crossing" of two potential surfaces is investigated theoretically using a two state eikonal model for the collision trajectories. The systems K/I and K/I_2 are studied for centre of mass collision energies in the range 20eV to 500eV, and total and differential cross sections for neutral and ionic scattering are calculated. The results are also compared to the Landau-Zener predictions where, for total cross sections, the results show good agreement, but for differential cross sections, only a qualitative agreement results.

The superthermal apparatus is described in the third Chapter. Innovations in the apparatus since the time of the last report include the use of the Lindholm-Gustafsson deceleration lens, the design of a new cross beam oven assembly, and the collecting of data by an on-line computer. The first two topics are adequately described, whilst the general mode of operation and the benefits obtained from using an on-line computer, are discussed.

A computer program designed to simulate ion lens systems was written at Shell Research Centre, Thornton. It was applied to the Shell Molecular beams apparatus and cured problems of beam instability. The program also investigated the Edinburgh molecular beam apparatus and found two important defects: firstly the image of the alkali metal source is larger than the entrance aperture of the Lindholm-Gustafsson deceleration lens; secondly, due to the application of a wrong potential to one element (G) of the deceleration lens, there was a large degree of beam divergence. These defects were rectified by doubling the entrance aperture of the lens and raising the potential of element G by a factor of eight. Resultant increases in beam intensity by a factor of ten have occurred and the new lens characteristics are reported fully in the fourth Chapter.

Chapter five discusses some methods of improving the existing apparatus to investigate inelastic processes by time of flight techniques. The theory behind time of flight processes are fully discussed and the merits of two experimental procedures are listed.

The last Chapter contains the experimental results obtained from the collision systems K/I_2, K/Br_2 and K/CH_3I at several laboratory collision energies between 100eV and 400eV.

The results for the K/I_2 system are compared to the theoretical predictions obtained in Chapter two. There is very good qualitative agreement between the two sets of results, but further

work is required before an exact fit will arise.

Differential cross section results for the K/Br_2 system are very similar to those for K/I_2. Not surprisingly, literature values for the potential parameters of the two systems are not too dissimilar.

Results from the K/CH_3I system reveal a great amount of scattering occurring at very large angles (greater than 500eV degrees). Further work is still required to analyse this system, but a preliminary analysis shows that at least two states contribute to large angle scattering.

Corrigenda

Thefollowing should be added to the text at the bottom of page 23:-

$$A_K(\ell)^2 = |C_K(\infty)|^2 \qquad 2.24$$

whilst the differential cross section for covalent scattering $\sigma_K(\theta)$ is defined as .....

The following should be added after the third paragraph on page 31:-

The large peak present at 320eV° in the 100eV covalent differential cross section plot should not be mistaken for a rainbow, as it appears at a position far greater than that predicted for a rainbow. The effect is due to interference between scattering from the repulsive branches of the two potentials. The effect has been magnified at this large angle because the cross section is multiplied by angle to the power seven thirds. Such a phenomenon is not noticeable when the cross section is multiplied by angle to the power four thirds.

CHAPTER 1

INTRODUCTION

A few decades ago, when it became clear that a knowledge of the fundamental nature of chemical reaction could not be obtained by conventional techniques, there followed a comparatively long period of refining new experimental methods to achieve this aim. The development of these fields depended heavily on technology, and fortunately, recent advances have now produced a period of experimental fruitfulness.

The use of molecular beams is one such technique. Whilst experiments involving one beam have been known since the time of Rutherford and Stern and Gerlach, those using two intersecting beams are comparatively new.

A molecular beam is a stream of particles well collimated in width and well defined in angular divergence and energy. Conditions are employed such that collisions between particles within one beam, or with residual particles in the vacuum system in which these experiments are performed, are highly improbable. Thus when two beams intersect within a very small volume, single collisions occur between particles of the beams, and their resultant effects are found by measuring the amount of scattering of one of the species involved.

The aim of these experiments is to evaluate the intermolecular potentials between the colliding species. As three types of collision process are possible, namely elastic, reactive and internal excitation of the species, research groups have looked at systems where one type of behaviour predominates [1-4]. However, a further topic of research,

mainly theoretical, has been devoted to tracing the origins of the various components of the potential [5-7], and this has often proved a valuable guideline to the experimenter.

Elastic scattering processes at thermal energies were the first studied as the beam sources were the simple orifice ovens. Hydrogen, the alkali metals, mercury and the rare gases were some of the first beam materials, and these early experiments examined the long range attractive branch of the potential [8,9]. Fortunately, rainbow angle scattering is observed at these energies.

The production of high energy beams [10,11], however, has provided a method for investigating the short range repulsive branch of the potential. The collision energies possible have now been extended up to 500eV and the energy dependence of many processes determined.

This is a very interesting region of study for such phenomena as electronic excitation and molecular dissociation can be observed. Also the energy range under which the Born-Oppenheimer approximation [1] remains valid can be investigated.

Knowledge of collisional processes at these high energies is of great interest to many fields. Not only does the chemistry of combustion and detonation gain fundamental knowledge from molecular beam results, but also the physics of the upper atmosphere and interstellar space. The evaluation of virial coefficients and transport

properties of gases for temperatures up to 15,000^{0}K can now be performed more accurately.

Inelastic processes were first investigated by observing the nature and intensity of radiation emitted from the newly formed excited species [12]. An alternative means was also found by state selection of the scattered products [13]. Further refined techniques involve energy analysis of beams before and after collision, and now time of flight techniques. The main problems in this type of work involve detecting or selecting the excited species and the very long counting times required to form a good statistical average for the scattered signal.

The first reaction to be studied by beam techniques was of potassium and hydrogen bromide [14,15]. Using a Langmuir-Taylor detector, the product could be discriminated from the reactant potassium beam. Further experiments followed using the alkali metals with the halogens and their hydrides [16] and also the alkylhalides [17].

Ion-neutral reactions form another prominent branch of reactive scattering. Charge transfer is one possible mechanism [18], whilst more general reactions of the type

$$A^+ + B \rightarrow C^+ + D$$

have been investigated [19]. Mass spectrometric detectors are used, and if the experiments are repeated using isotope effects, the reaction mechanism and collision complex can often be determined.

Of course scattering processes similar to the above mentioned are still being investigated whilst other new phenomena are being studied. New advances in elastic scattering employ beams of excited or metastable atoms. However these experiments have problems due to the relatively low intensity and short lifetimes of the species, whilst such beams are often mixtures of several metastable entities. Recent reports on time of flight methods by Pauly [20] and Toennies [21] have studied electronic and rotational excitations respectively, and this method looks most promising for studying inelastic collisions. Reactive scattering looks very interesting. Polanyi [22], Zare [23] and others are employing chemiluminescence and laser induced fluorescence to follow the partitioning of reaction energy into the internal degrees of freedom of the products. The steric effect of reactions is under investigation using beams of potassium and oriented methyl-halides [24,25], and these results will help clarify the properties of this much studied system. Finally, certain systems involving the "avoided crossing" of potential surfaces offer the prospect of determining two potential functions by following the scattering of only one species [26,27].

The vast amount of theoretical work performed has greatly advanced the state of experimental molecular beams. The use of classical mechanics, mathematically simple, is found inadequate to explain many scattering phenomena, whereas quantum mechanics yields correct solutions but only laboriously. Much of the work done has tended to simplify complex problems by use of approximation techniques.

Often the appropriate method depends on the type of collision expected. For instance the full quantal treatment using the partial wave expansion [2] can be simplified for soft collisions by the Born Approximation [2] whereas particular features of the scattering pattern such as rainbow or glory structure can be treated by the semiclassical approach of Ford and Wheeler [28].

In some instances workers prefer to invert the experimentally obtained scattering data to obtain the relevant intermolecular potential involved [29]. Alternatively the physics of a collision can be simulated using a particular model, finally comparing the theoretical and experimental scattering functions produced. Monte Carlo techniques [30] have been revived with a good deal of success whilst Anderson's method [31,32] of describing the internal and external states of a system during collision by quantum and classical mechanics respectively is now a standard technique.

Another important area of research has been the evaluation of electronic wave functions for highly complicated atoms. Hartree-Fock and Slater type orbital functions have been calculated by Herman and Skillman [33], and their work is of great value.

This thesis is a study of a few of the forementioned topics of research. The type of collision process studied has been in the superthermal energy range up to 500eV where fast alkali metal atoms collide with halogen and methyl iodide molecular beams of thermal energy. Some considerations of time of flight techniques have been

studied in order to modify the existing apparatus to calculate both elastic and inelastic differential cross section results for such systems. The systems K/I and K/I_2 have been studied theoretically using an eikonal approach and the validity of this method is investigated when the theoretical and experimental results for K/I_2 are compared.

CHAPTER 2

THEORETICAL STUDIES

Introduction

In the chemi-ionisation process of the type

$$A + B \rightarrow A^+ + B^-$$

the potential functions $H_{11}(R)$ and $H_{22}(R)$ for the neutral and ionic states of the system respectively are found to intersect at a certain internuclear separation R_x. If the symmetry of the two states is identical, then an "avoided crossing" can take place in this region [34] (Figure 2.1).

The Landau-Zener (LZ) theory [35,36] has been used almost exclusively to predict the probability p of an "avoided crossing" occurring in such a collision. This is given by

$$p = \exp(-\omega) \qquad 2.1$$

where

$$\omega = \frac{2\pi H_{12}^2}{\hbar v_1 |F_1 - F_2|} \qquad 2.2$$

with

$$F_i = \left| \frac{\partial H_{ii}}{\partial R} \right|_{R=R_x} \qquad 2.3$$

H_{12} is half the energy separation of the avoided crossing potential curves at the crossing distance R_x, whilst v_1 is the radial relative velocity at that point. If the ionic state is governed by a simple Coulombic potential, then ω may be rewritten as

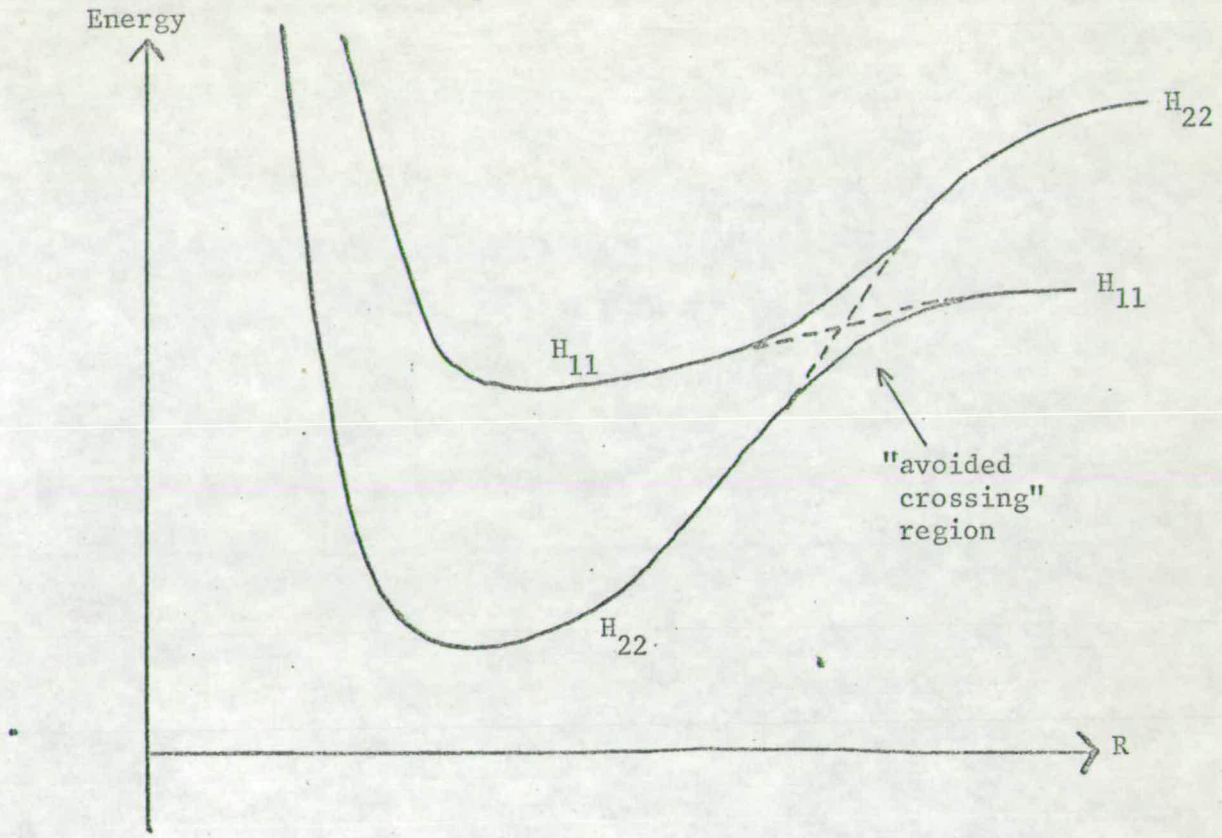

FIGURE 2.1 Occurrence of an "Avoided Crossing".

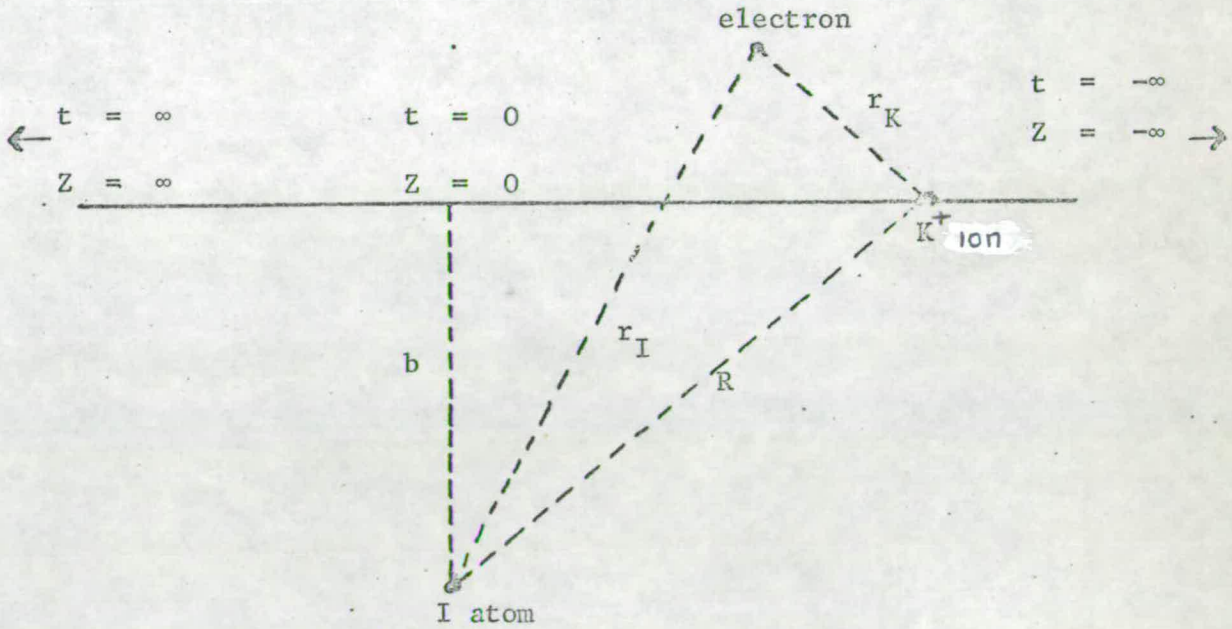

FIGURE 2.2 Trajectory Model for the Collision.

$$\omega = \frac{2\pi H_{12}^2 R_x^2}{\hbar v_1 e^2} \qquad 2.4$$

the value of F_1 being comparatively insignificant.

As each collision of interest involves two passes of the crossing region, the probability P of starting on the covalent curve H_{11} and finishing on the ionic curve H_{22} is given by

$$P = 2p(1-p) \qquad 2.5$$

This has a maximum value of one half.

Several modifications to this theory have emerged mainly by Steuckelberg [37], whilst others [38,39] have pointed out serious limitations.

Theory for the System K/I

The collisions in the eV energy range between potassium and iodine atoms are treated here in a manner less approximate than the LZ theory. Whilst a full quantal description can be applied at very low energies, the large number of partial waves involved at higher energies renders this approach totally impractical. The method chosen was an eikonal approach similar to that suggested by Anderson [31] and Birnbaum [32] and used by various other workers [40,41].

Essentially the nuclear and electronic motions of the system are described by classical and quantum mechanics respectively. As changes in the internal energy are likely to be small compared to the

translational energy, one can accurately assume a common translational path for all coupled internal states. Figure 2.2 is a sketch of the model used for the collision, the symbols employed being

b	the impact parameter
R	the internuclear separation
Z	the distance along the trajectory
r_K	the valence electron - potassium nucleus separation
r_I	the valence electron - iodine nucleus separation

Several assumptions are made in forming a theoretical model. These include:

1. A straight line trajectory for the colliding system
2. A one electron model is employed
3. Only two states of the system are considered. The system when neutral is described by the wave function Φ_K of energy E_K for the 4s ground state of potassium; when ionic by the wave function Φ_I of energy E_I describing the iodine ion. The first excited state of the system, where the valence electron is in the 4p state of potassium, is disregarded.
4. The relative motion of the system is not included in these wave functions.
5. The effect of overlap is disregarded.

In the process of collision, the system can be described by a wave function Ψ written as a mixture of atomic wave functions

$$\Psi = C_K(t)\Phi_K + C_I(t)\Phi_I \qquad 2.6$$

where the time dependent variables C_K and C_I represent the degree of mixing of the two states.

The Hamiltonian H for the system can be written as

$$H = H_o + V^K(r_K) + V^I(r_I) + V(R) \qquad 2.7$$

V(R) is the iodine atom - potassium ion potential, V^K the electron - potassium ion potential whilst V^I is the electron - iodine atom potential. H_o contains the kinetic energy terms of the Hamiltonian for the system.

From these definitions it is obvious that

$$(H_o + V^K)\Phi_K = E_K\Phi_K \qquad 2.8$$

$$(H_o + V^I)\Phi_I = E_I\Phi_I \qquad 2.9$$

The wave function Ψ is inserted into the time dependent Schrödinger equation

$$i\hbar \frac{\partial \Psi}{\partial t} = H\Psi \qquad 2.10$$

Multiplying the resulting equation by Φ^*_K and integrating over all spacial co-ordinates gives

$$i\hbar \frac{dc_K}{dt} = C_K H_{11}(R) + C_I H_{12}(R) \qquad 2.11$$

Repeating the same process but using Φ^*_I yields

$$i\hbar \frac{dc_I}{dt} = C_K H_{12}(R) + C_I H_{22}(R) \qquad 2.12$$

where, using equations (2.8) and (2.9),

$$H_{11}(R) = \int \Phi^*_K H \Phi_K d\tau = E_K + \int \Phi^*_K (V^I + V(R)) \Phi_K d\tau$$

$$H_{22}(R) = \int \Phi_I^* H \Phi_I d\tau = E_I + \int \Phi_I^* (V^K + V(R)) \Phi_I d\tau$$

$$H_{12}(R) = \int \Phi_K^* H \Phi_I d\tau = \int \Phi_I^* H \Phi_K d\tau \qquad 2.13$$

$H_{11}(R)$ and $H_{22}(R)$ are of the form shown in Figure 2.1, whilst $H_{12}(R_x)$ has the same definition as before. Fixing E_K as the arbitrary zero of energy, then at an infinite internuclear separation, H_{22} will have a value ΔE, the energy difference in the ionisation potential of potassium, 4.339eV [42], and the electron affinity of the iodine atom, 3.0616eV [43].

The shape of H_{22} has been calculated from spectroscopic measurements to have a well depth of 3.34eV [44] at an interparticle separation of 3.048Å [45]. Using atomic units where $\hbar = 1$, H_{22} can be expressed as

$$H_{22}(R) = A_2 \exp(-b_2 R) - \frac{1}{R} + \Delta E \qquad 2.14$$

where

$A_2 = 1.429 \times 10^{17}$ a.u. of energy

$b_2 = 7.821\ a_o$

$\Delta E = 0.046$ a.u. of energy

The form of $H_{11}(R)$ is to an extent arbitrary provided it has a very shallow well depth. The shape chosen was

$$H_{11}(R) = A_1 \exp(-b_1 R) - C/R^8 \qquad 2.15$$

with

$$A_1 = 3.3584 \text{ a.u. of energy}$$

$$b_2 = 1.9225\ a_o^{-1}$$

$$C = 5.519 \times 10^4 \text{ a.u. of energy } a_o^8$$

These two potential curves intersect at an internuclear separation of 21.3 a_o.

From the original definition of $H_{12}(R)$ from equations (2.13) and (2.7) and neglecting the effects of overlap, a simplified form is found in

$$H_{12}(R) = \int \Phi_I^* V^I(r_I) \Phi_K d\tau \qquad 2.16$$

Neglecting exchange effects, V^I can be evaluated by simple electrostatic theory, where electronic wave functions for the iodine atom [33] are used to form a radial charge distribution around the nucleus.

The potential form yielded is unrealistic but can be rectified by the use of a simple pseudopotential [46]. This postulates that the electron in question cannot penetrate the shell (5s orbital) of the iodine atom. Hence below this radial value (1.966 a_o) contributions

to the function H_{12} are zero. Mathematically, though not physically, this is equivalent to equating the interaction potential V^I in this region to zero. (See Figure 2.3).

Coulomb wave functions [47] were used for potassium whilst the 5p atomic wave function [33] for iodine was used to represent the ionic ground state. The function H_{12} could then be evaluated.

One further alteration was made. An experimental value for H_{12} of 1.4×10^{-3}eV at a crossing distance of 11.3Å has been suggested by Moutinho [48], and the calculated values were scaled accordingly.

Computation

The coupled differential equations (2.11) and (2.12) were solved by a numerical integration computer program using Hamming's Predictor-Corrector method. The variation of the complex quantities C_K and C_I can be followed provided initial conditions to the problem are supplied. Starting in the neutral channel implies that

$$|C_K(-\infty)| = 1$$

$$|C_I(-\infty)| = 0$$

At the end of the collision, the probabilities $P_K(b)$ and $P_I(b)$ of the system being neutral or ionic are given by

$$P_K(b) = |C_K(\infty)|^2$$

$$P_I(b) = |C_I(\infty)|^2 \qquad 2.17$$

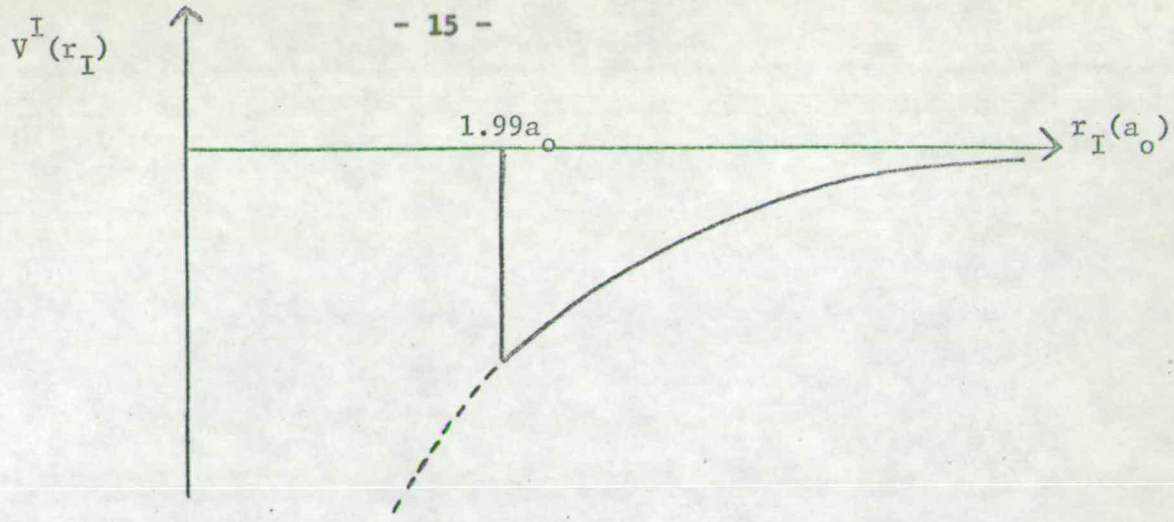

FIGURE 2.3 Effect of a Simple Pseudopotential on $V^I(r_I)$.

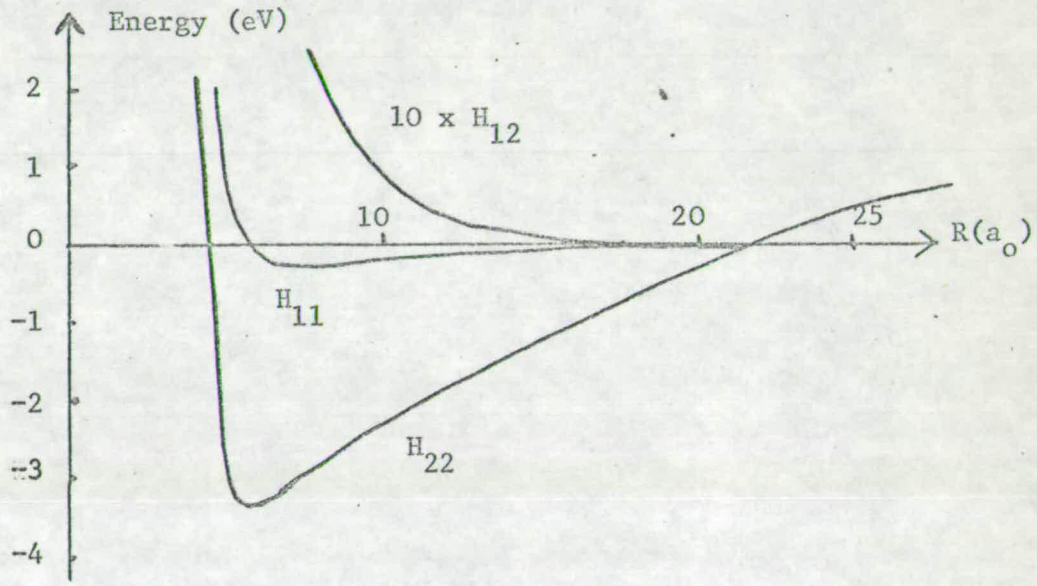

FIGURE 2.4 The Potential Functions $H_{11}(R)$, $H_{22}(R)$ and $H_{12}(R)$ for K/I

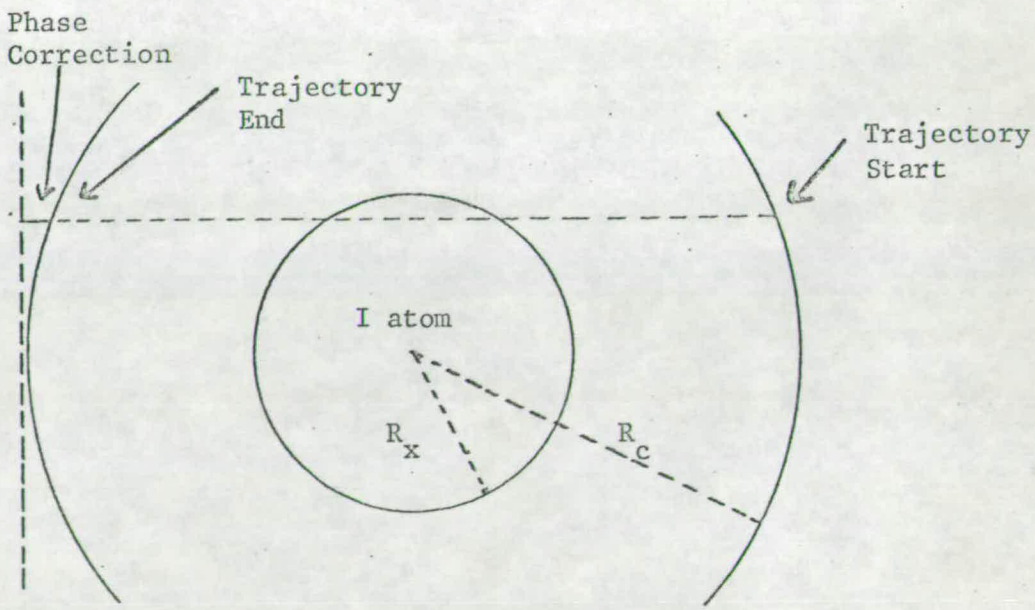

FIGURE 2.5 The Addition of a Phase Correction for the Ionic Channel at the End of Each Trajectory.

The total ionisation cross section Q_I is given by

$$Q_I = 2\pi \int_0^\infty P_I(b)\, b\,db \qquad 2.18$$

The program was tested for mathematical stability over a wide range of impact parameters and collision energies. The main test was to find a suitable integration step length for a given degree of accuracy. Too short a step length caused a large aggregation of "round-off" errors, whilst at the other extreme the calculations could not achieve the desired accuracy. However, a range of step length values existed which gave answers consistent to the fifth decimal place. The largest of these step lengths was chosen for the calculation.

Another test was to determine the start and finish points for each trajectory. The slow decay of the Coulombic term in the potential H_{22} necessitated starting the trajectories on the edge of a sphere of radius R_c, the "Coulomb radius", and terminating them on the other side. Provided R_c was greater than R_x, changes in R_c did not alter the final exit probabilities given by equation (2.17), nor the neutral channel phase shift γ_K where

$$\tan \gamma_K = \mathrm{Im}(c_K) \,/\, \mathrm{Re}(c_K) \qquad 2.19$$

It did however, alter the ionic channel phase shift γ_I

$$\tan \gamma_I = \mathrm{Im}(c_I) \,/\, \mathrm{Re}(c_I) \qquad 2.20$$

This is evident from equations (2.11) and (2.12), where c_K will not change around R_c as both H_{11} and H_{12} are zero. But as H_{22} is non zero, there will still be a variation in C_I. This has become evident with the unequal path lengths of the two sets of trajectories.

To overcome this difficulty, the trajectories were evaluated for a Coulomb radius of 50 a_o and a small phase correction was added to equate the effective path lengths of the trajectories after the points of closest interparticle separation (Figure 2.5). This correction is determined by noting that around Coulomb radius H_{22} will have an approximate value of ΔE. The phase correction required is therefore $\Delta E.\Delta t/\hbar$ where Δt is the extra time required to effect an equal path length. However this correction is only required at the end of the trajectory where c_I is non zero.

K/I Results

The computations were carried out for a series of relative collision energies from 100eV down to 5eV.

Figure 2.6 shows for several impact parameters at 100eV the variation of probability of ionisation with distance along the trajectory path, z. These pictures clearly demonstrate that changes of state can occur well within, though not much outside, the crossing region. The change of state follows an oscillatory pattern which increases with interaction time as the impact parameter decreases.

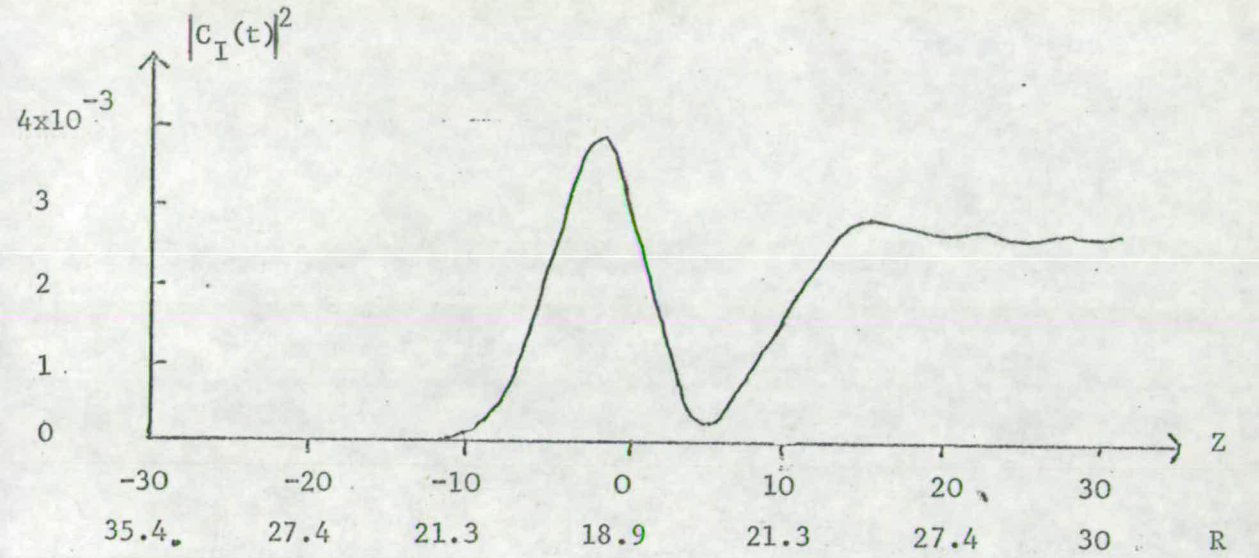

Energy = 100eV b = 18.9 a_o

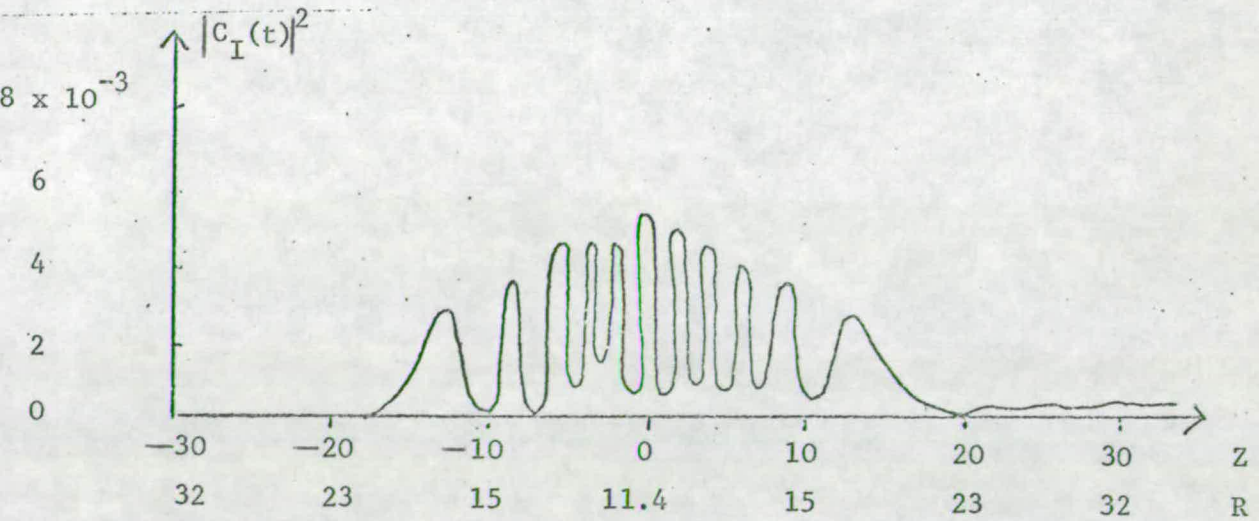

Energy = 100eV b = 11.4 a_o

FIGURE 2.6 Plots of probability of ionisation as a function of distance, Z, along the trajectory.

Plots of probability of ionisation against impact parameter for a series of energies are shown in Figure 2.7. Like the previous Figure, the probability of ionisation is very low indeed, but increases with a fall in collision energy. Once again the frequency of the oscillatory behavious of the plots increases with interaction time (i.e. lower energy).

Also plotted by the dashed curves are the ionisation probabilities predicted by the LZ theory given by equations (2.1) to (2.5). The LZ theory regards the collision as two distinct passages of the crossing whilst the eikonal approach will reveal any interference effects between the two crossings. Hence at impact parameters near the value of R_x, the greater dissimilarity between the LZ and eikonal plots will arise. Elsewhere, the LZ predicted results give a good average for the eikonal values.

This last fact is further exemplified by the plot of the ionisation total cross sections predicted by the LZ theory and the eikonal approach as a function of collision energy (Figure 2.8). The fit is much closer than the graph can possibly show and relevant points from the plot are shown in Table 2.1. As the degree of mixing is exceptionally low for this system, there is no observable peak in the total cross section plot, but the cross section does rise with a fall in collision energy.

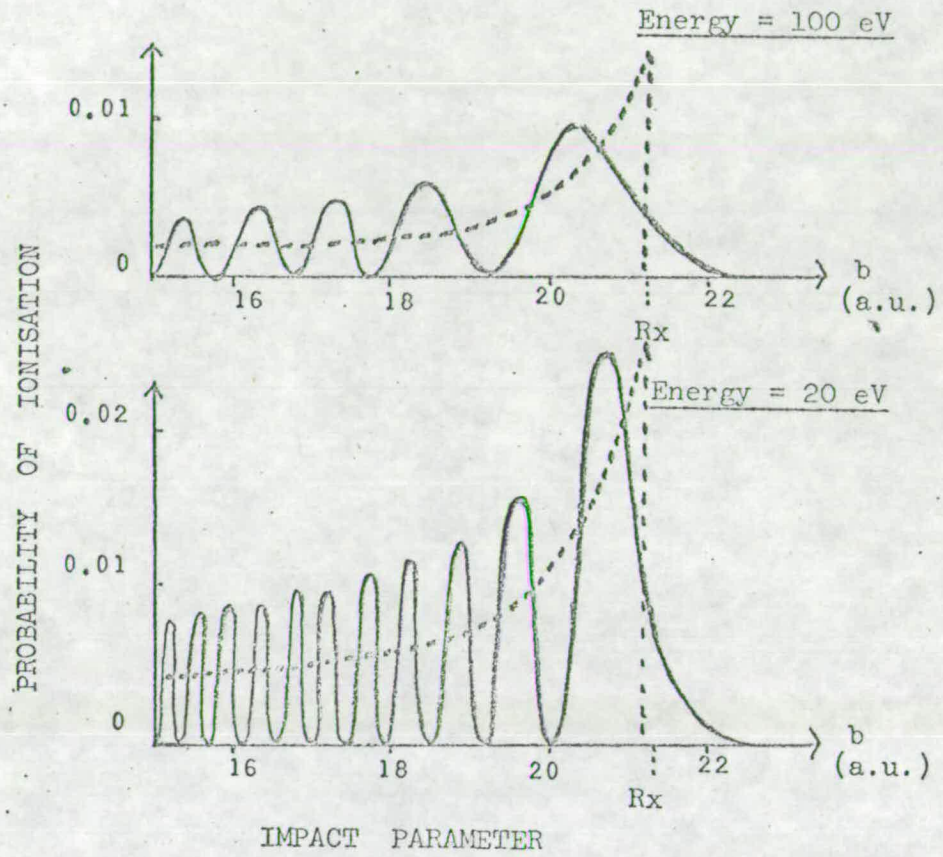

FIGURE 2.7 Probability of ionisation versus impact parameter for the system K/I.

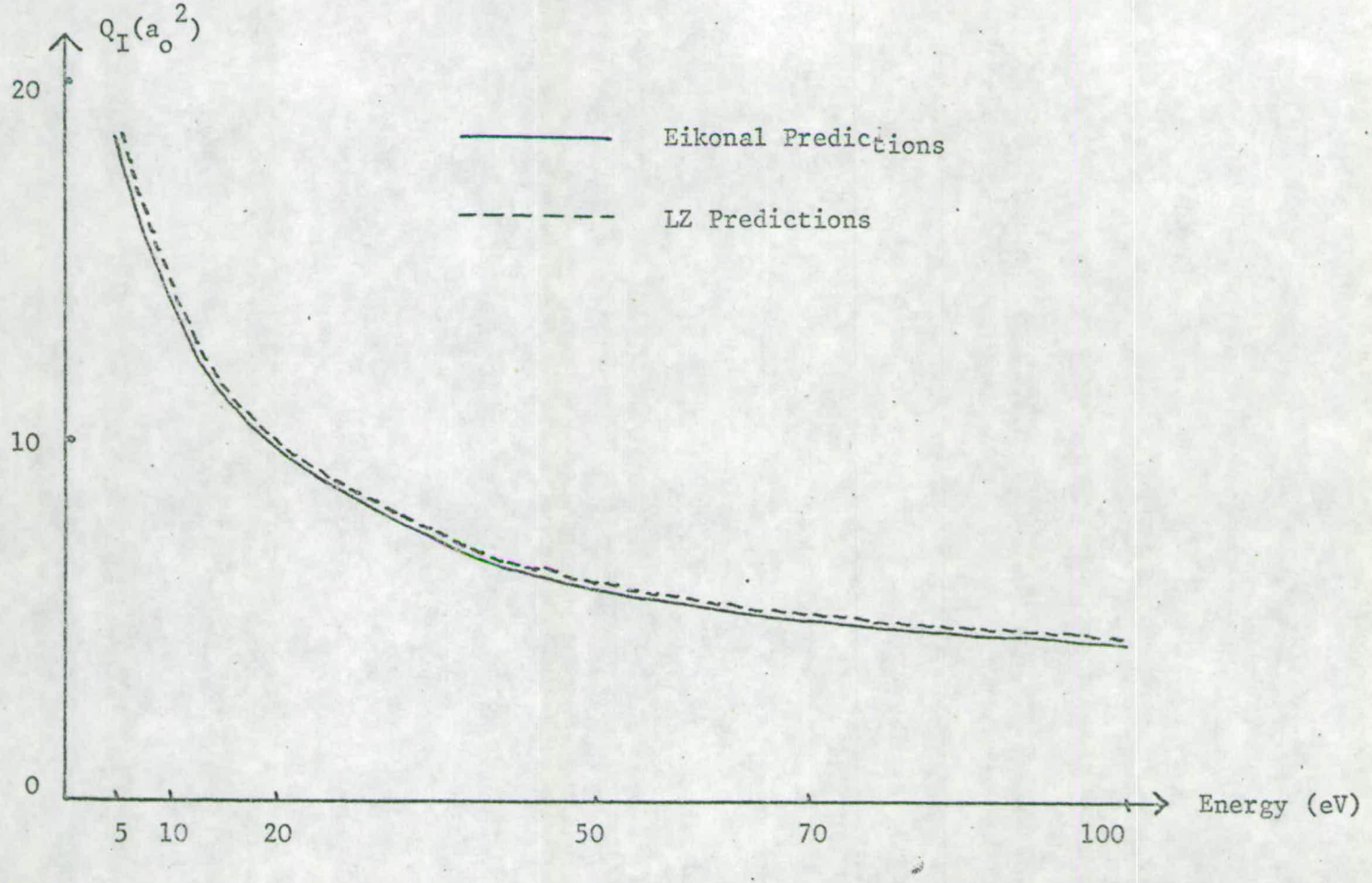

FIGURE 2.8 Total Cross Section for Ionisation, Q_I, for the System K/I as a function of Energy.

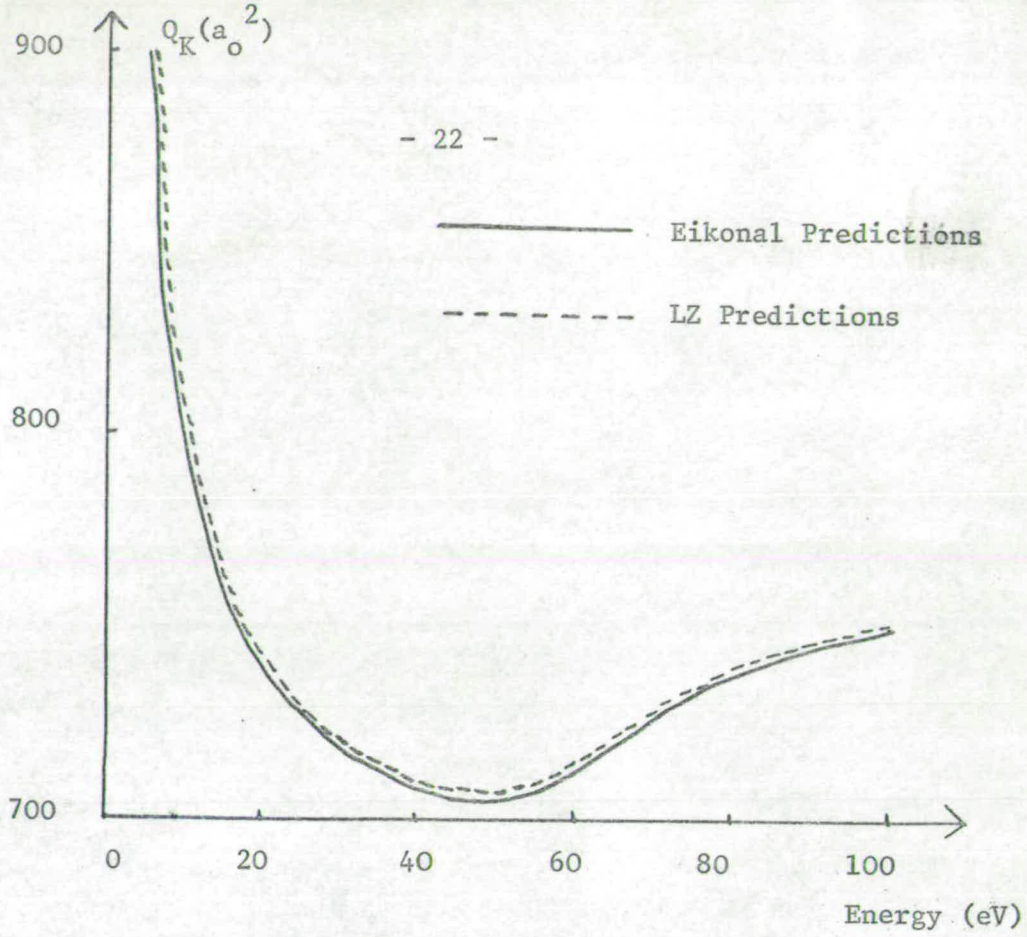

FIGURE 2.9 Total Cross Section for Neutral Scattering, Q_K, for the System K/I as a function of Energy.

Energy (eV)	Eikonal X-Section (a_o^2)	LZ X-Section (a_o^2)
100	4.44	4.50
70	5.08	5.46
50	5.97	6.46
20	9.83	10.23
10	13.84	14.34
5	18.36	20.16

TABLE 2.1 Comparison of Eikonal and LZ predictions for the total Cross Section for Chemi Ionisation.

K/I Differential Cross Sections

In order to compute the total covalent cross section and the differential cross sections for covalent and ionic scattering, it is necessary to employ partial wave theory [49,2].

Partial wave analysis utilises the fact that a plane wave of particles impinging on a target is composed of an effectively infinite set of quantum angular momentum states $\underline{\ell}$ described by angular momentum numbers ℓ. For a given trajectory of impact parameter b and velocity v, then the relationship

$$\sqrt{\ell(\ell+1)}\,\hbar = \mu v b \qquad 2.21$$

exists, where μ is the reduced mass of the system.

The total cross section for covalent scattering is given by Q_K where

$$Q_K = \frac{4\pi}{k_K^2} \sum_{\ell=0}^{\infty} A_K(\ell)^2 \,(2\ell+1)\sin^2\gamma_K(\ell) \qquad 2.22$$

where

$$k_K^2 = \frac{2\mu}{\hbar^2} E \qquad 2.23$$

E is the relative translational energy of the system. The amplitude $A_K(\ell)$ of the ℓ'th partial wave is given by

$$\sigma_K(\theta) = f_K^*(\theta)\, f_K(\theta)$$

where

$$f_K(\theta) = \frac{1}{2ik_K} \sum_{\ell=0}^{\infty} (2\ell+1)\,(A_K(\ell)e^{2i\gamma_K(\ell)}-1)\, P_\ell(\cos\theta) \qquad 2.25$$

$P_\ell(\cos\theta)$ is the Legendre polynomial.

The differential cross section $\sigma_I(\theta)$ for ionic scattering is similarly defined by

$$\sigma_I(\theta) = f_I^*(\theta)\, f_I(\theta)$$

where

$$f_I(\theta) = \frac{1}{2ik_I} \sum_{\ell=0}^{\infty} (2\ell+1)\, A_I(\ell)e^{2i\gamma_I(\ell)} P_\ell(\cos\theta) \qquad 2.26$$

The ionic phase shift is given by equation (2.20) with the added correction, whilst

$$k_I^2 = \frac{2\mu}{\hbar^2}(E - \Delta E) \qquad 2.27$$

$$A_I(\ell)^2 = |C_I(\infty)|^2 \qquad 2.28$$

The differential cross sections can now be computed using the previously determined amplitude and phase functions for trajectories down to 5 a_o, whilst below this value the random phase approximation [2] can be applied.

It helps in the computation to replace the summation in equations (2.25) and (2.26) by an integral, but care must be taken in doing so. Substitution of typical values in equation (2.21) shows that for impact parameters just greater than the value of R_x, a value of 15,000 is obtained for ℓ. The Legendre polynomial will be of this order and represents an oscillating function with angular periodicity of $2\pi/15,000$, namely 0.024 degrees.

Tests were performed to investigate the validity of replacing the summation by a numerical integration. Amplitudes and phase shifts for partial waves not evaluated by the trajectory calculations were found by interpolation of the calculated ones. The contributions to the 100eV covalent differential cross section at various angles up to 1.2 degrees from a small range, about $8a_o$, of impact parameters was calculated. This was done using the summation formula and for various integration step lengths of ℓ partial waves. Table 2.2 shows the results obtained.

At very small angles consistency of about 5% was achieved for most step length values. At larger angles, the answers diverged with increasing step length. It was decided therefore that an integration step length of no more than five partial waves should be chosen whilst the full summation would be carried out at larger angles.

The integration routine, a parabolic method, was tested using various known analytical integrations. The divergence of the two sets of answers was never more than 0.001%.

	Angle (degrees)					
1 interval	0.1	0.2	0.3	0.4	0.5	0.6
1	258665.2	10885.8	7879.9	11344.6	972.8	1250.9
2	259270.4	11015.2	7822.6	11356.1	990.2	1233.0
3	260151.7	11352.7	7641.2	11367.8	1040.3	1183.7
4	260057.7	11023.2	7868.3	11383.3	984.0	1242.3
5	260091.9	10978.2	7915.8	11419.4	987.7	1240.9
10	262070.9	11064.1	7961.3	11439.2	972.4	1256.1
15	266130.2	12836.8	7042.1	11545.3	1279.9	964.7
20	266042.1	11098.2	8211.9	11602.1	947.6	1298.6

	Angle (degrees)					
1 interval	0.7	0.8	0.9	1.0	1.1	1.2
1	1902.1	151.3	250.1	400.0	65.9	20.8
2	1899.1	156.3	241.9	396.9	68.9	18.5
3	1898.3	173.8	218.5	388.4	76.8	13.3
4	1898.2	153.2	246.1	401.0	70.4	17.9
5	1898.3	154.9	241.4	394.7	68.9	18.3
10	1893.8	151.3	241.8	392.0	69.4	17.2
15	1836.9	240.4	133.1	340.6	110.3	0.7
20	1888.4	137.5	260.1	412.3	79.7	13.2

TABLE 2.2 Effect of Varying the Partial Wave or l spacing in the numerical Integration of the Differential Cross Sections at Several Angles.

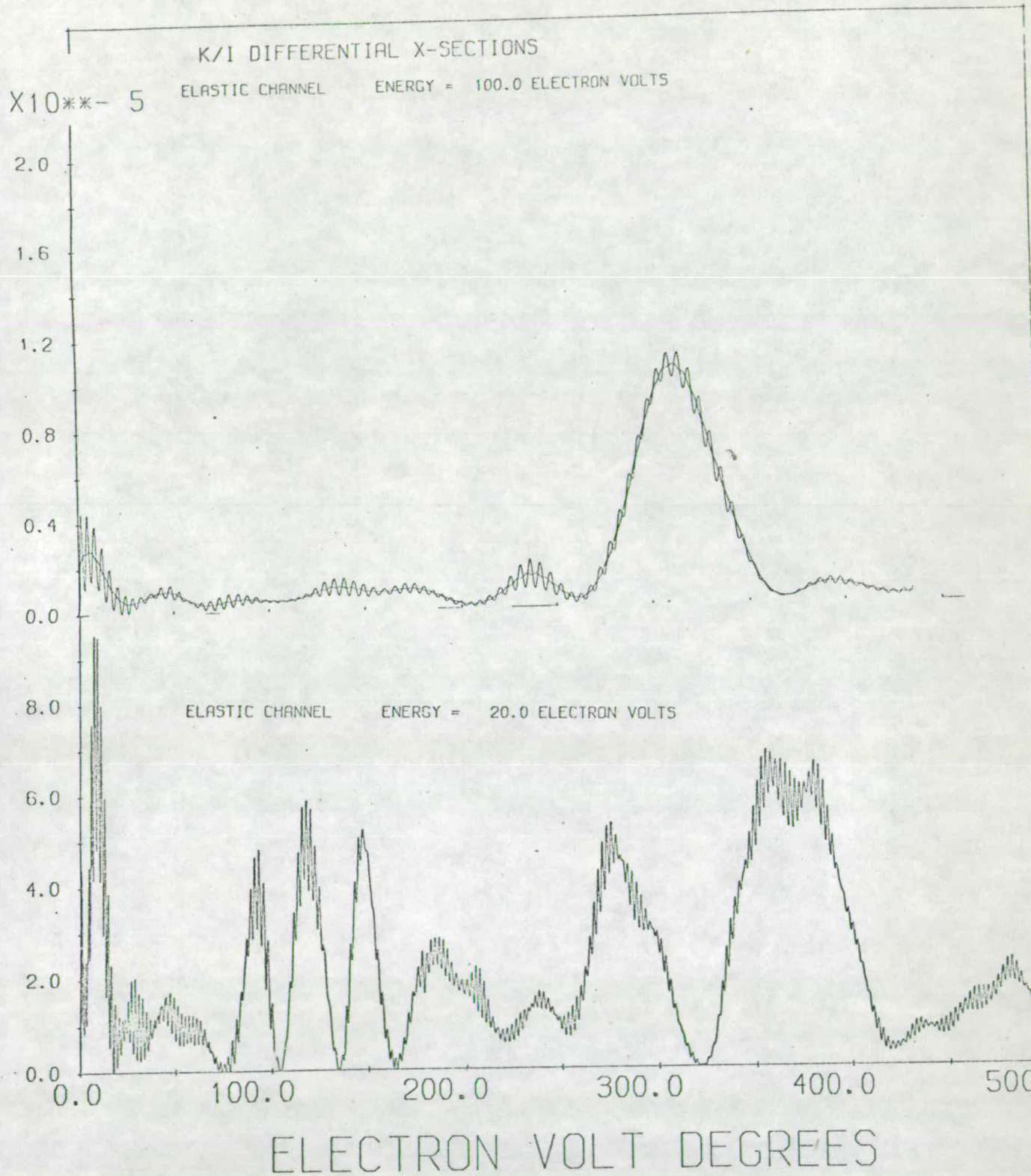

FIGURE 2.10 Differential Cross Sections for Elastic Scattering in the K/I System at 100eV and 20eV.

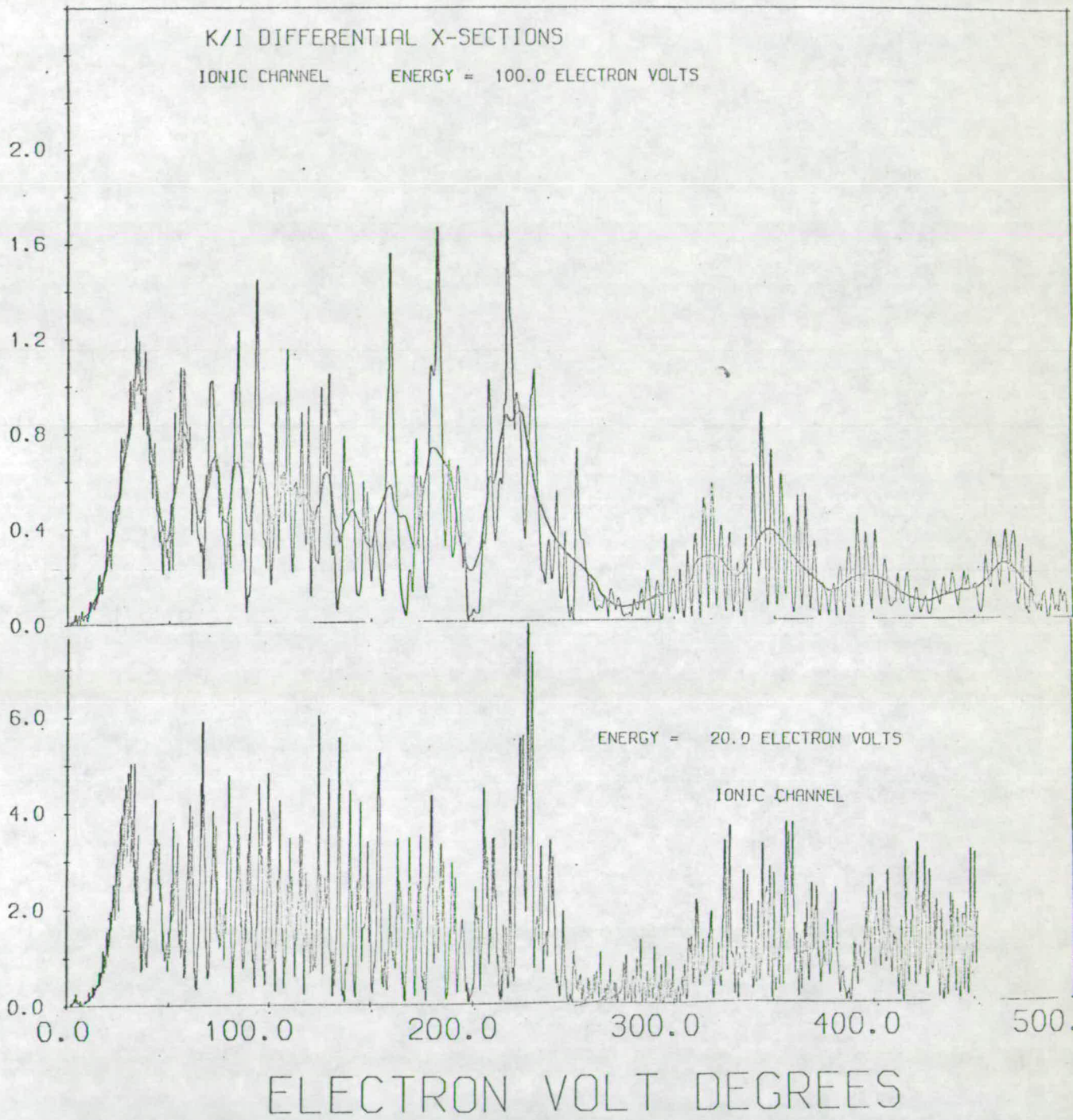

FIGURE 2.11 Differential Cross Sections for Ionic Scattering in the K/I System at 100eV and 20eV.

Results for these calculations are shown in Figure 2.10 for neutral scattering at 100eV and 20eV collision energy and in Figure 2.11 for ionic scattering at the same energies.

Interpretation of K/I Differential Cross Section Results

The differential cross sections are the results of adiabatic and non-adiabatic behaviour, and their respective contributions must be identified.

To do so, the trajectory calculations were repeated with no mixing of the two states, i.e. $H_{12}(R) \equiv 0$. The trajectories were initiated with equal unit amplitudes in each channel, and therefore two phase shift corrections (previously defined) were added to the ionic channel results. For each trajectory, the phase shifts of both channels were noted at each passage of the crossing point and at the termination of the trajectory.

Suppose p_1, p_1^1 were the phase shifts of the covalent and ionic channels at the first crossing point, p_2, p_2^1 those at the second and p_3, p_3^1 those at the end of the trajectory. The correct combination of these phase components will give all possible types of behaviour. Thus starting and finishing in the covalent state, the phase shifts for trajectories experiencing the shallow and deep wells will be given by P_{cov}^{I} and P_{cov}^{II} respectively, where

$$P_{cov}^{I} = p_3$$

$$P_{cov}^{II} = p_1 + (p_2^1 - p_1^1) + (p_3 - p_2)$$

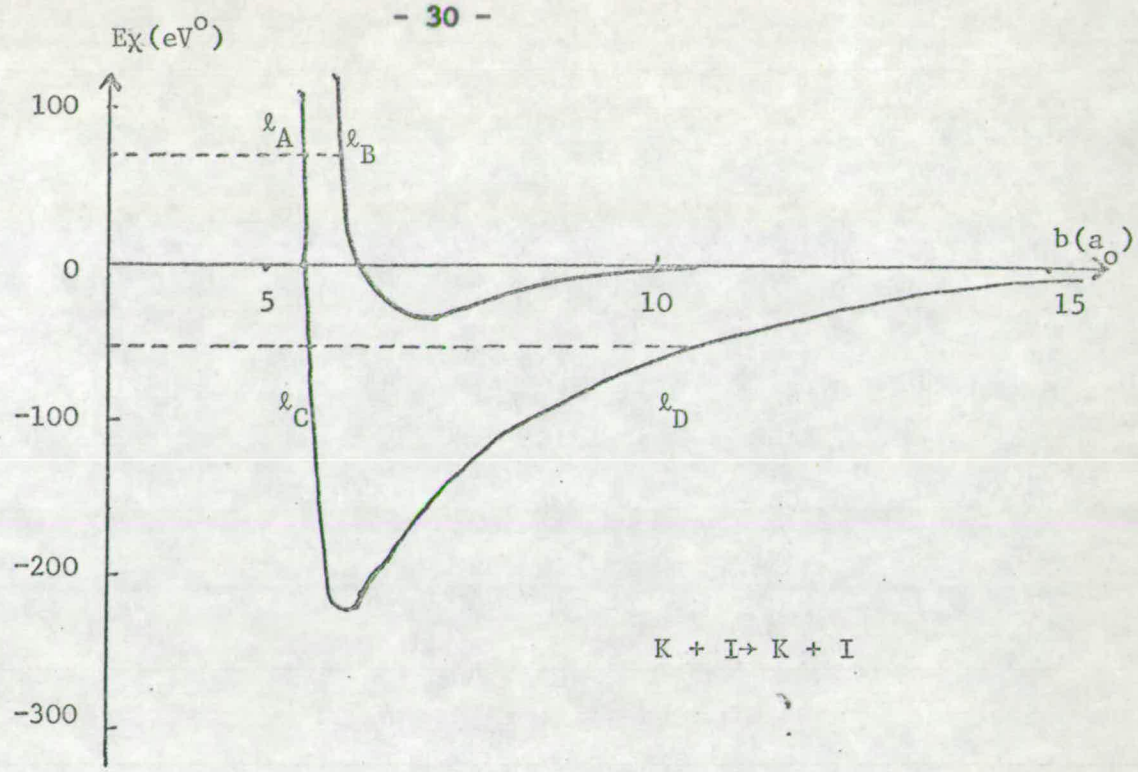

FIGURE 2.12 Deflection Functions for Shallow and Deep Well Neutral Scattering.

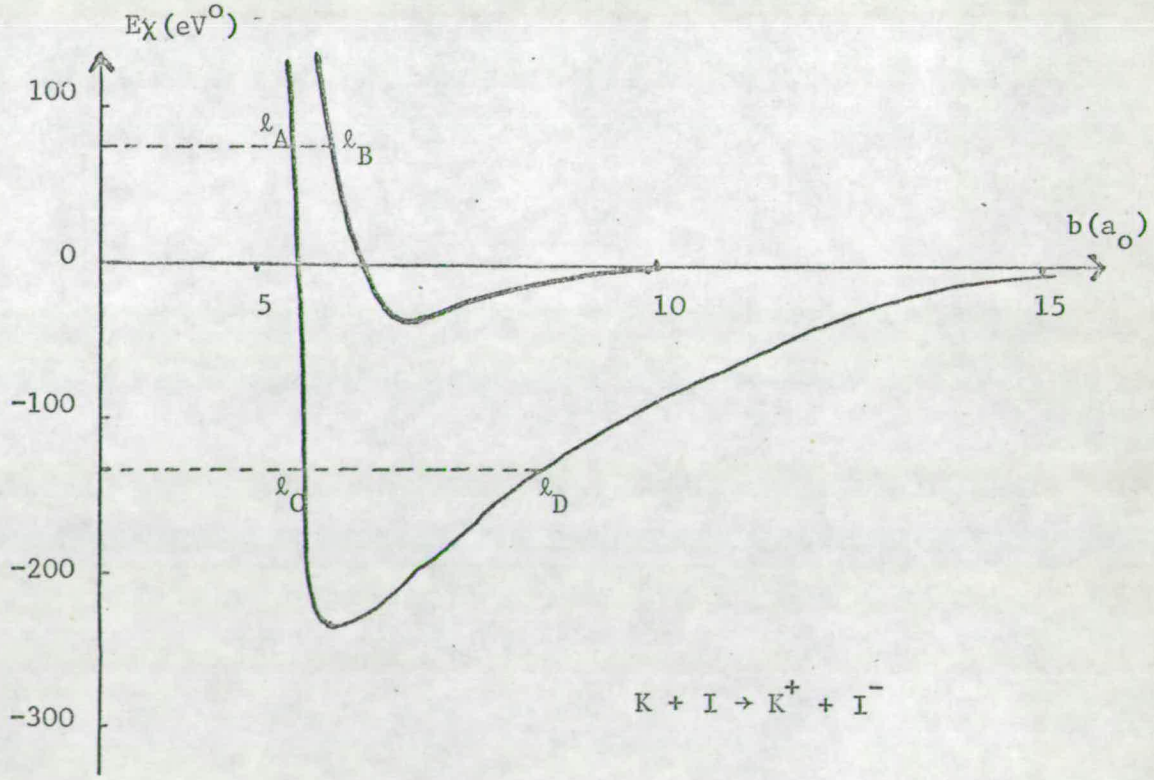

FIGURE 2.13 Deflection Functions for Shallow and Deep Well Ionic Scattering.

Knowing that the deflection function χ is given by

$$\chi = 2 \frac{d\gamma}{d\ell} \qquad 2.29$$

where γ is the relevant phase shift function, deflection curves for the above four cases can be mapped out. These are shown in Figures 2.12 and 2.13 for covalent and ionic scattering respectively.

Rainbows in the covalent scattering curves are at 34eV^{o} due to $H_{11}(R)$ and at 224eV^{o} due to $H_{22}(R)$, whilst for ionic scattering they appear at 40eV^{o} and 234eV^{o}.

From these results it is obvious that the shallow well rainbow is present at 15eV^{o} in both covalent differential cross section plots, whilst no deep well rainbow can be identified. However, as very little covalently scattered material has experienced the deeper potential, any resultant effects will be small and easily smothered by the scattering from the repulsive branch of the shallow potential. Hence the energy correspondence of the two plots breaks down after the shallow well rainbow.

The fine structure present is from contributions at ℓ_c and ℓ_D of separation $\Delta\ell$. The periodicity $\Delta\theta$ of this structure, ranging from 0.04 to 0.055 degrees at 100eV can be predicted from the formula

$$\Delta\theta = 2\pi / \Delta\ell \qquad 2.30$$

This yields a $\Delta\ell$ value of 8600 to 6500 partial waves, and the energy dependence of this feature behaves as expected.

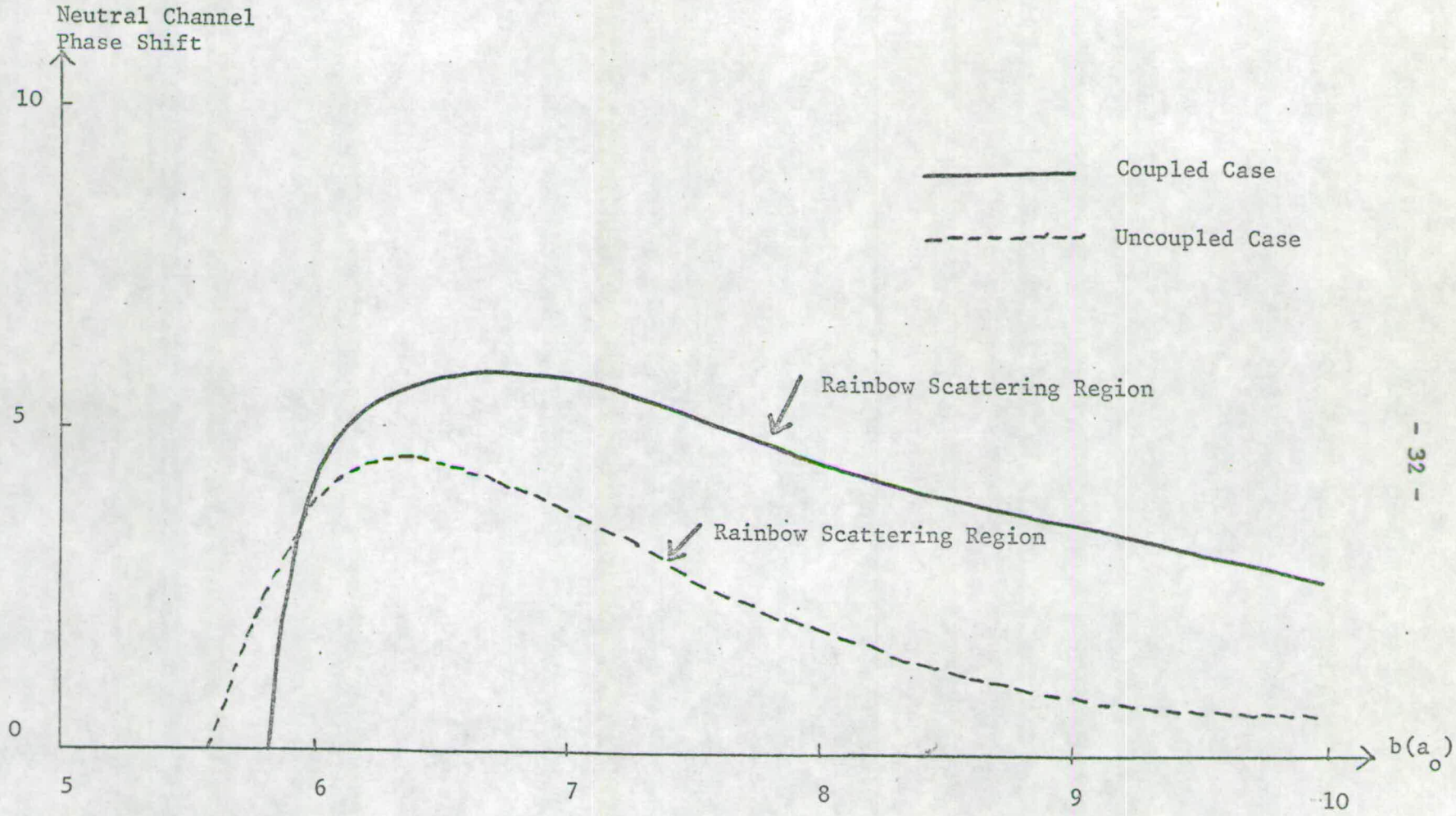

FIGURE 2.14 Effect of Coupling of the Two States on the Neutral Channel Phase Shift.

The two rainbows in the ionic differential cross section might be expected to appear more distinctly than in the covalent cross section. The energy scaling of the cross sections at 100eV and 20eV are almost exact with shallow and deep well rainbows at 36eV° and 230eV° respectively, as predicted by Figure 2.13. There appears a fairly regular periodicity, about 12eV°, in the structure between the rainbows, derived from scattering branches ℓ_C and ℓ_D. After the second rainbow, scattering occurs from the two repulsive branches. As the angle of scattering increases, the separation of the two interfacing branches ℓ_A and ℓ_B will decrease, and, according to equation (2.30), the angular separation between the maxima in the differential cross section plots should increase. This is in fact observed.

One problem is that results for the uncoupled cases predict larger rainbow angles for shallow well scattering in both channels. This can be explained by Figure 2.14 where the phase shifts for trajectories in the coupled and uncoupled cases are shown as a function of impact parameter. Around the range of impact parameters contributing to rainbow scattering, coupling will cause the phase shifts to increase due to the pull of the deeper potential. However, the relative increase in the phase shift curve is greater for trajectories of higher impact parameter, where coupling to the ionic channel is greater and the slope of the curve becomes less. Hence a much lower rainbow angle will result. For deep well scattering, the

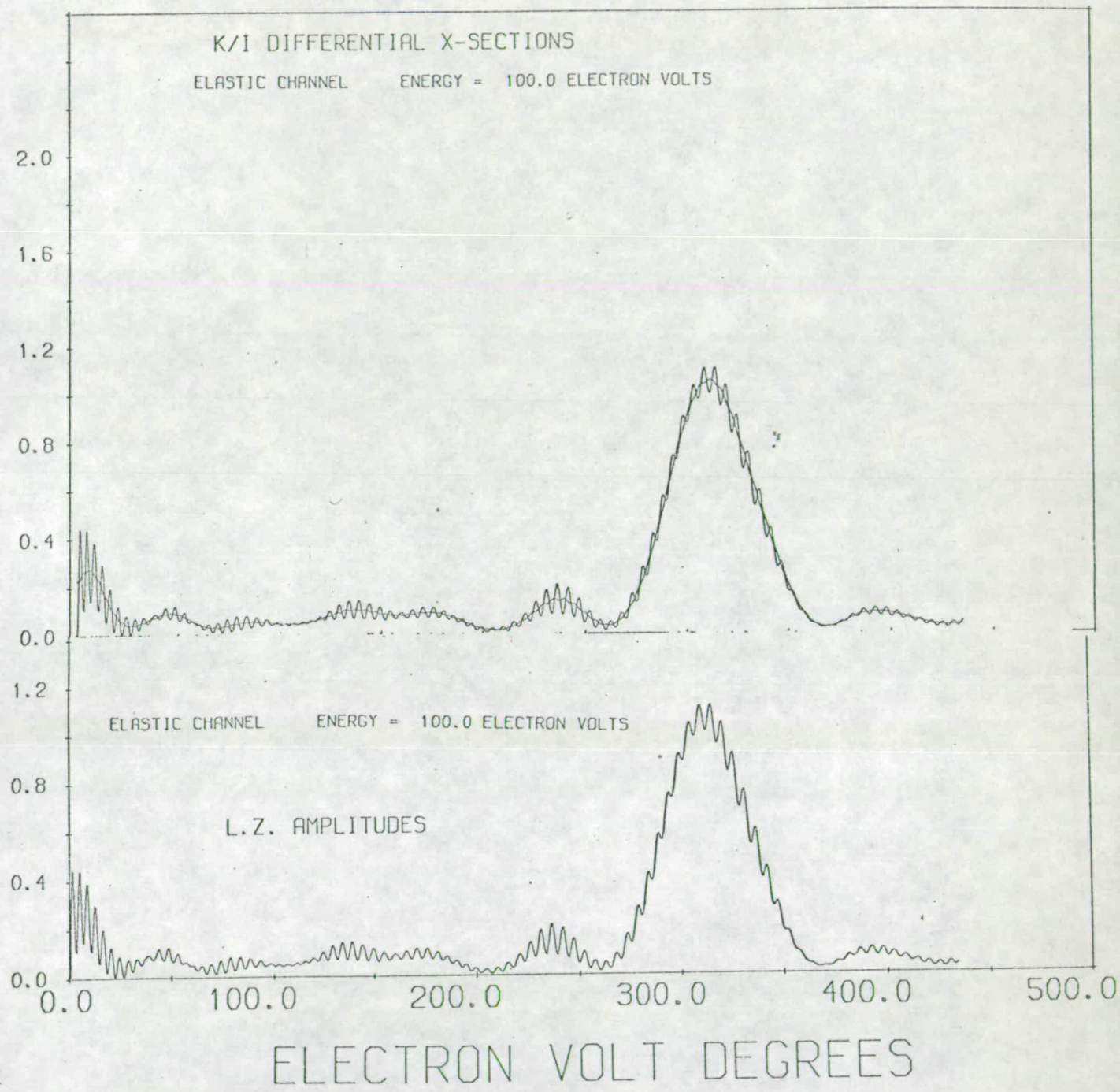

FIGURE 2.15 Elastic Differential Cross Sections at 100eV for K/I using (top) eikonal amplitude and phase shifts and (lower) using LZ amplitudes and eikonal phase shifts.

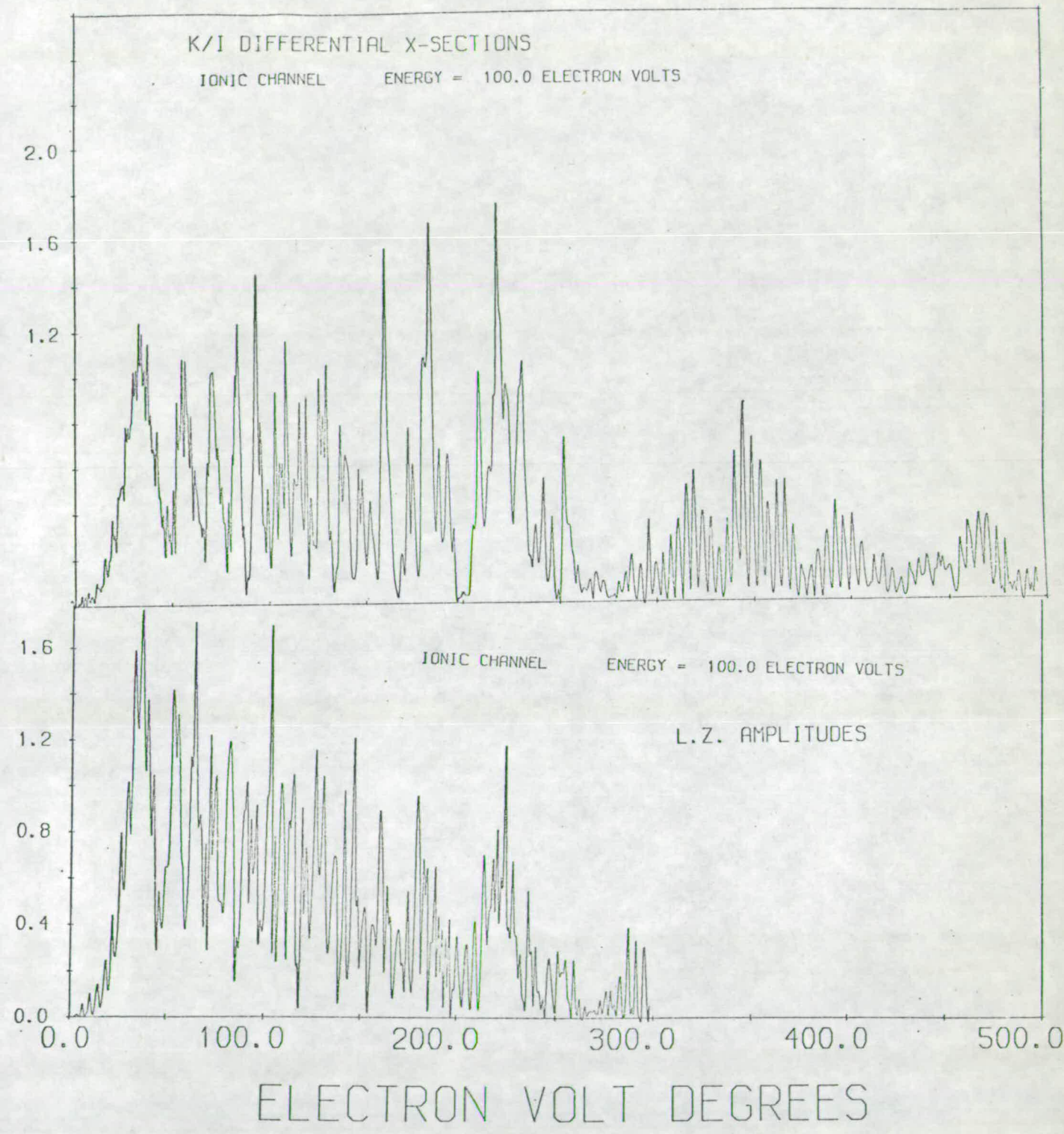

FIGURE 2.16 Ionic Differential Cross Sections at 100eV for K/I using (top) eikonal amplitude and phase shifts and (lower) using LZ amplitudes and eikonal phase shifts.

effect of coupling to the very shallow well is negligible, and rainbows predicted in both coupled and uncoupled cases for the ionic channel are in good agreement.

The differential cross sections for neutral and ionic scattering were found for a collision energy of 100eV using scattered wave amplitudes predicted by the LZ theory and phase shifts calculated from the eikonal approach. These are compared with cross sections using amplitudes and phase shifts from the eikonal approach in Figure 2.15 for neutral scattering and Figure 2.16 for ionic scattering.

The covalent curves are both identical, but that is not surprising for their wave amplitudes differ by less than one per cent from unity. Using both amplitudes in equation (2.25) will reveal no detectable difference.

The corresponding ionic curves agree in that peaks occur at the same angles, but the respective peak heights do not match. Both amplitudes, however, have been shown to differ considerably and as the cross sectional plots are based on equation (2.26), the respective peak heights cannot be expected to match.

The Collision System K/I_2

The interesting feature of the collision system K/I_2 is that unlike K/I, the coupling between the covalent and ionic states is quite strong at the crossing.

In studying this system, the iodine molecule is regarded as a sphere, and hence the rotational and vibrational motions of the molecule are not considered. Also, the possibility of molecular dissociation is disregarded. Otherwise the same model has been assumed as for the K/I case and the relevant equations are again (2.11) and (2.12). However, the forms of $H_{11}(R)$, $H_{22}(R)$ and $H_{12}(R)$ used therein have to be redefined.

Using atomic units of energy where $\hbar = 1$,

$$H_{11}(R) = 4\varepsilon \left\{ \left(\frac{\sigma}{R}\right)^{12} - \left(\frac{\sigma}{R}\right)^{6} \right\} \qquad 2.31$$

where

ε = 0.01 atomic units of energy

σ = 6.5 a_o

The ionic potential $H_{22}(R)$ is assumed to have the same form as before but the electron affinity for the iodine molecule will cause a change in the attractive branch. Several often widely varying values for this quantity have been quoted, but the one chosen was 2.3eV [50]. Effecting this change in equation (2.14) yields the ionic potential form.

Use of the above two potential forms involves a crossing distance of 13.4 a_o. The shape of $H_{12}(R)$ as obtained from equation (2.16) was scaled accordingly to meet Moutinho's suggested value of 0.04eV [48].

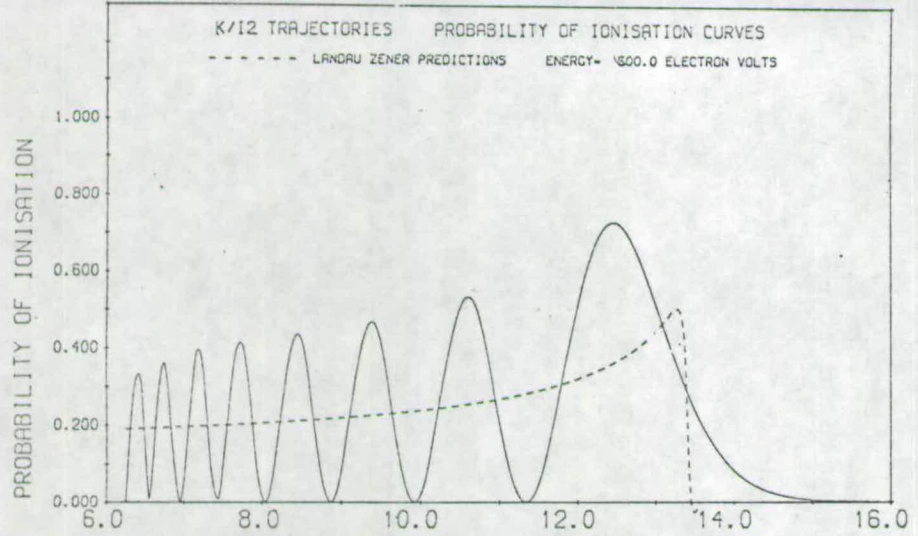

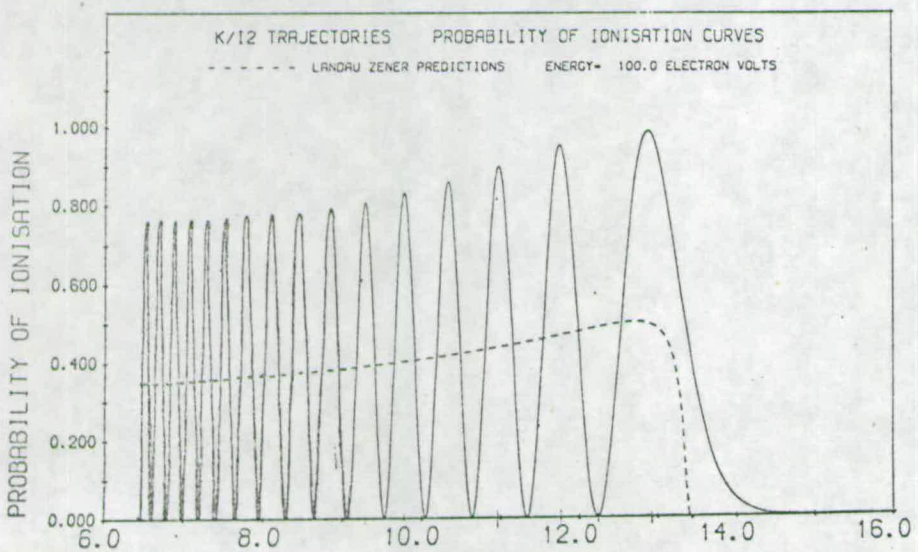

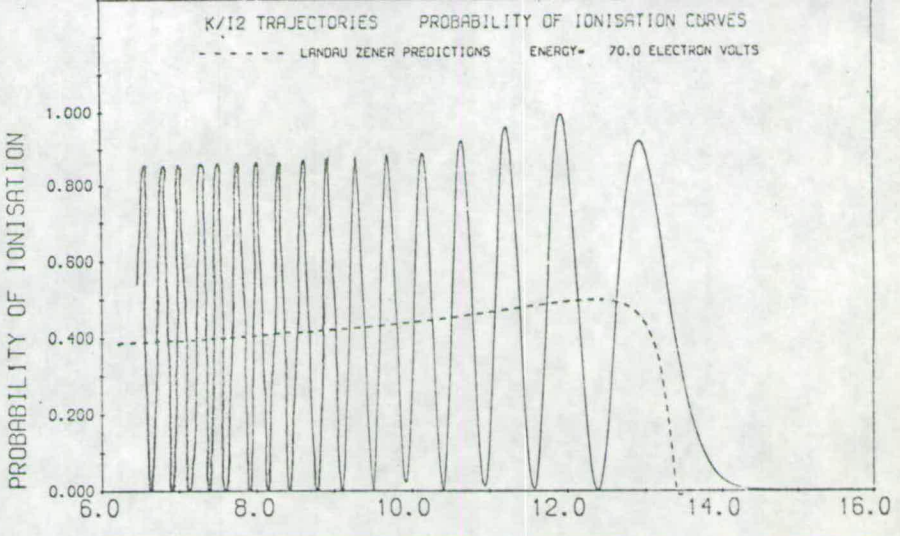

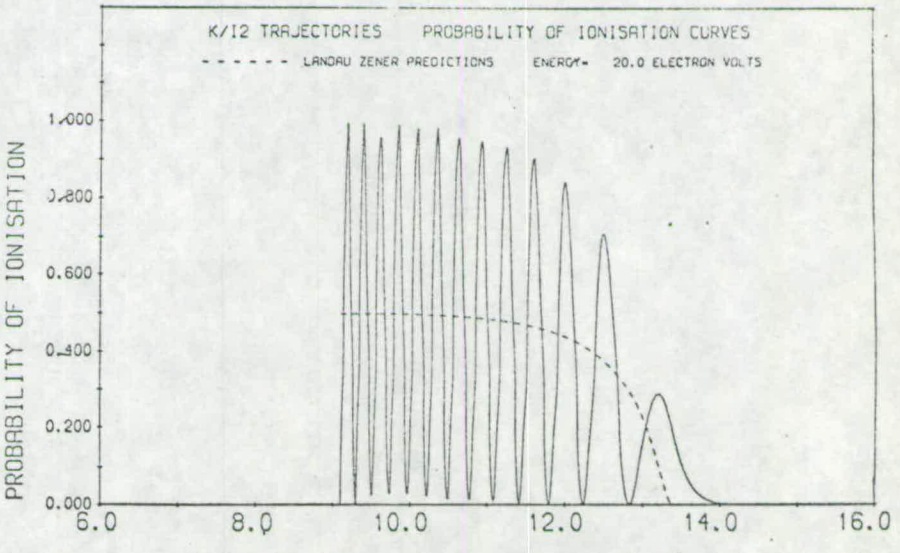

FIGURE 2.17 Probability of ionisation against Impact Parameter for the K/I_2 System.

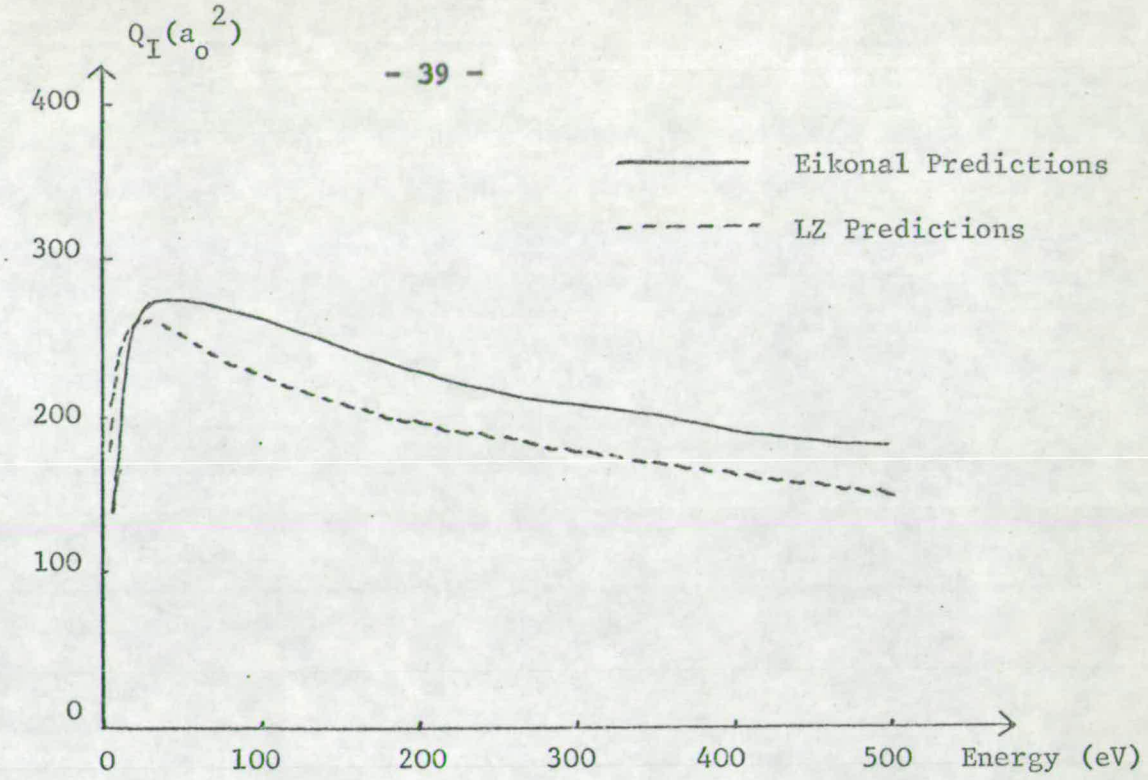

FIGURE 2.18 Total Cross Section for Ionisation Q_I for the System K/I_2 as a Function of Energy.

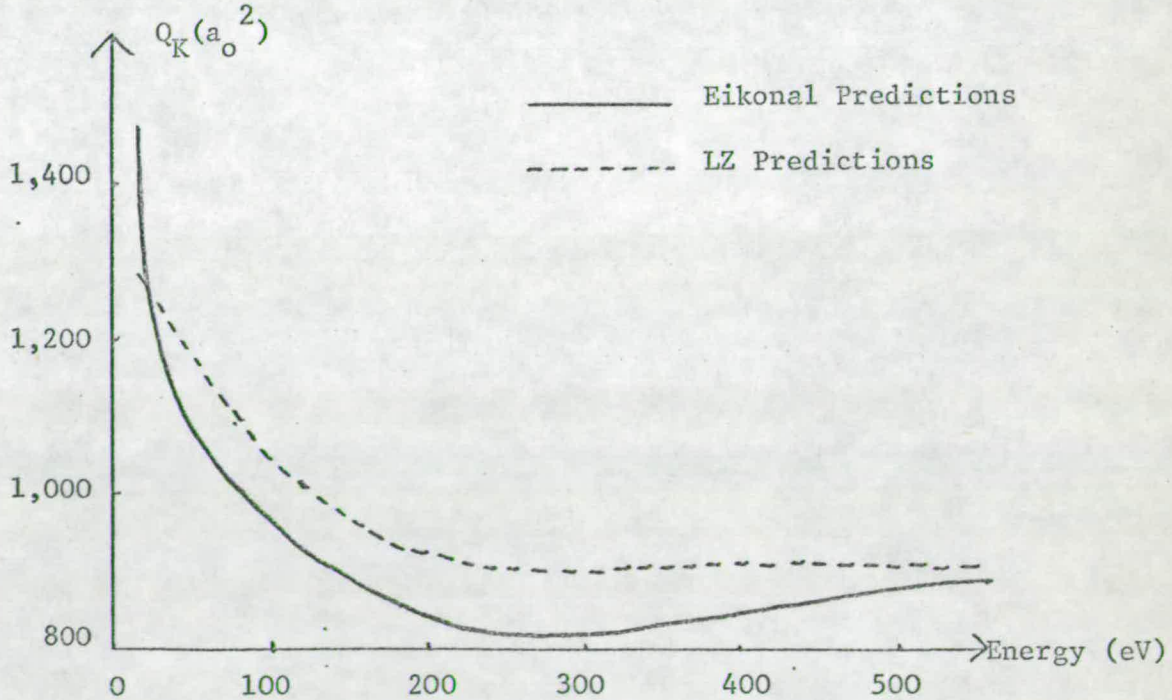

FIGURE 2.19 Total Cross Section for Neutral Scattering, Q_K, for the System K/I_2 as a Function of Energy.

The same computational precautions were observed and calculations for this system were performed for relative collision energies of 10eV to 500eV.

Figure 2.17 shows for a series of collision energies the dependence of ionisation probability on impact parameter, whereas Figures 2.18 and 2.19 show the total cross sections for ionic and covalent scattering respectively. Results predicted by the LZ theory are shown by the dashed curves.

It is obvious that mixing of the two states has much increased and the two types of cross section are of the same magnitude. The peak in the ionic total cross section occurs at an energy of about 30eV, where for most trajectories the mixing of the two states is at a maximum.

K/I_2 Differential Cross Section Results

The differential cross sections for covalent and ionic scattering at collision energies of 100eV and 20eV for the system K/I_2 are shown in Figures 2.20 and 2.21. In the plots for neutral scattering the very low angle peaks are much larger than shown and are cut off at a cross section value of 2×10^5. This was done to follow the much less intense peaks occurring in the differential cross section at larger angles.

Again trajectory calculations were performed for the uncoupled case to find the adiabatic and non-adiabatic rainbows for

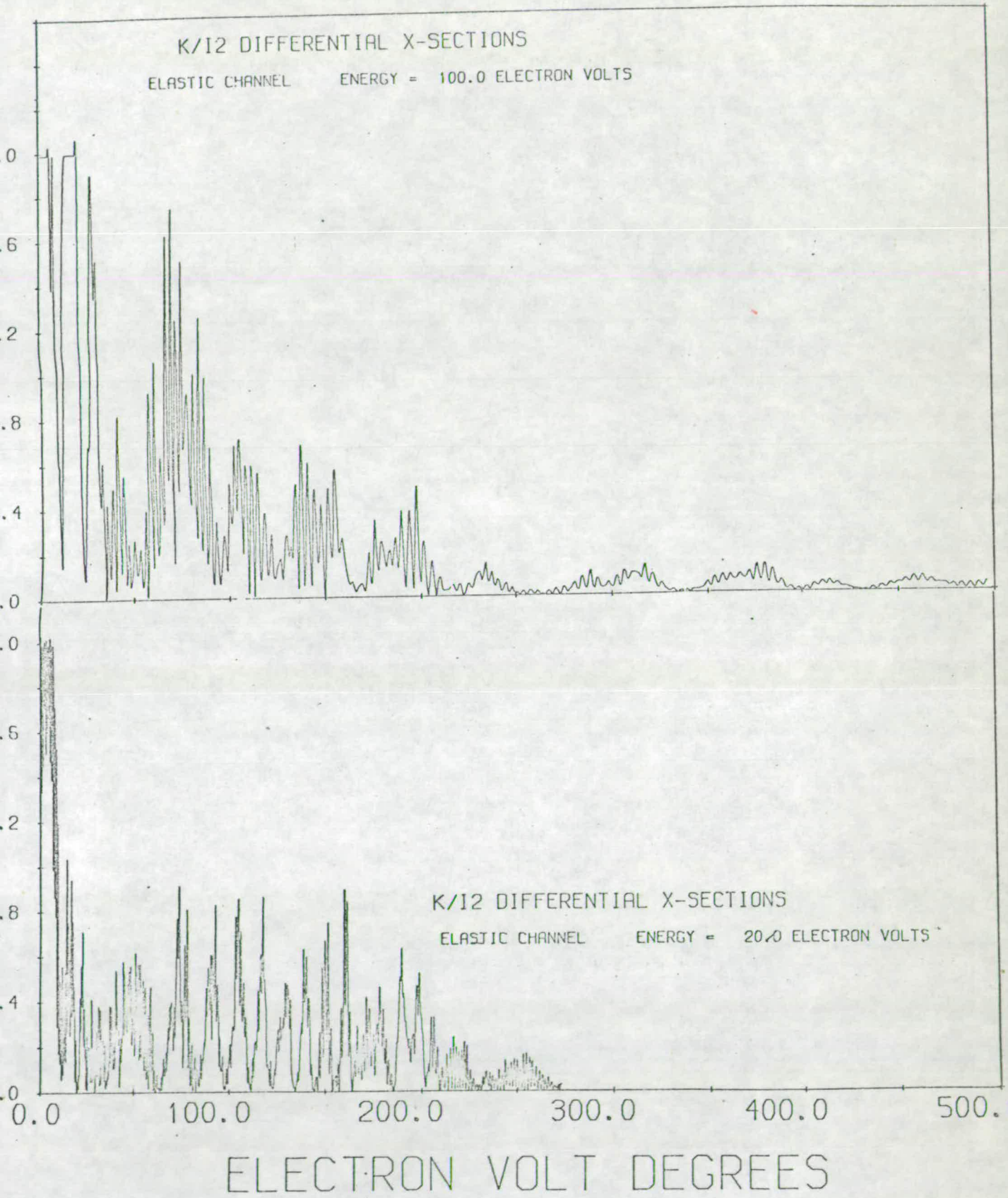

FIGURE 2.20 Differential Cross Sections for Elastic Scattering of the K/I_2 System.

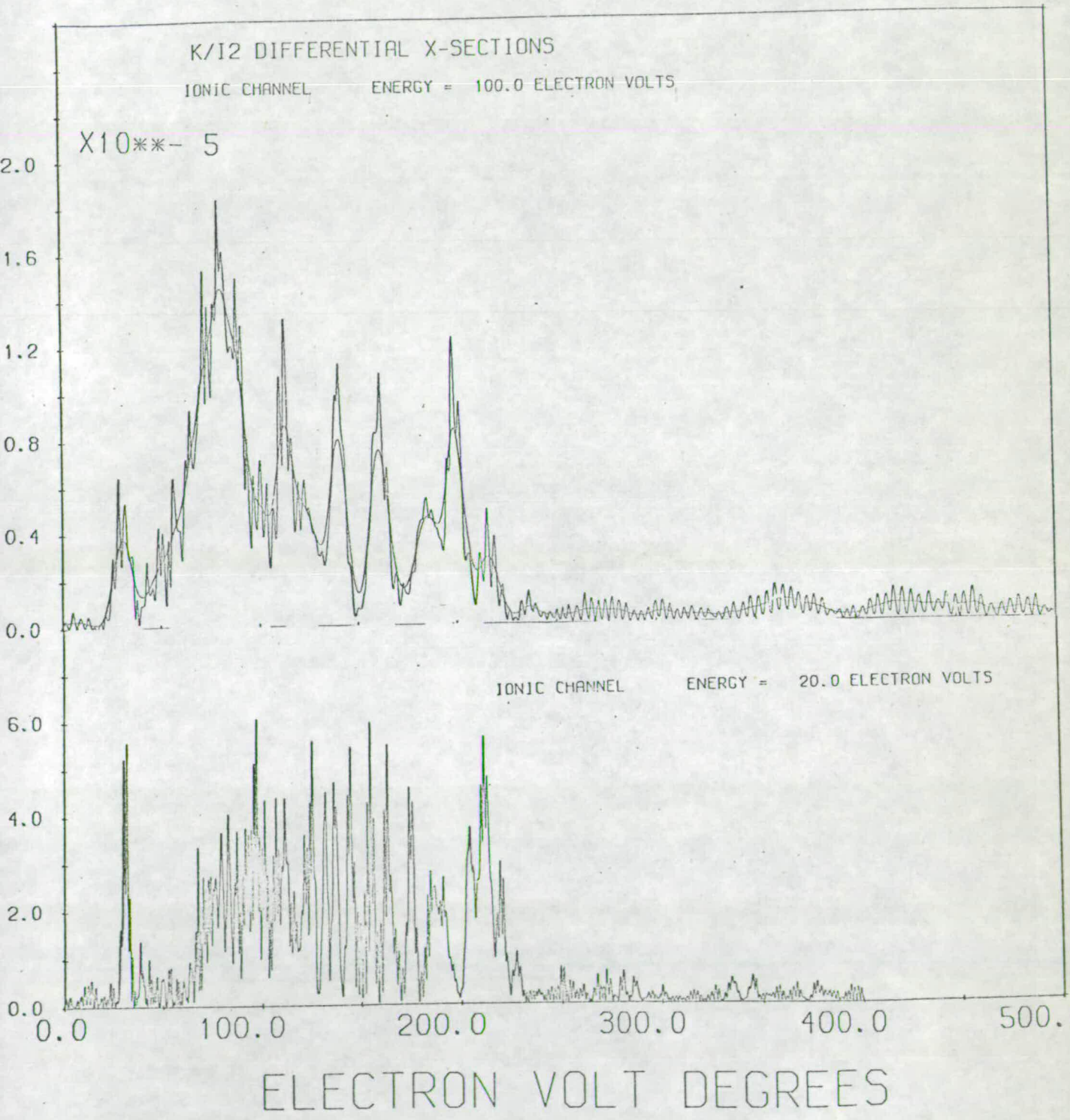

FIGURE 2.21 Differential Cross Sections for Ionic Scattering in the K/I_2 system.

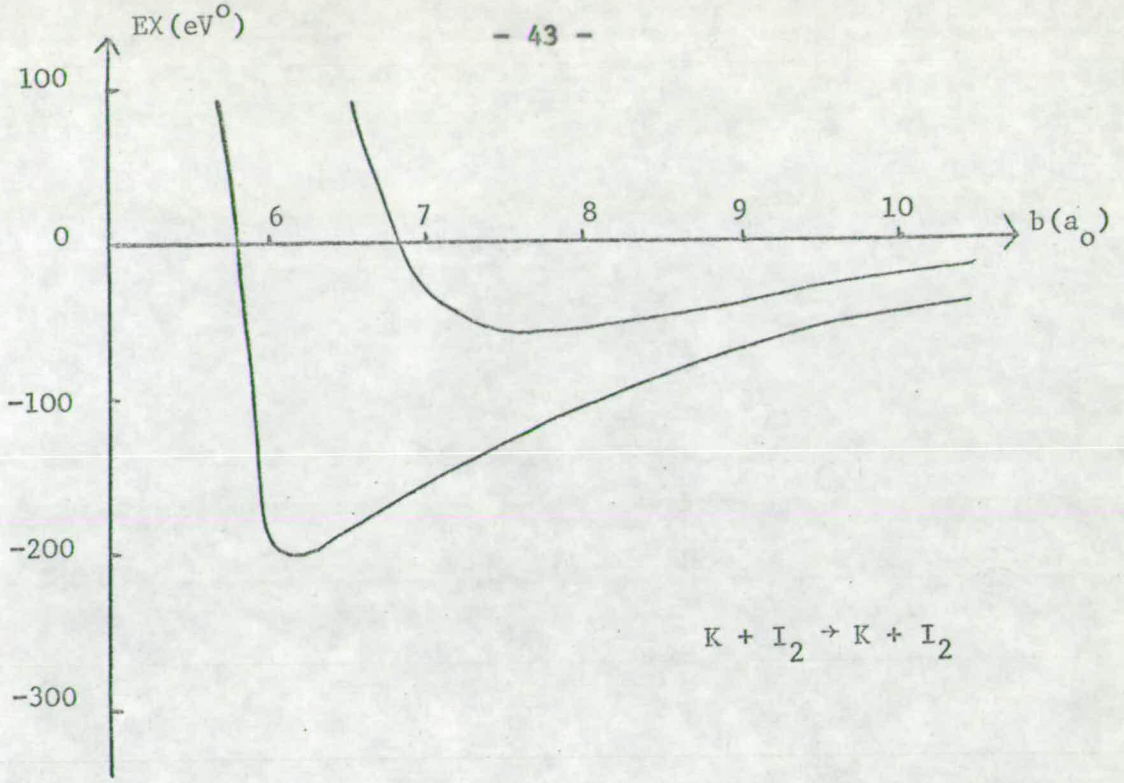

FIGURE 2.22 Deflection Functions for Shallow and Deep Well Neutral Scattering.

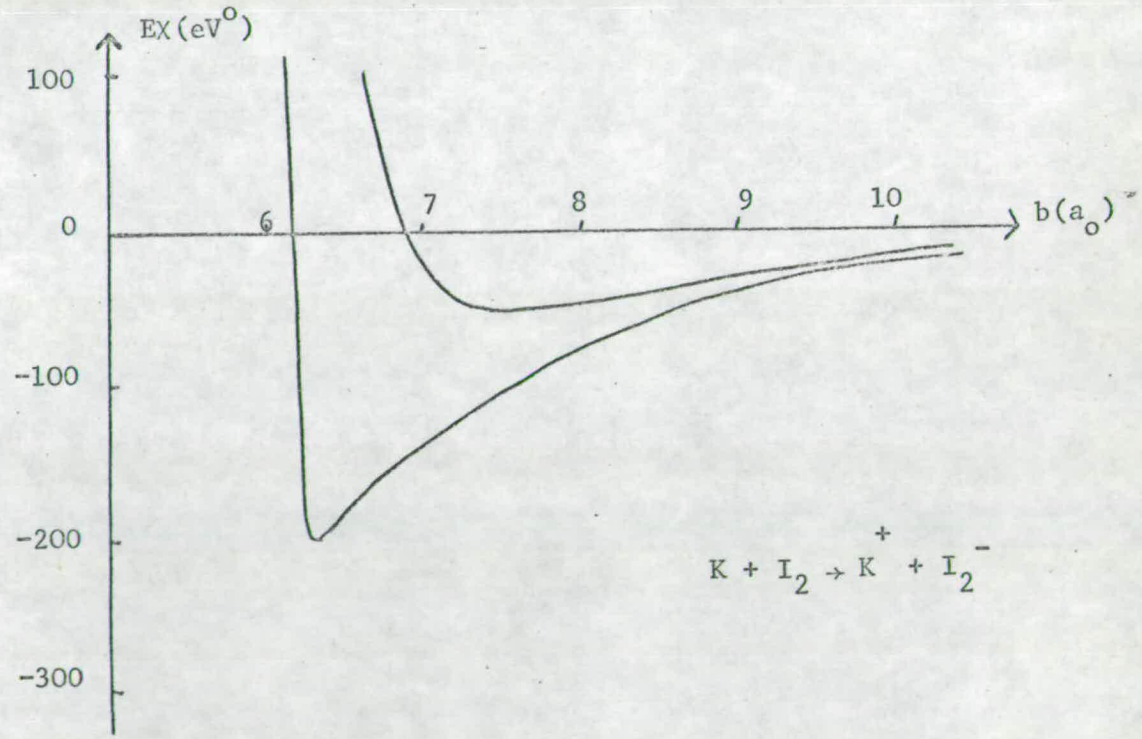

FIGURE 2.23 Deflection Functions for Shallow and Deep Well Ionic Scattering.

both types of scattering (Figures 2.22 and 2.23). The shallow and deep well rainbows for covalent scattering are predicted at 50eV° and 195eV° respectively, and these appear in the 20eV cross section plot. Those for ionic scattering are predicted at 45eV° and 205eV° respectively. In the coupled case they appear at 40eV° and 210eV°.

However, the 100eV differential cross section for covalent scattering cannot be explained by the above treatment.

An interesting phenomenon occurs when the phase shifts for the covalent channel are investigated (Figure 2.24). At low energies such as 20eV, the phase shift is similar to the usual semiclassical function, whilst at higher energies of 100eV and 500eV there are distinct fluctuations present. (These have also been found by Kupperman [51] in solving a two state time dependent problem using an alternative formulation). These are due to the relative mixing of the two states, as can be seen from 100eV case in Figure 2.25, where the phase shift curve for the coupled case is compared to that for shallow well covalent scattering.

The deflection function corresponding to the coupled phase shift curve is shown in Figure 2.26. All the maxima in the deflection function occur when the scattered amplitude for the covalent channel is at a minimum. Conversely the minima in the deflection function appearing at impact parameters below 12 a_o arise when the scattering amplitude is at a maximum. The deflection function minimum arising at an impact parameter of 12.8 a_o corresponds

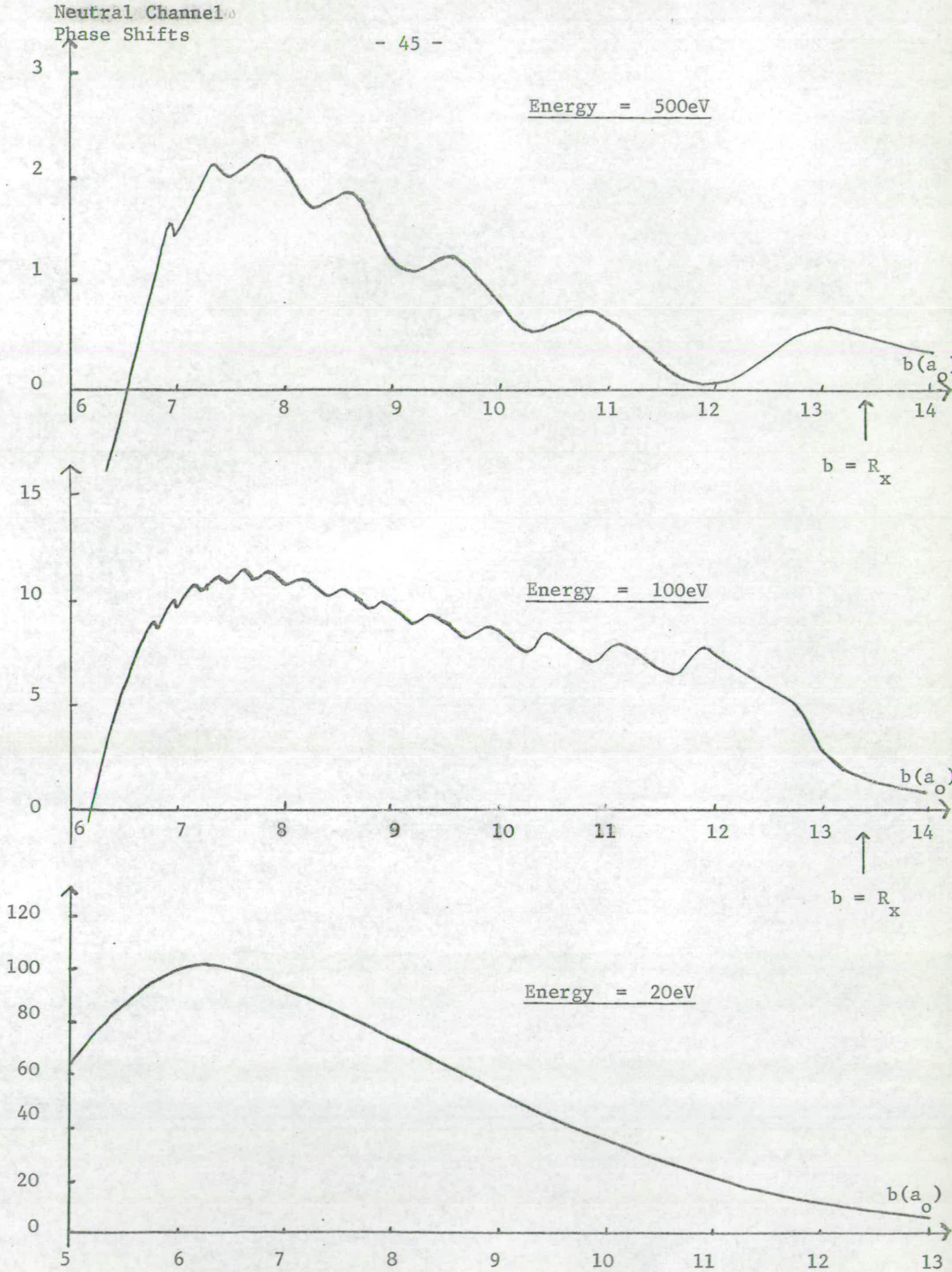

FIGURE 2.24 Variation of the Neutral Channel Phase Shift of System K/I_2 with Energy.

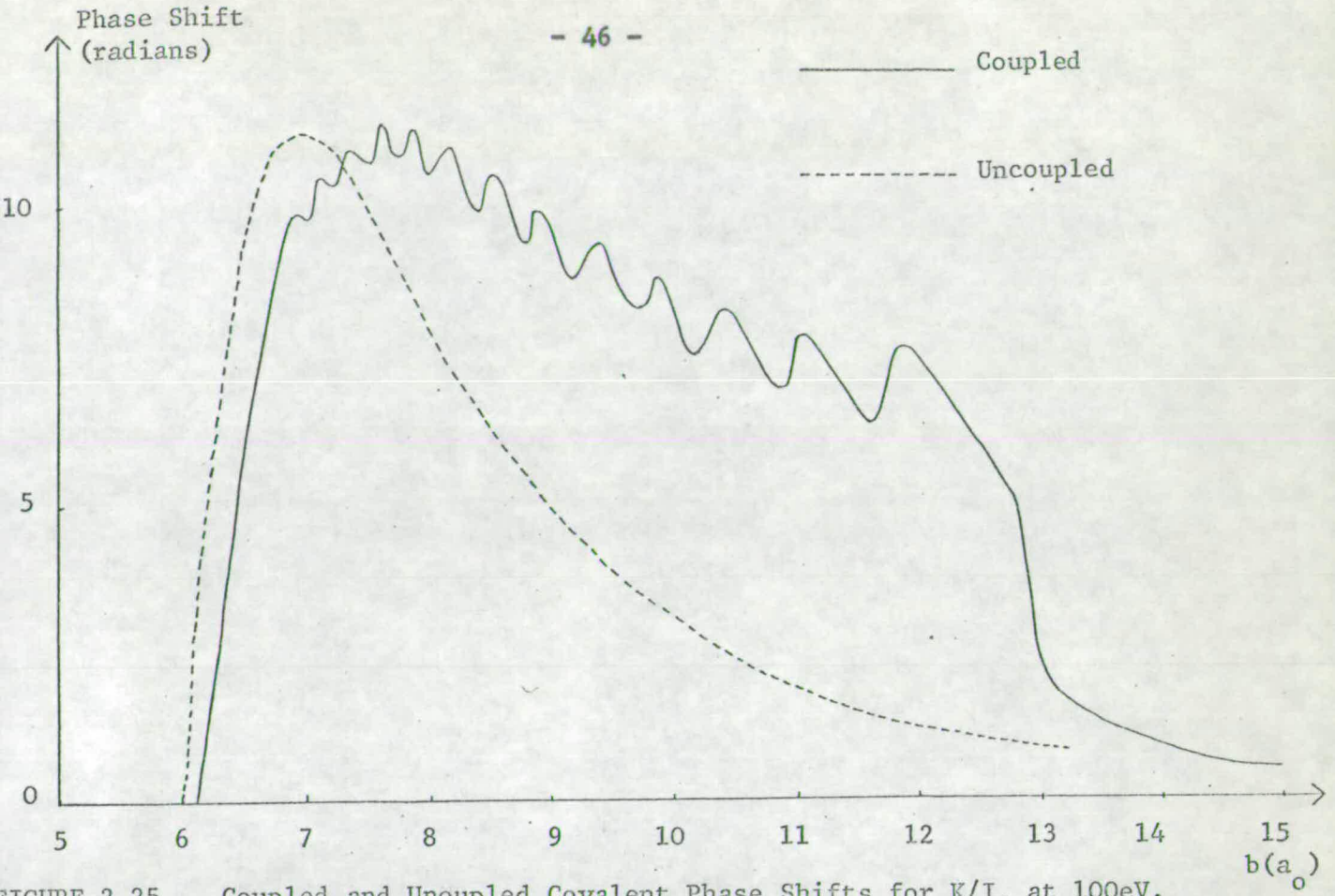

FIGURE 2.25 Coupled and Unoupled Covalent Phase Shifts for K/I_2 at 100eV.

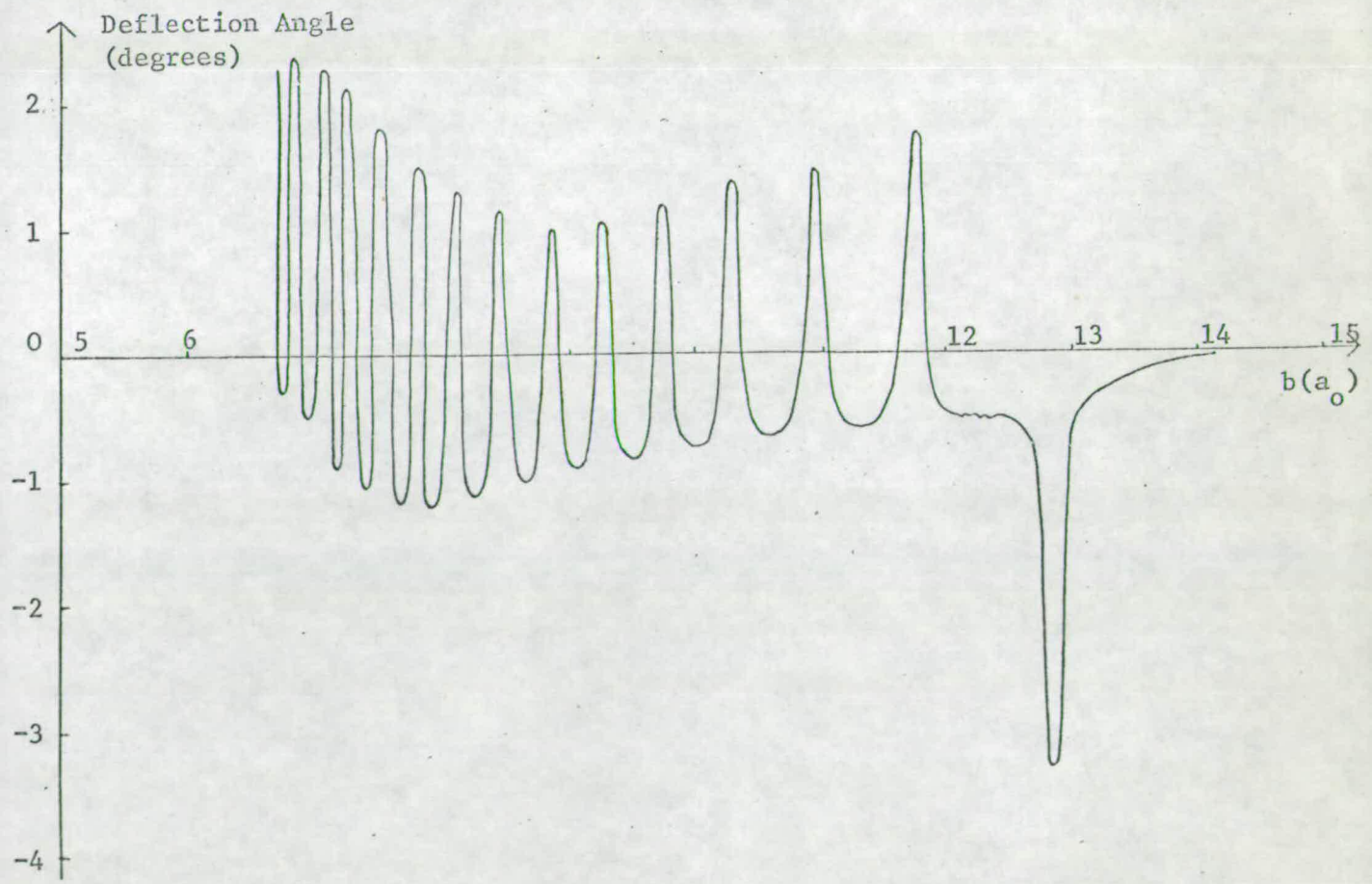

FIGURE 2.26 Deflection Curve corresponding to the Coupled Phase Shift.

Impact Parameters (a_o) for			
χ(max)	χ(min)	A_K(max)	A_K(min)
	12.85		12.92
11.725			11.775
	11.30	11.25	
10.95			10.95
	10.60	10.65	
10.30			10.37
	10.05	10.05	
9.75			9.75
	9.50	9.55	
9.27			9.275
	9.05	9.05	
8.83			8.85
	8.60	8.65	
8.45			8.45
	8.25	8.28	
8.10			8.10
	7.90	7.95	
7.78			7.78
	7.65	7.65	
7.50			7.53
	7.40	7.40	
7.25			7.28
	7.18	7.19	
7.05			7.08
	6.96	6.97	

TABLE 2.3 The Correspondence between the extrema in the deflection function and the extrema in the scattered wave amplitude for the neutral channel of the K/I_2 system. (Energy = 100eV).

to a minimum in the scattering amplitude. Hence no rainbow arises from this branch of the deflection function. The above features can be observed by comparing Figures 2.26 and 2.17 and from Table 2.3.

Not only does the magnitude of a branch of the semiclassical differential cross section depend on the scattered amplitude of the waves, but also on the reciprocal of $d\chi/db$. This differential remains very large round the minima in the deflection function, and hence contributions from these regions have a lower weight.

Further, several minima appear in the deflection function between scattering angles of 0.6 to 1.2 degrees, and these form another series of peaks between 60 and 120eV^{o} in the covalent differential cross section plot at 100eV. This is not so in the 20eV case due to the smooth phase shift function obtained.

The covalent and ionic differential cross sections are shown in Figures 2.27 and 2.28 in comparison to the differential cross sections obtained when the scattered wave amplitudes are those obtained from the LZ theory. Peaks occur at approximately the same angular scattering positions, but the heights of the two sets of corresponding peaks are quite different. This is most apparent for the shallow well rainbow in the ionic curves.

The theoretical and experimental results for neutral scattering in the K/I_2 system will be compared in Chapter 6.

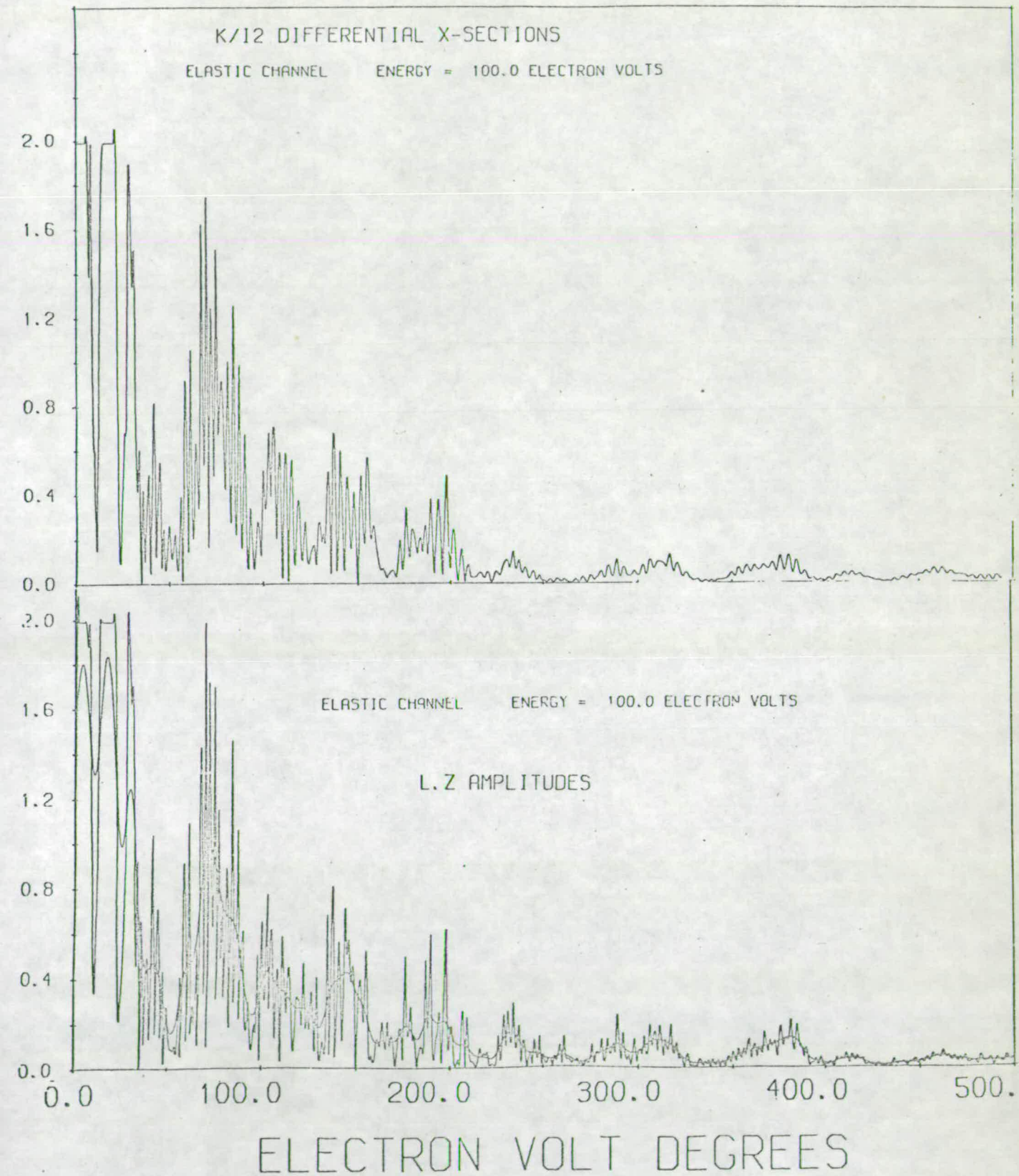

FIGURE 2.27 Elastic Differential Cross Sections at 100eV for K/I_2 using (top) eikonal amplitudes and phase shifts and (lower) using LZ amplitudes and eikonal phase shifts.

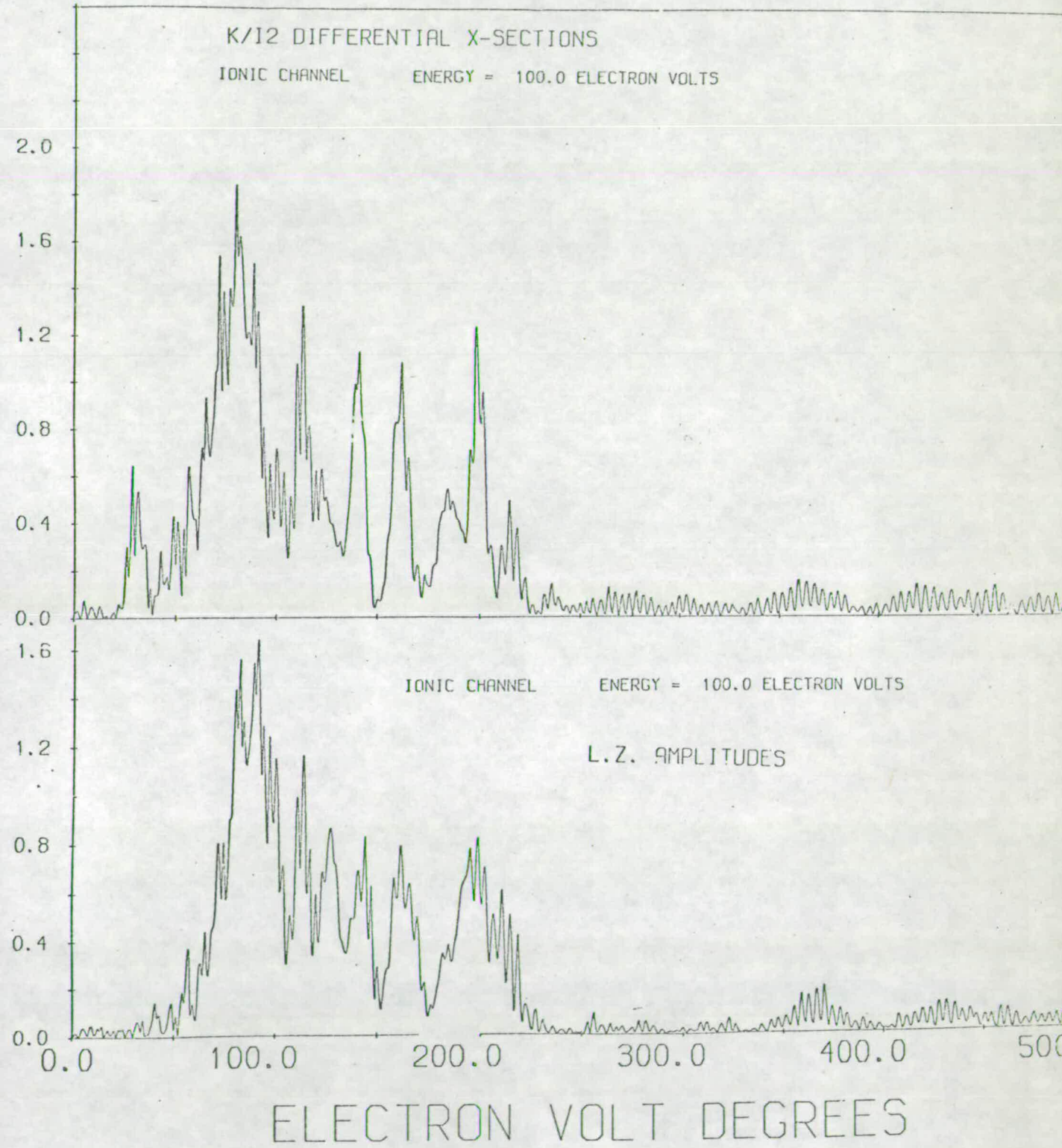

FIGURE 2.28 Ionic Differential Cross Sections at 100eV for K/I_2 using (top) eikonal amplitudes and phase shifts and (lower) using LZ amplitudes and eikonal phase shifts.

The System Na/I

Whilst work on the system Na/I was not performed in this laboratory, differential cross section results for ionic scattering have been obtained by Delvigne and Los [52]. Being another example of "avoided crossing", a comparison of their method of analysis with this work is interesting.

In the theoretical approach, amplitudes of scattered waves were obtained using the LZ theory. Classical deflection functions were used from which were derived the relevant phase shifts. Ionic differential cross section results were obtained using the classical formula.

One difficulty is met when calculating rainbow angles, where the reciprocal of dX/db produces a singularity. The deep well rainbow is thus omitted from the cross section plots.

When the experimental and theoretical Na/I results are compared, a good qualitative fit is observed. An exact fit did not result when the value of H_{12} was altered in the theoretical calculations. If, however, H_{12} was regarded not as a constant value but as a function of interparticle separation, then better agreement of experimental and theoretical results might follow, as another variable, the range of H_{12}, has been introduced.

Despite the differences in the theoretical models and the different potential functions used, results for the two systems K/I and Na/I show good qualitative agreement. However, K/I differential cross sections computed from amplitudes and phase shifts determined by the eikonal model gave good qualitative but not quantitative agreement when compared to those evaluated using eikonal phase shifts and amplitudes predicted by the LZ theory.

Conclusions

The LZ theory accounts fairly well for the elastic and ionic total cross sections. This arises from the fact that it predicts a good average for the ionic transition probabilities. When the differential cross sections are calculated firstly using amplitude and phase functions from the eikonal paaroach and secondly using LZ predicted amplitudes and eikonal phase shifts, a good qualitative agreement results. Peaks are found at the same angles in both cases, but the heights of the corresponding peaks often disagree.

This type of work also gives information on the coupling parameter H_{12} at the crossing point and the potential functions $H_{11}(R)$ and $H_{22}(R)$. Information about the repulsive parts of the deflection curves can be obtained from scattering on the dark side of the deep well rainbow.

Experimentally, it is more advantageous to follow the ionic scattering of the system as, according to the LZ theory, equal

amounts of ionically scattered material experience the shallow and deep well potentials. The differential cross section plots have shown that both rainbows are equally distinct for ionic scattering, but not necessarily so for neutral scattering.

This work has also shown some of the errors involved in applying classical theory to predict scattering phenomena. Classical theory will always yield smooth deflection and phase shift function curves. It would therefore be impossible to account for certain features of the differential cross sections if the above two functions were truly oscillatory.

The main limitations of the above model must be examined. The consideration of only two states of the colliding system is the most serious, especially in the case of the iodine molecule where the possibilities of rotational and vibrational excitation and molecular dissociation might become important in certain energy regions. Electronic excitation of the colliding species by multipole - multipole interactions should be considered in a more sophisticated model.

Work is taking place in this laboratory on the collision system K/I where more than two states of the system are considered and a straight line path for the trajectory is not assumed.

CHAPTER 3

EXPERIMENTAL

Introduction

Several points must be taken into consideration when designing a molecular beams apparatus. Not only must it perform the more immediate experiments, and do so well, but it must have a built-in versatility to allow for modification in obtaining more detailed information. A sense of foresight is therefore invaluable.

The superthermal apparatus was primarily designed to obtain differential cross sections for all types of scattering processes without distinguishing between them; and then to ascertain the respective magnitude of each by a time of flight process. Several of the former class have been done well, with some preliminary tests of the latter showing that a little more refinement is still required.

General Description

The study of differential cross sections arising from collisions of alkali metal atoms with some other species (such as halogen atoms and molecules, mercury, methyl iodide, etc) in the energy range of 5eV to 500eV, was the aim in designing the apparatus. This seemed the most interesting energy region, as beams in this range were comparatively new and collisions outside this range had been extensively studied.

The apparatus was described in great detail by Duchart [53], and whilst that description will be more detailed, any innovation

since then will be described adequately here.

The fast alkali atom beam is produced by ionising the metal atom, accelerating it electrostatically to the desired energy, and then neutralising the ions by resonant charge transfer. This fast, collimated neutral beam collides with a second beam, travelling at thermal energies and at right angles to the first, and the angular scattering of the former detected by a heated wire filament.

If the cross beam is chopped regularly, the amounts of signal plus noise, and then noise can be measured, and over a period of a few minutes, a statistical value of the scattered signal is found. This technique was used to allow measurements of very weak signals, and to help eliminate noise in the experiment.

All relevant information from the information was fed to an on-line computer which partly analysed the raw data.

Figure 3.1 shows a sketch of the apparatus. There are five separately pumped chambers with positioned apertures between each: the first contains the ion source and accelerating lens; the second the deceleration lens and neutralisation chamber; the third chamber is the scattering chamber; whilst the fourth chamber produces the cross beam and removes any unused beam material. The fifth chamber, the only one which can be isolated from the rest of the system, contains the detector and can be pumped almost continuously.

Key to Figure 3.1

A	Alkali Oven Source
B	Acceleration Lens
C	Deceleration Lens
D	Neutralisation Chamber
E	Main Beam Collimation Slits
F	Scattering Centre
G	Detector Element
H	Flexible Stainless Steel Bellows
J	Cross Beam Oven
K	Ion Deflection Plates
L	Ion Collector Plate

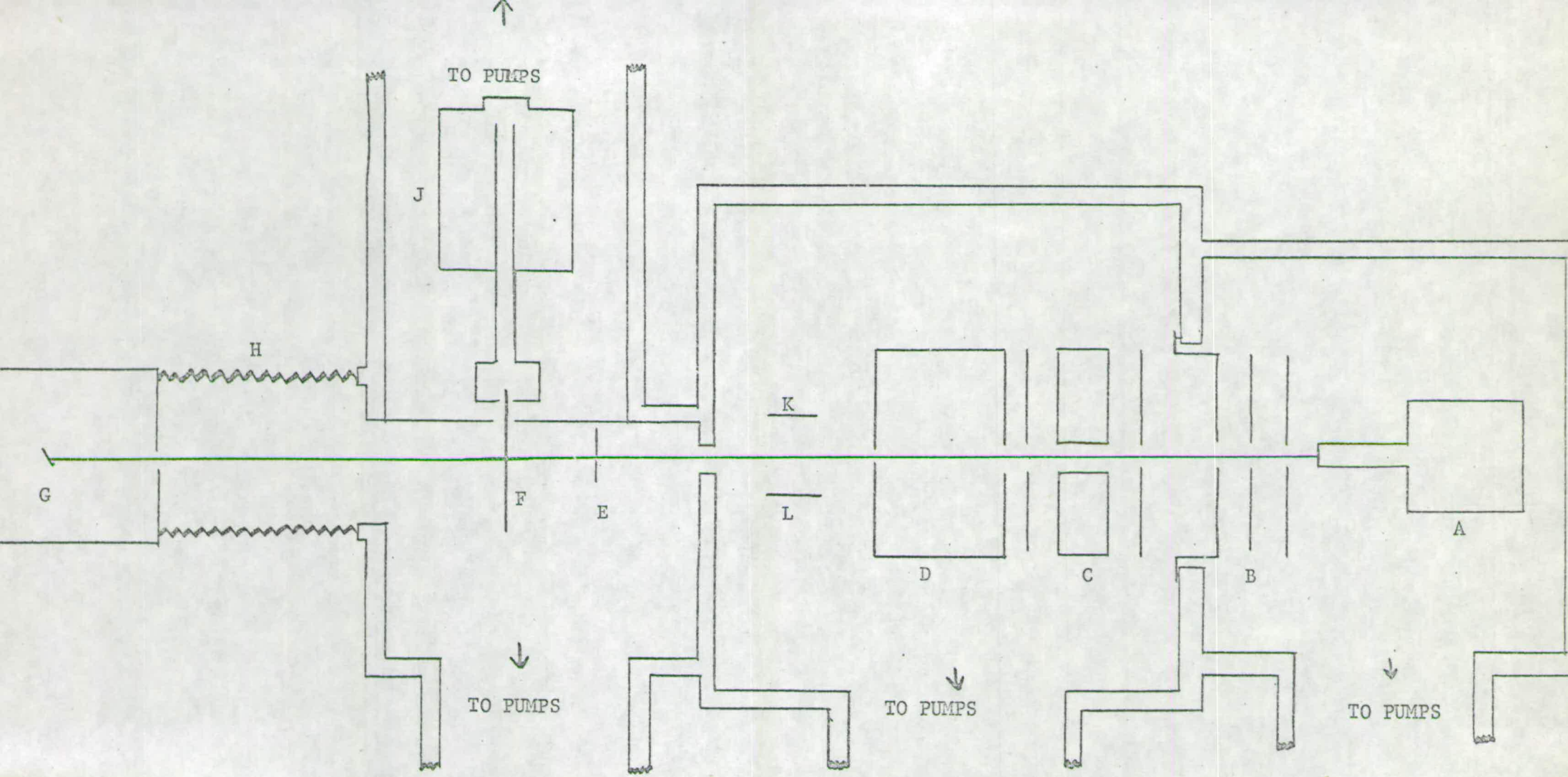

FIGURE 3.1 A Schematic Diagram of the Apparatus. The Detector moves in a plane perpendicular to the paper.

This last chamber is attached to the scattering chamber by means of flexible stainless steel bellows, allowing the detector to swing through angles of $\pm 5^{o}$, which is sufficient for this type of collision.

Vacuum Considerations

The feasibility of beam experiments depends partly on a good vacuum. The only interesting collisions are those which occur between the two beams within their small volume of intersection. Collisions between beam molecules and background gas should be minimised, and a pressure of 10^{-6} torr ensures that the mean free path of beam particles of 100eV energy is far greater than the apparatus dimensions.

The first four chambers of the apparatus are pumped primarily by three rotary pumps which produce a vacuum of about 0.02 torr. These are further supplemented by Leybold oil diffusion pumps, having water cooled ring baffles, and, in order to prevent oil or any other condensible material from reaching the main experimental system, Leybold liquid nitrogen cooled baffles were installed directly above the pumps. Such a system has a pumping speed of about 1000 litres per second, and a vacuum of 10^{-5} - 10^{-6} torr was achieved easily.

Liquid nitrogen cooled cold traps were made for each of the first four chambers to catch any remaining condensible material. This is especially desirable in the scattering chamber where a

comparatively high pressure results in a large amount of background scattering of the main beam. With these traps installed, pressures of 10^{-6} - 10^{-7} torr can be maintained.

Initially chambers three and four were one, but it was thought that by separating them, allowing only a small aperture for the transfer of the cross beam, a much better pressure could be obtained in the scattering region. Any unused material or leaks from the cross beam oven itself could then be pumped quickly away. This action has been fully vindicated.

The bellows, too, acted as a collecting place for condensibles which vapourised badly under vacuum. Heating the bellows during the first six or seven hours of pumpdown minimised this effect.

The chambers were made of Quickfit 4-way or 6-way glass pieces, separated by stainless steel flanges. Rubber 'O' rings sealed the glass-metal junctions, whilst soft copper gaskets made metal-metal flange joints leak tight.

Pressure measurement gauges were liberally spread over the apparatus. A Pirani gauge positioned between each rotary and diffusion pump told the rough backing pressures, whilst ion gauges gave the pressures in each experimental chamber. An analytical ion gauge was also attached to the scattering chamber to detail the cause of a bad pressure when it arose.

The detector chamber was treated differently. At first, this chamber was open to the rest of the system, but once an optimum vacuum had been achieved, it was isolated by means of a gate valve. An ion pump, which could then be operated continuously, produced a vacuum of about 2×10^{-8} torr.

Main Beam Source Chamber

Several different techniques have been used for producing fast beams [54-56], but the one chosen here is that of ionisation - acceleration - neutralisation.

The process of surface ionisation was used for the beam in its initial stages. Whilst this technique is almost entirely restricted to the alkali metals, it is around 90% efficient.

In practice, this is achieved fairly easily by passing alkali metal vapour from an oven through a molybdenum tube which has welded to it a porous tungsten disc. A radiation heater positioned round the disc could achieve a temperature of at least 1500°K in the tungsten, and, as the vapour passes through, ionisation occurs.

The efficiency of this process is at first governed by the Saha equation [57]

$$\frac{n+}{n} \propto \exp\left(\frac{I - W}{kT}\right) \qquad 3.1$$

where n+/n is the ratio of emergent ions to neutrals, I is the

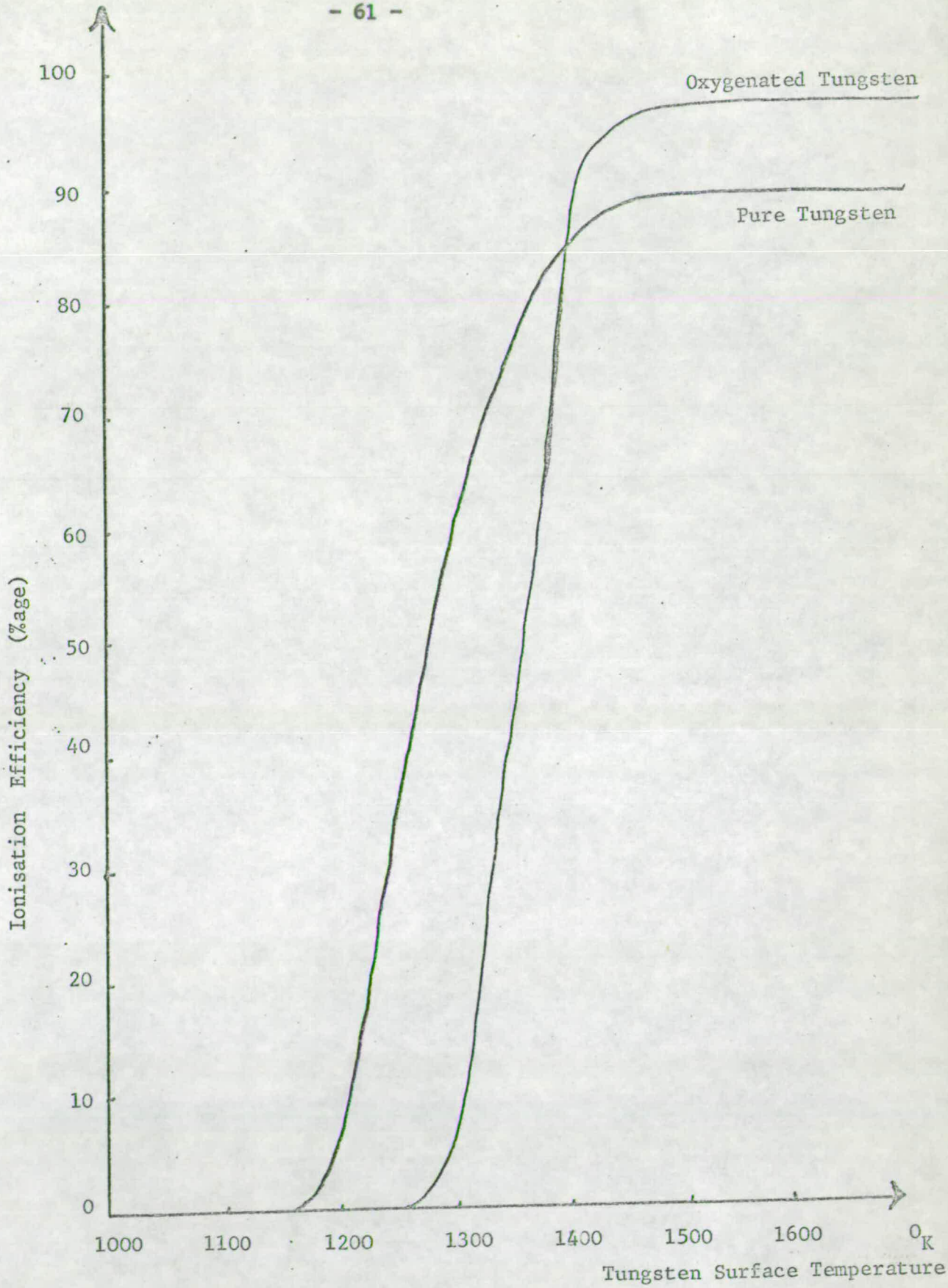

FIGURE 3.2 Ionisation Efficiency of Potassium on Heated Porous Tungsten.

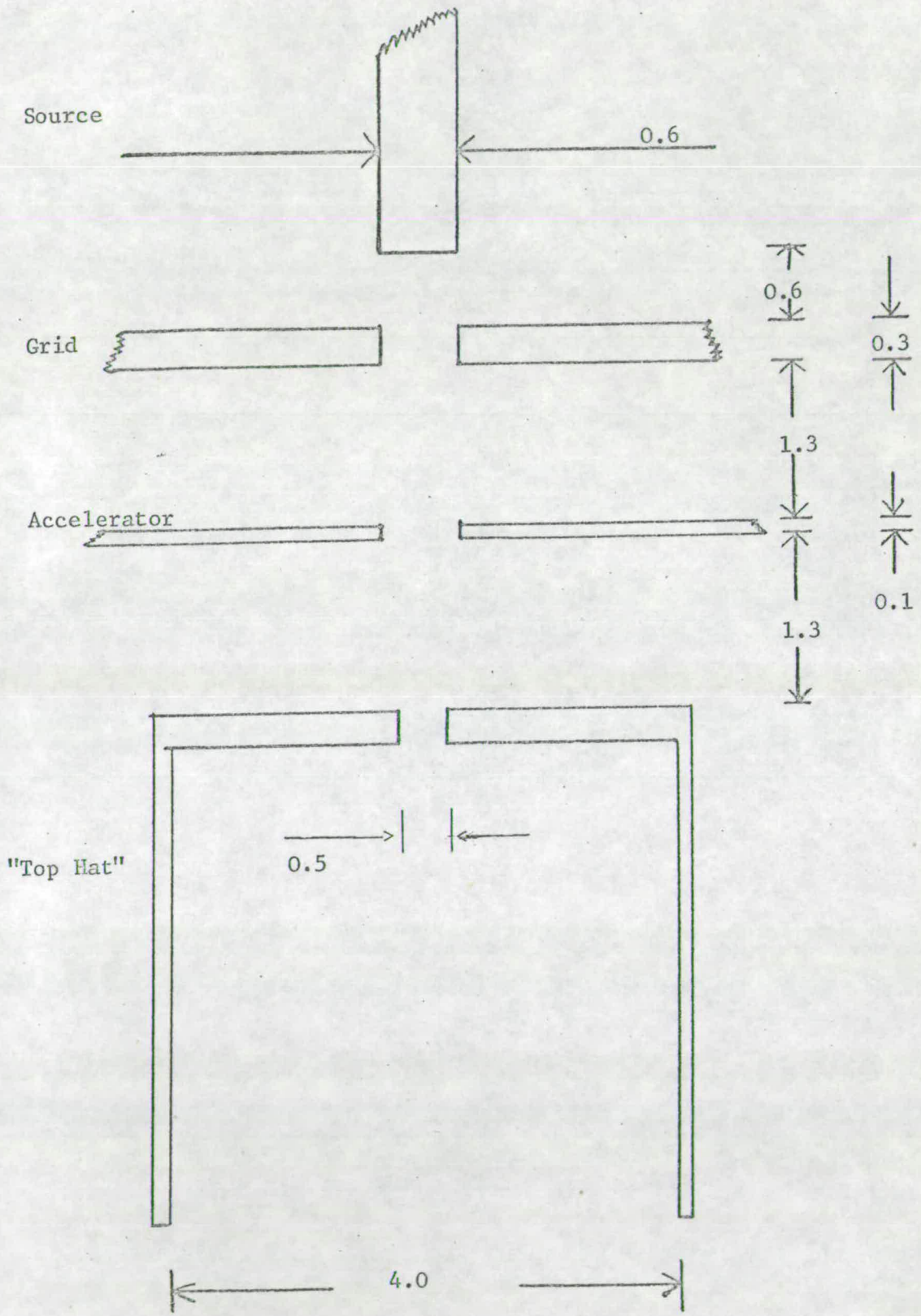

FIGURE 3.3 The Acceleration Lens or Extraction Stage of the Ion Gun (Dimensions in cms).

ionisation potential of the alkali metal, and W is the work function of the system, taken as 4.7eV. Above a certain temperature T, the efficiency remains constant. Figure 3.2 shows how effectively potassium (I = 4.3eV) can be ionised [58].

The thermal effect of producing ions on the surface will undoubtedly be limited by space charge effects there unless extracted quickly. Simpson and Kuyatt [59] proposed to draw the ions rapidly from the surface by a high potential and then decelerate them to the required energy by use of a multistage gun. As opposed to unipotential guns, this system is capable of producing beams of high intensity and low convergence angle for a wide range of energies.

The acceleration stage of the ion gun, which, but for two points, is similar to those used by other workers [59-61], is show in Figure 3.3. The source voltage Vo will finally determine the beam energy, whilst the grid voltage Vg and accelerator voltage Va will determine thefocussing of the beam and its extraction from the source respectively.

One dissimilarity in design is the fourth element, the "top hat", a long cylindrical tube with a small aperture at one end, which was mounted on and insulated from the bulkhead separating chambers one and two. Held at a potential of Va, this maintained a constant electric field for ions transferring from the first to second chambers.

The second alteration was in moving the grid plate further from the source. With the separation as recommended by Soa [60], alkali metal spillage often caused short circuits between the source and grid, with the beam stability suffering greatly. With this increased spacing, beam stability has improved a great deal.

It should also be pointed out here that the work performed in Chapter 4 of this thesis was done with the shorter source-grid separation. This alteration does not, however, invalidate any of the results therein.

The Neutralisation Chamber

The purpose of this second chamber is to decelerate the ions to a given energy, neutralise them, and deflect any ionic species still present. All pieces of equipment used are shown in Figure 3.4. After the "top hat", the ions are steered by a three piece element (Figure 3.5) into the Lindholm-Gustafsson deceleration lens. Ion currents are measured on a set of quadrupoles (Figure 3.6). By finding the optimum steering conditions for maximum current on the "up" quadrupole and then the "right" quadrupole, the beam can be directed through the neutralisation chamber where, on exit, it is defined in width.

The neutralisation process requires pure material of the same type as the beam which, when vapourised, results in a charge exchange

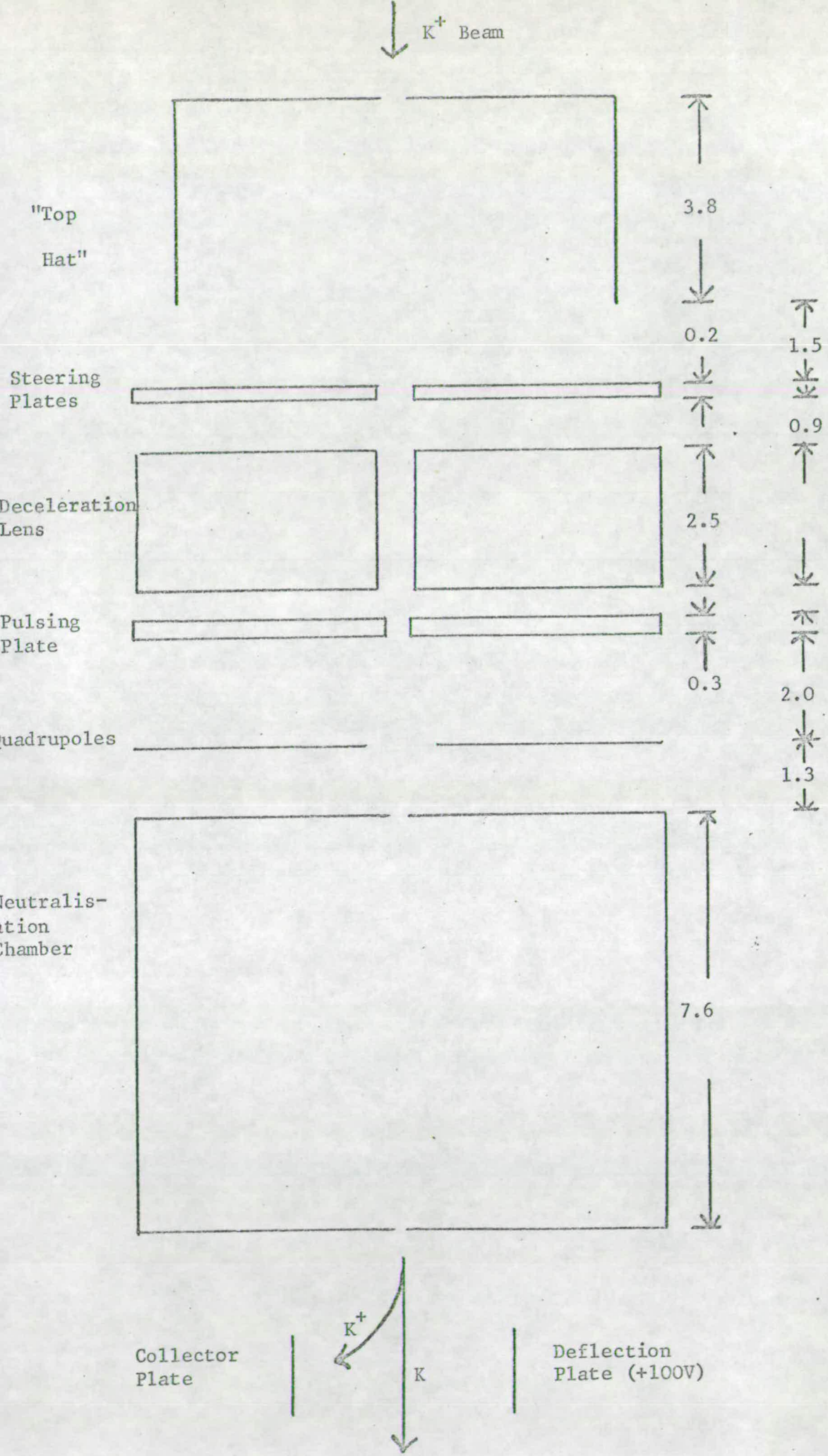

FIGURE 3.4 Sketch of the Second Chamber of the Apparatus (Measurements in cms).

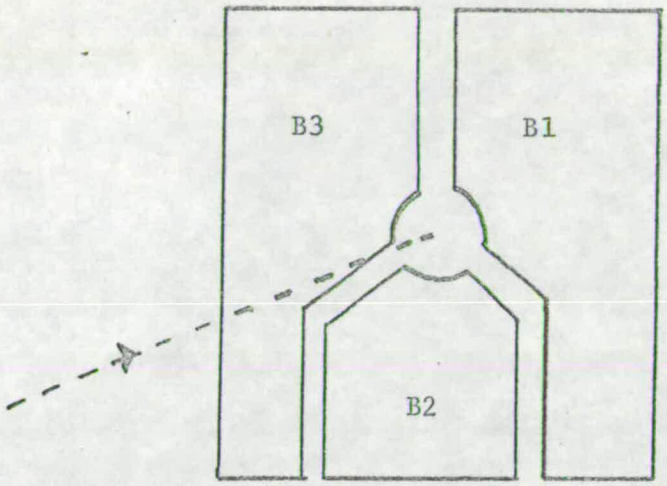

Plate Potentials

$V(B1) = 0 \rightarrow V_A - (0 \rightarrow 100V)$

$V(B2) = V(B1) \pm 100V$

$V(B3) = V(B1) \pm 100V$

FIGURE 3.5 The Pre-Deceleration Lens Steering Plates.

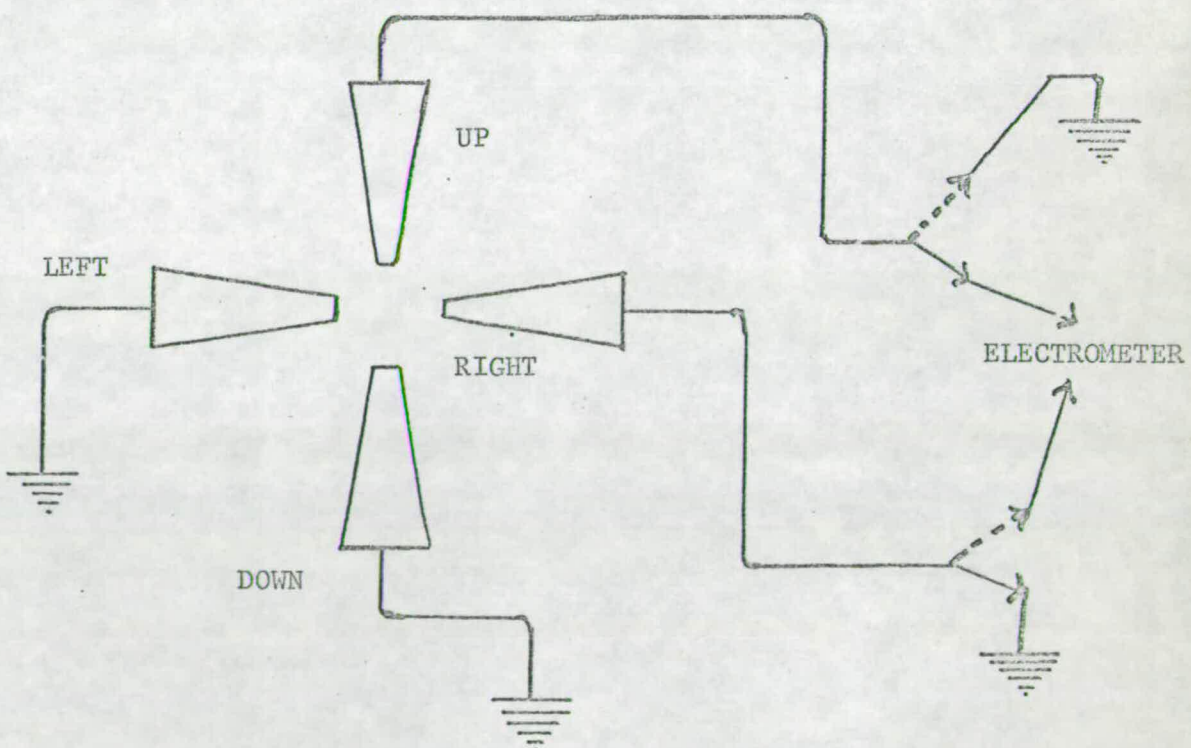

FIGURE 3.6 The Quadrupole Assembly.

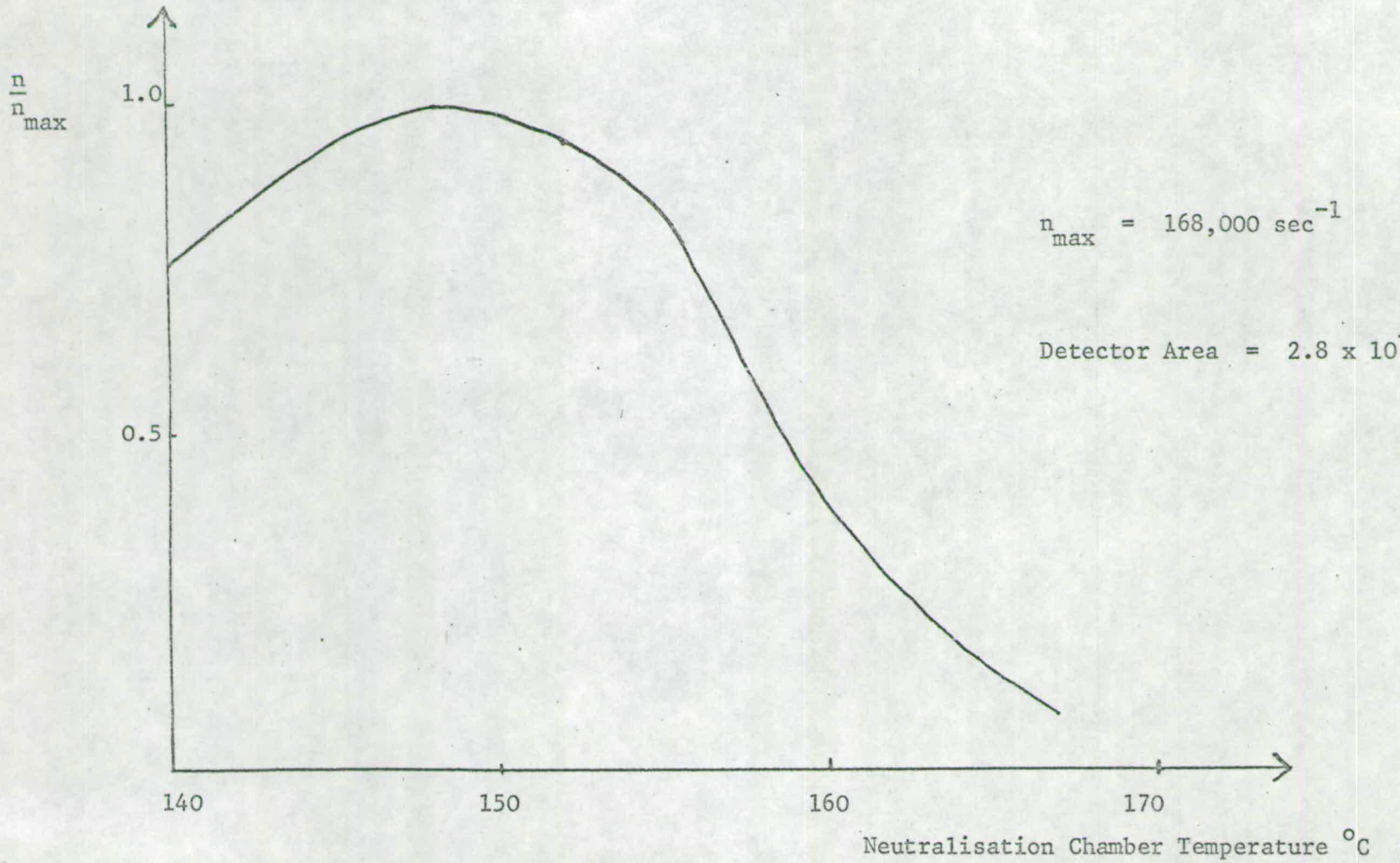

FIGURE 3.7 Neutralisation Efficiency (n sec^{-1}) versus Neutralisation Chamber Temperature.

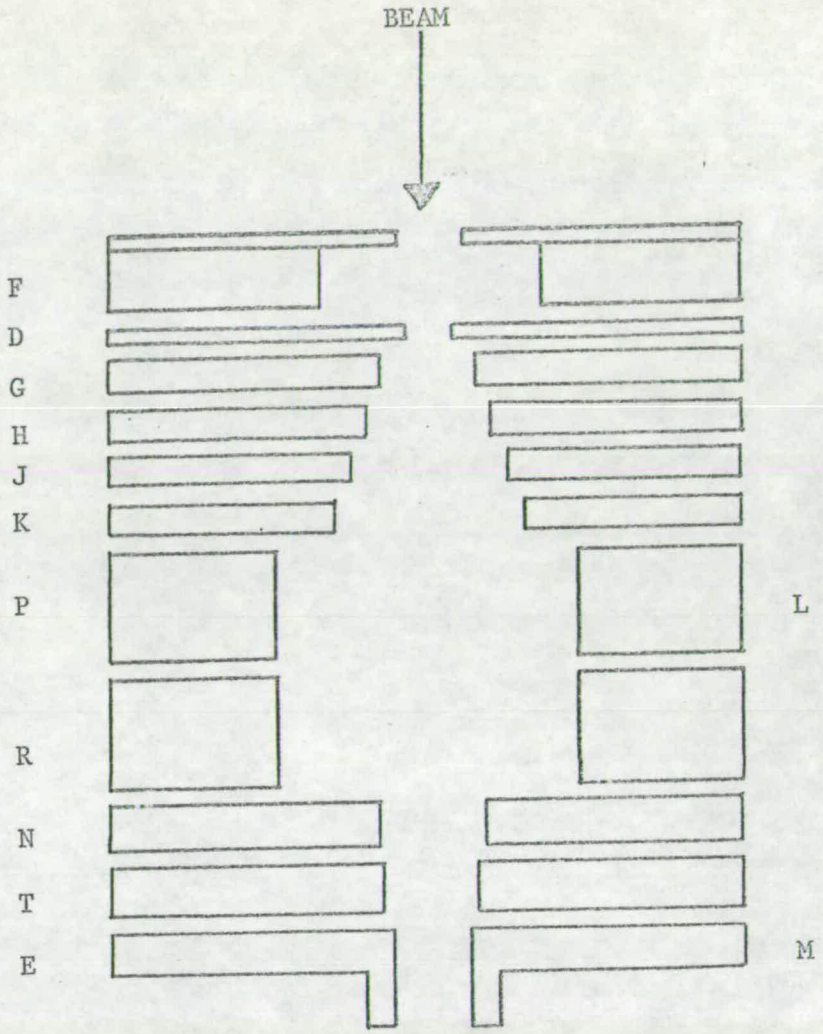

N Focusing Plate

L Vertical Steering Plate

E,M Horizontal Steering Plates

FIGURE 3.8 The Lindholm - Gustafsson Deceleration Lens (Plate S has been Omitted).

Lens Element	Aperture Diameter (cms)	Thickness (cms)
F	0.203* ; 0.711	0.051 ; 0.208
D	0.152	0.051
G	0.305	0.102
H	0.406	0.102
J	0.508	0.102
K	0.609	0.102
P,L	0.952	0.356
R	0.952	0.356
N	0.356	0.153
T	0.305	0.153
E,M	0.254	0.318

Lens Elements are separated by insulated washers 0.051 cms thick.

Lens Element	Element Potential ($\%V_A$)
F	83%
D	100%
G	85%*
H	42%
J	17%
K	14%
P	8.5%
L	8.5% $\pm$ 50V
R	6.7%
N	5.0% $\pm$ 50V
T	3.3%
E	0 - 50V
M	V(E) $\pm$ 10V

TABLE 3.1 Characteristics of the Lindholm - Gustafsson Lens (* See Chapter 4 for these characteristics).

process with a fast ion beam. With this chamber at earth potential, the energy of the emergent neutral beam is Vo (source potential) electron volts.

The fraction of ions neutralised by this method is given by the Beer-Lambert law

$$I/_{Io} = 1 - \exp(-n\sigma\ell) \qquad 3.2$$

where n is the number density of the vapour, σ the charge transfer cross section ($\sim 200\text{Å}^2$)[63] and ℓ is the length of the chamber. Conversely, if the vapour pressure is too large, the beam is lost by multiple collisions within the chamber. Hollstein and Pauly [64] argue that

$$n\sigma\ell \sim 1 \qquad 3.3$$

gives the optimum condition, which in this case requires the neutralisation chamber at a temperature of 150°C for the correct value of n. A careful experimental plot round this temperature has shown the relative efficiency of this process (Figure 3.7).

Cross Beam and Scattering Chambers

The cross beam and scattering chambers were designed to reduce the total pressure in the latter, thereby minimising scattering by the background gas. By separating these two chambers, leaving only a small aperture for the transfer of the cross beam, differential pumping can be achieved in both regions.

The above description was achieved in the following manner. A dural tube of 16cms diameter was fitted into the uppermost vertical neck of the Quickfit six-way glass crosspiece, and this was to house both chambers. The cross beam mount (Figure 3.9) was then positioned within this tube till it rested on the rails running through the apparatus (this is described under 'Alignment Considerations' in this chapter), whilst a rubber 'O'-ring made a vacuum seal between the middle base plate of the mount and the dural tube. The lower chamber thus formed contained the main beam defining slits 0.041 x 0.318 cms and a photo-sensitive device, whilst the cross beam oven and the beam chopper assembly (a rotating slotted disc) were to be found in the upper chamber. The middle base plate contained two apertures, one for the passage of the beam and the other to allow light from a bulb in the fourth chamber to reach a photocell attached to the lower part of this plate. These apertures were positioned such that when the light beam was being chopped, so also was the cross beam. Positioned close to the beam aperture and on the underside of this base plate were heaters to prevent condensation of the beam material.

Cross Beam Oven

There are two ways of achieving a cross beam: externally by using a gas line; or internally by having an oven supply within the fourth chamber. Whilst the former might be restricted to gaseous or volatile liquid samples, it is undoubtedly preferable for its ease of handling. However, the cross beam oven source (Figure 3.10),

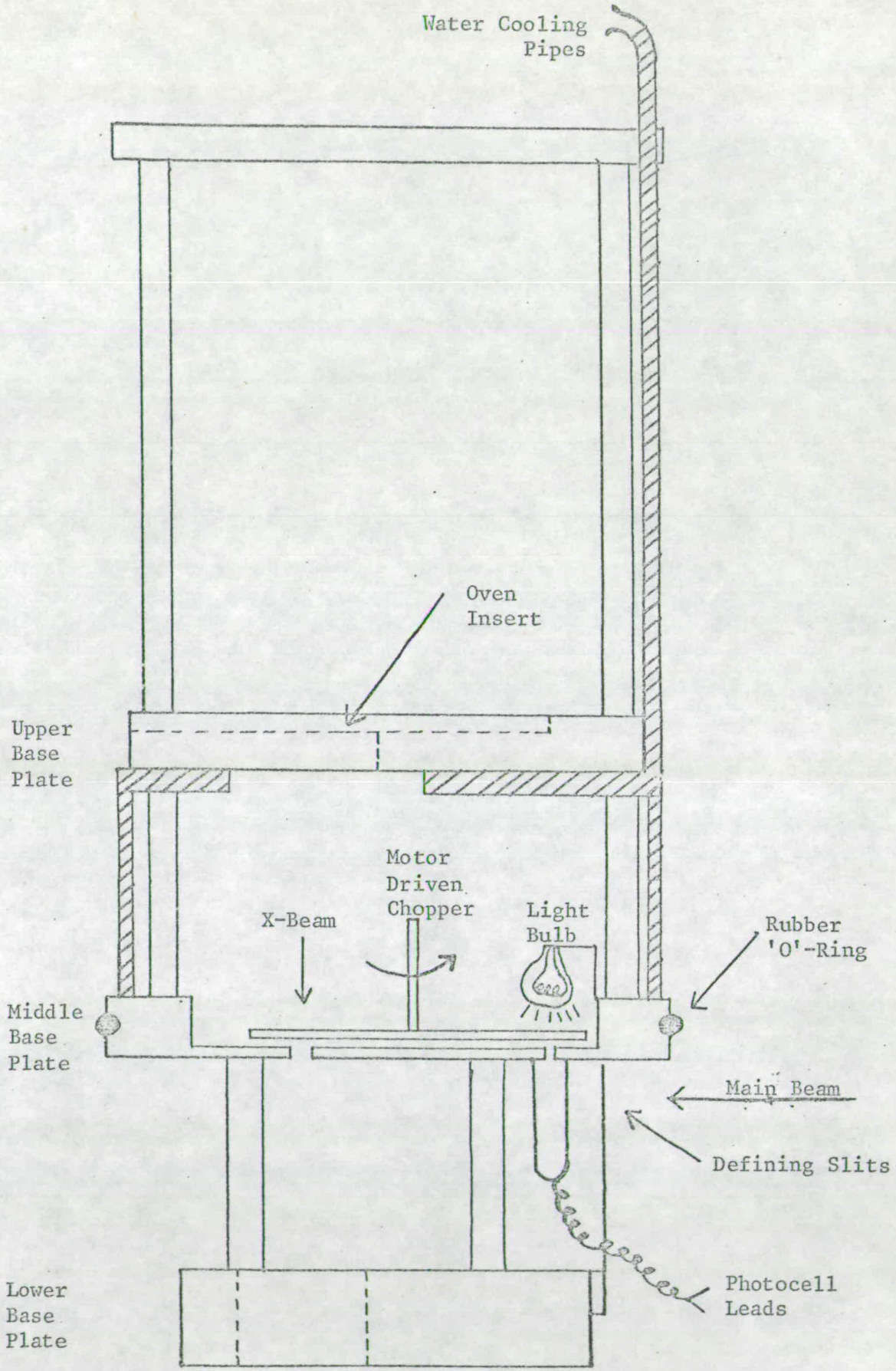

FIGURE 3.9 The Cross Beam Oven Mount

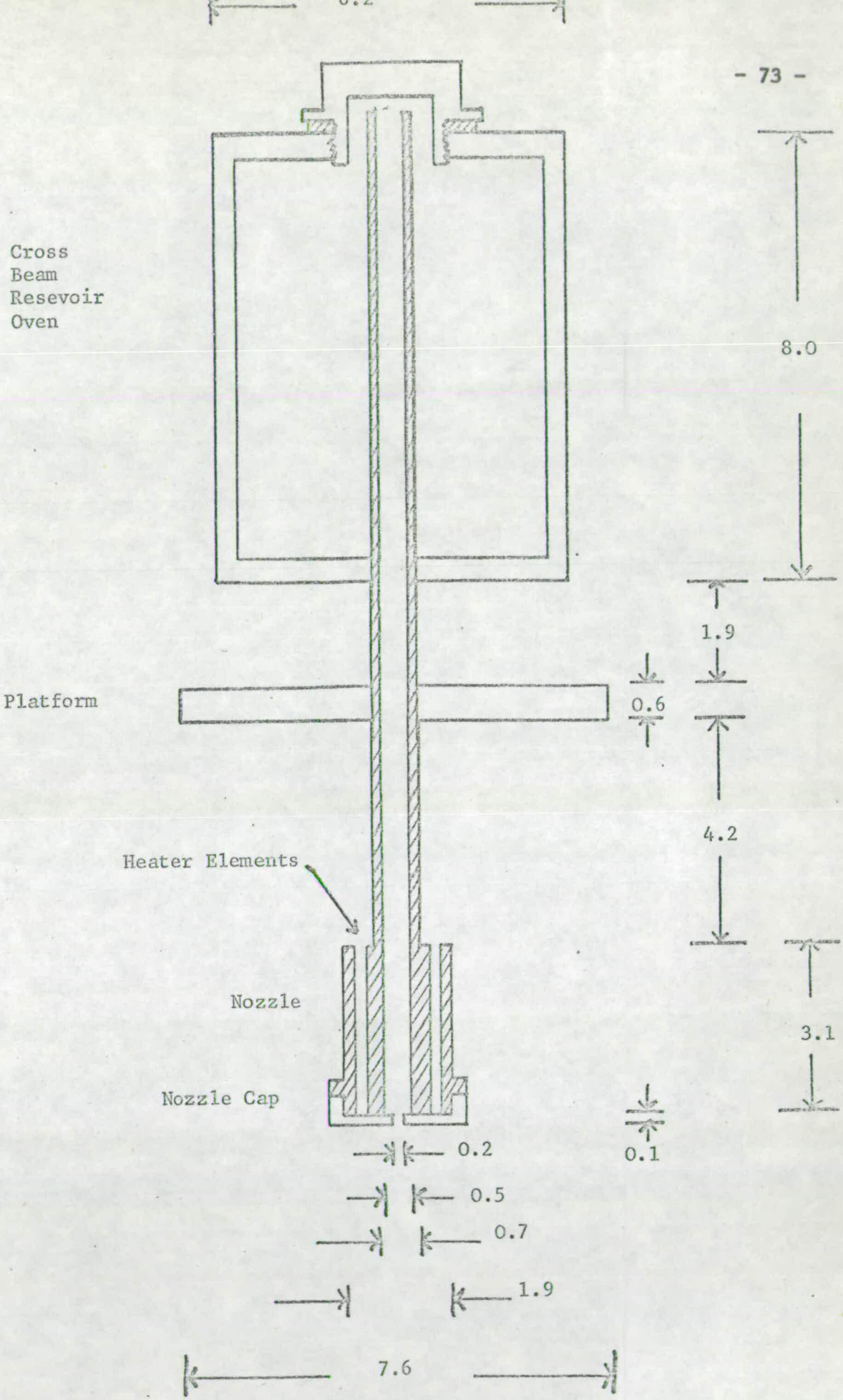

FIGURE 3.10 Cross Beam Oven (Dimensions in cms).

designed mainly for the production of iodine molecule and iodine atom beams, will be described first.

The system consisted of two separately heated chambers joined by a stainless steel tube. The larger chamber acted as a resevoir for the cross beam material, which, in the case of iodine, when heated to a temperature of 60 -70°C gave a steady flow of vapour, enough to produce a 5 -10% attenuation of the main beam. The second chamber, or nozzle was 6.7cms distant from the first. At this point dissociation of the iodine molecules can take place by raising the nozzle to a sufficient temperature. Otherwise it is kept warm (~100°C) to prevent condensation of the beam material.

The beam is also collimated at the nozzle. Two circular discs of 0.9cms diameter were cut from 22 carat gold, one from a sheet 0.01cms thick, and the other from gold micromesh. A slit of dimension 0.038cms x 0.4cms was cut from the centre of the first, and the two discs were positioned and secured between the nozzle and the nozzle cap. Under operating conditions when the nozzle is hot, the gold will act as a seal against leakage.

Often, a very careful check on temperatures in the assembly is required, and thermocouples were inserted into the nozzle, the pipe in the vicinity of the platform, and in the beam material resevoir.

The oven can now be located and secured into the cross beam mount, with the platform sitting in an inset on the upper base plate. The gold slits are in alignment with the calculated path of the main beam, and altered till this condition is achieved.

Iodine Atom Beam

To obtain an iodine atom beam, the nozzle must be heated to a sufficiently high temperature to dissociate the molecules, whilst the oven must not overheat (not more than 70°C) to produce a massive cross beam.

Assuming the species in the cross beam to be in equilibrium, the partial pressures for both types of material in the system

$$\underset{(1-\alpha)}{I_2} \rightleftharpoons \underset{2\alpha}{2I}$$

where α is the degree of dissociation, is

$$p_{I_2} = \frac{1-\alpha}{1+\alpha} \cdot p_{total} \qquad p_I = \frac{2\alpha}{1+\alpha} \cdot p_{total}$$

The pressure equilibrium constant $K_p(\tau)$ at τ°K for this system is

$$K_p(\tau) = \frac{p_I^2}{p_{I_2}} = \frac{4\alpha^2}{1-\alpha^2} \cdot p_{total}$$

and hence

$$\alpha^2 = \frac{K_p(\tau)}{(K_p(\tau) + 4\, p_{total})}$$

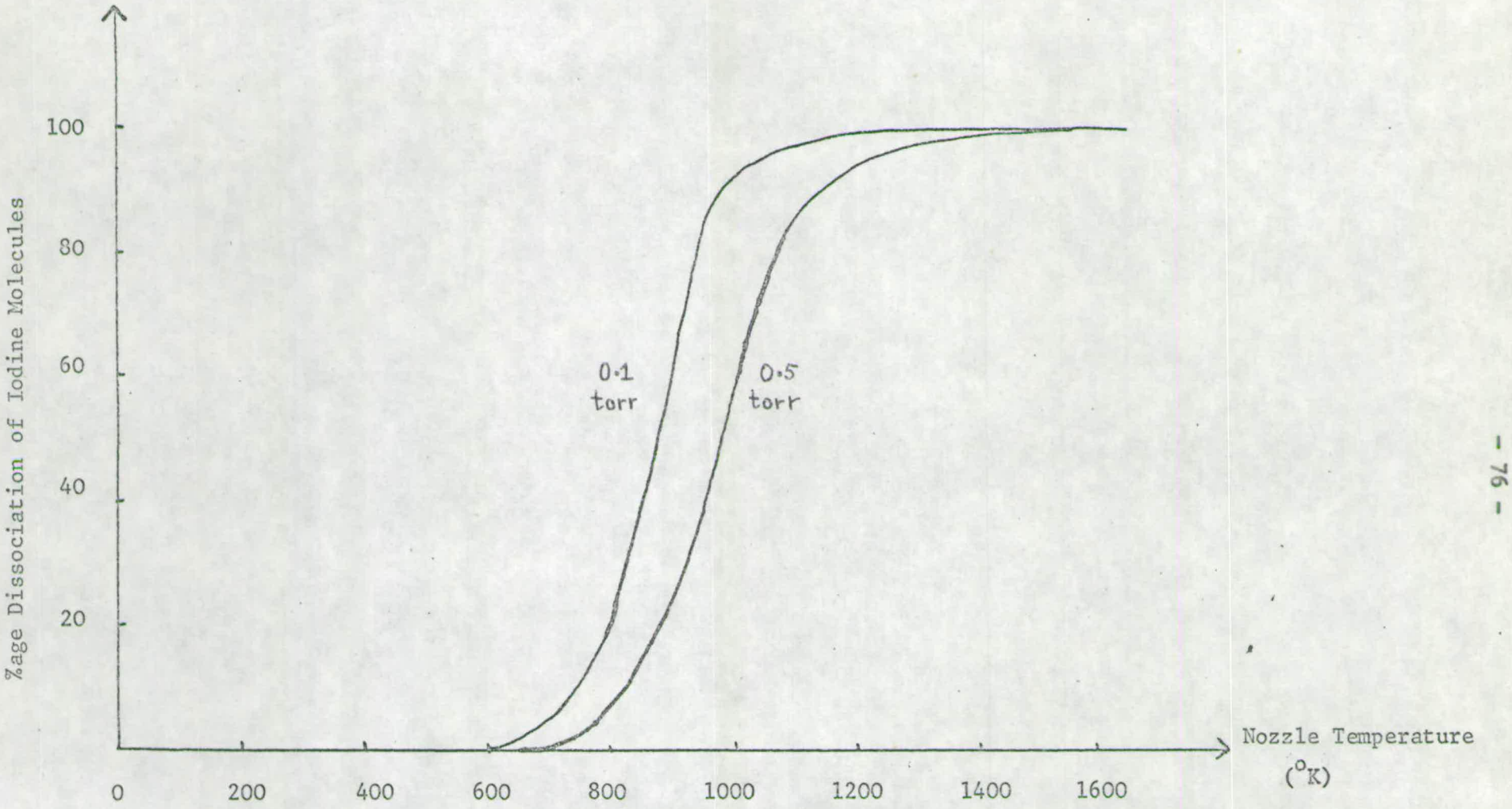

FIGURE 3.11 Percentage of Dissociation for two Pressures of Iodine Beams Against Nozzle Temperature.

Using values for $K_p(\tau)^{90}$, the percentage dissociation for I_2 was found for various temperatures (Figure 3.11) and beam pressures.

Moutinho [48] found the beam pressure to be 1.6×10^{-3} torr on coming from the nozzle into a good vacuum, and watching the variation of ionisation cross section with nozzle temperature, found that a value of $900^{\circ}K$ was sufficient to produce at least 95% dissociation,

When this was tested experimentally, even with the middle and upper base plates of the cross beam mount water cooled, the oven resevoir surpassed $100^{\circ}C$. The pipe connecting the resevoir and nozzle had to be thinned to a wall thickness of 0.25cms to prevent this enormous thermal feedback.

Tantalum wire, carrying 9-10 Amps current, was used in heater elements for the nozzle, whilst the beam was collimated by very pure gold slits. These materials can withstand the high temperatures required.

Gas Line Production of a Cross Beam

The advantages of employing a gas line are numerous, for any faults developing in this system can be rectified externally. If the cross beam material diminishes, or a new scattering species is required then by isolating the gas line, the material can be replenished or replaced. Furthermore, once a good cross beam has been achieved, it can run almost indefinitely without any great attention.

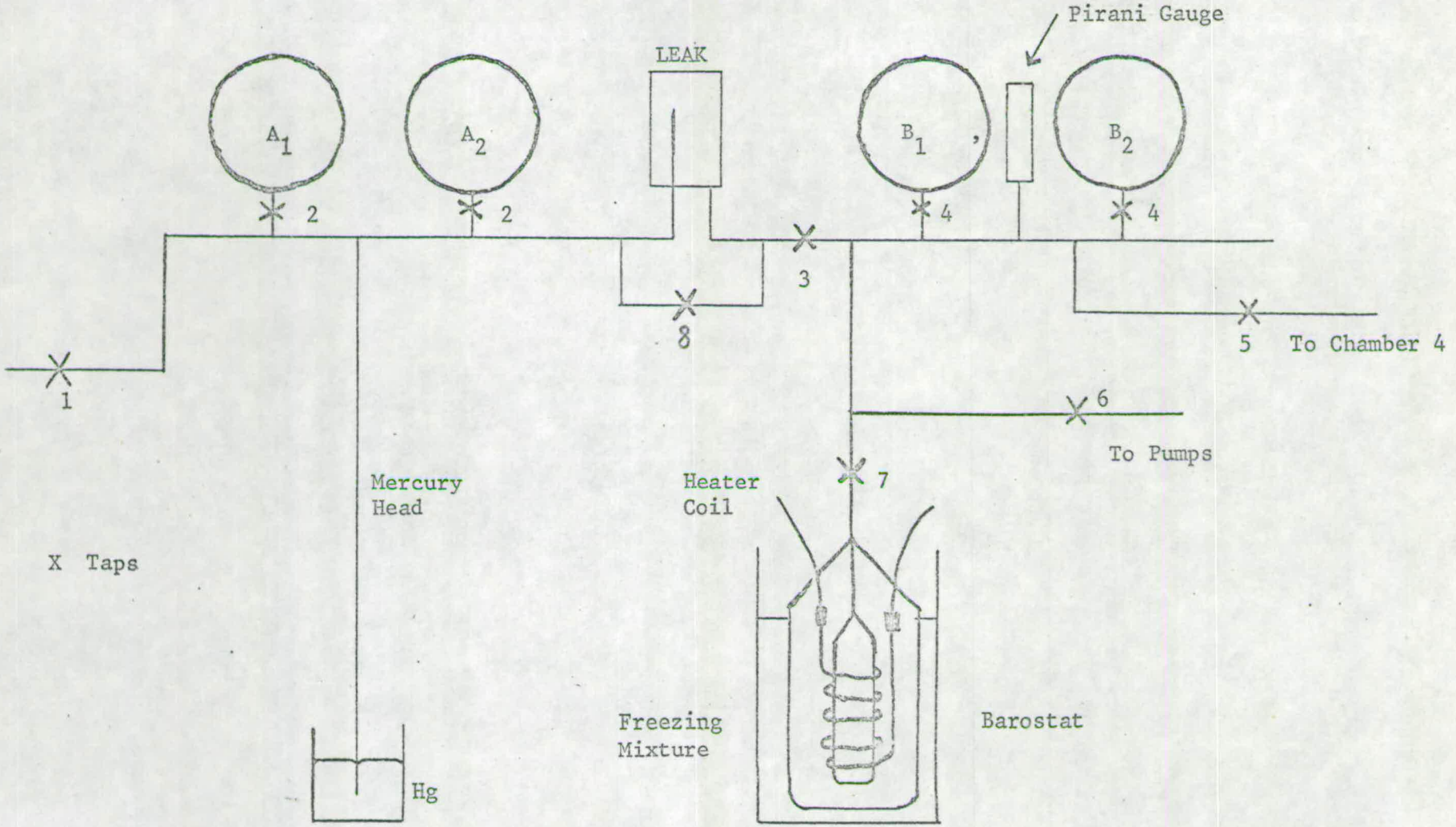

FIGURE 3.12 The Gas Line Method for Delivery of a Cross Beam.

Figure 3.12 is a sketch of a typical gas line, with the line at tap 5 leading to the main experimental system. Inside the fourth chamber, the line is attached to an assembly similar to the cross beam oven, having a heated nozzle and a platform, but with an external pipe which is linked to the gas line extension.

Using a volatile liquid as the cross beam material, a sample is placed in a glass tube which is attached below tap 7. Heating wire and asbestos string are wound round this tube, and the system enclosed within another thicker bore glass tube. A freezing mixture, generally dry ice and acetone, surrounds this to freeze the liquid. By warming the frozen liquid under vacuum, a beam can be produced to attenuate the main beam to any desired degree.

With the liquid frozen, all taps except one and five are opened and the system evacuated. Opening tap five next equilibrates the vacuum in the gas line and in the main experimental system. Taps three and six are closed and the liquid warmed to produce a cross beam. Bulbs B1 and B2, when filled with vapour, act as ballasts to minimise any sudden fluctuations.

For a gaseous sample, the barostat is not required. Once the system has been evacuated, taps six, seven and eight are closed, as is the tap on bulb A2. A sample of gas is entered through tap one, which is then closed, and the gas flow into the experimental system regulated by the leak, just before tap three. If the main beam

attenuation is too large, bulb A2 is gradually opened. Conversely, more gas is entered through tap one if the attenuation is too low.

The Detector Chamber

The detection system was based on the E.A.I. Quad 250 quadrupole mass spectrometer. Neutral potassium atoms were surface ionised on a heated tungsten/platinum filament and focussed into the mass spectrometer by use of a simple lens, before accelerating into the channel electron multiplier. This signal was amplified further externally.

This latter instrument can multiply a single ion pulse into 10^8 electrons in about 10 nonoseconds. Generally the amplification is linear, but if the ion flux is too high (> 4×10^5 ions/sec), space charge saturation of the secondary electrons occurs, and no further increase in output signal arises.

The arrangement is shown in Figure 3.13. Whilst the filament bias and focus plate potentials are variable, the optimum focussing voltages are stated. The filament, heated by a current of 0.5 Amps, attained a temperature sufficient to ionise very fast potassium atoms but not those at thermal energy.

The detection system was installed in a stainless steel chamber, secured on a movable platform, such that the detector could swing in a horizontal arc of $\pm 5^{\circ}$ of radius 61cms with the centre

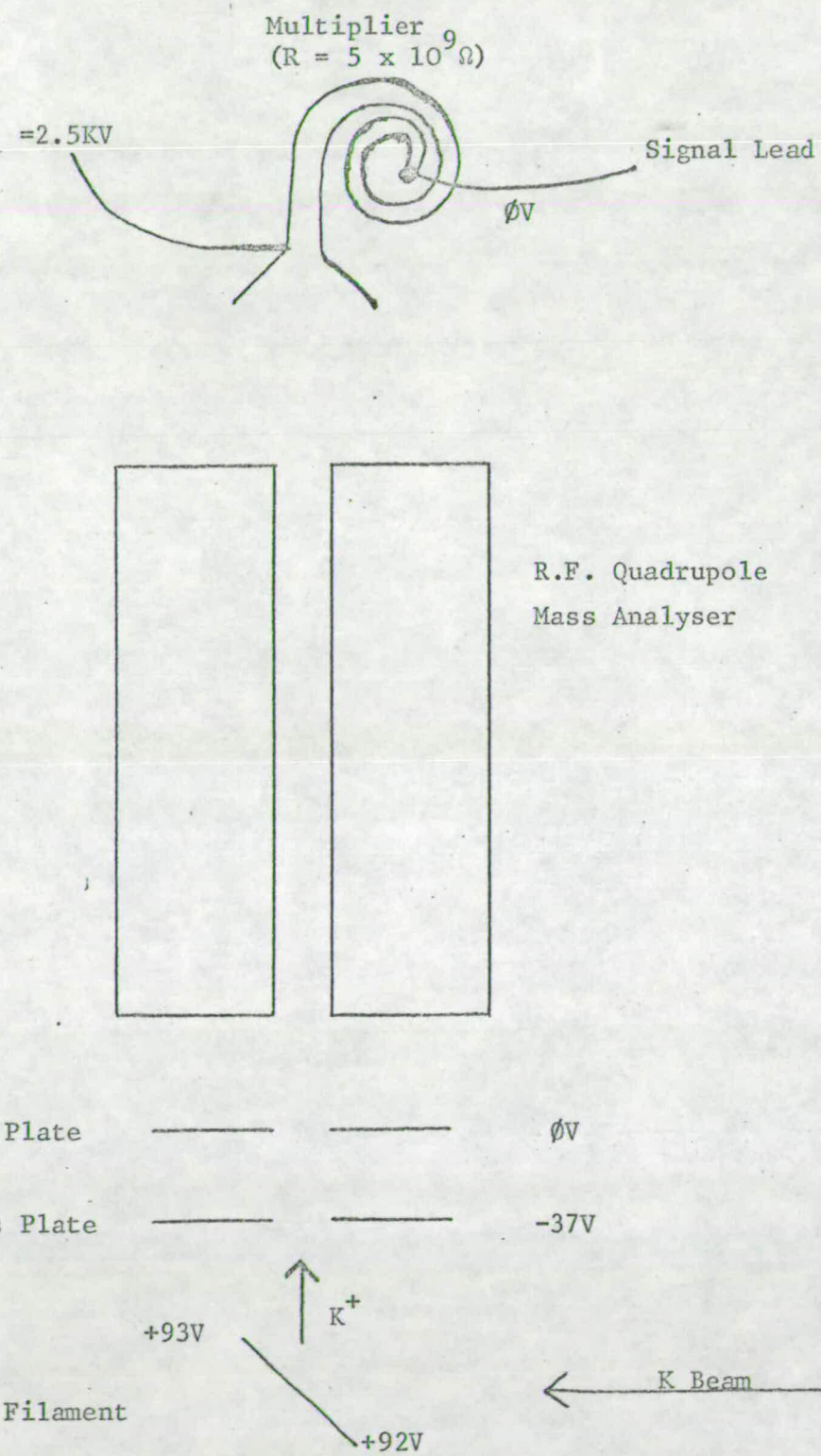

FIGURE 3.13 The Detector Chamber

coinciding with the midpoint of the scattering region. The linear displacement of this platform, and hence the angular position of the detector, can be measured to high precision by a 'Teletrak' linear transducer whose sensor is magnetically coupled to a drive block on the platform. The detector displacement could be measured accurately to give an angular resolution of 0.002° if required, although much larger increments were used.

Alignment Considerations

The experimental arrangement described so far depends on many critical parameters, the most immediate being a good alignment of apertures for oven, lens elements and beam defining slits. It is of great advantage if as few apertures as possible need continual alignment checking, and especially if this test is both quick and accurate.

Base plates were specially designed to support ovens and lens systems, having two grooves machined in them so they could be located accurately on two horizontal, parallel stainless steel bars running through the apparatus. Two alignment pins were made on similar base plates with the pin heads representing the position of the main beam. When they sat on the steel bars, a telescope could be accurately sighted along the main beam path, and hence all apertures could be aligned exactly.

This procedure is facilitated, and indeed necessary for aligning the cross beam, by employing an optical bench which simulates the steel bars in the apparatus. A line parallel to the main beam path is engraved on the lower base plate of the cross beam mount. When the mount is rested on a special stand on the rails of the optical bench, this scribed line runs parallel to the alignment pins. Thus the cross beam slits must be coincident with this line, and this can be easily checked as there is a hole in the middle of the lower base plate.

With all experimental components positioned in the apparatus, the telescope is aligned and focussed on the detector filament, the ion pump having been removed. The filament is silhouetted and adjusted to good alignment. Moreover, the aperture of the gate valve can be aligned in the same operation. This procedure can be checked by replacing the telescope with a laser.

The detector chamber, though, can withstand slight misalignment, for it is mounted on a horizontally rotatable turn-table, whose vertical position can also be adjusted. Under operating conditions, the detector is altered till an optimum beam intensity is recorded.

Beam Performance

Duchart [53] described the theoretically expected values for the main beam performance and compared them to the values obtained

experimentally. The reader is referred for this discussion to the above mentioned work, and this section will discuss the increase in beam intensity since Duchart's experiments.

Ion currents were measured at the source, plate F of the deceleration lens, the 'up' and 'right' quadrupoles and the collector in the post neutralisation chamber deflection plates. The figures below are for 100eV beams of potassium and are shown for optimum current on each collector. Also shown is the measured maximum count rate on the detector. It must also be noted that in Duchart's experiments, the Lindholm-Gustafsson deceleration lens had not been implemented, and the quadrupoles were used as steering plates.

Collector	Previous Performance	Present Performance
Source	5×10^{-4} A	5×10^{-4} A
Plate F	-	3×10^{-6} A
'Up' Quadrupole	-	1×10^{-7} A
'Right' Quadrupole	-	5×10^{-8} A
Post Neutralisation	8.8×10^{-10} A	8×10^{-9} A
Detector	7.5×10^{4} Sec^{-1}	2×10^{5} Sec^{-1}

As the angular area of the detector is 2.8×10^{-6} steradians, the measured flux there is 7.1×10^{10} particles sec^{-1} $ster^{-1}$ as opposed to Duchart's 2.7×10^{10} particles sec^{-1} $ster^{-1}$. Taking the detector and multiplier efficiencies as 50% and that of the mass

analyser as 8% (as Duchart did), the flux on the detector would be 3.7×10^{12} particles sec^{-1} $ster^{-1}$.

Several different energies of potassium atom can be measured at the detector. Thermal atoms from the neutralisation chamber will not be detected if the filament current is low enough, <0.5 Amps.

There is always the possibility of ions forming on lens elements other than the source. This can be found by turning the source potential to zero volts. As the grid potential is positive, this prevents any ions formed on the source reaching the post neutralisation chamber collector plate. If the current recorded here is not zero, then ions are being formed on some other lens element in the system. Generally this phenomenon is caused by operating the ioniser heater in the first chamber at too high a temperature.

Another problem is caused by spillage of potassium on the lens elements. This forms a potassium vapour cloud which tends to neutralise any ion beam passing through it. The potassium atoms formed then have an undefined energy. This point of unwanted neutralisation can easily be found as lens steering plates before this region, but not after it, will be able to alter the count rate on the detector. Again, the cause for this phenomenon will be as before, the high operating conditions of the ioniser heater.

Modulation System

The signal at the detector when two cross beams collide contains several components, namely

a. main beam atoms scattered by the cross beam

b. main beam atoms scattered by the background gas

c. at small angles, the unscattered main beam

d. electronic noise, e.g. from the multiplier

Constituent a is the desired quantity, the others being regarded as noise. The last component is essentially random whilst b and c vary with fluctuations in the main beam intensity and background gas pressure.

Modulation techniques [65] have been employed to remove noise from the desired scattered signal, whereby the cross beam is switched 'on' and 'off' at a regular modulation frequency. This is achieved by synchronously chopping the cross beam and a light beam to a photocell by a rotating toothed wheel disc.

The reference signal from the photocell (of width 14 msec) is amplified by a Schmitt Trigger [53] and the opening of the scalar counters A and B are partially controlled by delay lines fed with this amplified signal (Figure 3.14). The signal is first delayed (DELAY 1) and split into two lines, one leaving it unaffected, the other delaying it further (DELAY 2) by half a modulation cycle. On passing the Switch unit, the signals are defined in width (WIDTHS 1,2) before amplification. Delay and width units are used, firstly to allow for the flight time of the cross beam to the scattering

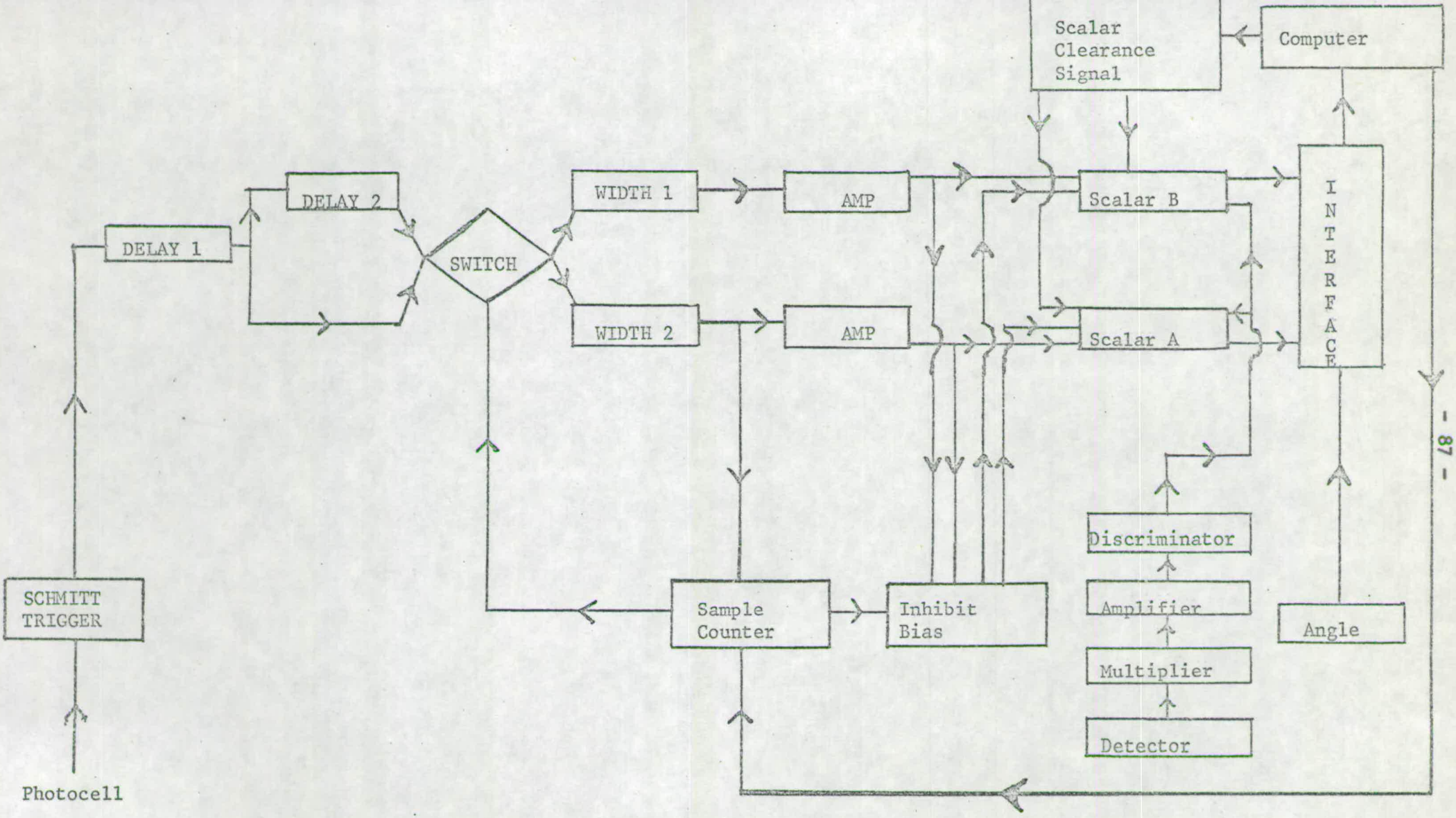

FIGURE 3.14 The Electronics of the Modulation System.

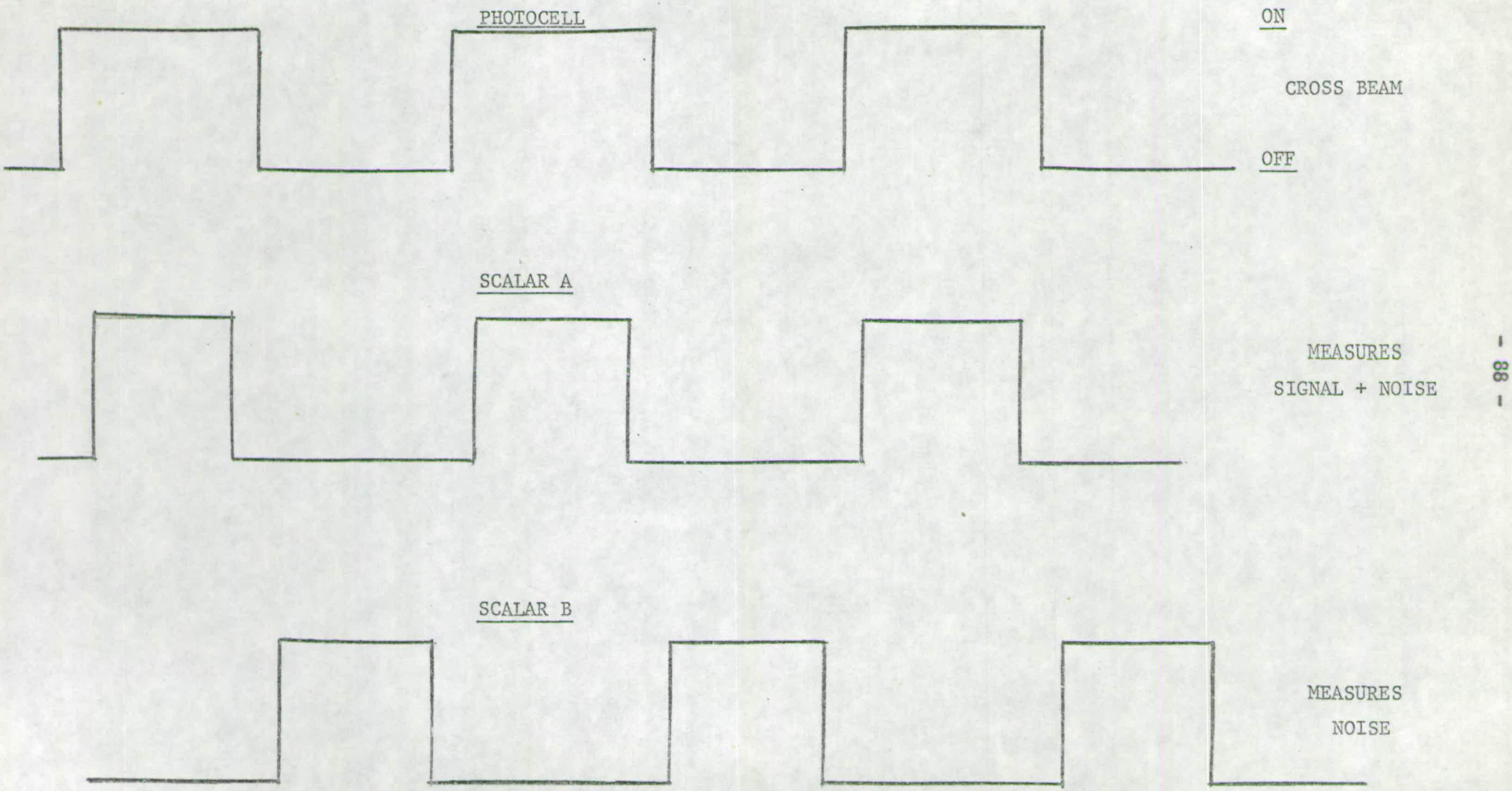

FIGURE 3.14a The open times of Scalar Counters A and B with respect to the photocell signal.

centre (∿ 100 μsecs), secondly to avoid fringe effects in the cross beam pulse, but mainly to allow separate measurements of noise and signal plus noise counts.

Scalar counters A and B are controlled by the Inhibit Bias, which acts like an .AND. gate. Only when the sample counter and delay lines are of a positive voltage will the Inhibit Bias allow the Scalars to collect data from the detector.

The sample counter is controlled mainly by the computer. When transfer of collected data is taking place, the sample counter is inhibited (negative bias) and only on a signal from the computer will it function in its normal positive bias mode.

The sample counter records the data collection time. Positive pulses (one for each modulation cycle) from Width 1 are fed into the Watesta sampling counter, and a set number n (usually forty) modulation cycles are counted. Data transfer from the interface to the computer then takes place (0.1 msec) during which time counting stops.

The signal from the computer clears the sample counter and allows it to restart counting. At each restart, the Switch unit is activated and thus alters the delay lines. For instance, if Delay 1 and Width 1 from one line and Delays 1 and 2 and Width 2 form the other, then Scalars A and B will record the amount of signal plus noise and noise respectively. On switching, Delay 1 and Width 2 form one line allowing Scalar B to record the signal plus noise,

whilst the line comprising Delays 1 and 2 and Width 1 will open Scalar A to record the noise. This switching process is repeated about one hundred times, until enough data has been recorded at that angle. As shown in the next paragraph, bias in the counters is eliminated.

The modulation system is slightly different from that employed by Duchart, being due to the very rapid data transfer time to the computer. The restart signal from the computer generally occurs some way along an incoming pulse from Width 1 and counting begins in the sample counter and Scalar A. If x is the fraction of this pulse at which counting begins, then for every n modulation cycles seen by Scalar B, Scalar A will see (n - x) cycles. Denoting the signal and noise counting frequencies as S and N Hz respectively, the counts on Scalars A and B in two successive batches of n modulation cycles will be A1 and B1, and A2 and B2 respectively, where

$$A1 = (n - x)W1(S + N) \qquad B1 = nW2N$$

$$A2 = (n - x)W1N \qquad B2 = nW2(S + N)$$

Here W1 and W2 are the open times for lines 1 and 2. Thus the sum

$$(A1 - B1) + (B2 - A2) = \{W1(n - x) + W2n\}\, S$$

will give a value for the scattered signal, and remove any bias in the scalar counters.

Work is in progress at the moment to overcome the slight problem caused by the data transfer time, thus making x = 0.

Data Collection

The means of collecting vast amounts of data from this type of experiment is a matter of prime importance, and for this, an on-line PDP-11 computer was employed. The success of this work is mainly due to another colleague and his report [66] will be more detailed than the description here.

The process is started by reading paper tape programs into the computer. These programs control the experiment to a large extent, and once read in, the data is transferred but not collected by the computer. Collecting of data is started by an operator's signal from the apparatus interface to the computer.

The following experimental variables are read in:

1. Start Sentence Code
2. Count in Scalar A
3. Count in Scalar B
4. Angle
5. Mode

+1 if Scalar A counts signal plus noise
Scalar B counts noise

0 if Scalar A counts noise
Scalar B counts signal plus noise

6. Manual Flags

7. End Sentence Code

These variables at each data transfer form a standard sentence which is read in binary code language. The start sentence and end sentence codes are constant parameters throughout the experiment, whilst the mode alternates from +1 to 0 each time the switch unit in the modulation system is employed.

Because of the mode change, sentences are accepted or rejected in pairs. If two successive sentences contain the same mode, they are rejected. Generally the first of the pair should have a +1 mode signal, the second a zero.

Incomplete or malformed sentences are detected by the lack of the correct start sentence and end sentence codes at the expected positions. Reading will only start when the correct start sentence code is encountered. Again a pair of sentences containing either fault is rejected.

The manual flags are generally set in the normal run code when data is being read. However, one manual flag from the interface will stop the collecting, but not the reading of the data, whilst another will restart the collecting process. This allows the operator to optimise the main beam signal whenever necessary.

When enough data has been read at one angle, the computer stops reading data and powers a motor to drive the detector to the next desired angle. On its destination data collection recommences.

The angles are chosen at random within a given angular range θ_1 to θ_2, where θ_1 is slightly to one side of the main beam axis and θ^2 is about 5^o to the other side. The detector is started at an angle θ_{ref} very near the main beam axis. After reading data for every n angles, the detector is returned to θ_{ref}. If the attenuation or the intensity of the main beam has changed significantly since the last reading at θ_{ref}, warning is given to the operator via a teletype. Otherwise the data collected at θ_{ref} at various times show the time drift of the experimental properties such as beam intensity, detector efficiency, etc.

Preliminary Analysis of the Data

If the computer reads a sentence of data every forty modulation cycles, i.e. every 280 msecs, then an experiment lasting four days will produce about 10^6 data sets. It is important that the computer should be able to handle this vast amount of data.

The computer will read data at each angle until it finds 2N ($\sim$ 200) sentences that have passed the rejection tests. This is stored in the computer core whilst preliminary data analysis takes place. Firstly, any bias in the Scalar counters is eliminated (this was discussed under the Modulation System) to give N values of the

scattered signal. A mean of these N values is found, and the standard deviation of these points from the mean evaluated. If any point differs by more than two standard deviations from the mean, then it is rejected as a spurious signal. A new mean and standard deviation of the remaining points are found and the test is performed again. After this, final values of the mean and standard deviation are evaluated, giving a 95% confidence limit in the results. These two values along with the value of the angle are written to a disc in the computer. The original 2N sentences, being obsolete, are wiped from the core memory.

This exemplifies some of the advantages of using an on-line computer as opposed to a paper tape punch, the previous method of data collection. The computer will read data until it finds N pairs of correctly formed sentences. Paper tape has to take the first N pairs, and many could be faulty due to any temporary punching malfunction. Also, the data transfer time is much quicker and more experimental time for data collection is allowed. As previously demonstrated, the experimenter can be warned of any large fluctuations in the beam intensities. More importantly, data transferred to the disc in the computer can be examined without interrupting the experiment, and if the angular scan is too small or too large, corrections can be made immediately.

Relationship Between LAB and COM References

Whilst an experimental plot of scattered main beam intensity is observed in a laboratory (LAB) frame of reference, theoreticians prefer to investigate the system from a centre of mass (COM) viewpoint. Whilst this greatly simplifies the problem, accurate conversions between the two frames of reference are essential, and several reviews have considered the topic [67].

This description will be confined to the type of experiment previously described where the beams intersect at right angles and scattering in the out of plane direction is observed.

Figure 3.15 shows the velocity vector diagram before collision, whilst Figure 3.16 looks at the change in the first particle vector due to collision. In general, two particles of mass m_1 and m_2 of LAB velocities v_1 and v_2 intersect at right angles, giving a COM velocity v_c and relative velocity v_r. The vectors u_1 and u_2 are the velocities of particles one and two with respect to the centre of mass velocity. The angle between v_1 and v_c is denoted by α whilst O_c and O are the origins of the COM and LAB frames of reference respectively.

After collision, the particles may change masses to m_1^1 and m_2^1, LAB velocities to v_1^1 and v_2^1 and COM velocities to u_1^1 and u_2^1. The deflection angles of the primary particle are given by Φ and θ respectively in the LAB and COM frames.

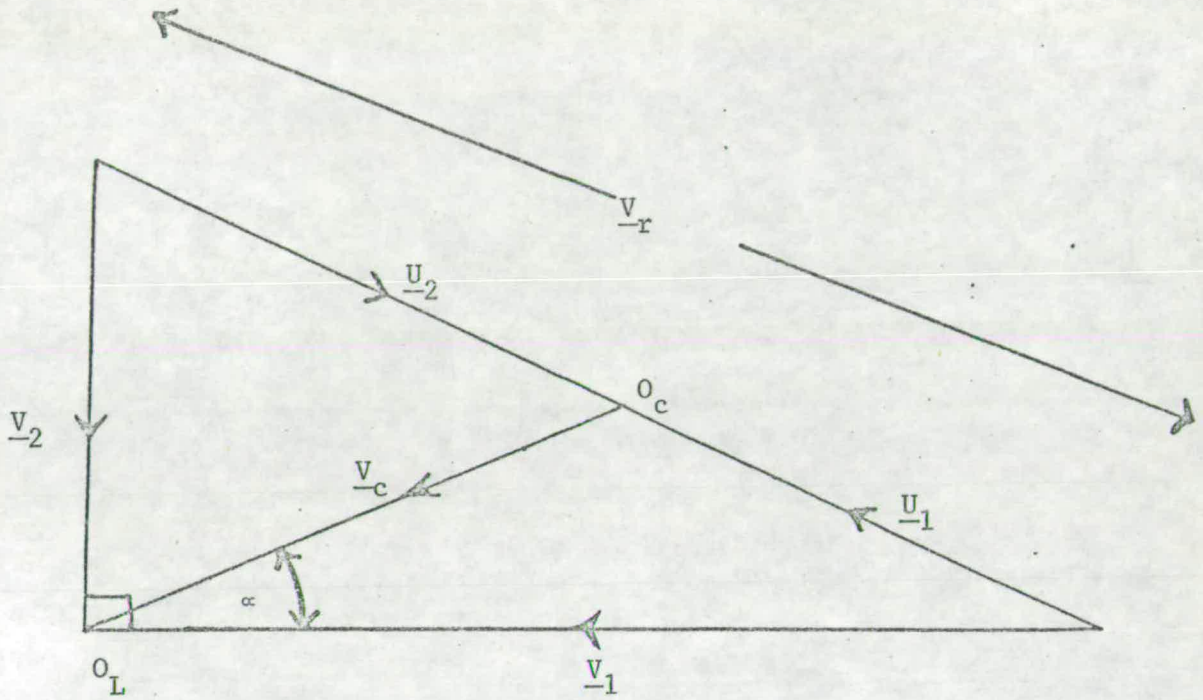

FIGURE 3.15 Newton Diagramme before Collision

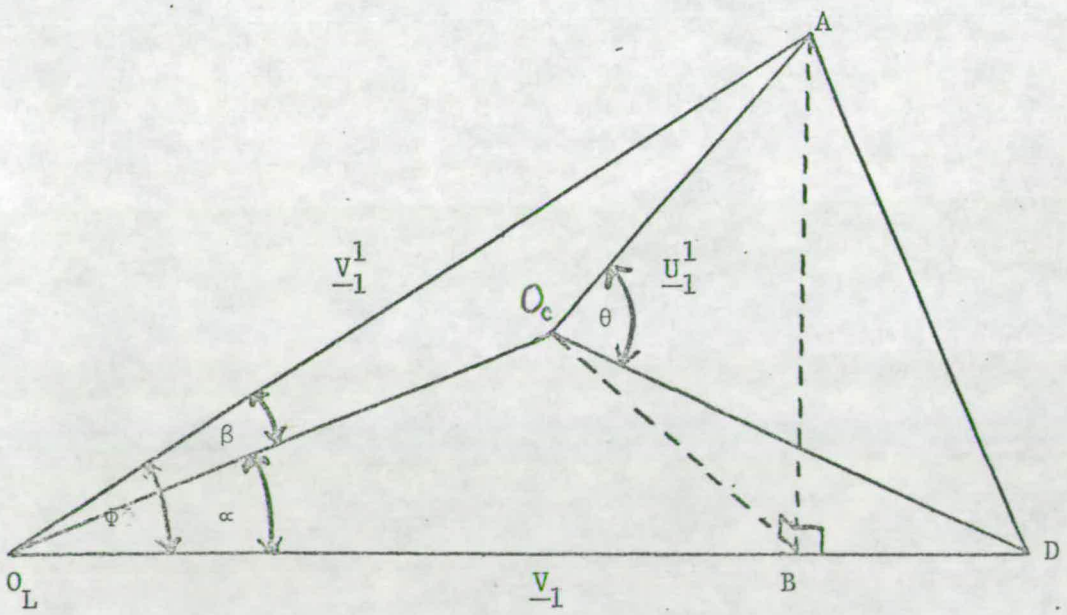

$\angle O_C O_L D = \alpha$ $\quad$ $\angle A O_C D = \theta$

$\angle A O_L O_C = \beta$ $\quad$ $\angle A O_L D = \Phi$

FIGURE 3.16 Newton Diagramme for Scattering of Primary Particle

It is evident that

$$m_1 + m_2 = m_1^1 + m_2^1 = m_o \qquad 3.4$$

$$m_1\underline{v}_1 + m_2\underline{v}_2 = m_1^1\underline{v}_1^1 + m_2^1\underline{v}_2^1 = m_o\underline{v}_c \qquad 3.5$$

whilst

$$\underline{v}_r = \underline{v}_1 - \underline{v}_2 = \underline{u}_1 - \underline{u}_2 \qquad 3.6$$

$$\underline{v}_1 = \underline{u}_1 + \underline{v}_c \qquad 3.7$$

$$\underline{v}_2 = \underline{u}_2 + \underline{v}_c$$

Thus using equations (3.5) and (3.7) in equation (3.4)

$$m_1\underline{u}_1 + m_2\underline{u}_2 = 0 \qquad 3.8$$

now

$$v_r^2 = v_1^2 + v_2^2 \qquad 3.9$$

Substituting equation (3.6) into (3.8) and using (3.9),

$$u_1 = \frac{\mu}{m_1}(v_1^2 + v_2^2)^{\frac{1}{2}}, \quad u_2 = \frac{\mu}{m_2}(v_1^2 + v_2^2)^{\frac{1}{2}} \qquad 3.10$$

where μ is the reduced mass of the system.

Now it is easy to show that

$$v_c^2 = (m_1^2v_1^2 + m_2^2v_2^2)/(m_1 + m_2) \qquad 3.11$$

and that

$$\alpha = \arccos\left\{\frac{v_c^2 + v_1^2 - u_1^2}{2v_1v_c}\right\} \qquad 3.12$$

E_o, the relative initial kinetic energy, is given by

$$E_o = \tfrac{1}{2} \mu v_r^2 \qquad 3.13$$

The magnitude of u_1^1 is given by

$$u_1^1 = u_1 \frac{m_1 m_2^1}{m_1^1 m_2} \left(1 - \frac{\Delta E}{E_o}\right)^{\frac{1}{2}} \qquad 3.14$$

where ΔE is the endothermicity of the process. For elastic scattering,

$$m_1 = m_1^1 \ , \ m_2 = m_2^1 \ , \ \Delta E = 0 \ , \ u_1^1 = u_1$$

Now

$$u_1^2 = v_c^2 + v_1^{1\,2} - 2 v_c v_1^1 \cos\beta$$

and hence

$$v_1^1 = v_c \cos\beta \pm \left(v_c^2 \cos^2\beta - v_c^2 + u_1^{1\,2}\right)^{\frac{1}{2}} \qquad 3.15$$

Using the dihedral angle theorum,

$$\cos\beta = \cos\alpha \cos\Phi$$

and hence v_1^1 can be found in terms of known parameters for a given value of Φ.

Using the common length AD, it is found that

$$u_1^2 + u_1^{1\,2} - 2u_1 u_1^1 \cos\theta = AD^2 = v_1^2 + v_1^{1\,2} - 2v_1 v_1^1 \cos\Phi$$

and hence

$$\theta = \arccos\left\{\frac{u_1^2 + u_1^{1\,2} - (v_1^2 + v_1^{1\,2}) + 2v_1 v_1^1 \cos\Phi}{2u_1 u_1^1}\right\} \qquad 3.16$$

Thus for a given LAB scattering angle Φ, values for θ can be found. The number of values of θ found will depend entirely on the solution to equation (3.15) for v_1^1 where answers must be real and positive.

This is best described pictorially by forming a sphere of radius u_1^1 with centre O_c. If a given LAB scattering angle Φ produces a vector passing through this sphere, then real solutions for θ can occur.

Differential cross sections as seen in LAB and COM frames have to be weighted differently. Suppose scattering of the primary particle from angles θ to $\theta+d\theta$ occurs in the COM system, passing normally through an element of area dA. This will subtend a solid angle of $dw = dA/u_1^{1\,2}$ to the COM, whilst $dw_L = dA|\cos\alpha|/v_1^{1\,2}$ to the scattering zone. The vector v^1 thuse makes an angle α from the normal to this small element of area, the normal vector being u_1^1. Thus

$$\cos\alpha = (u_1^{1\,2} + v_1^{1\,2} - v_c^2)/2u_1^1 v_1^1$$

Hence the LAB differential cross section can be obtained by multiplying its counterpart in the COM by the ratio dw/dw_L where

$$\frac{dw}{dw_L} = \left|\frac{v_1^1}{u_1^1}\right|^2 / \cos\alpha$$

Effect of Finite Apparatus Functions

In an ideal experiment two infinitely narrow beams of high and infinitely stable intensity will produce on an infinitely small detector, a scattering function $f(\theta,\Phi)$, where θ and Φ are the horizontal and vertical angular positions of the detector. In reality, apparatus functions such as the main beam width and finite detector size must be taken into account. Parameters such as the energy distributions in the beam, $\sim$0.1eV as compared to a relative energy of 100eV, are unimportant whilst it has been shown [68] that the finite size of the cross beam is negligible for small angle scattering.

Now a beam of finite width will produce a scattering function $G(\theta,\Phi)$ given by the integration over the main beam cross sectional area.

$$G(\theta,\Phi) = \int_{-x_o}^{x_o} \int_{-y_o}^{y_o} I(x,y) f(\theta - \frac{x}{\ell}, \Phi - \frac{y}{\ell}) dx dy$$

Here, all angles are in radians, ℓ is the distance of the detector to the scattering centre, and x, y are the horizontal and vertical displacements from the main beam centre. If the beam is cylindrical of radius r_o, the radial displacement co-ordinate r is

$$r^2 = x^2 + y^2$$

and hence

$$r_o^2 = x_o^2 + y_o^2$$

I(x,y) is the intensity of the main beam at displacement (x,y), and I(r) is taken as trapezoidal in shape.

Averaging the signal $G(\theta,\Phi)$ over the detector width and height is similar. In this experiment, the detector is only moved horizontally, and scattering in the vertical plane is not examined. Thus the parameter Φ can be eliminated to give an experimental intensity scan of $F(\theta)$. If the detector is centred on the position $(\theta, 0)$ and the half angles subtended from the width and height of the detector to the scattering centre are given by $\delta\theta$ and $\delta\Phi$, then

$$F(\theta) = \int_{-\delta\theta}^{\delta\theta} \int_{-\delta\Phi}^{\delta\Phi} G(\theta+\alpha,\beta)\, d\alpha d\beta$$

Now

$$\delta\theta = \frac{W}{2\ell} \text{ radians} \qquad \delta\Phi = \frac{h}{2\ell} \text{ radians}$$

with h and W being the height and width of the detector. In practice, W = 0.05 cms, h = 0.787 cms and ℓ = 61 cms.

$F(\theta)$ might then be regarded as an experimentally obtained scattering function, but to perform a quadruple deconvolution to obtain $f(\theta,\Phi)$ involves many difficulties.

The procedure therefore is to take an ideal scattering function, produced from a theoretical approach, and impose upon it the effects of finite apparatus functions. By comparison of the resulting function with the experimentally obtained data, the

applicability of the theoretical model can be investigated.

The effects of the apparatus averaging is to smooth out any very fine oscillatory structure that might be expected to appear in a scattering pattern. The longer wavelength oscillations will not disappear, but peaks in the differential cross section will become slightly broader.

CHAPTER 4

ION LENS STUDIES

Simulation of Electrostatic Ion Lens Systems Using a Computer

In an experiment involving the use of ion beams, it is necessary that the behaviour of such particles is fully understood in order to achieve optimum working conditions. In practice, these ions are controlled by electrostatic lenses, comprising a series of thin metal plates or cylinders held at certain fixed potentials, which focus the particles to a desired region, whilst at the same time effectively fixing their energy.

The theories of geometrical ion optics give a good starting point in studying ionic behaviour, but these theories break down, especially when high values of space charge are involved, but mainly because the lens elements do not act independently.

The best available method is in applying the equations of motion to an ion moving through a potential field which has been previously calculated. This, in fact, forms the basis of a computer program which has been used to investigate the performances of various ion lenses [69].

Theory and Calculation

The first duty of the program is in solving Laplace's equation

$$\frac{d^2V}{dx^2} + \frac{d^2V}{dy^2} + \frac{d^2V}{dz^2} = 0 \qquad 4.1$$

where V is the potential at a point in cartesian space (x, y, z).

If the effects of space charge are to be included, then the Poisson equation must be solved

$$\frac{d^2V}{dx^2} + \frac{d^2V}{dy^2} + \frac{d^2V}{dz^2} = -\rho/\varepsilon_o \qquad 4.2$$

where

ρ = value of the space charge at the point (x, y, z)

ε_o = the absolute permittivity constant.

Using cylindrical polar co-ordinates (r, θ, z) equation (4.2) reduces to

$$\frac{1}{r}\frac{\partial}{\partial r}\left(r\frac{\partial V}{\partial r}\right) + \frac{\partial^2 V}{\partial z^2} = -\rho/\varepsilon_o \qquad 4.3$$

the θ derivates being equated to zero as axial symmetry is assumed.

The evaluation of the potential field in the r - z plane can be performed for non analytical solutions of the above expression, and is done here by a relaxation technique.

Expressing the partial derivatives of equation (4.3) in terms of finite differences, the potential field at each grid point can be found using the field values at its four nearest neighbouring grid points. During each iteration of the field, the maximum value of the difference between the consecutive approximations for any point is calculated and printed out. Successive approximations are continued until this accuracy parameter falls below a certain level specified by the user.

This accuracy parameter is useful in determining the effect of space charge on the system. Lacking space charge, the parameter quickly converges to a low value. This also is true when the amount of space charge is small. Larger quantities, however, cause this parameter to be forever unsettled. Thus convergence to a low value ensures the mathematical stability of the potential field using this method.

The basic laws of motion in an electrostatic field now enable ion trajectories to be computed. Again, employing cylindrical polar co-ordinates, the three basic equations can be manipulated to eliminate the parameter of time, thus resulting in the more convenient differential equation

$$\frac{d}{dz}\left(\frac{dr}{dz}\right) = \frac{1}{2V}\left[1 + \left(\frac{dr}{dz}\right)^2\right]\left(\frac{\partial V}{\partial r} - \frac{\partial V}{\partial z} \cdot \frac{dr}{dz}\right) \qquad 4.4$$

Here, dr/dz is simply the tangent of the angle the trajectory makes with the positive z-axis at the point (r, z). Given a potential field V(r, z) as calculated above, along with starting conditions supplied by the user, the tangent, and hence r, can be evaluated along the length of the ionic trajectory.

Capabilities, Requirements and Limitations of the Program

Whilst some of the options in the program are only valid under certain conditions, the vast majority of ion lens' properties can be found very accurately. Indeed, the versatility of the program

coupled with the degree of accuracy possible, is its most attractive feature. Several of the most important options are listed below, and as will become evident, the input data required by the program is both simple and minimal.

The solution to Laplace's equation is both quickly and accurately performed, even for large, complex fields. The main requirements at this stage are the characteristics of the lens elements, namely their radial and axial co-ordinates along with their applied potential. Also required is the fineness of the mesh system for the potential field. Thus any lens element broader than two mesh points in the axial direction should be regarded as a cylinder.

Poisson's equation takes as its first approximate solution the values obtained from solving Laplace's formula. Also determined at this step is the percentage of source current transmitted past each lens element. The requirements for this stage are the ion current at the source and the ionic mass expressed in gram-moles, along with the radial and angular distribution of ions at the source. Random trajectories are generated at the source, and, weighted with the proportion of initial ion current peculiar to both their point and angle of origin, the above two characteristics are found. The limitations of space charge on the potential field have been mentioned before and need no further explanation.

Once mathematical stability of the potential field has been achieved, specific trajectories can be followed through the system. These trajectories can have any initial conditions, these being determined by the user, and up to eight such trajectories are available to him.

There are several reasons why this program and its corresponding experimental system will not agree exactly. The plate potentials as input to the program are those registered by a power supply or measured by a voltmeter external to the experimental system. With such effects as contact potentials, the actual plate potentials need not necessarily be of the values stated. The program itself assumes a perfect experimental line-up of the element apertures, and should therefore be ignorant of such things as steering plates. When such a situation occurs, an average potential of the split parts of the element must be fed into the program. Another experimental difficulty is in the build-up of surface charge on the lens elements resulting in local and generally short lived perturbations of the field. The program has no ability to take these into account. Lastly the radial and angular distributions of the ions at the source are very often not known exactly, and rough models have to suffice.

However, these discrepancies should cause at most minor errors in the calculation, whilst it must not be forgotten that improvements in the first order behaviour of the lens system are the

only worthwhile targets.

Program Tests on the Shell Molecular Beams Apparatus

The above description of the lens program is sufficient to test most systems, and its first task was to detect any faults in the molecular beams apparatus at Shell Research (Thornton, Cheshire).

Ion beams such as CO^+ are formed by electron bombardment and after extraction are mass analysed by a radio frequency quadrupole lens before being introduced into the lens system starting at the reference plate. Thus a large angular divergence in ion trajectories appears at the source.

Ions are then accelerated to a high energy by an acceleration lens, and then decelerated to a final energy of around 10eV by a Lindholm - Gustafsson lens [62].

At the time of investigation, the main fault with the apparatus was the instability of the ion beam, its position of maximum intensity varying by as much as twenty degrees in either horizontal or vertical planes in the matter of a few minutes. It was decided therefore to test the lens system in two parts, taking first the acceleration stage and the first lens plate F of the deceleration lens.

Table 4.1 shows the characteristics of this stage, whilst the voltages used were those found in an experiment to give a maximum

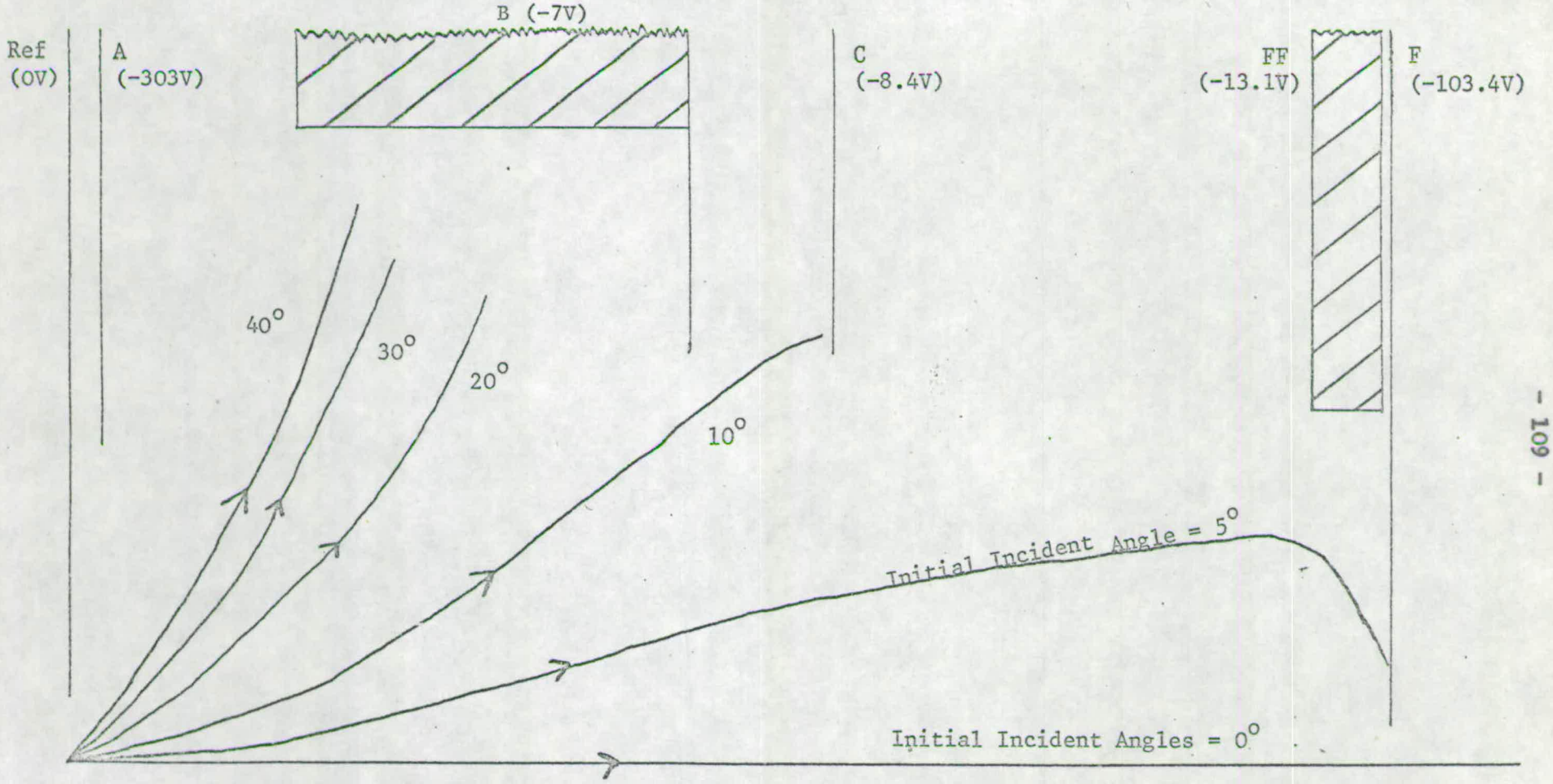

FIGURE 4.1 CO^+ Ion Trajectories for the Acceleration Lens of the Shell Apparatus under the conditions of Table 4.1

Lens Element	Aperture Radius	Axial Co-ordinate	Element Thickness	Element Potential
	Dimensions in Inches			Volts
Reference	0.05	0.0	0.01	0
A	0.25	0.11	0.01	-303.0
B	0.50;0.32	0.91;2.44	1.53;0.01	- 7.0
C	0.32	3.03	0.01	- 8.4
FF	0.25	4.91	0.25	- 13.1
F	0.03	5.18	0.01	-103.4

TABLE 4.1 Characteristics of the Shell Acceleration Lens.

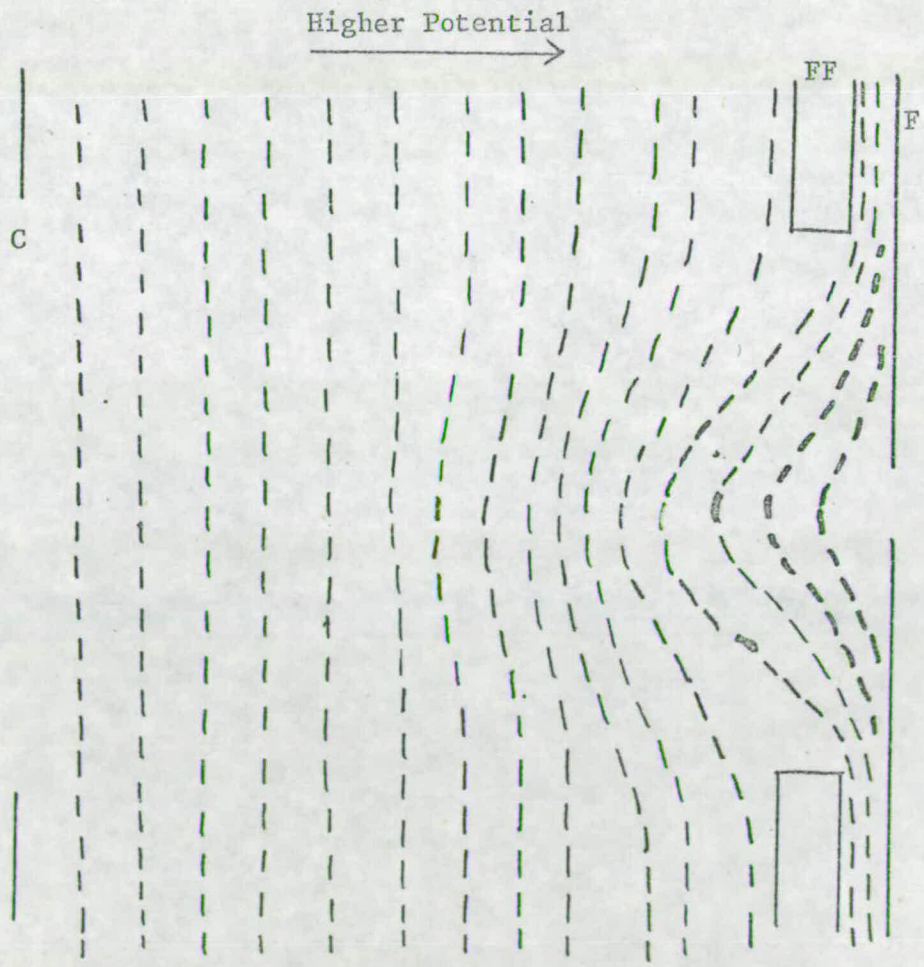

FIGURE 4.2 Potential Field around the Lens Elements C, FF and F under the conditions described in Table 4.1.

beam intensity. Plate FF is a split lens plate designed to steer the beam into the deceleration lens.

The main output from the program was the set of specific trajectories starting from the origin and having initial angles of incidence of 5°, 10°, 20°, 30° and 40°, respectively, results of which can be seen in Figure 4.1. Of these trajectories, only the 5° ion reached anywhere near the final plate. The most alarming feature, though, is the final angle of incidence on striking the exit plate. Were it to have passed through this stage, it would have very little chance of proceeding further.

This behaviour is illuminated by examining the potential field in the region of the last three plates (Figure 4.2). Field penetration from Plate F is small near C, but is very marked round about the final aperture, where two elements of widely differing values of potential and size of aperture are brought into such close contact. Any ions - though these would have to travel very close to the axis - which managed to reach the exit of the deceleration lens would be greatly affected near plate FF by any slight change in voltage. This, no doubt, is the cause of angular instability in the beam.

As for one further point, the calculated transmission through this first stage was evaluated as 4.0%, which is not too different from the experimental value of 5.5%.

Using the above information, the experiment was altered by simply connecting plates F and FF together, and the desired result was achieved. Though the transmitted intensity did not increase, the beam had become perfectly stable, even when tested over a period of several hours.

Table 4.2 shows the new lens element potentials required to achieve a maximum transmitted beam intensity, and on simulating this case, specific trajectories of the kind shown in Figure 4.3 were produced. As expected, the ions have very steady paths towards the exit plates, and are also slightly more focused.

Lens Element	Potential (Volts)
Reference	0.0
A	- 305.0
B	- 8.7
C	- 44.2
FF	- 73.1
F	- 73.1

TABLE 4.2: NEW EXPERIMENTAL POTENTIALS PRODUCING A STABLE BEAM FOR THE ACCELERATION LENS.

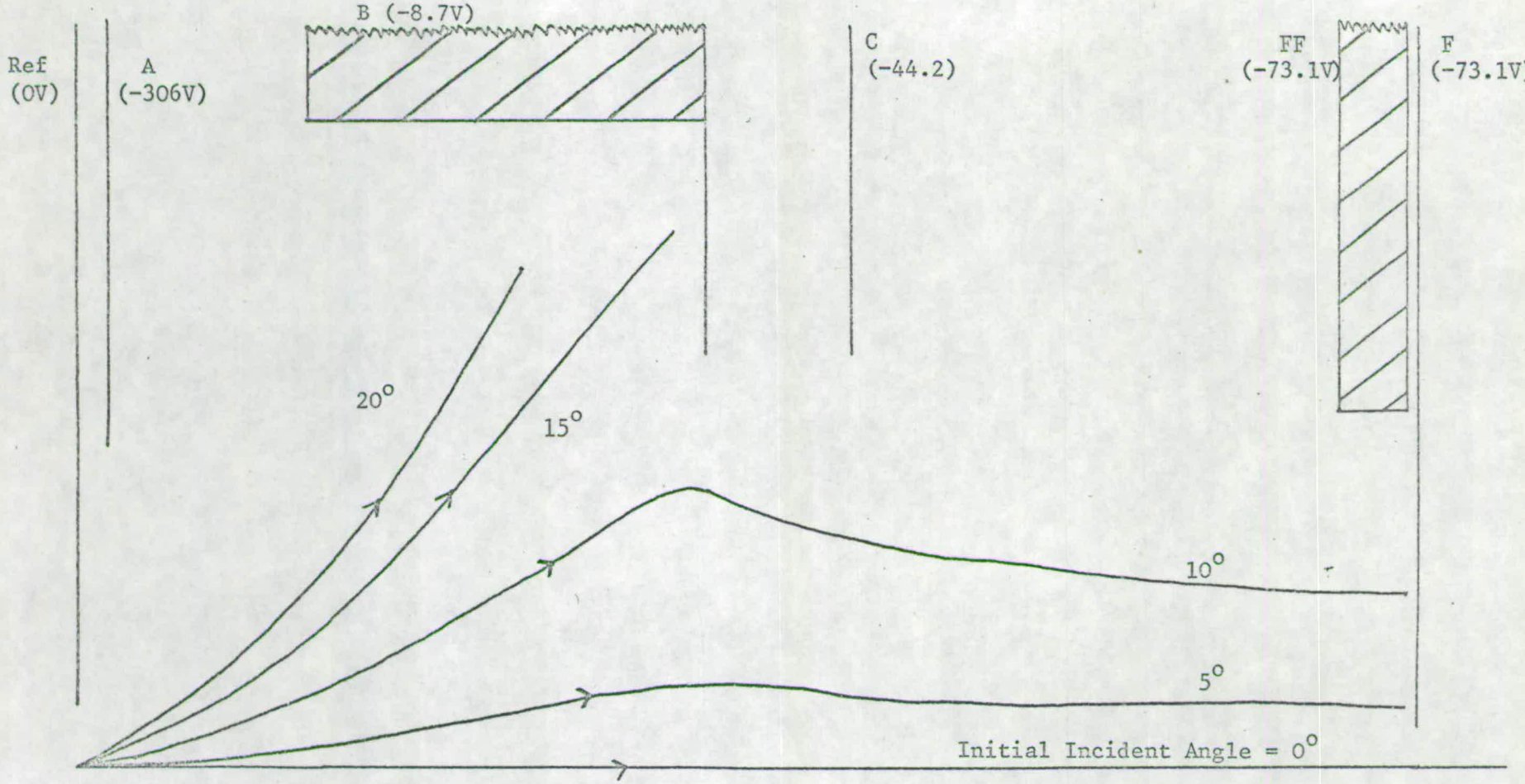

FIGURE 4.3 CO^+ Ion Trajectories for the Acceleration Lens of the Shell Apparatus using the Potentials stated in Table 4.2

Now that a stable ion beam has been achieved, the next aim is in improving the transmission characteristics through the lens. The greatest intensity loss, as exhibited by the specific trajectories in Figures 4.2 and 4.3, occurs at cylinder B, which attracts ions of moderate angular divergence. There seems to be very little focusing, although a small degree of convergence takes place with ions passing the final plate of the cylinder.

An examination of the potential field around cylinder B explains why ions are attracted to it (Figure 4.4a). The suggestion was made that focusing could be achieved by reducing cylinder B to a uniform radius, giving the type of field shown in Figure 4.4b.

Without changing any lens element potentials, the computer simulated the situation where the radius of cylinder B was made uniform at 0.32 ins. The focal properties were now dramatically altered (as can be seen in Figure 4.5), where all the ion trajectories are brought to a focus at about two inches along the axis.

Were the voltage of cylinder B changed, to say -40V, then the focal length for the system might be extended to the exit aperture. Figure 4.6 shows the effect of this suggestion, and the program indicates a fourfold increase in transmission through the exit plate.

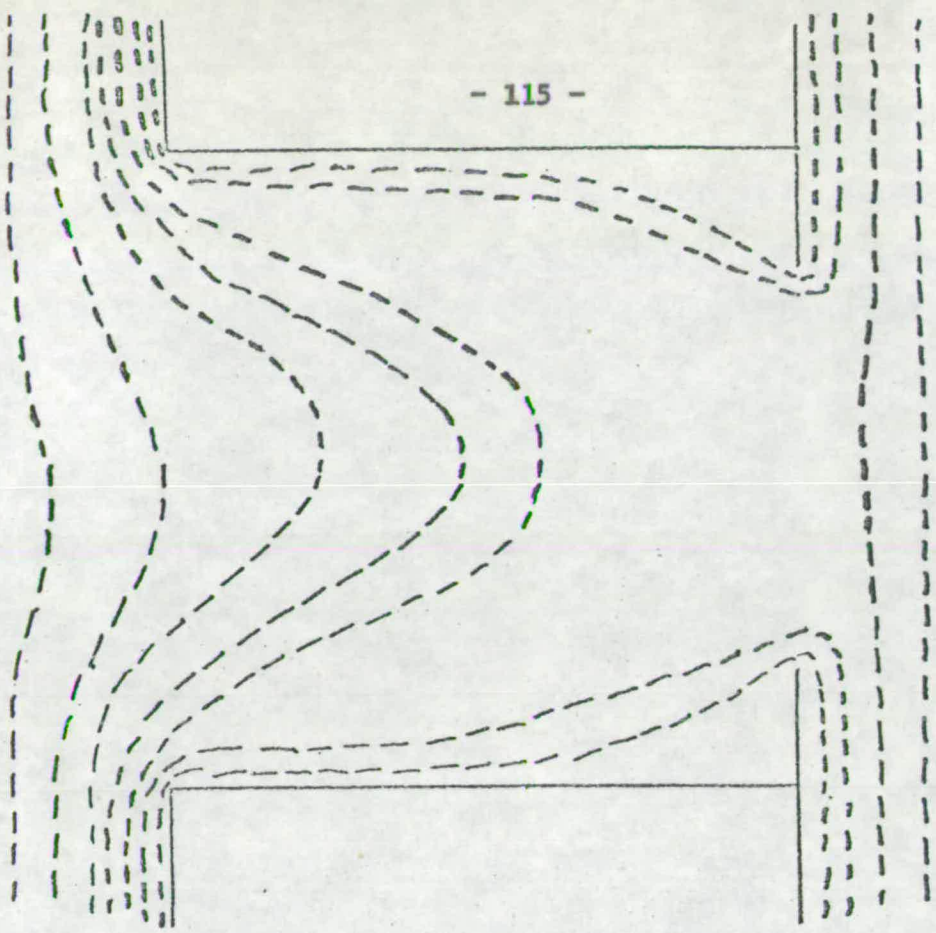

FIGURE 4.4a Potential Field around Cylinder B under Conditions described in Table 4.1.

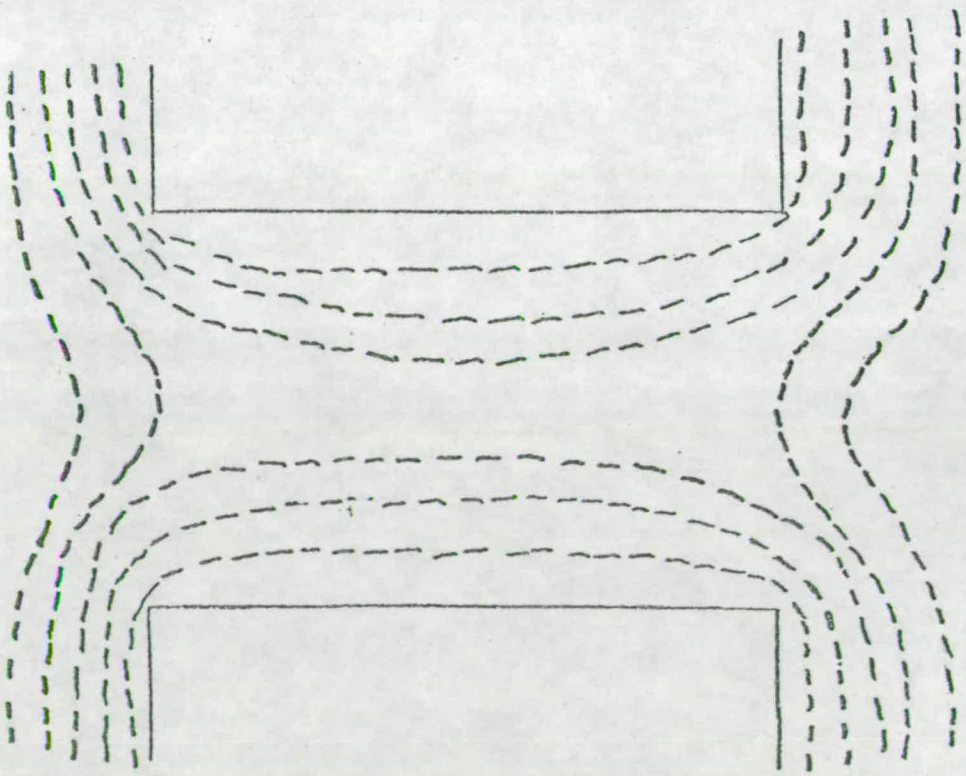

FIGURE 4.4b Potential Field around Cylinder B which has a Uniform Radius.

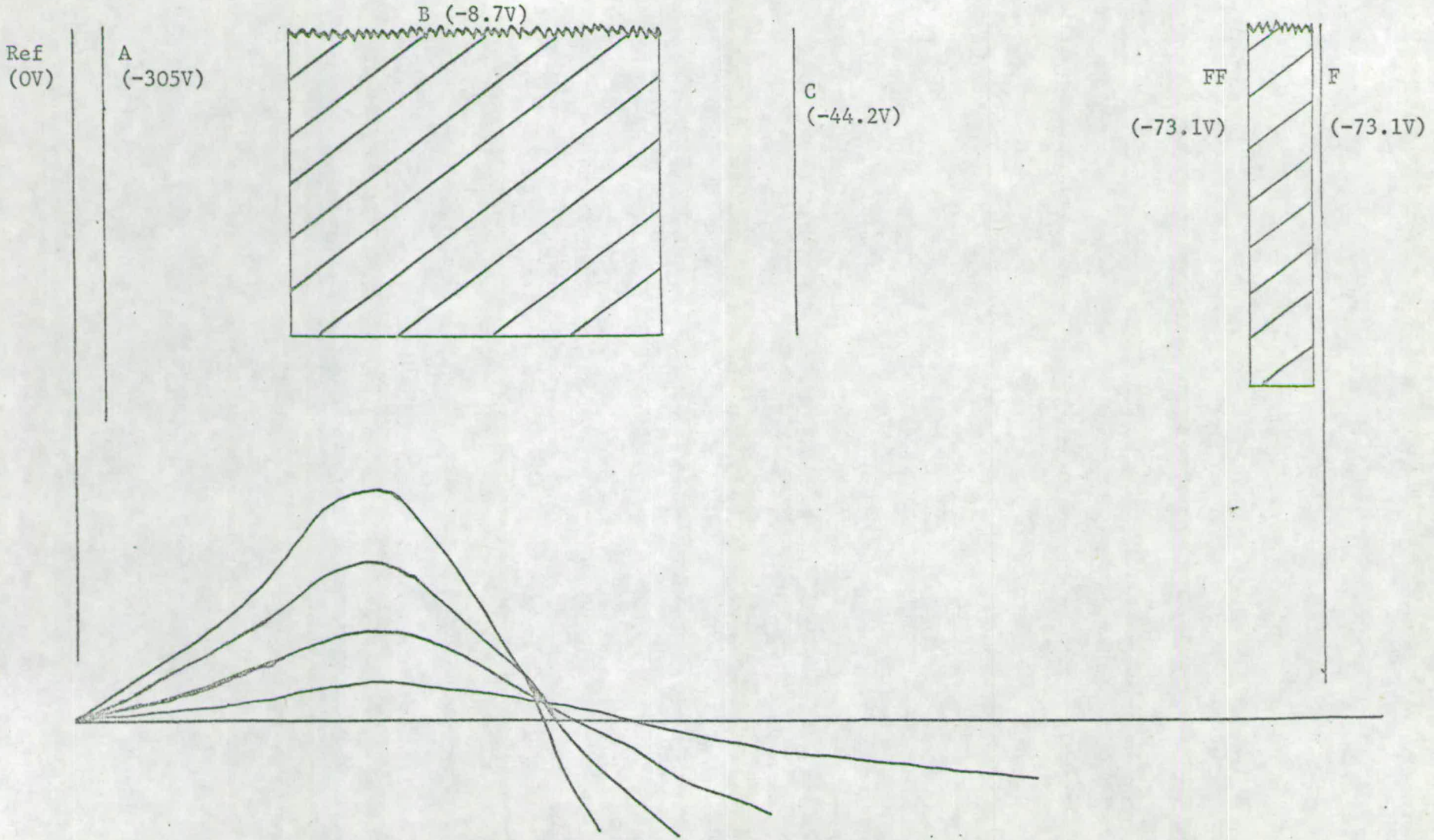

FIGURE 4.5 Effect of Reducing the Radius of Cylinder B to a Uniform Value.

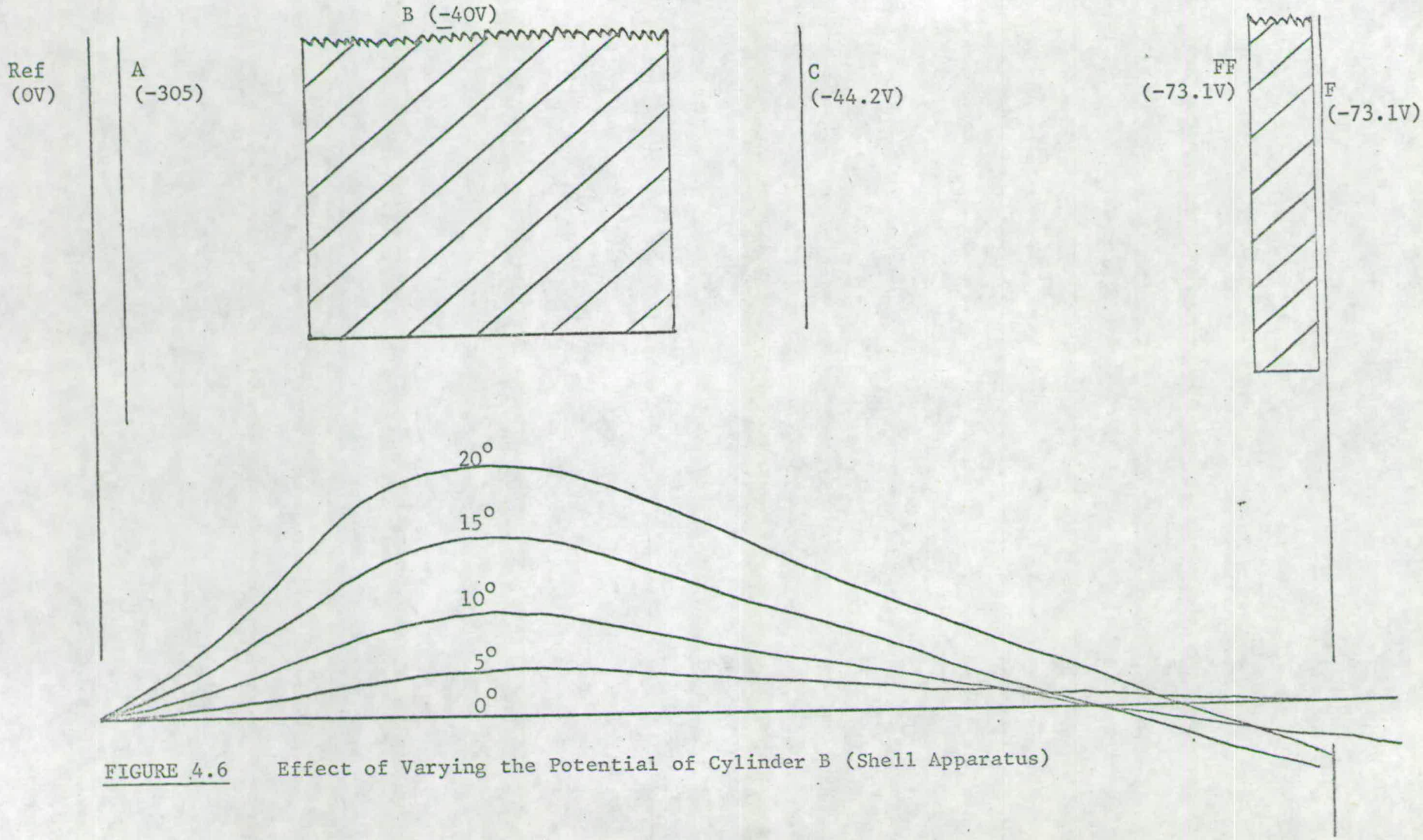

FIGURE 4.6 Effect of Varying the Potential of Cylinder B (Shell Apparatus)

Later experiments involving the modified geometry of cylinder B haveshown that, whilst an increase in final intensity by a factor of two was achieved, the exact increase predicted by the computer did not materialise. Once again, the exact matching of those results is only of secondary interest, provided that the same gross effects are similar.

Tests on the Lindholm - Gustafsson deceleration lens are reported further on in this chapter.

Program Tests on the Edinburgh Molecular Beam Apparatus

The theory and design of this apparatus have been described before in Chapter 3 of this thesis. Ions, formed on a porous tungsten disc, are accelerated to very high energies before being decelerated to a final energy of about 100eV.

The main concern was in combining the acceleration and deceleration stages, and in particular, finding if the deceleration lens, built according to the recommended dimensions [70,71], could accommodate thesize of the source image. Also of importance was the angular divergence of the ions entering the second lens.

The first part of the procedure was as before, where the program examined the acceleration stage and the first plate F of the deceleration lens, the physical dimensions of which are shown in Table 4.3.

Element	Aperture Radius	Axial Co-Ordinate	Element Thickness
Source	0.3	0.0	-
Grid	0.3	0.25	0.3
Accelerator	0.3	1.75	0.1
"Top Hat"	0.2 ; 2.5	3.65 ; 3.95	0.3 ; 3.8
B	0.3	9.25	0.2
F	0.051	10.35	0.05

TABLE 4.3: DIMENSIONS (cms) FOR ELEMENTS IN THE ACCELERATION LENS (AXIAL CO-ORDINATE GIVEN FOR THE FIRST FACE OF A THICK ELEMENT).

Element	Potential (Volts)
Source	+ 100
Grid	+ 51
Accelerator	- 405
"Top Hat"	- 405
B	- 355
F	- 336

TABLE 4.4: LENS ELEMENT POTENTIALS FOR MAXIMUM TRANSMISSION THROUGH PLATE F.

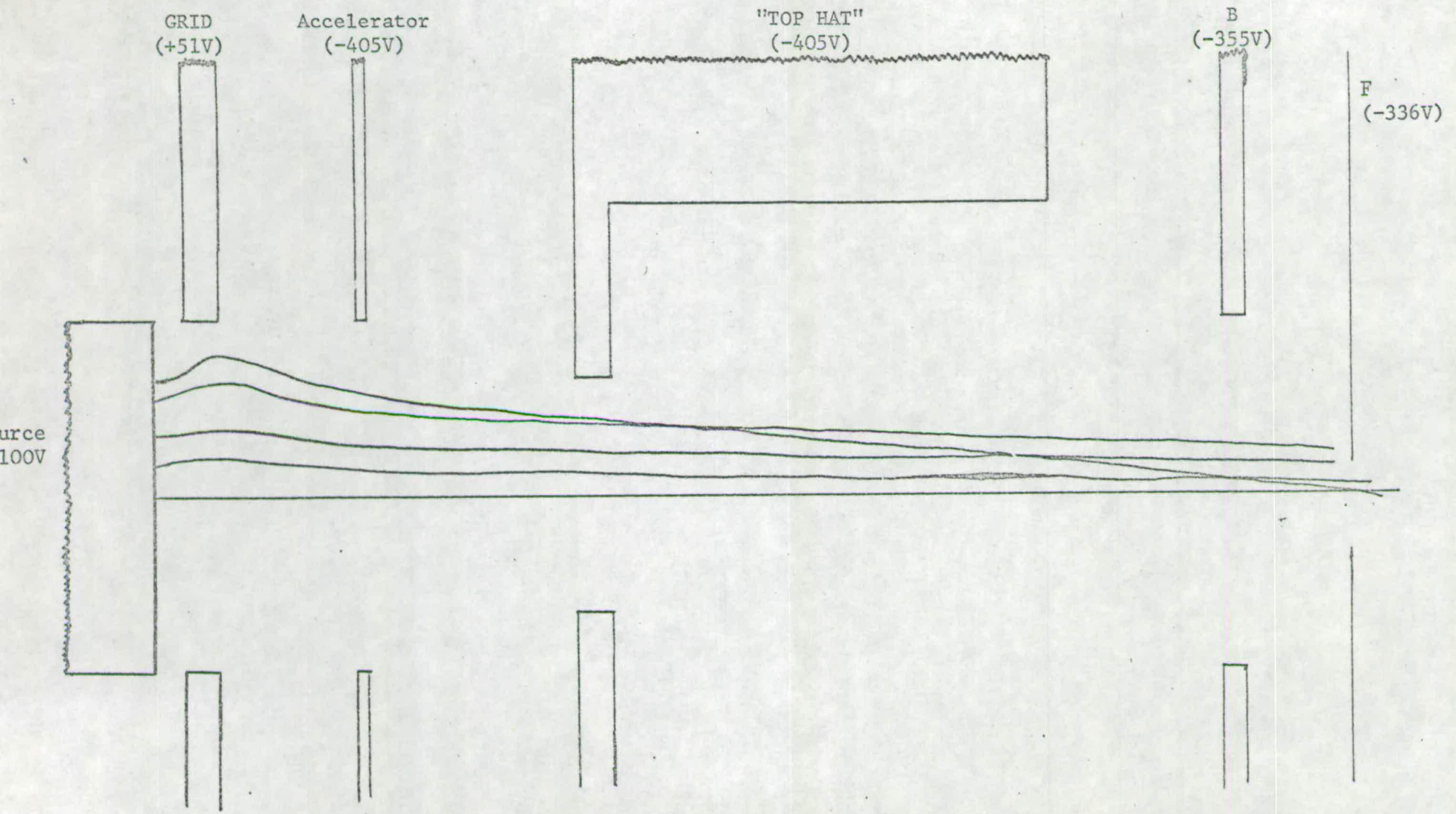

FIGURE 4.7 Specific Trajectories for the Acceleration Lens (Edinburgh Apparatus) for the Case of Maximum Transmission.

The program examined the case for maximum transmission through plate F, the lens element potentials used being obtained experimentally (Table 4.4). The radius of the larger aperture of the "top hat" was reduced to 0.5 cms to allow a finer potential field mesh. This does not produce any change in the potential field, as the "top hat" produces a large region of equipotential.

Ions, assumed to be at rest on the source, are accelerated by the field and initially can be regarded as moving perpendicular to the source. Specific trajectories starting with zero angle of incidence and from various radial distances on the source are shown in Figure 4.7.

No major errors in accelerating the beam are found here, and ions are transmitted with very low angular divergence (less than 0.1 degrees). However, an increase in transmission can be achieved by increasing the aperture of plate F.

If this case is rerun several times, changing only the exit aperture slightly, a rough idea of the beam profile on plate F can be mapped by plotting the final transmission as a function of aperture radius.

Table 4.5 shows these results.

Radius of Exit Aperture F (cms)	Final Transmission as %age Source Current
0.02	5.8
0.04	31.1
0.06	75.7
0.08	75.7
0.10	75.7

TABLE 4.5: EFFECT ON FINAL TRANSMISSION OF VARYING THE FINAL PLATE APERTURE. (EXPERIMENTAL APERTURE RADIUS IS AT 0.051 cms).

The existing radius of the exit plate is obviously not large enough, with about 20% of the possible transmitted current lost. Whilst it might be thought that a slight increase might suffice, it must be pointed out that these tests were run on a much reduced value (by a factor of about 100) of the source current. As the effect of increased space charge would be to broaden the beam profile, an increase in the exit plate radius by a factor of two is recommended. Whether this results in doubling the scale of the deceleration lens will be found in the next series of tests.

Tests on the Lindholm - Gustafsson Lens

The main purpose of this lens is to produce an axial field of the form

$$V(z) = a \exp(-bz) \qquad 4.5$$

where a, b are positive constants. The way of achieving this experimentally has been described adequately in Chapter 3, and this system is common to both Shell Research and Edinburgh molecular beam machines.

In studying this lens, the whole ionic path from source to the exit aperture of the charge exchange chamber was considered, a total distance of 24.85 cms. One minor change, the doubling of the aperture of plate F, was made, otherwise the dimensions are as described in Table 3.1. Using the accelerating voltage of -336V in Table 4.4 for the deceleration lens, the lens element voltages as used by Rose [70] were employed.

Figure 4.8 shows the value of this exercise. Studies on the acceleration lens have shown that all ions entering the second lens are effectively travelling paraxially. However, those nearest the axis soon develop a fair degree of divergence, but alarm must be expressed for those even further away.

The reason for this is not difficult to spot, as all ion paths are now affected by one lens element, namely plate G.

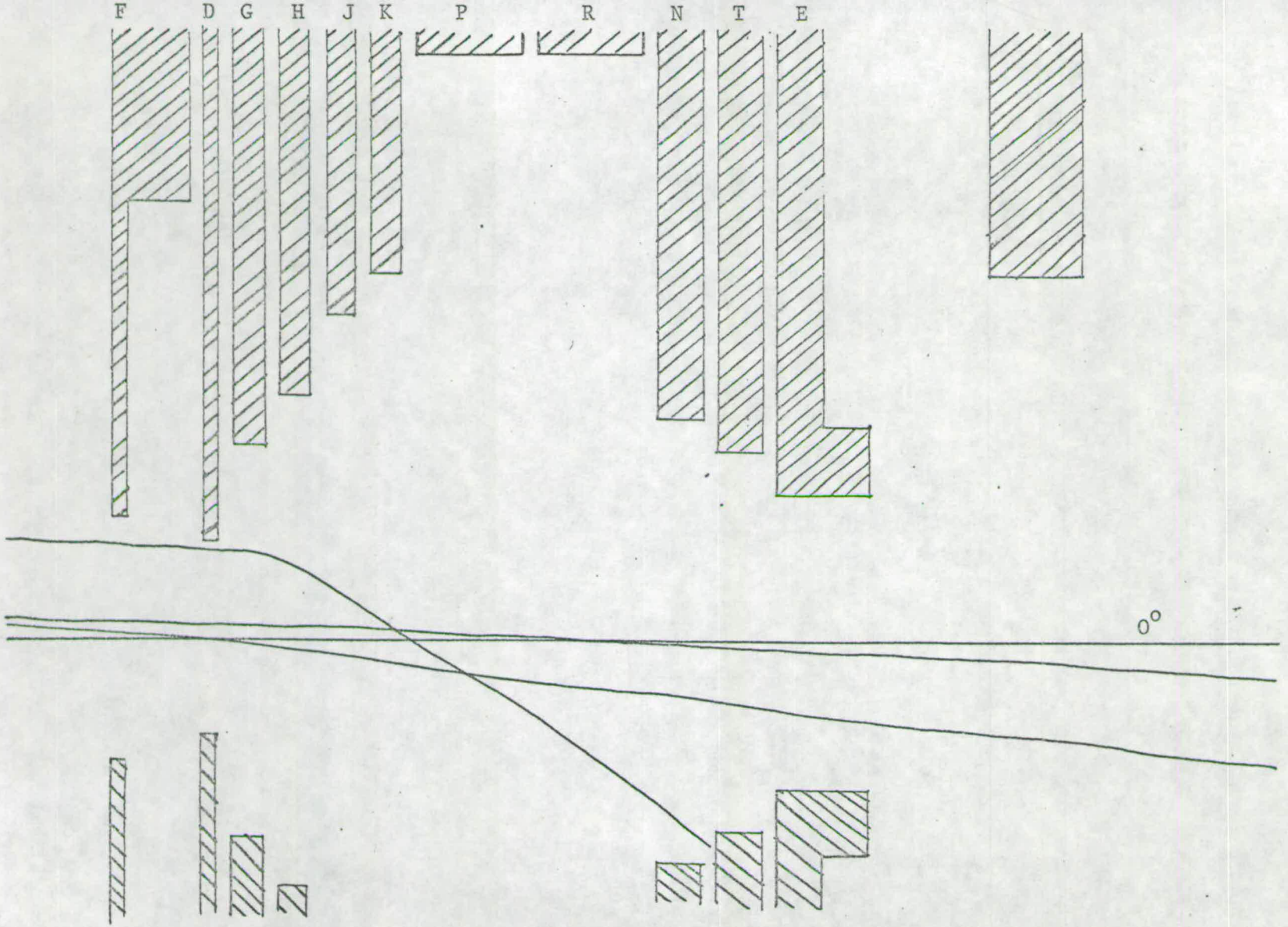

FIGURE 4.8 Specific Trajectories for the Lindholm - Gustafsson Lens where V_G = 10% V_A.

Looking at the decay in acceleration potential throughout this lens (Table 3.1), this element deviates substantially from the manner desired by equation (4.5). Examination of the field in this region (Figure 4.9) shows an excessive curving of the equipotential lines, thereby greatly affecting ionic behaviour. It seems that plate G should have a potential of 70 - 90% of the accelerating voltage in order to form a much less curved field.

All specific trajectories are not shown in Figure 4.8, but Table 4.6 summarises the results. Shown first is the radial starting value, Rstart, on the source, and subsequent columns show the eventual destination (zstop, Rstop) and final angular divergence (αstop) of each ion path.

The total transmission through the system was found to be one percent.

A rough estimate of the more correct value of the potential of plate G might be 70% of the accelerating voltage. Ion trajectories for this simulated case are shown in Figure 4.10, and Table 4.7, similar to Table 4.6, shows the summary of their history.

There is no doubt that a vast improvement has taken place, the transmission having increased from one to three percent now. A greater convergence of the specific ion trajectories have resulted in most cases, and their final angular divergence has decreased drastically.

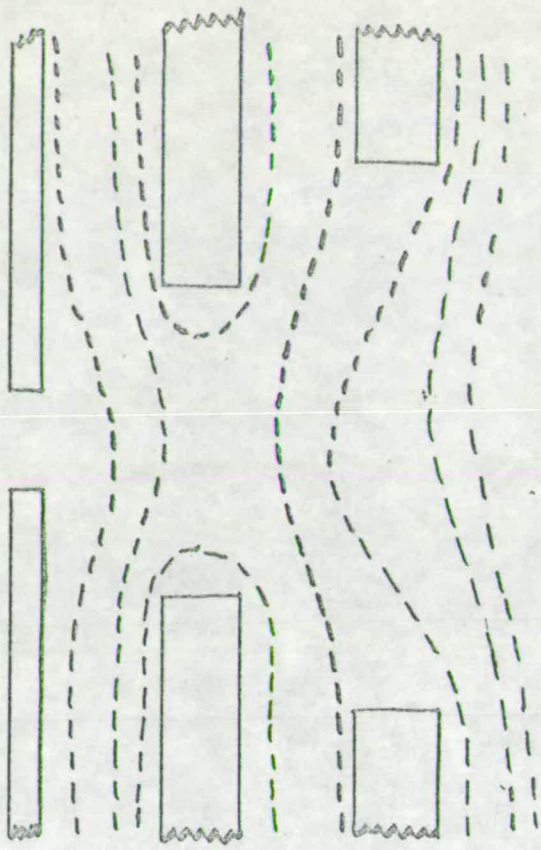

FIGURE 4.9 Potential Field round plate G where V_G = 10% V_A.

R_{start} (cms)	Stopping Plate	Z_{stop} (cms)	R_{stop} (cms)	α_{stop} (degrees)
0.0	-	∞	0	0
0.05	N.C. Exit	24.85	-0.170	0.85
0.10	N.C. Exit	16.85	-0.327	3.5
0.13	Element T	12.35	-0.168	11.0
0.16	N.C. Exit	16.85	-0.439	5.0
0.20	N.C. Exit	16.85	-0.171	1.2

TABLE 4.6 End points of ion trajectories entering the deceleration lens where V_G = 10% V_A (N.C. = Neutralisation Chamber).

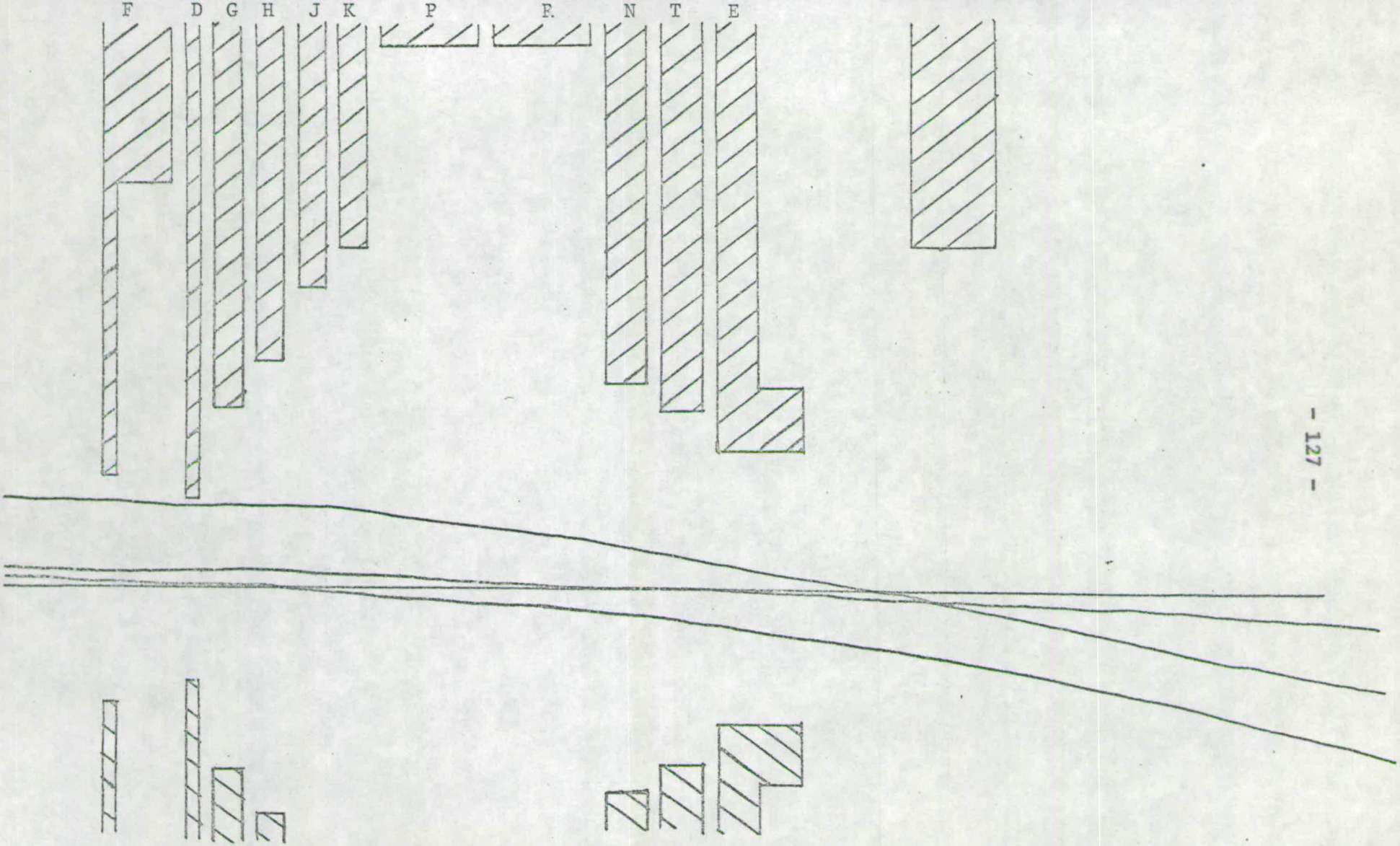

FIGURE 4.10 Specific Trajectories for the Lindholm - Gustafsson Lens where V_G = 70% V_A.

R_{start} (cms)	Stopping Plate	Z_{stop} (cms)	R_{stop} (cms)	α_{stop} (degrees)
0.0	-	∞	0	0
0.05	C.E.C. exit	24.85	-0.124	0.5
0.10	C.E.C. ent.	16.85	-0.139	1.95
0.13	C.E.C. ent.	16.85	-0.289	3.8
0.16	C.E.C. ent.	16.85	-0.167	2.5
0.20	C.E.C. ent.	16.85	-0.186	1.7

TABLE 4.7 End Points for Ion Paths Entering the Deceleration Lens (V_G = 70% V_{ACC}). (C.E.C. Charge Exchange Chamber)

Beam Energy (eV)	V_A (Volts)	I_{max} (Amps)
200	-460	5.7×10^{-9}
100	-300	2.6×10^{-9}
50	-300	1.9×10^{-9}
30	-250	1.1×10^{-9}

TABLE 4.8 Beam Energy, Accelerating Voltage V_A, and Maximum Transmitted Ion Current for Figure 4.14.

Experimental Verification of Predicted Results

Two possible modes of improvement have been suggested by the previous work: that of widening the aperture of plate F; and that of finding a more suitable potential for plate G. The means of testing these effects was by measurement of the ion current transmitted through the neutralisation chamber.

Under optimum focusing conditions, the previous best value for such a current was about 4×10^{-10} Amps at 100eV. Doubling the entrance plate aperture brought this value to $\sim 10^{-9}$ Amps.

With this aperture at its new enlarged value, tests on the potential of plate G were carried out. Figure 4.11 shows a plot of the ratio of transmitted current I to maximum transmitted current I_{max} against the voltage of G, described as a percentage of the accelerating potential V_A. With the beam energy fixed at 100eV, two values of V_A were used, these being -400V and -300V. Whilst the maximum transmitted current was different in the two cases, being 1.45×10^{-9} Amps and 2.6×10^{-9} Amps respectively, the curves were very similar, having a plateau maximum for V_G between 70% and 90% V_A. This is much better than for the recommended potential of 10% V_A by a factor of two or three.

Figure 4.12 is similar to the previous figure, but only one value of V_A has been used for each of the four beam energies. All relevant figures for this graph are included in Table 4.8.

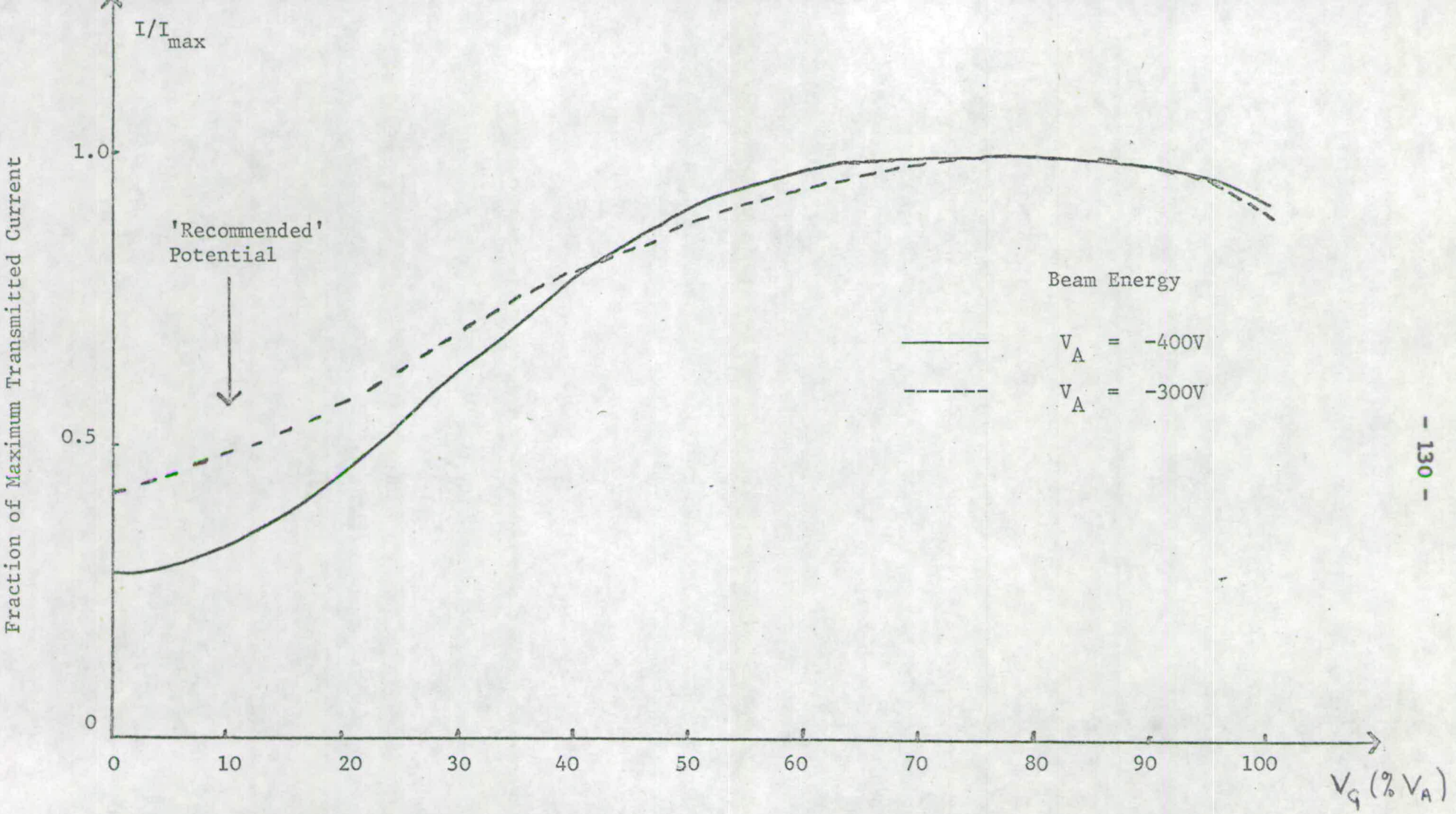

FIGURE 4.11 Variation of Current Transmitted Through the Neutralisation Chamber as a Function of Element G Potential.

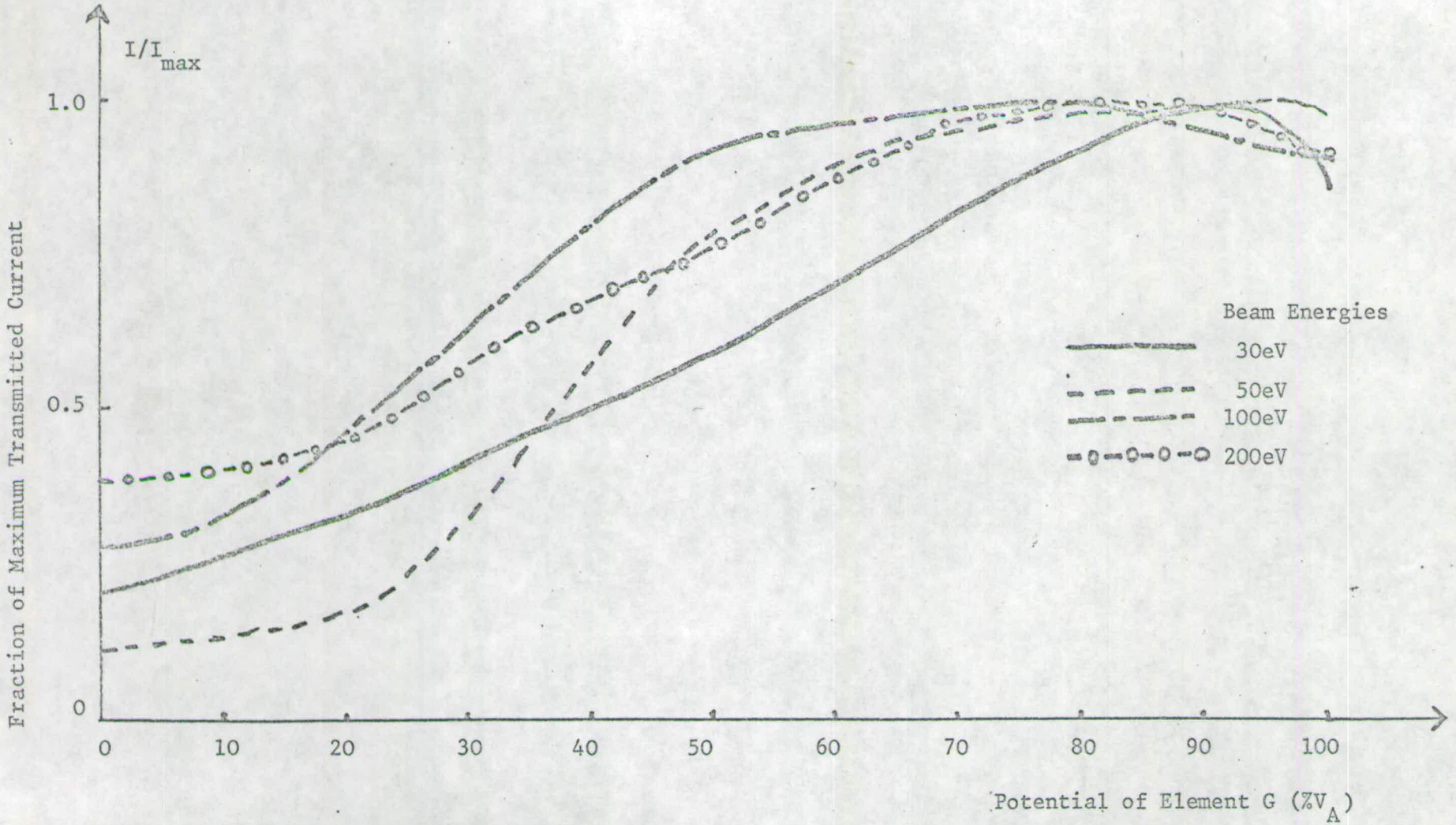

FIGURE 4.12 Transmission Characteristics of the Deceleration Lens as a Function of Element G Potential for four Beam Energies.

The curves are again very similar in shape with wide maxima in the range 70 to 90% V_A. That the focal properties of the assembly have been improved was seen in the increased sensitivity of the ion beam at optimum transmission to small changes in steering plate potentials.

These last results then enable the potential of the element G to be fixed at about 80% V_A, for the elements are fed by a power supply via a resistance chain.

A chance to test these new lens characteristics on beams of less than 20eV energy was offered by the Shell apparatus. The lens was constructed as originally intended, having, unlike the Edinburgh version, the final beam collimating plate S.

Experimental tests showed that no substantial increase in beam intensity occurred with plate G at its new high value, but this could be explained on two counts. Firstly, low energy beams are affected more by space charge considerations, and this lens is probably operating in the space charge limit [70]. Thus better transmission at plate G will not necessarily increase the final transmission. Secondly, with plate G in a divergent mode, the defocused beam can be later focused by the variable plates N and E. This again is more likely with low energy beams.

If, however, plates N and E are placed in the midpoints of their range, the most intense beams are obtained when plate G is in

the region of 60 - 80% of the accelerating voltage; and, further, beam stability improves significantly. This tends to give more credence to the second explanation.

Further Points on the Deceleration Lens

An interesting section in a review featuring the Lindholm - Gustafsson lens by J.B. Hasted [62] reads:

> The field has a potential of the form
>
> $$V(x) = a \exp(-bx)$$
>
> where a, b are positive constants. . . . . Detailed calculation by Willmore of the path followed by an ion confirms that the deviation is much reduced. Gustafsson and Lindholm have found, however, that an exponential field actually produces more deviation than certain empirically designed apertures . . . . . .

These two seemingly contradictory statements above can be explained in the light of this chapter. Willmore did prove than an exponentially decaying field has a converging effect, but did not show that this was produced by the lens in question. Neither did Lindholm and Gustafsson who wrongly assumed that the desired effect had been achieved by their lens, and some shade of doubt was cast by them on these calculations.

Conclusion

There is no doubt that this type of program is of great value in improving ion optic systems. Even standard lenses assumed to be operating at optimum efficiency can be improved.

Previously properties of ion systems were determined by fairly approximate formulae [73] which could not handle potential fields where elements were closely spaced. This program overcomes this problem.

However, it should only be used to detect major faults in a system and never to find the optimum focusing potentials for a series of lens elements. An experiment can give this answer more quickly and accurately.

CHAPTER 5

TIME OF FLIGHT STUDIES

Introduction

Several different techniques have been employed to investigate inelastic collisional processes.

Electron impact spectroscopy of such substances as N_2, CO and NH_3 have been investigated in the hope of detecting electric - quadrupole and singlet - triplet transitions [74]. A well collimated beam of electrons is velocity analysed by magnetic-electrostatic analysers before and after collision with the target molecule. An electron impact spectrum, namely the plot of intensity of scattered electrons for a particular energy loss against that particular energy loss, is formed. Peaks are present, corresponding to vibrational transitions during one electronic excitation, with the spectrum extending to energy losses of as much as eleven electron volts.

Ion impact spectroscopy is technically similar [75]. One experiment involving H^+ and H_2^+ in the energy range of 150 - 500eV on targets such as N_2, CO, C_2H_2 and C_2H_4* demonstrated energy losses of up to 10eV, but more importantly, a high specificity in the choice of transition.

Electron and ion impact spectroscopy are useful in studying inelastic processes involving charged particles, but cannot be extended to cover neutral-neutral collisions. However, several workers have looked at the excited species formed during an inelastic

collision. For instance, by studying the intensity and wavelength of light emitted when a fast sodium beam collides with NO_2 or SO_2, total excitation cross sections as functions of wavelength and collision energy can be found.[12]. Other workers [13] have state selected the excited species formed.

Time of flight processes, however, are most recent, and several important sets of results [20,21,77] have been obtained. It has the advantage of being applicable to both ion and neutral beam reactions.

The chapter fully discusses some theoretical considerations behind a time of flight experiment, and then comments on some preliminary experimental tests on the apparatus described in Chapter 3.

Convolution of Time of Flight Results

If a delta function pulse of unit amplitude starting from the source undergoes a collisional process, either elastic or inelastic, then it wou ld have a time of flight (analogue) spectrum given by F(t), where t is the arrival time. This might include information on the energy spread within the pulse, and any effect caused by the collisional process.

If now the pulse from the source has a certain width D, then the arrival spectrum is given by the convolution integral

$$A(t) = \int_0^D I(\lambda)\, F(t-\lambda)\, d\lambda \qquad 5.1$$

where $I(\lambda)$ is the intensity of the pulse at a given pulse time parameter λ. For a square wave pulse, then

$$A(t) \propto \int_0^D F(t-\lambda)\, d\lambda \qquad 5.2$$

On arriving at the detector, the signal will be gated, or counted by successive channels of say a multi channel analyser. If the channel starts counting at a time to and remains open till $t_o + t_g$, then the number of counts recorded in this channel will be

$$M(t_o) = \int_{t_o}^{t_o + t_g} A(t)\, dt \qquad 5.3$$

Thus the arrival spectrum will be in the form of a histogram, having been formed by the convolution over two gate functions of widths D and t_g.

Elastic Collision Processes

In evaluating the arrival spectrum for a delta function pulse undergoing elastic scattering, the main parameters will be

d the total flight path

m the mass of the main beam particle

E the superimposed beam energy

Ions produced in the apparatus previously described will have a Maxwellian velocity distribution [61] at a tungsten disc temperature T, given by

$$n(v)dv = c\, v^2 \exp(-v^2/\alpha^2)dv \qquad 5.4$$

where v = the thermal velocity

α = the most probable thermal velocity

c = the Maxwellian normalisation constant

If the ions gain an energy E by electrostatic acceleration, the thermal velocity v will be transformed to a higher velocity V where

$$v^2 = V^2 - \frac{2E}{m} \quad \text{and} \quad vdv = VdV \qquad 5.5$$

Substituting (5.5) into (5.4), the final velocity distribution is found to be

$$n(V)dV = cV\left\{V^2-\frac{2E}{m}\right\}^{\frac{1}{2}} \exp\left\{\frac{-(V^2-2E/m)}{\alpha^2}\right\}dV \qquad 5.6$$

If the pulse is formed after acceleration, a particle of velocity V will arise at a time t given by

$$V = d/t \quad \text{and} \quad dV = \frac{d}{t^2}\,dt \qquad 5.7$$

Substituting V and dV into (5.6) yields the form of F(t) as

$$F(t) = \frac{cd^2}{t^3} B \exp-(B/\alpha)^2 \qquad 5.7$$

where

$$B^2 = \frac{d^2}{t^2} - \frac{2E}{m}$$

with the provision that F(t) is real, and greater than or equal to zero. Thus if the term

$$d^2/t^2 - 2E/m$$

becomes less than zero, F(t) automatically becomes zero, thus ruling out any contribution by thermal velocities against the beam direction.

Taking the values of

d = 120 cms

m = 39.1 a.m.u. (for Potassium)

T = 1500°K

a computer program found the shape and properties of F(t) for various values of E. Figure 5.1 shows a typical spectral shape, whilst the main characteristics are found in Table 5.1.

The important features, however, are:

a. The curves have a sharp cut-off point where

$$t = d/V_o$$

where V_o is given by $E = \frac{1}{2}mV_o^2$

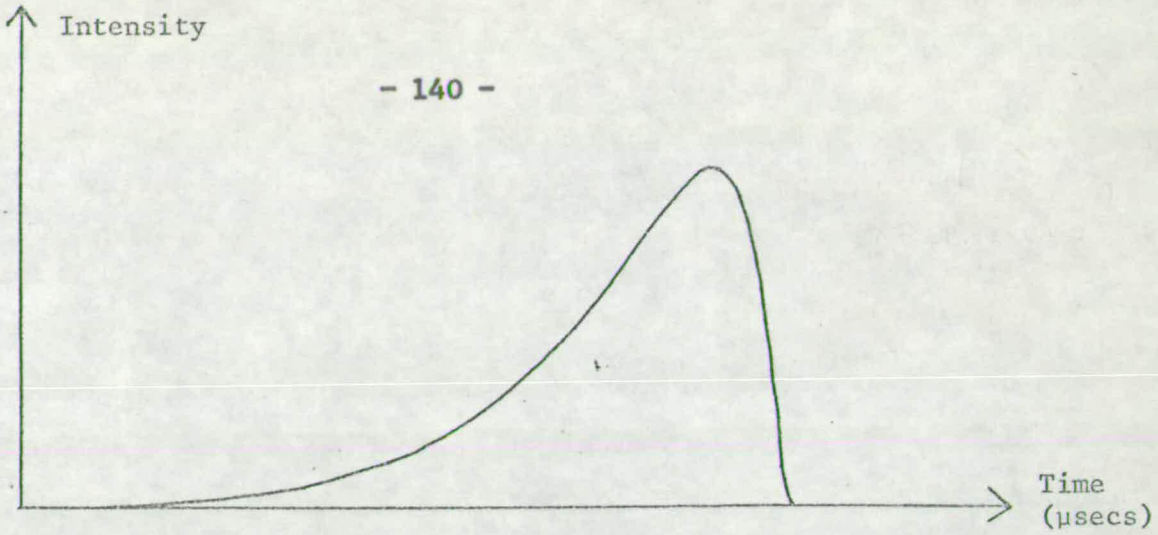

FIGURE 5.1 Typical Arrival of Spectrum for a Delta Function suffering Elastic Collision.

Beam Energy (e.V)	Peak Height (arbitrary)	Peak Arrival Time (μsecs)	Half Width (μsecs)
100	1765	54.04	0.063
90	1510	56.97	0.072
80	1360	60.42	0.087
70	1035	64.59	0.107
60	820	69.76	0.135
50	625	76.41	0.176
40	445	85.41	0.234
30	290	98.59	0.432
20	159	120.67	0.710
10	57	170.40	1.960

TABLE 5.1 Characteristics of the Arrival Spectra for a Delta Function Pulse suffering Elastic Collision (Flight Path = 120 cms).

b. the tail part of the curve occurs on the fast side of the peak height, i.e. to the lower values of t, whilst there is a sharp drop after the peak height has been achieved.

c. the pulse spreads more rapidly and decreases in amplitude at lower beam energies, where the thermal contribution is a greater fraction of the total energy.

The first two points are important, as any inelastic peaks will occur at high values of t.

The shapes of finite width pulses can be found using equations (5.2) and (5.8), and taking a square wave of width 1 microsecond, the arrival spectra can be computed for various values of E, the superimposed beam energy. The main properties are contained in Table 5.2, but these can be summarised as follows:

a. from 100eV down to 30eV, the curves all had halfwidths of 1 microsecond, and to within 2%, the same peak height.

b. down to energies of 40eV, the curves retained most of their square wave origins, although thermal spreading occurred at the edges.

c. below 30eV, the curves began to look more like delta function responses, because the thermal spread was becoming more important. The half widths of the curves increased dramatically, and not surprisingly, the peak heights fell substantially in this range.

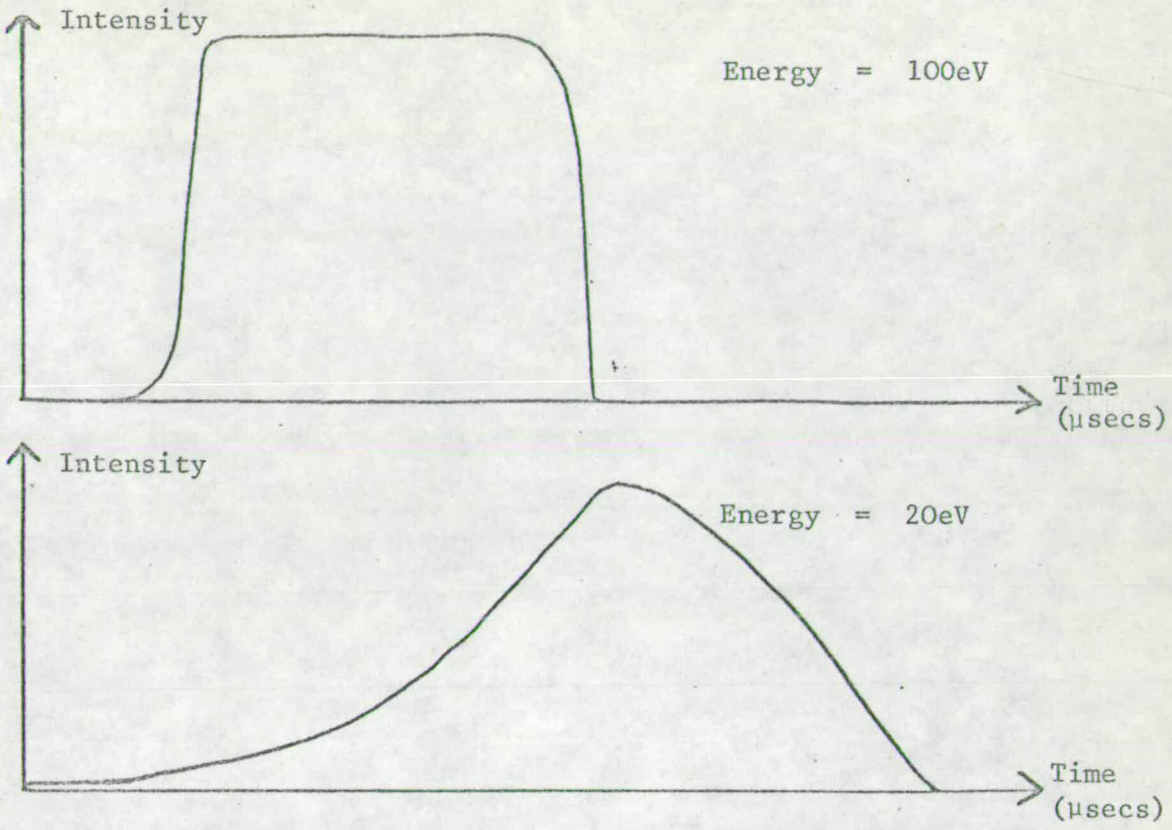

FIGURE 5.2 Typical Arrival Spectra for a 1 μsec Square Wave Pulse suffering Elastic Collision.

Beam Energy (e.V)	Peak Height (arbitrary)	Peak Arrival Time (μsecs)	Half Width (μsecs)
100	955	54.52	1.00
90	955	57.44	1.00
80	955	60.89	1.00
70	955	65.04	1.00
60	955	70.21	1.00
50	955	76.84	1.00
40	950	85.52	1.00
30	935	98.70	1.00
20	800	120.88	1.12
10	390	170.80	2.11

TABLE 5.2 Characteristics of the Arrival Spectra for a 1μsec Square Wave Pulse Suffering Elastic Collision.

Inelastic Collision Processes

The main purpose in studying of flight methods is of course to investigate inelastic and reactive collsions at all possible beam energies. The first step is to find the delta function response F(t) to an energy change ΔE, occurring at a distance ℓ from the source and hence at $(d-\ell)$ from the detector.

Now a particle of velocity V will have a new velocity U on gaining an energy ΔE, where

$$U = XV \qquad 5.9$$

and

$$X^2 = 1 + \Delta E/E \qquad 5.10$$

The arrival time at the detector under the above collision process will be

$$t = \frac{\ell}{V} + \frac{d-\ell}{U}$$

and hence

$$t = Y_{/V} \qquad 5.11$$

where

$$Y = \ell + \frac{(d-\ell)}{X} \qquad 5.12$$

Thus

$$V = Y_{/t} \quad \text{and} \quad dV = (Y_{/t^2})dt \qquad 5.13$$

Substituting for V and dV in equation (5.6) results in a form for F(t)

$$F(t) = \frac{cY^2}{t^3} B \exp-(B/\alpha)^2 \qquad 5.14$$

where $$B^2 = \frac{Y^2}{t^2} - \frac{2E}{m}$$

If E were zero, X would be unity and Y = d, and the corresponding equation for elastic scattering (i.e. 5.8) would occur.

The above equation, in conjunction with (5.2), would predict the arrival spectrum for a 1 microsecond square wave pulse. The shapes of these curves are similar to those for elastic scattering, and could be considered as elastic peaks delayed by a fraction of a microsecond.

It was this property which caused these results to be of disappointing consequence. For if it were assumed that all channels were of equal amplitude, then a typical spectrum for a beam energy of 100eV and energy changes of -2eV, -4eV and -6eV would look like Figure 5.3. Even this type of picture, with its relatively large energy losses, would prove difficult to resolve. Furthermore, the elastic channel will in most cases be the dominant one, and will tend to smother the more intersting inelastic peaks.

Reactive Scattering

Reactive scattering can be dealt with in a similar manner to inelastic scattering. Such processes as

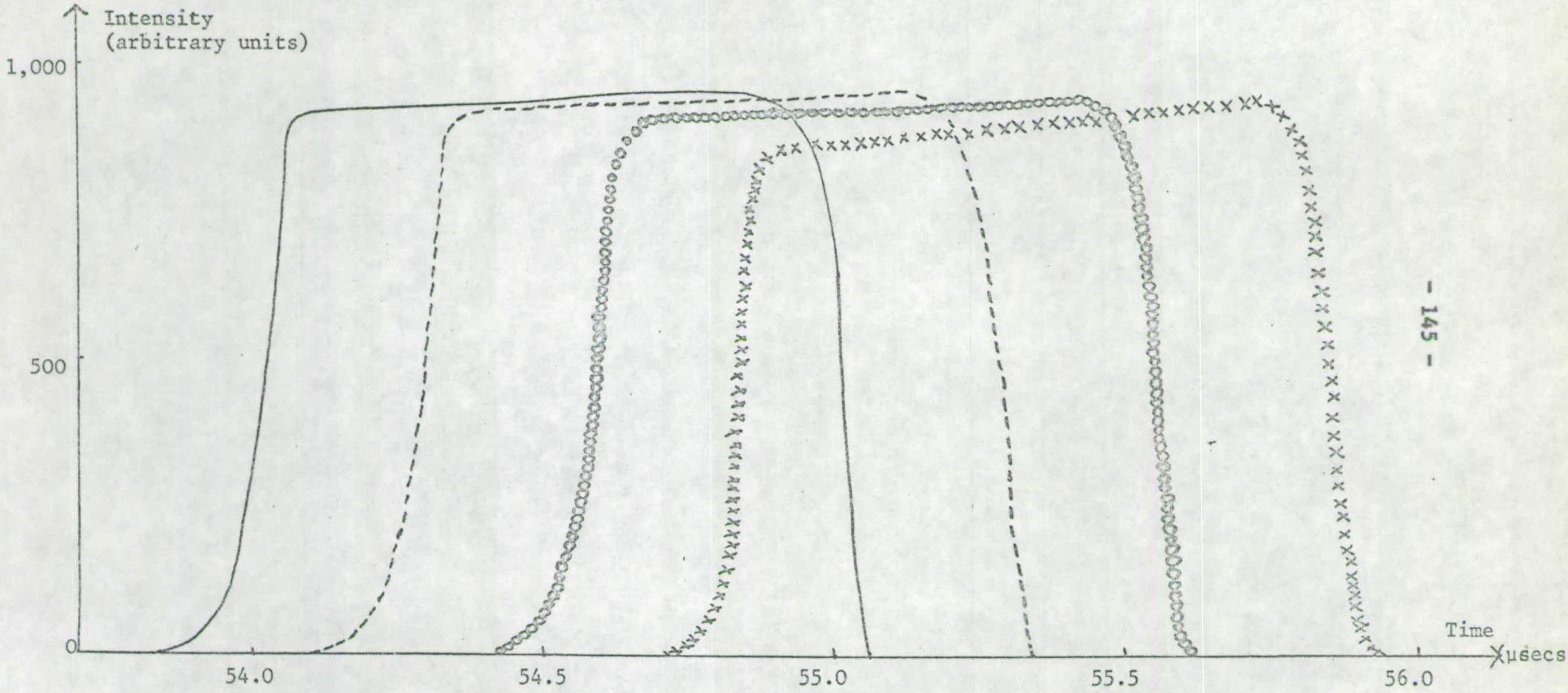

FIGURE 5.3 Spectrum for a 1μsec Square Wave Pulse suffering Energy Losses of 0eV(—), 2eV(---), 4eV (ooooo), 6eV(xxxx).

$$K + I \rightarrow K^+ + I^-$$

$$K + I_2 \rightarrow K + I + I$$

will involve an energy change at the scattering centre, whilst

$$K + I \rightarrow KI$$

$$K + I_2 \rightarrow KI + I$$

will involve changes in mass of the main beam species.

The arrival spectrum for the latter type of process will depend much on the change in mass, but the delay can be anything upwards of 100 μsecs at a beam energy of 100eV, thus lengthening the extent of the spectrum.

Very little will be said here of this process, but such reactive peaks are best found by the method of cross correlation, which will be dealt with later.

Velocity Modulation

As the main beam material is initially in ionic form, it is possible to control its behaviour to some degree by the use of electrostatic or magnetic fields. It is thus hoped to focus, or at least narrow considerably the width of the pulse sent from the source.

Velocity modulation finds its origins in nuclear physics, and has been utilised extensively since. Its main feature is to slow

down by a predetermined amount the first ions in the pulse and speed up the ions in the latter part. Its main disadvantage is that even although this is achieved, an increase in the velocity distribution occurs, causing a loss in the energy resolution of cross sections. But this may be the only way open to the experimenter, and in some cases this factor might be of minimal importance.

Space charge effects within the pulse, where the mutual repulsion of the charges tends to elongate the pulse against the force of modulation, have been found unimportant for pulses in the microsecond region, but can become critical in the nanosecond range [78].

In deriving the form for an energy modulation function, monochromatic velocity within the pulse is assumed. If therefore the pulse can be focused, the real life case might only have a very narrow spread due to the thermal velocity distribution of the beam material.

Velocity Modulation for a Pulse Undergoing Elastic Collision

Suppose a square wave pulse of time width D, energy E and monochromatic velocity V_o is modulated by an energy function $G(\lambda)$. This could be achieved by imposing a varying voltage $G(\lambda)$ on a lens element floating at a certain potential. All the particles then should arrive at the detector at the same time as particles from the middle of the pulse, which are unchanged in velocity. A particle

leaving at time λ changes its energy to $E + G(\lambda)$ and its velocity to U, where

$$U = MV_o \qquad 5.15$$

and

$$M^2 = 1 + \frac{G(\lambda)}{E} \qquad 5.16$$

The arrival time $t(\lambda)$ for such a particle will be

$$t(\lambda) = \lambda + \frac{d}{U} = \lambda + \frac{d}{MV_o} \qquad 5.17$$

The arrival time $t(D/2)$ for a particle leaving at the middle of the pulse will be

$$t(D/2) = D/2 + D/V_o \qquad 5.18$$

Equating (5.17) and (5.18) gives

$$M = \frac{d/V_o}{\{d/V_o + D/2 - \lambda\}} \qquad 5.19$$

and

$$G(\lambda) = E \left\{\frac{(d/V_o)^2}{(d/V_o + D/2 - \lambda)^2} - 1\right\} \qquad 5.20$$

Applying this to a pulse with a velocity distribution, but letting V_o be the superimposed beam velocity, the arrival time for a

particle of velocity V will be

$$t = \lambda + d/(MV)$$

and hence

$$V = \frac{d}{M(t-\lambda)} \quad \text{and} \quad dV = \frac{d}{M(t-\lambda)^2}\,dt \qquad 5.21$$

On substitution of V and dV into equation (5.6), the arrival spectrum of a modulated pulse can be found as

$$A_{el.mod}(t) = cd^2 \int_0^D \frac{B}{M^2(t-\lambda)^3} \exp -\left(\frac{B}{\alpha}\right)^2 d\lambda$$

where

$$B = \frac{d^2}{M^2(t-\lambda)^2} - \frac{2E}{m} \qquad 5.22$$

A program was compiled to test this effect on a 1 μsec wave pulse, and the results are summarised in Table 5.3.

On comparing the results for the half widths of these curves, it is obvious that velocity modulation has focused the ions to achieve a delta function response. Figure 5.4 shows this for two beam energies.

The equation for the velocity modulation function G(λ) was plotted for various values of E, the main beam energy, and was found to be essentially linear, as shown in Figure 5.5

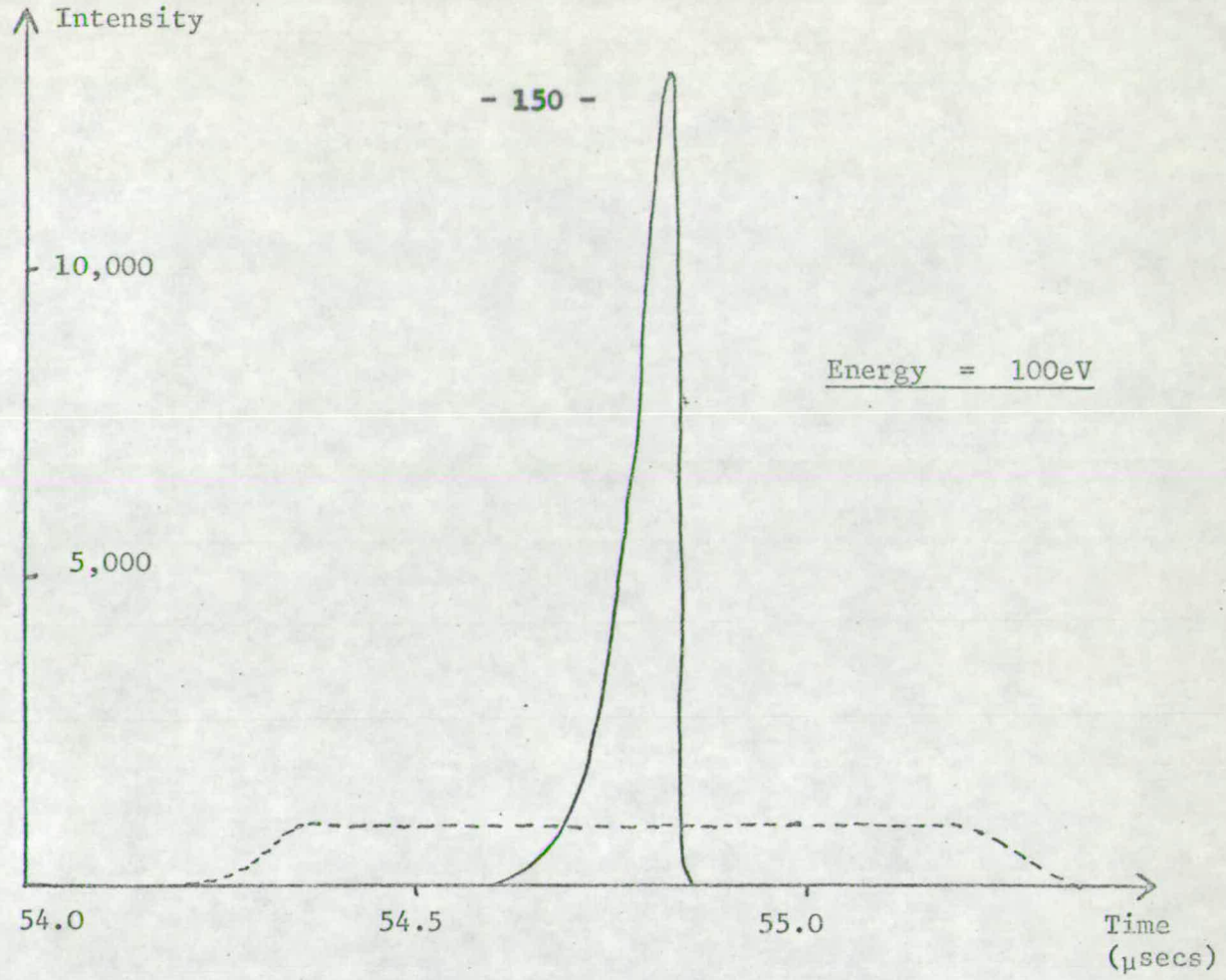

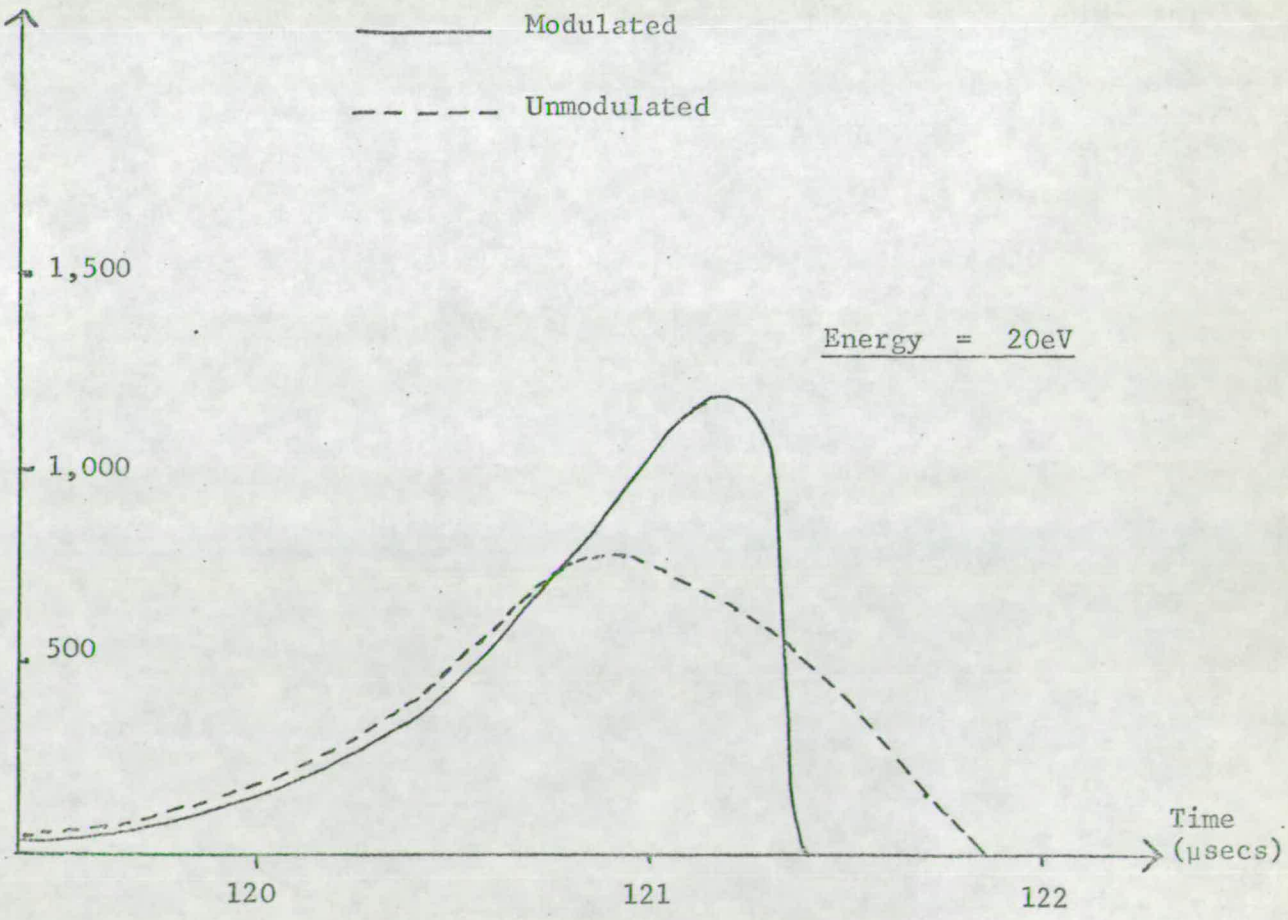

FIGURE 5.4 Effect of Velocity Modulation on a 1 μsec Square Wave Pulse.

Beam Energy (eV)	Peak Time (μsecs)	Half Width (μsecs)	Peak Height* (Modulated)	Peak Height* (Unmodulated)	Ratio (Mod/Unmod)
100	54.54	0.063	13,200	955	13.82
90	57.47	0.074	11,300	955	11.83
80	60.92	0.087	9,500	955	9.94
70	65.09	0.105	7,750	955	8.12
60	70.26	0.135	6,150	955	6.44
50	76.91	0.180	4,670	955	4.89
40	85.91	0.248	3,350	950	3.53
30	99.09	0.384	2,175	935	2.32
20	121.19	0.700	1,190	800	1.49
10	170.90	1.95	425	390	1.09

* Peak Height units are similar

TABLE 5.3 The effect of Velocity Modulation on a 1 μsec Pulse undergoing Elastic Collision.

Beam Energy (e.V)	h (e.V.)	Energy Res Loss %	Peak Height Ratio (mod/unmod)	En.Res.Loss / Pk.Ht.Ratio
100	1.876	1.876	13.82	0.136
90	1.600	1.777	11.83	0.150
80	1.340	1.675	9.94	0.169
70	1.096	1.566	8.12	0.192
60	0.869	1.448	6.44	0.225
50	0.660	1.321	4.89	0.270
40	0.472	1.180	3.53	0.334
30	0.306	1.021	2.32	0.440
20	0.166	0.832	1.49	0.558
10	0.059	0.587	1.09	0.539

TABLE 5.4. The Advantages of Velocity Modulating Beams of various Energies.

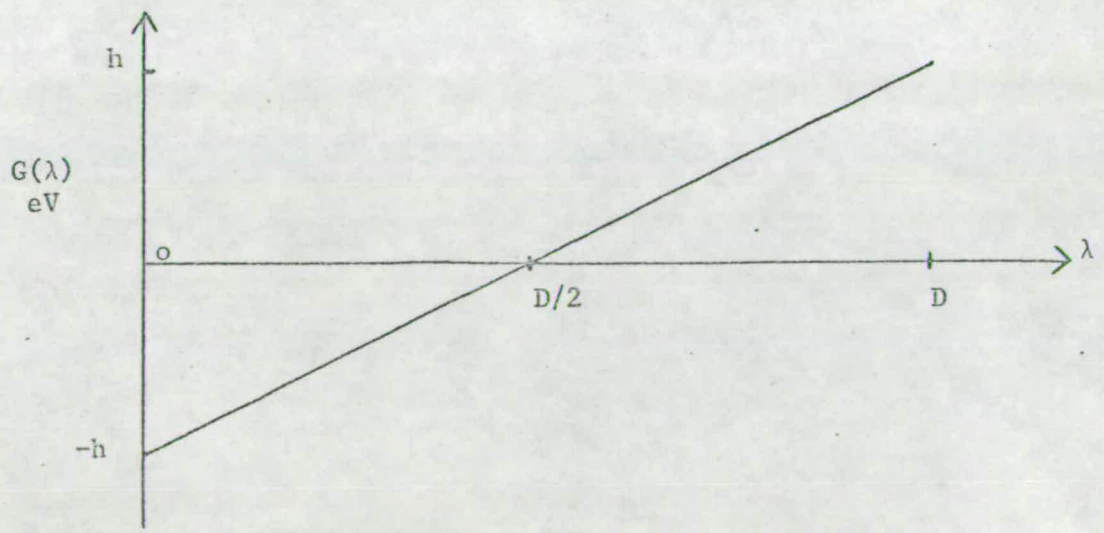

FIGURE 5.5 Typical Velocity Modulation Function

If the intercept on the energy axis is denoted by h, then the approximate change in energy resolution for a beam of mean energy E is h/E. Table 5.4 lists the values of h, the loss in energy resolution and the ratio of peak heights for modulated and unmodulated signals for various beam energies. Finally, the ratio of energy resolution loss to peak height ratios is given, and experiments will be more accurate at low values of this quotient.

Velocity Modulation for a Pulse Undergoing an Inelastic Collision

If a pulse of monochromatic velocity V_o and energy E is velocity modulated by a function $G(\lambda)$ at the source, its new velocity U will be given by equations (5.15) and (5.16). If at a distance ℓ along its flight path it suffers an energy loss ΔE, its new velocity U^1 is given by equations (5.9) and (5.10). By following a treatment similar to the last section

$$M = \frac{Y/V_o}{(Y/V_o + D_{/2} - \lambda)} \qquad 5.23$$

and

$$G(\lambda) = E\{\frac{(Y/V_o)^2}{(Y/V_o + D/_2 - \lambda)^2} - 1\} \qquad 5.24$$

The spectrum for a modulated pulse of length D containing the usual spread of energies is therefore

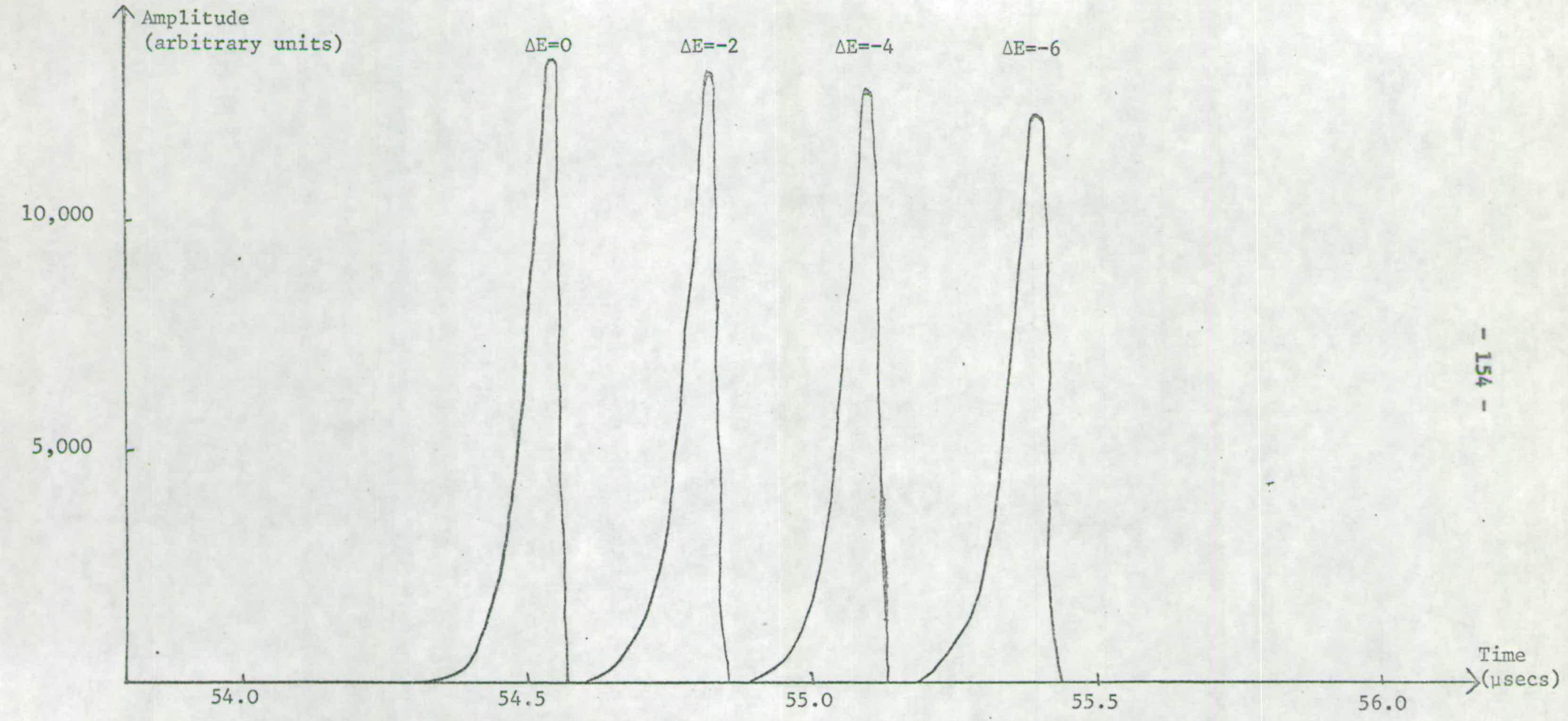

FIGURE 5.6 Spectrum for a Velocity Modulated 1 μsec Square Wave Pulse suffering Energy Losses of 0, 2, 4, 6 eV.

$$A_{el.mod}(t) = CY^2 \int_0^D \frac{B}{M^2(t-\lambda)^3} \exp - (B/\alpha)^2 d\lambda \qquad 5.25$$

where

$$B^2 = \frac{Y^2}{M^2(t-\lambda)^2} - \frac{2E}{m}$$

Various values of E and ΔE were chosen for a 1 μsec wide pulse, and Figure 5.6 shows the spectrum for modulated function having energy losses of 0, 2, 4, 6eV respectively. Comparison with Figure 5.3, the corresponding unodulated case, shows that the peaks are now much narrower and far more intense, and are in fact comparable to delta function responses for similar collisional processes.

Modulating for the optimum signal in one channel resulted in a negligible change from the optimum signals for the other channels. Thus the inelastic peaks will still remain as clear when the modulation function optimises the elastic channel signal.

Velocity Modulation Techniques in Nuclear Physics

The purpose of velocity modulation techniques in nuclear physics is to focus a short intense pulse of ions on a neutron source target, thereby releasing a correspondingly sharp neutron pulse.

Mobley [79] devised the first practical technique, resulting in increased neutron currents by a factor of about one hundred. This

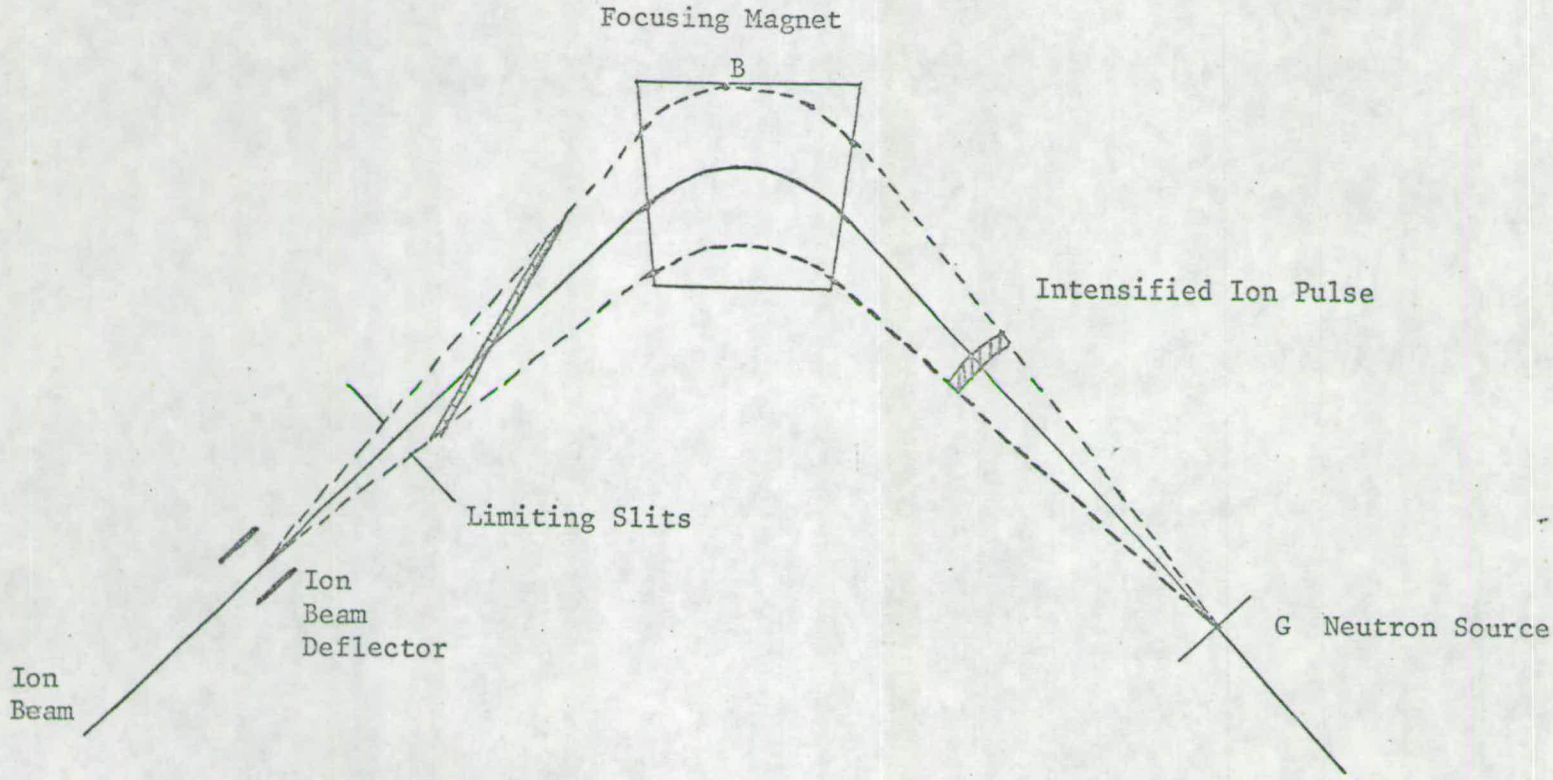

FIGURE 5.7 Mobley's method for producing an intense ion pulse of short duration.

is achieved by periodically deflecting the ion beam at point A on to a focusing magnet B which in turn bends the ion path towards the target at G. It is due to the difference in path lengths taken by ions from different times in the pulse that convergence at G is obtained. Many workers [80,81] have taken advantage of this technique which is sketched in Figure 5.7.

The klystron bunching method where ions essentially keep a straight path was developed by the Russians Flerov and Tamanov [82], but it is well described by Lefevre, Borchers and Poppe [83]. The ions are bunched by impressing a sinusoidal modulation function in the radio frequency range to four cylinders narrowly separated from each other, through which the ions pass. The separation of the bunches is therefore the distance that ions of a fixed energy will travel in a time equal to half the radio frequency time period. Consequently, the pulse can be narrowed by a factor of ten, the main limitation being the thermal spread in velocities originating at the source.

Experimental Difficulties with Velocity Modulation

Problems unfortunately arise when velocity modulation is attempted on the apparatus previously described. It would be carried out by use of a variable but controlled potential applied to the last lens plate of the deceleration lens. Here the particles are changed slightly in energy, and remain so until they reach the detector. But by placing the neutralisation chamber at earth potential a few centimetres from this lens element, this effect is destroyed, and no

energy difference will exist between any of these particles after this point.

Focusing the particles on the entrance of the neutralisation chamber would require an energy distribution in the beam of about fifty times greater than that previously calculated, the modulation function being approximately inversely proportioned to the focusing distance. This is far too great a distortion.

An alternative method is to apply the modulating potential to the main beam oven, and focus the particles on the neutralisation chamber entrance. This would have to be a trial and error attempt, as the potentials of the lens elements after this point will affect the flight time down the apparatus.

If the problem mentioned can be overcome, then velocity modulation offers the great advantage of using all the available main beam material for signal measurement. If the spectrum to be measured is S microseconds long, then applying the modulation potential every S microseconds will produce the optimum repitition for producing a signal.

The Techniques of Auto and Cross Correlation

An ingenious way of producing a delta function response signal is that of cross correlation, using random word theory. Applying a random word at the source implies pulsing the beam on (represented by + 1) or off (represented by - 1) in a random fashion after a set

interval of time, say ten nanoseconds, and repeating this pattern every 2^N intervals, N being an integer.

If the random word input signal x(t) has an autocorrelation function $Q_{xx}(\tau)$ given by definition as

$$Q_{xx}(\tau) = \int_o^T x(t)x(t-\tau)dt \qquad 5.26$$

where T is the time length of the experiment, then a delta function should result at the origin. The cross correlation function $Q_{xy}(\tau)$, given by

$$Q_{xy}(\tau) = \int_o^T x(t)y(t-\tau)dt = \int_o^T x(t-\tau)y(t)dt \qquad 5.27$$

where y(t) is the signal at the detector at time t, will represent a delta function response for the flight and collision.

A pseudo random word, as better explained by Los [84], produces the desired effects previously described. This was tested on a computer program using a 512 (i.e. 2^9) bit word for a beam at 100eV undergoing elastic collisions. The autocorrelation was a delta function, whilst the cross correlation produced at the expected delta function response.

This is more advantageous than velocity modulation, as no energy distortion within the beam occurs. Another advantage is in the gradual elimination of random noise from the data. If n(t) was the random noise variation with respect to time, and the noiseless

signal was denoted by y(t), then the signal Y(t) at the detector would be

$$Y(t) = y(t) + n(t) \qquad 5.28$$

The corresponding cross correlation function would be

$$Q_{xy}(\tau) = \int_0^T x(t-\tau)Y(t)dt$$

$$= \int_0^T x(t-\tau)y(t)dt + \int_0^T x(t-\tau)n(t)dt \qquad 5.29$$

As T, the total time for the experimental increases, the second term on the right will vanish if both x and n are truly random.

The Analytical Procedure for Time of Flight Spectra

From the preceeding discussion, it is obvious that most time of flight spectra will consist of a fairly dominant elastic channel, with perhaps several smaller inelastic channels appearing. Whilst it is fortunate that the curve for delta function responses have a sharp cut-off towards higher values of time where inelastic peaks arise, it is quite likely that the peaks will be much broader, and some smaller channels might be smothered. A rigorous analysis program is therefore required to deal with all possible situations.

The problem is to fit a given spectrum into a series of nonlinear functions, and methods of doing so have been fairly well described [86,87].

The method chosen was that of least squares using the principle of steepest descent, a very old but reliable technique. A standard library program at the Edinburgh Regional Computing Centre fitted these requirements, and hence DAPRO formed the main part of the analysis program.

The handling of this subroutine is quite straightforward. The program merely requires the number of unknown parameters to be fitted, a real function supplied by the user containing the analytical form of the spectrum using these unknowns, and an initial set of guesses for these unknowns. These guesses were found not to be too critical, being used mainly as starting values for the program in its search, and values correct to within twenty percent avoided instability appearing in the procedure. These unknowns had to be of the same order of magnitude to prevent instability, but this problem is easily overcome.

Mathematical Features of DAPRO

If a typical spectrum were read in as a series of N values $y_i, i=1,N$ to be fitted to an analytical form $f_i(t,\alpha,\beta)$ where t is the independent variable, then the best values for the two unknowns α,β will arise when

$$\Phi = \sum_{i=1}^{N} (y_i - f_i)^2$$

the square of the difference between experimental and fitted values is a minimum.

If an error contour map of Φ were drawn against the two variables α,β, the resulting pattern would be that in Figure 5.8.

L is the point of least error, with contours nearer L having a lower error value. (For a linear problem, the contours would be elliptical). For a function of M unknowns, similar contours would result in M dimensional space.

With initial estimates of α,β, the error function value might correspond to point I, from which the program will take a small step along the path of steepest descent. After each step, a new evaluation of the direction is made until eventually point L is reached. A tolerance parameter is included in the subroutine to stop the search at any desired accuracy.

Simulated Experimental Spectra

The reaction of DAPRO to a series of simulated experimental spectra, comprised from a varying number of particles and containing random noise, will reveal the program's capabilities.

A typical spectrum was composed using equations (5.8) and (5.14), premultiplying each channel by P, the number of particles in the spectrum, and an amplitude factor a_i where

$$0 < a_i < 1 \qquad \sum_i a_i = 1$$

FIGURE 5.8 Error Counter Map for a Non-Linear Problem of Two Variables α, β.

Unknown Number	Type of Unknown	First Estimate	True Value
1	Amplitude	0.900	0.850
2	Amplitude	0.100	0.080
3	Amplitude	0.022	0.025
4	Amplitude	0.017	0.020
5	Amplitude	0.014	0.015
6	Amplitude	0.007	0.010
7	Beam Energy	101.0	100.0
8	Energy Loss	- 1.1	- 1.0
9	Energy Loss	- 1.4	- 1.5
10	Energy Loss	- 1.9	- 2.0
11	Energy Loss	- 2.3	- 2.2
12	Energy Loss	- 3.1	- 3.0

TABLE 5.5 Description of Unknown Parameters V_i contained in the Simulated Spectrum, with First Estimates for their values as input to DAPRO (V_i is linked to V_{i+6}).

An elastic channel of energy 100eV and five inelastic channels of energy losses of 1.0, 1.5, 2.0, 2.2 and 3.0eV were chosen. Table 5.5 lists the parameters of the spectrum and the first guesses put into DAPRO for these as unknowns.

This spectrum was then convoluted with a detector gate of width 10 nanoseconds, and statistical noise was added to each channel in a Gaussian fashion, where the standard deviation of this random noise was equal to the square root of the pure signal in that channel. Thus as the number of particles in the spectrum increased, the effect of noise fell.

The program was set up to perform two iterations of the searching technique, with the new estimates for the unknowns obtained for the next part of the search, and the process was repeated fifteen times.

It is best at this stage to define a few terms before proceeding. Let

A_i = the true value for the i'th unknown parameter

V_i = the calculated value of the i'th unknown parameter

$\overline{V}_i$ = the average value of V_i obtained after several sets of iterations

D_i = the absolute value of the fractional error for the i'th unknown

$$= \left| \frac{V_i - A_i}{A_i} \right|$$

$\bar{D}_i$ = the average value of D_i obtained after several sets of iterations.

Thus by following the values of D_i and $\bar{D}_i$ for each unknown the behaviour of the program can be traced.

Twelve Unknown Parameters Used in DAPRO

Initially the amplitudes, beam energy and energy loss terms, a total of twelve in all, were regarded as unknowns, whose values are recorded in Table 5.5. This was done such that, for i less than seven, Vi was an amplitude whilst V_{i+6} was the corresponding energy term.

Figure 5.9 shows for spectra containing 10^5 and 10^8 particles respectively how quickly and accurately the best values for the unknowns can be achieved. This is exemplified for the third and ninth variables by the plot of $Log_{10}(D_3)$ against $Log_{10}(D_9)$, where the points shown indicate the accuracy after each set of two iterations.

It is obvious that the spectrum containing the greater number of particles yields more accurate values for the unknowns and does so more rapidly. However, for the first three sets of iterations in

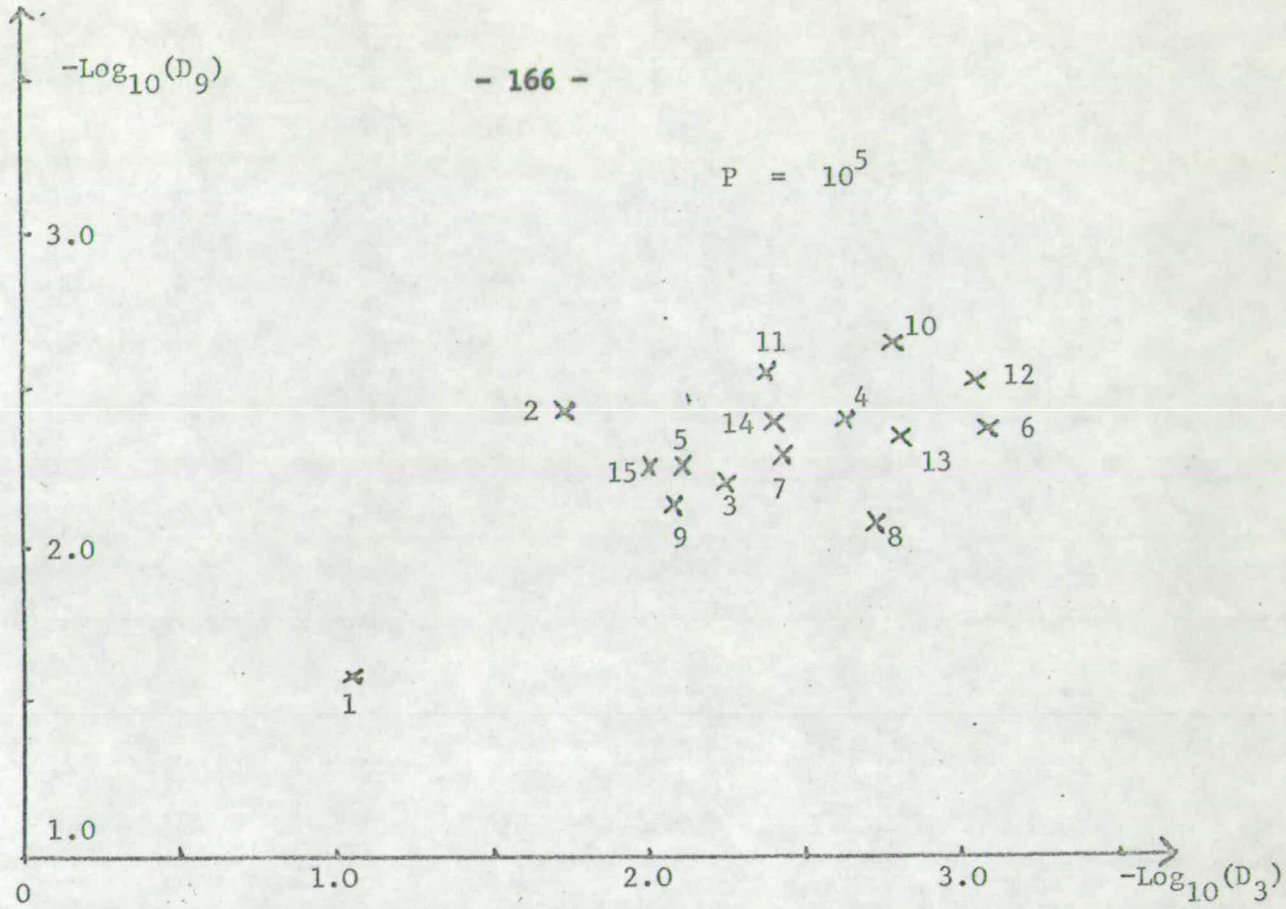

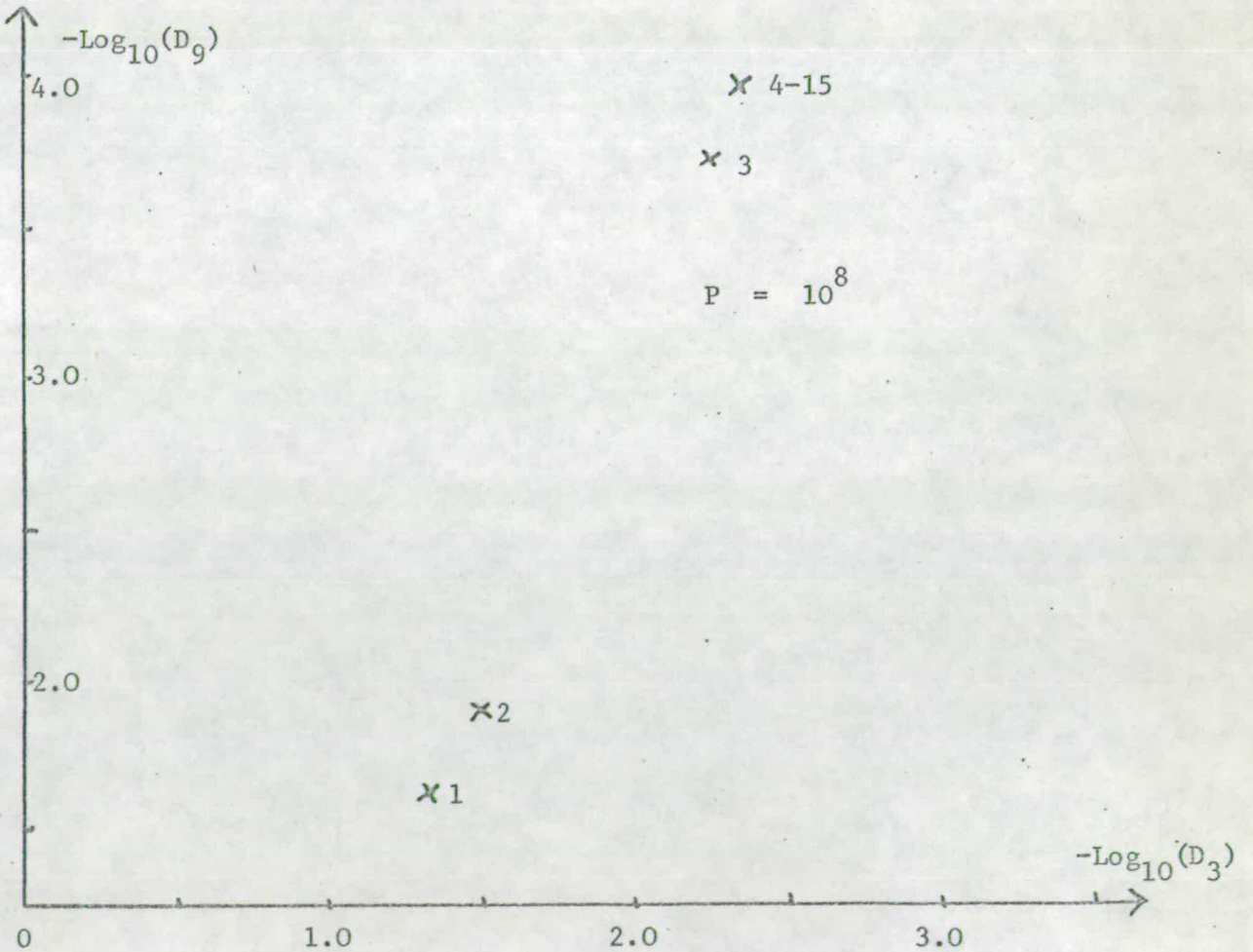

FIGURE 5.9 The Convergence of the Solution for Spectra containing different numbers of particles P.

both cases, the estimates become more accurate, and thereafter circle around a mean value. The circling is quite large in the case of 10^5 particles and very small in the case with 10^8 particles. The effect of noise on the type of solutions for the unknown parameters is exemplified by the spectrum containing 10^5 particles.

Subsequently it is best to disregard the first three estimates for each unknown and concentrate on the remaining twelve. This was done for spectra containing 10^5 to 10^8 particles, where in each case $\overline{D}_i$ was found by averaging over the twelve relevant values of D_i for each variable. Figure 5.10 is a plot of $Log_{10}(\overline{D}_i)$ against $Log_{10}(P)$.

In general, the accuracy of the estimate for the amplitude follows that for its corresponding energy term. Remembering that a value of -2.0 for $Log_{10}(\overline{D}_i)$ represents an accuracy of 1%, it is easy to follow the degree of accuracy found for each parameter. Relating this to experiment, this precision can be achieved with a counting rate of 5×10^4 sec^{-1} for 200 secs - although this should be regarded as a lower limit - which might only be obtained near the main beam centre.

A further feature of the program is that the consistency of the solutions obtained after each set of two iterations follows the accuracy of the solutions. Taking the fifth parameter as an example, Table 5.6 lists the best values for V_5 and D_5 along with the values

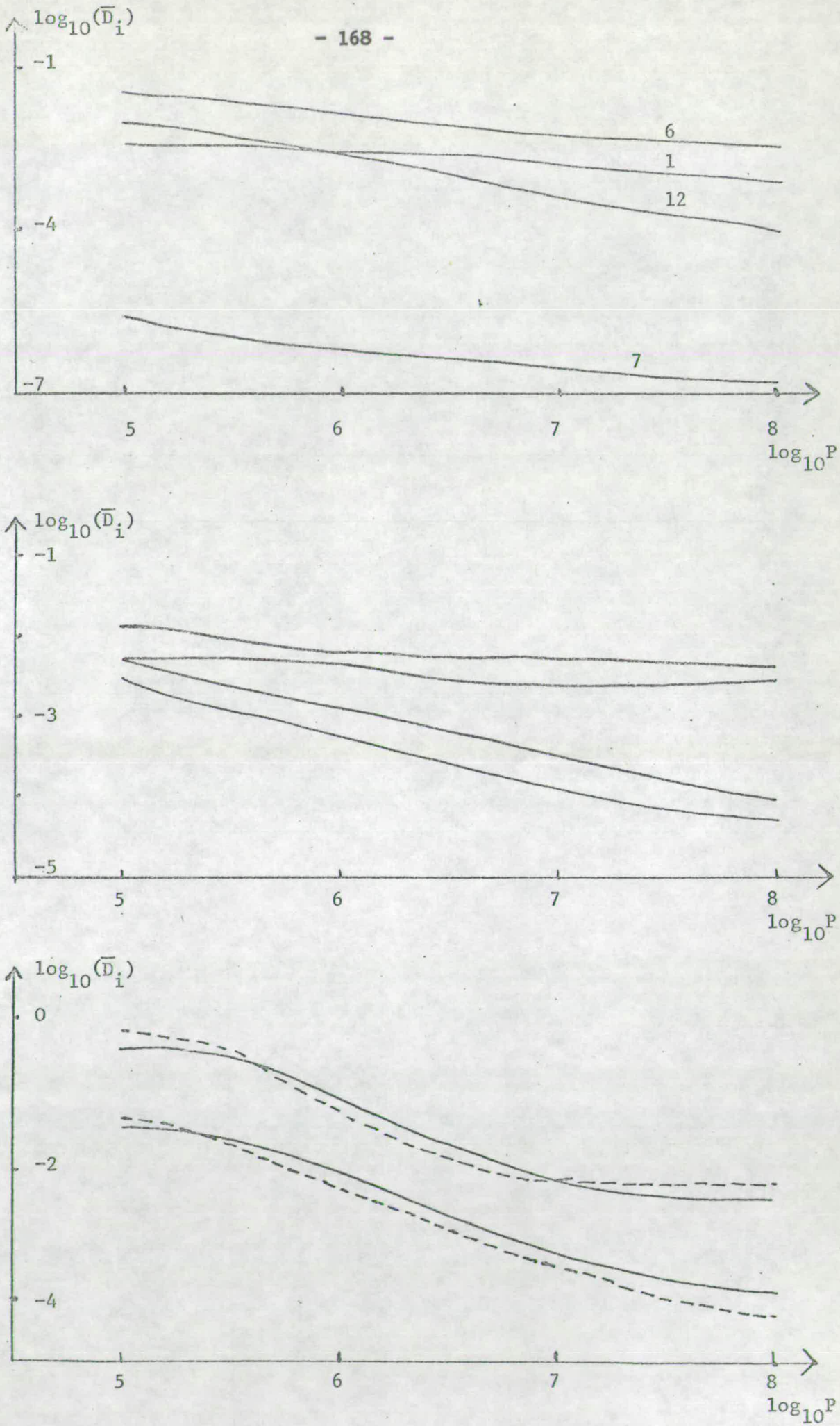

FIGURE 5.10 Dependence of Accuracy of Parameters (12) on the Total Number of Particles P in the Spectrum.

P	V_5 (Best Value)	$\bar{V}_5$ (Average Value)	D_5 (Best Value)	$\bar{D}_5$ (Average Value)
10^5	0.02215	0.02824	0.47719	0.80851
10^6	0.01481	0.01586	0.0.236	0.08741
10^7	0.01490	0.01490	0.00661	0.00664
10^8	0.01493	0.01493	0.00462	0.00463

TABLE 5.6 The Consistency of the Solutions from DAPRO as exemplified by the fifth unknown.

for $\overline{V}_5$ and $\overline{D}_5$. Thus as the spectrum becomes less noisy and the accuracy of the solutions increase, V_i and $\overline{V}_i$ become similar as do D_i and $\overline{D}_i$.

Six Unknowns Used in DAPRO

If the parameters such as main beam energy and energy losses for a system are known or have been found using the program with the twelve unknowns, the problem can be greatly simplified by having six unknowns, the amplitudes, to be evaluated.

With the same spectra as before, this procedure was much quicker in execution. The plots of $Log_{10}(\overline{D}_i)$ against $Log_{10}(P)$ are shown in Figure 5.11, where P could now range from 10^3 to 10^8 particles. Comparison with Figure 5.10 shows that these variables achieve a far greater accuracy. The main advantage is that the program can now deal more effectively with rougher spectra. This is obviously a valuable tool when angles become large and the counting rate drops dramatically.

Time of Flight Experiments

The analysis program described has been used successfully to determine the lifetime of a metastable mercury atom at thermal energies by a time of flight process [87]. It has also been used on an experimental spectrum obtained from the superthermal apparatus.

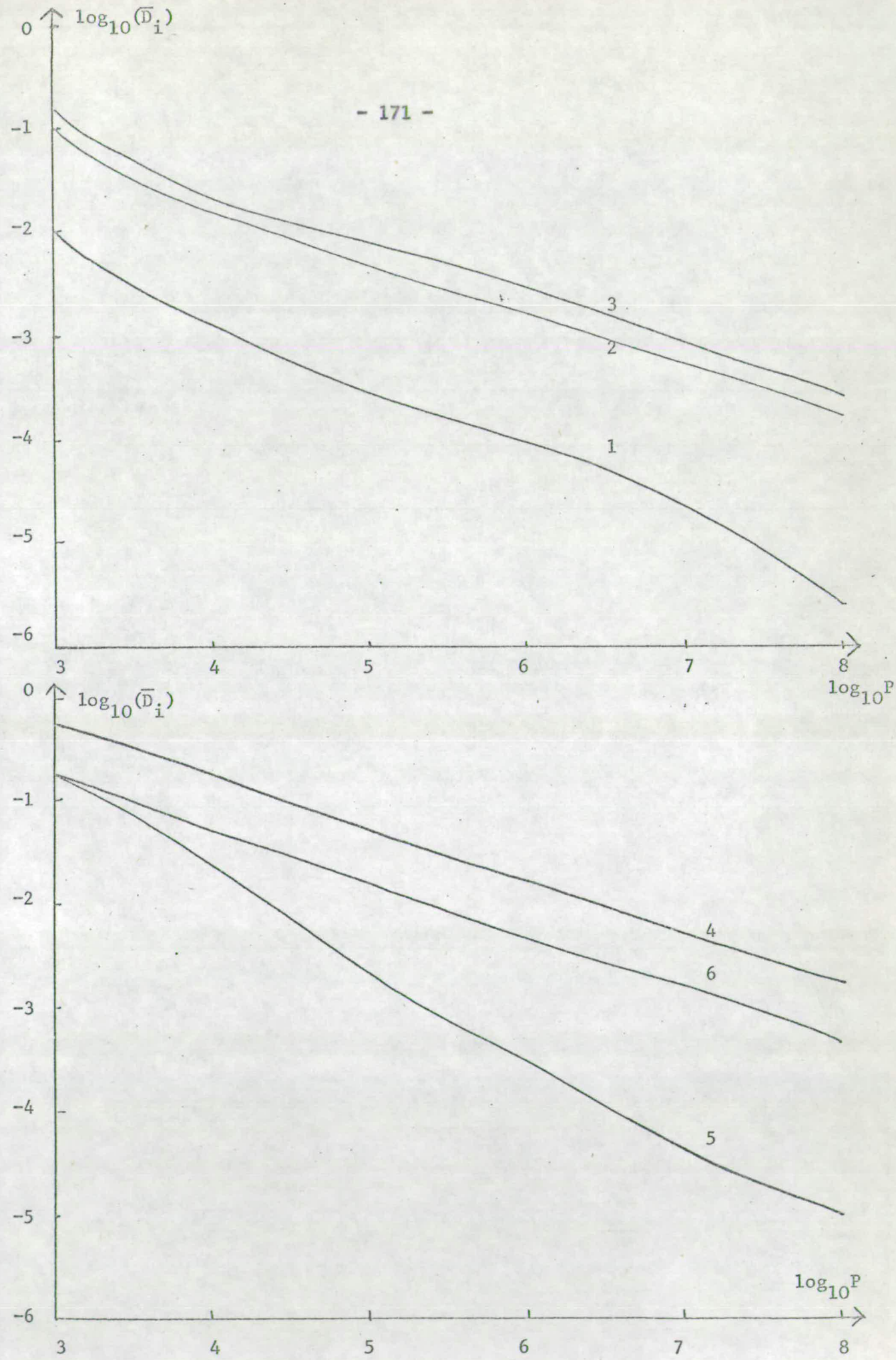

FIGURE 5.11 Dependence of Accuracy of Parameters (6) on the Total Number of Particles P in the Spectrum.

The program first attempted to fit a form to a (presumed 1 μsec) pulse of 100eV potassium atoms, whose spectrum could be adequately described by the form

$$y(t) = a_o \exp - \{b(t-t_o)^2\}$$

where a_o was theamplitude, t_o the arrival time and b a width parameter. Unfortunately the half width of this signal was about three microseconds, and when a cross beam of Br_2 scattered the main beam, no other peaks could be found at several angles. In some cases counting lasted for seven hours to achieve a moderately defined spectrum.

Experimentally the ion beam was pulsed using a split lens element after the deceleration lens. The two parts were connected by a 50 Ω resistor one part being at earth potential, whilst a pulsing potential was applied to the other. Unfortunately, the resistor was a coil wound type, having a high inductance, and hence sharply defined pulses could not have been expected. Even attempting to form pulses of 0.5 and 1 μsecs resulted in 3 μsec width pulses. Unfortunately time did not permit a modified assembly to be tested.

A modest attempt was made to evaluate the time of flight t^1 from the detector to the electron multiplier. A beam of energy E, velocity V_o, mass m and pulse width D will have a peak arrival time t given by

$$t = D/2 + \frac{d}{V_o} + t^1 = D/2 + t^1 + d\left(\frac{m}{2E}\right)^{\frac{1}{2}}$$

where d is as before. When t is plotted against $E^{-\frac{1}{2}}$ for various values of E, t^1 can be found if D is known. This was found to be about 14 μsecs, but again this experiment will have to be repeated.

CHAPTER 6

EXPERIMENTAL RESULTS AND DISCUSSION

Differential cross section results for the scattering of neutral potassium atoms were obtained for three collision systems at a series of laboratory collision energies. These were:

Collision System	Laboratory Collision Energy
K/I_2	100eV
	200eV
K/Br_2	100eV
	200eV
	250eV
	300eV
K/CH_3I	100eV
	200eV
	250eV
	300eV
	400eV

The systems are also listed in the chronological order of study.

In the K/I_2 results, about 280 samples of the scattered signal were obtained at each angle to form a good statistical average. However, the scattered signal was not determined at enough angles to follow exactly the oscillations present in the differential cross

section plots.

It was therefore decided to reduce the sampling of the scattered signal at each angle to 90 samples and hence measure the scattered signal at three times as many angles.

Also from the time that the K/I_2 results were obtained to the time the K/Br_2 and K/CH_3I systems were investigated, the experimental system had been changed slightly to effect a greater main beam stability. As mentioned in Chapter 3, this involved moving the grid of the acceleration lens to a greater distance from the source, thus preventing any temporary leakage current (and hence main beam instability) due to short circuiting by potassium between these two lens elements.

The results of these changes certainly produced better experimental differential cross section plots. Except for measurements at very small angles, less than 50eV°, the oscillations have been traced out accurately. Whilst it may not be obvious from the differential cross section plots (which will be shown later), the standard deviations in the scattered signals are much reduced, even although fewer samples have been taken. This is attributable to the increase in the main beam stability.

The System K/I_2

Results were obtained for the collision system K/I_2 at laboratory energies of 100eV and 200eV. The differential cross sections for the scattering of neutral potassium are shown in Figures 6.1 and 6.2 for 100eV and 200eV respectively. The top plot in each figure shows the actual experimental points obtained whilst the lower plot reveals the smoothed experimental data as it appears in the COM system.

It must be pointed out that in both cases very large peaks were obtained at low angles, less than $25eV^{o}$. These peaks are not shown above a certain value in order to reveal the peaks that occur at angles larger than $25eV^{o}$. This was also done for the covalent differential cross sections produced by the eikonal model discussed in Chapter 2.

The two experimental plots show very good agreement on an energy scaling basis, where very large peaks appear within $25eV^{o}$, and a diminution of scattered intensity is observed at higher angles.

These experimental plots should be compared to the theoretical cross section plots obtained by the eikonal model discussed in Chapter 2. This comparison is shown in Figure 6.3. Whilst the plots in this figure are for slightly different COM energies, the energy scaling is very good, and the envelopes of the two curves show very good qualitative agreement.

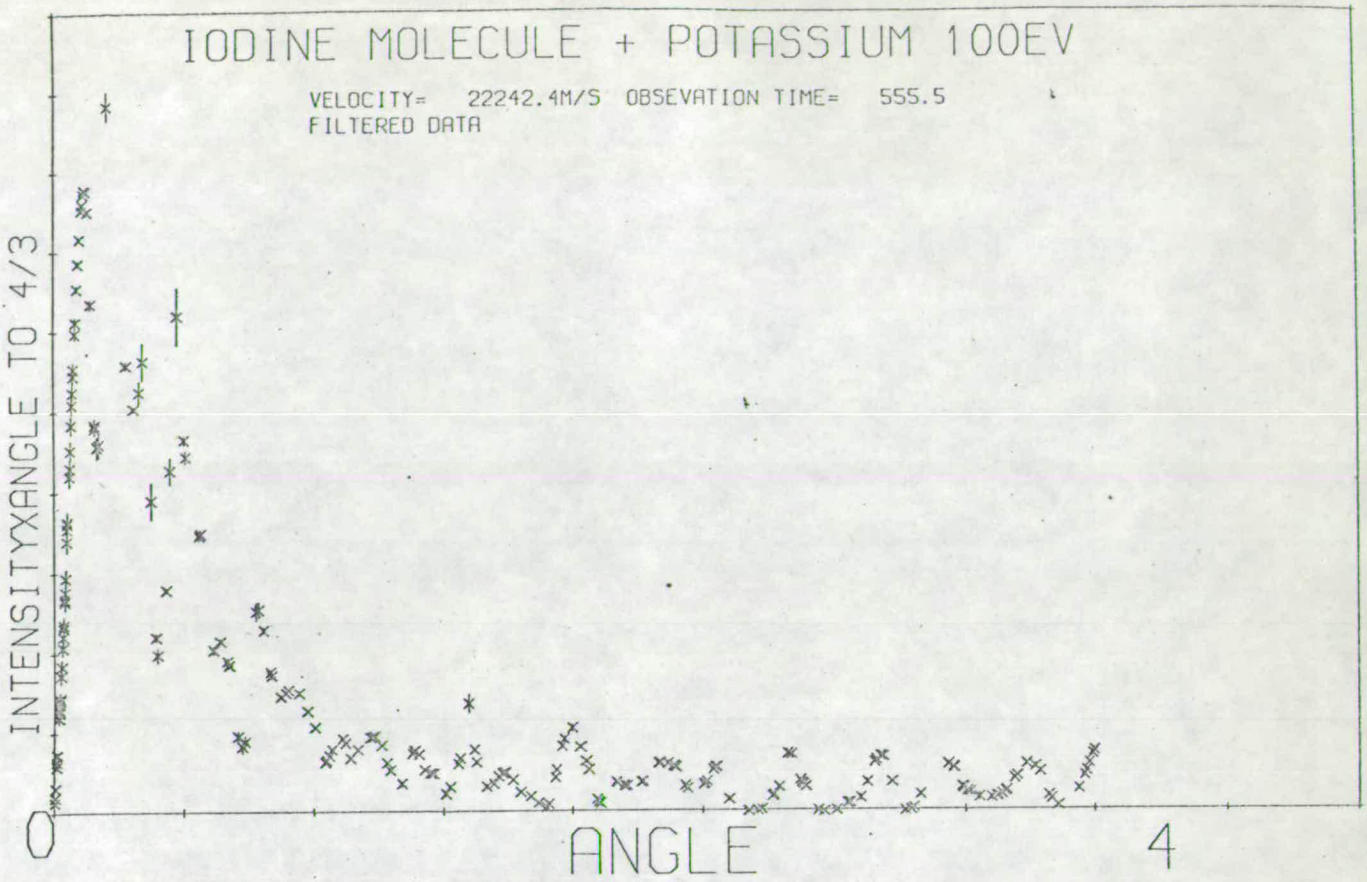

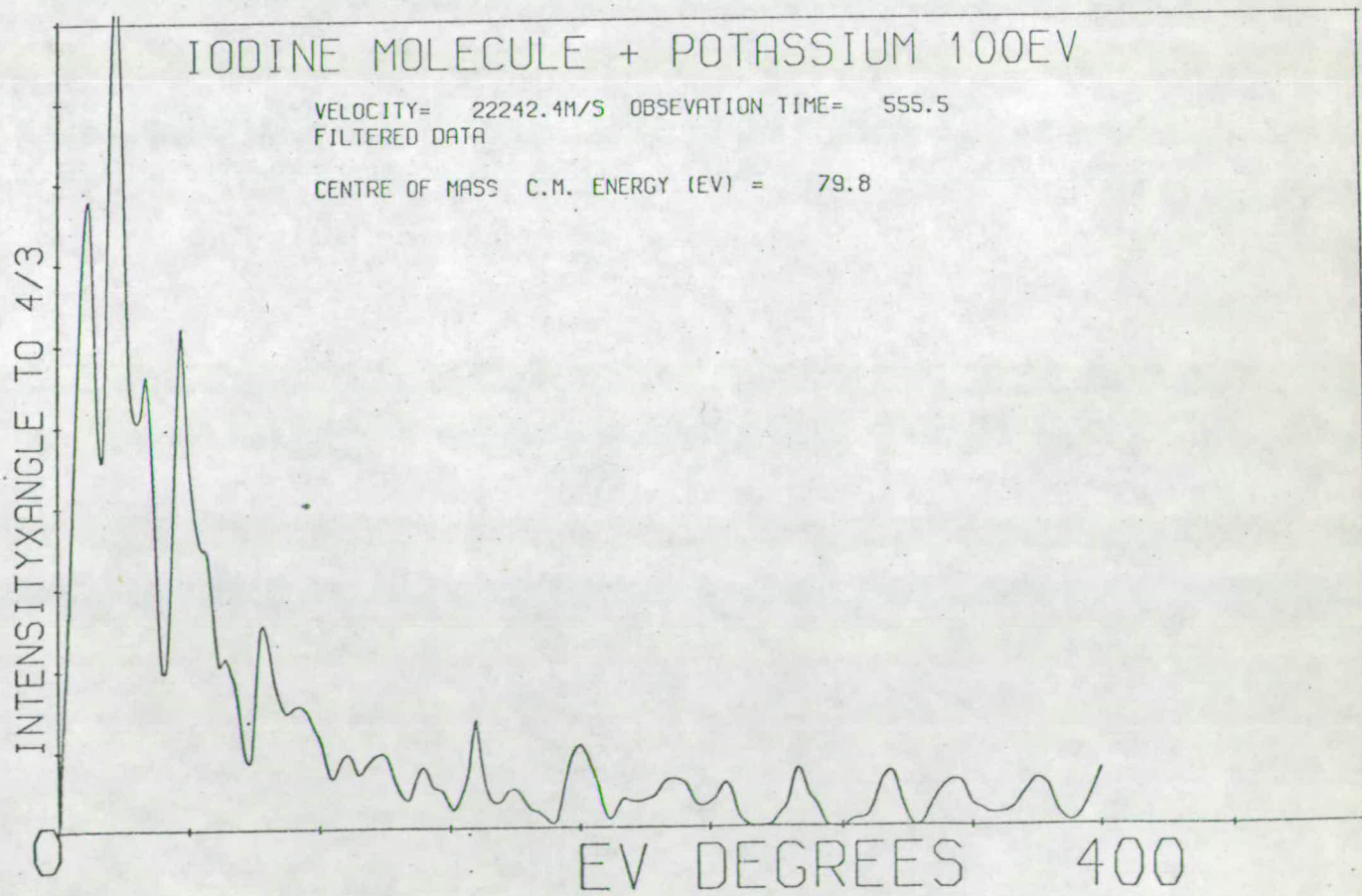

FIGURE 6.1 Differential Cross Section for neutral scattering in the system K/I_2 at 100eV.

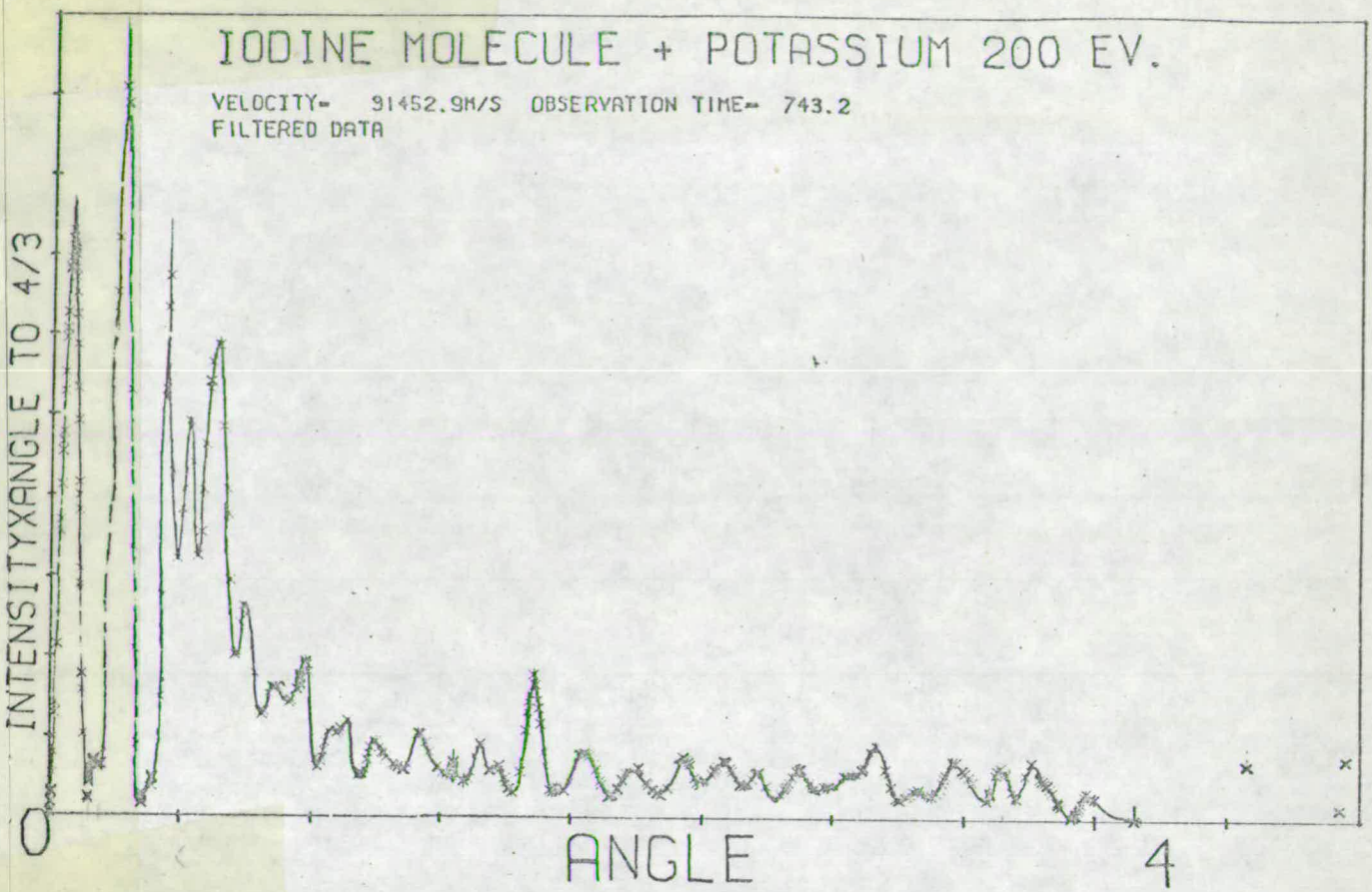

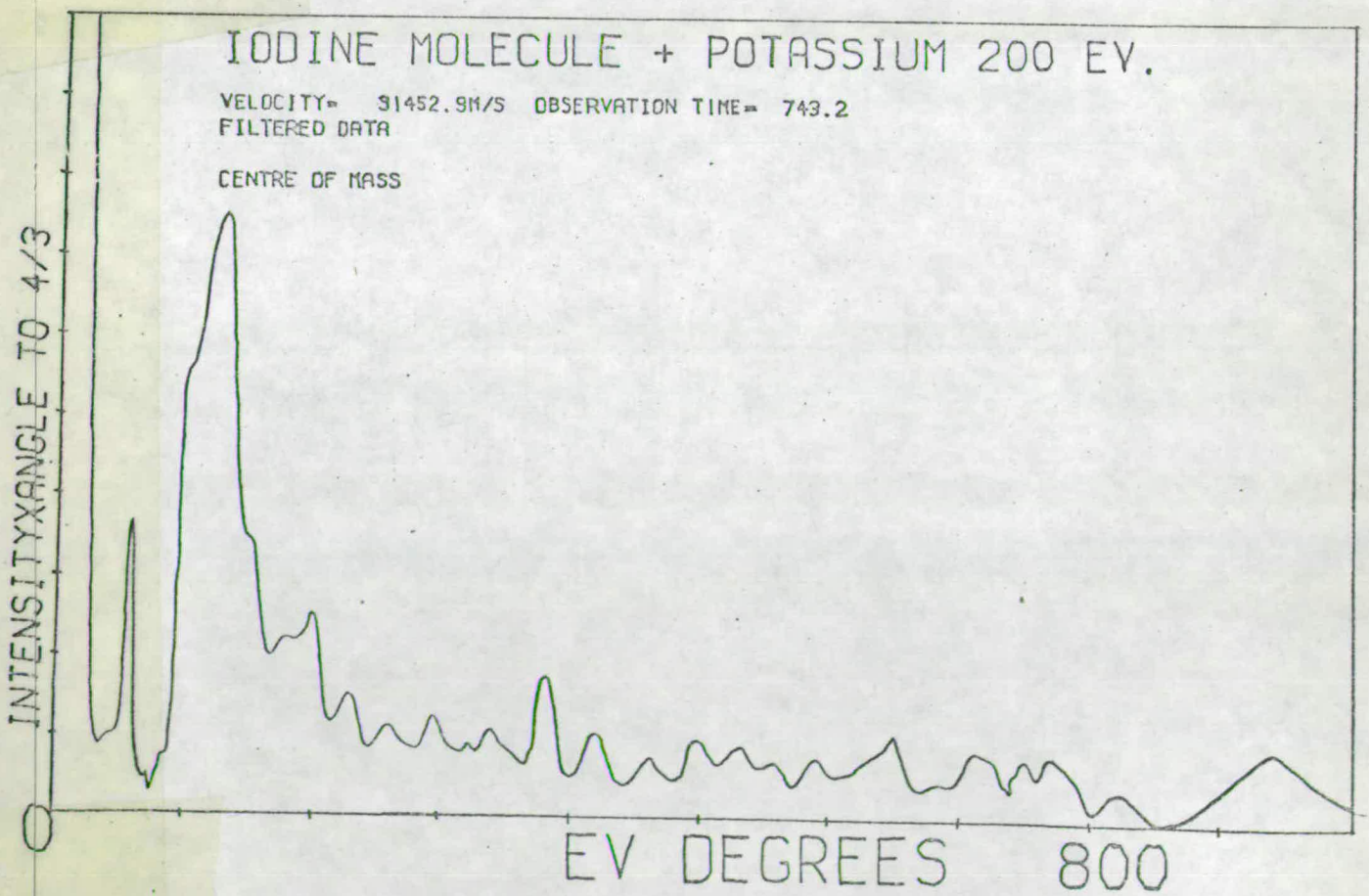

FIGURE 6.2 Differential Cross Section for neutral scattering in the system K/I_2 at 200eV. .

However, the most intense peaks, due to scattering by the shallow well potential function, occur at smaller scattering angles in the experimental plot, and hence it might be thought that the value of 0.01eV for the shallow well depth of $H_{11}(R)$ in the theoretical model is too large.

The scattering at large angles, greater than 200eV degrees, is due to interference effects between potassium atoms experiencing the repulsive walls of the shallow and deep well deflection functions shown in Figure 2.22. The separation of the peaks $\Delta\theta$ is about twice as great in the theoretical plot, and, according to the equation

$$\Delta\theta = \frac{2\pi}{\Delta\ell} \qquad 6.1$$

where $\Delta\ell$ is the partial wave separation of the contributing branches, the theoretical value of $\Delta\ell$ is about half that in the experimental plot. Thus the two repulsive walls of the potentials $H_{11}(R)$ and $H_{22}(R)$ should be spaced further apart than implied by the functions in the theoretical model.

The scattering of neutral potassium atoms for the collision system K/I_2 at a laboratory energy of 100eV has been studied by Duchart [53]. Unfortunately the results only extend to 100eV degrees and the sampling of scattered signal in this range is very scarce. No worthwhile comparison can therefore be made between Duchart's results and the ones presented in this thesis.

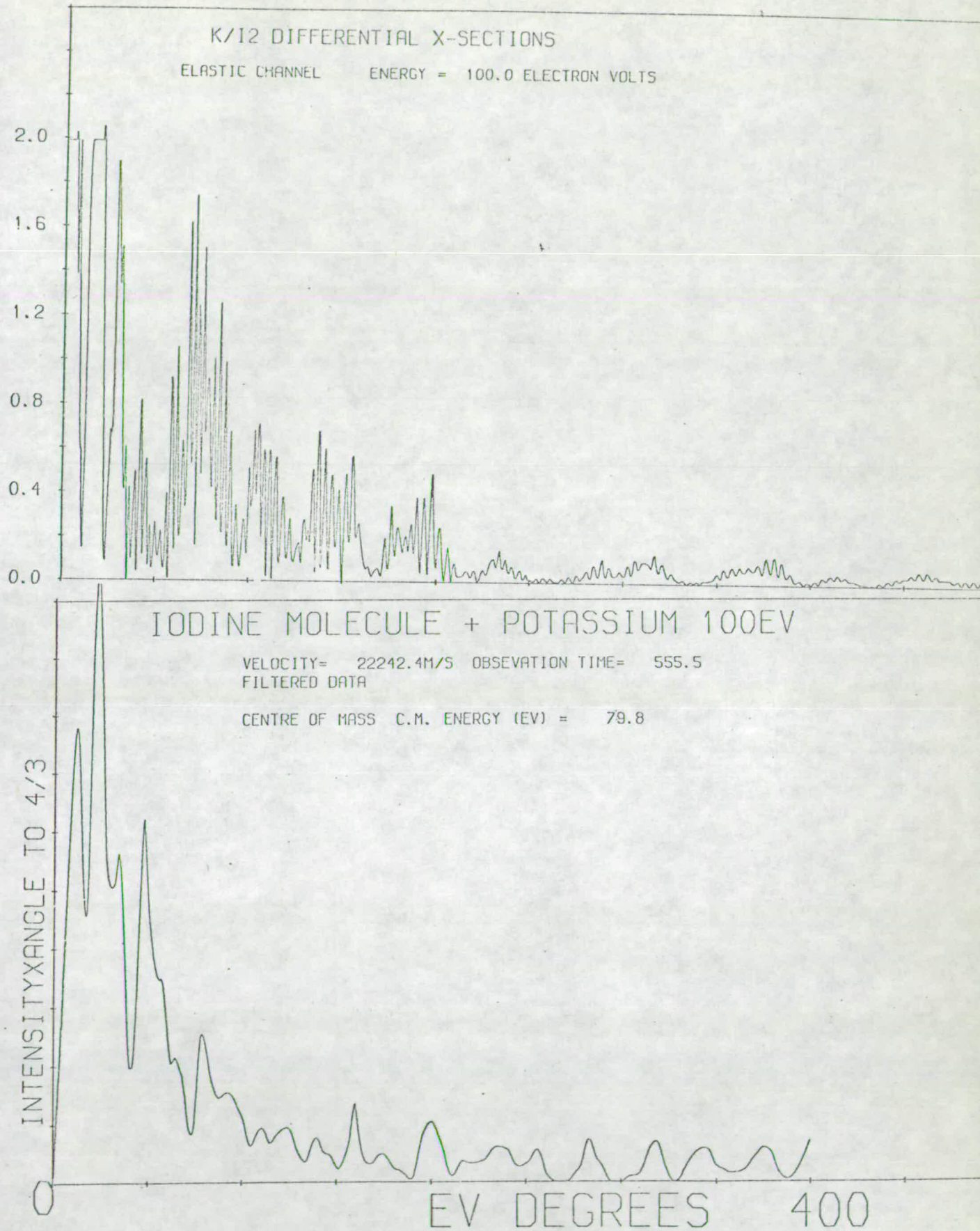

FIGURE 6.3 Comparison of experimental and theoretical neutral differential cross section plots for K/I_2.

However, chemi-ionisation cross sections for K/I_2 at COM energies of 6.25 and 11.25eV have been measured by Delvigne and Los [88]. The shallow well rainbow appears round about 25eV degrees as compared with 31eV degrees in the eikonal model. This gives further confirmation that the depth of the shallow well potential in the eikonal model is too large.

The deep well rainbow for ionic scattering as predicted by the eikonal approach in Chapter 2, appears at 210eV degrees. In the measurements by Delvigne and Los, it appears in the range 170 - 200eV degrees. Delvigne and Los's results are not very well resolved in this range of experimental data, due possibly to the 20% energy spread in the main beam (which was obtained by a sputtering source). There is a very slow reduction in scattered intensity after the last peak (at 170eV degrees) in the differential cross section, and, were this region to be better resolved, a more accurate position of the deep well rainbow might be estimated.

In conclusion, it can be said that the eikonal model used in the theoretical approach gives a good description of the experimental results from the K/I_2 system. By varying the parameters employed in the shallow well potential $H_{11}(R)$, the positions of the shallow well rainbows in the theoretical and experimental differential cross section plots can be made to match. Also the repulsive branches of the two potential functions $H_{11}(R)$ and $H_{22}(R)$ are not as closely spaced as implied in the theoretical model.

The values of $H_{12}(R_x)$ and the electron affinity of the I_2 molecule should also be varied in the theoretical model to see if better agreement between the theoretical and experimental cross section plots will result. Altering the value of $H_{12}(R_x)$ will change the peak heights in the differential cross section plots. If the value for the electron affinity of the iodine molecule is decreased, then the crossing distance R_x between the two adiabatic potential curves $H_{11}(R)$ and $H_{22}(R)$ will decrease. The attractive branch of the ionic potential should become steeper, and this will affect the scattering observed between the shallow and deep well rainbows.

The Collision System K/Br_2

The scattering of neutral potassium atoms for the system K/Br_2 was measured for laboratory collision energies of 100eV, 200eV, 250eV and 300eV. These are shown in Figures 6.4 to 6.7 respectively, where the top plot in each figure shows the actual experimental measurements, and the lower plot the smoothed differential cross section as it appears in the COM frame of reference.

Delvigne and Los [88] have studied the chemi-ionisation cross sections of K/Br_2 at collision energies of 6.9eV and 10.36eV. The crossing distance R_x of the covalent and ionic potential functions of the system was determined as 11 a_o, whilst the coupling function

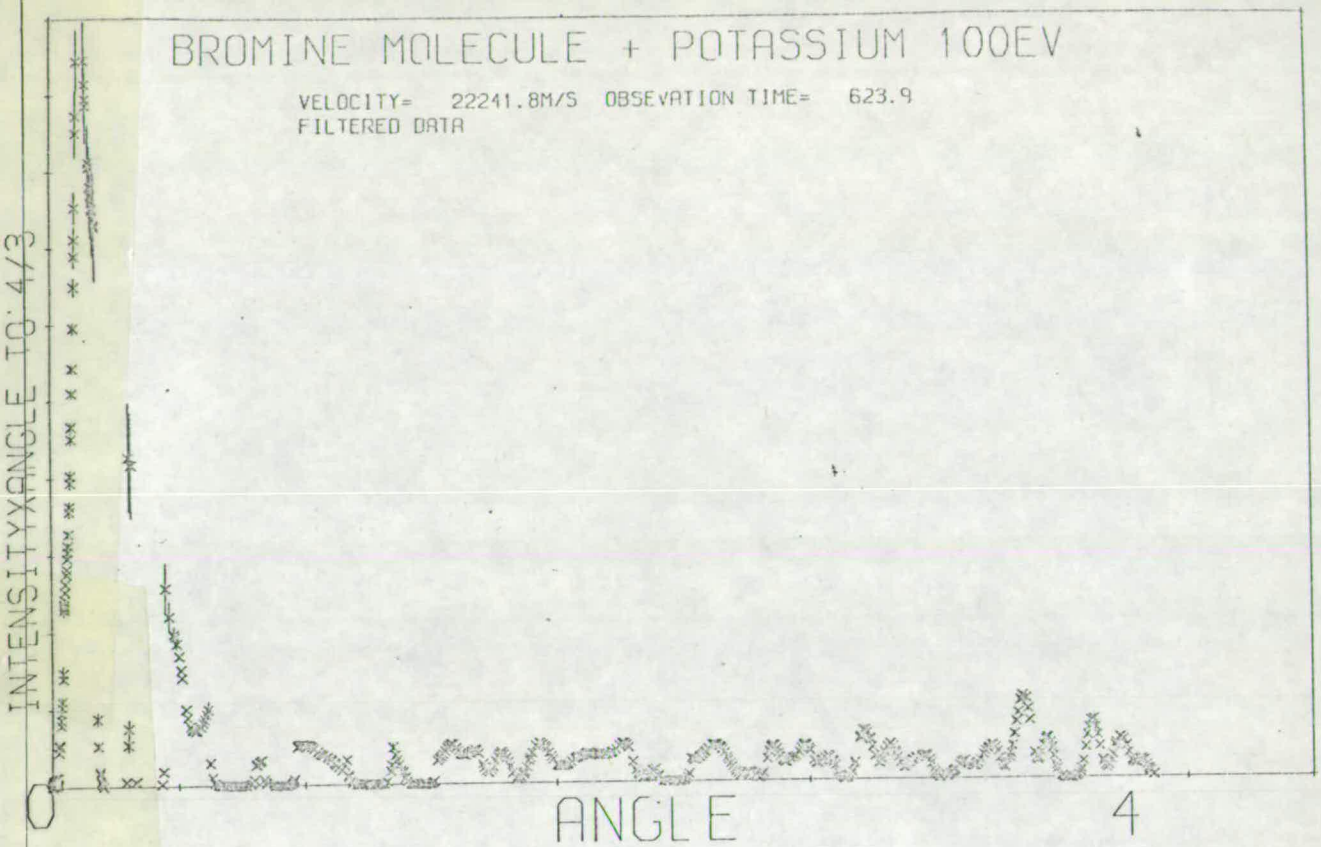

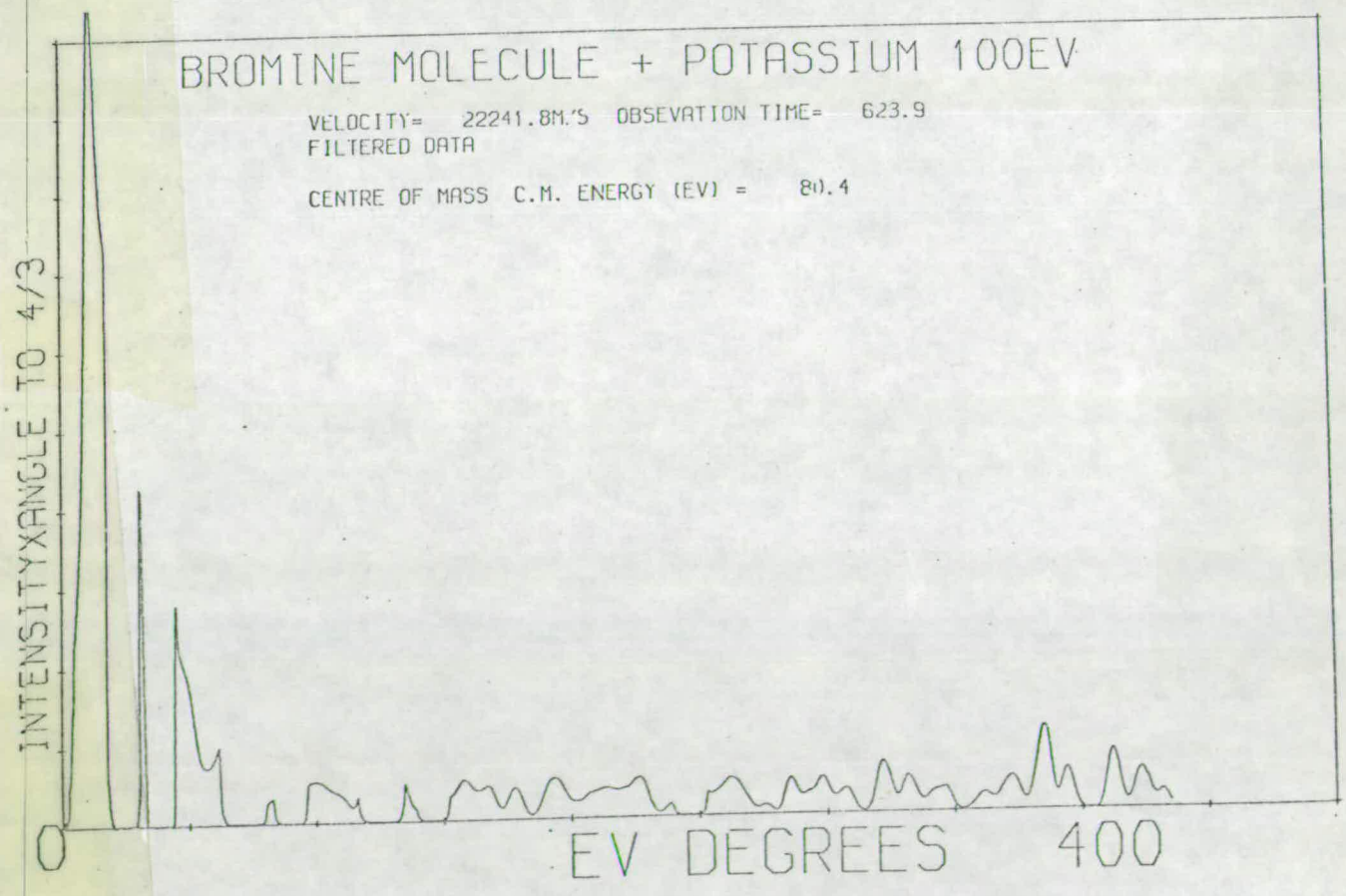

FIGURE 6.4 Neutral Differential Cross Section at 100eV for K/Br_2.

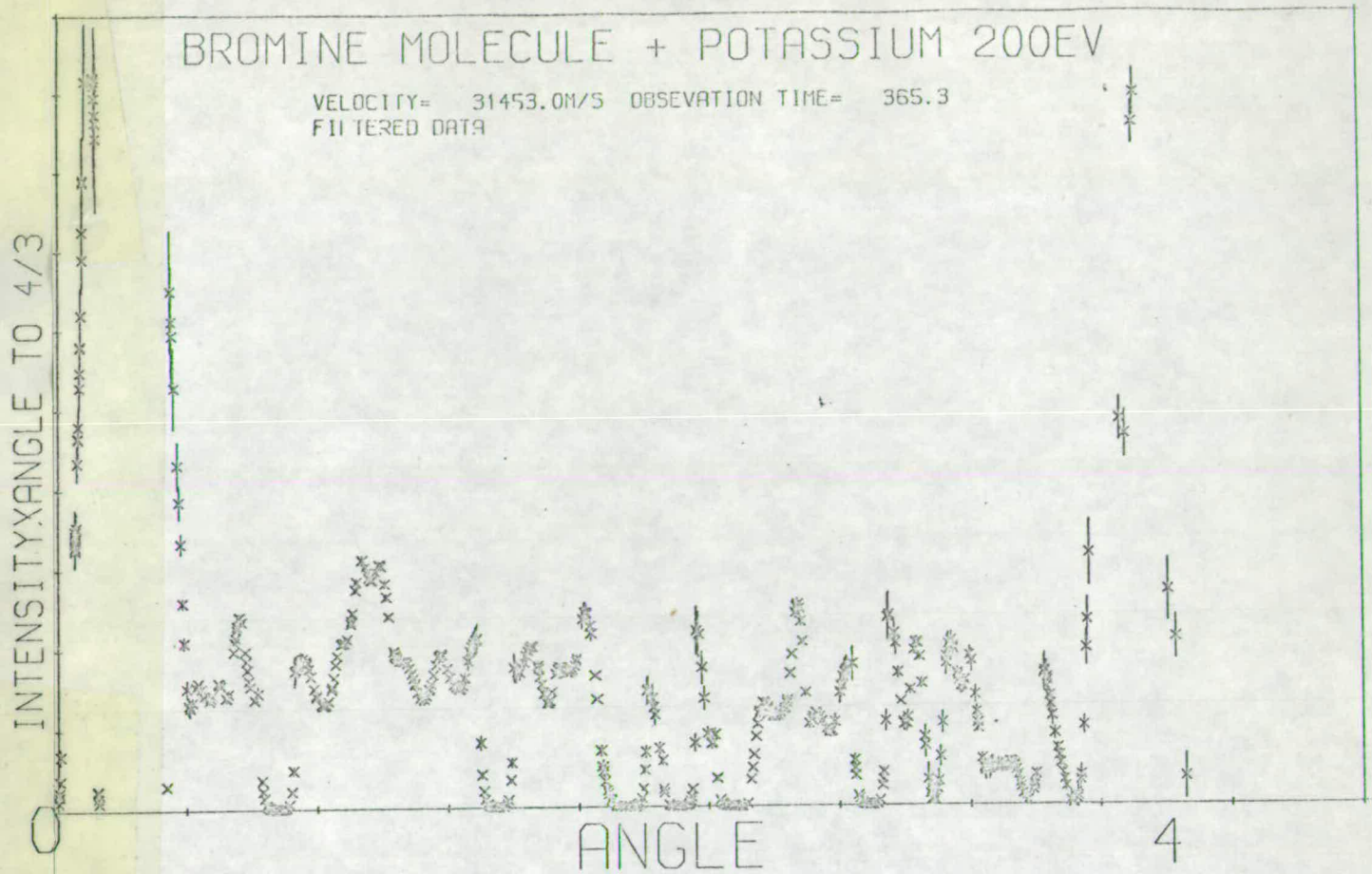

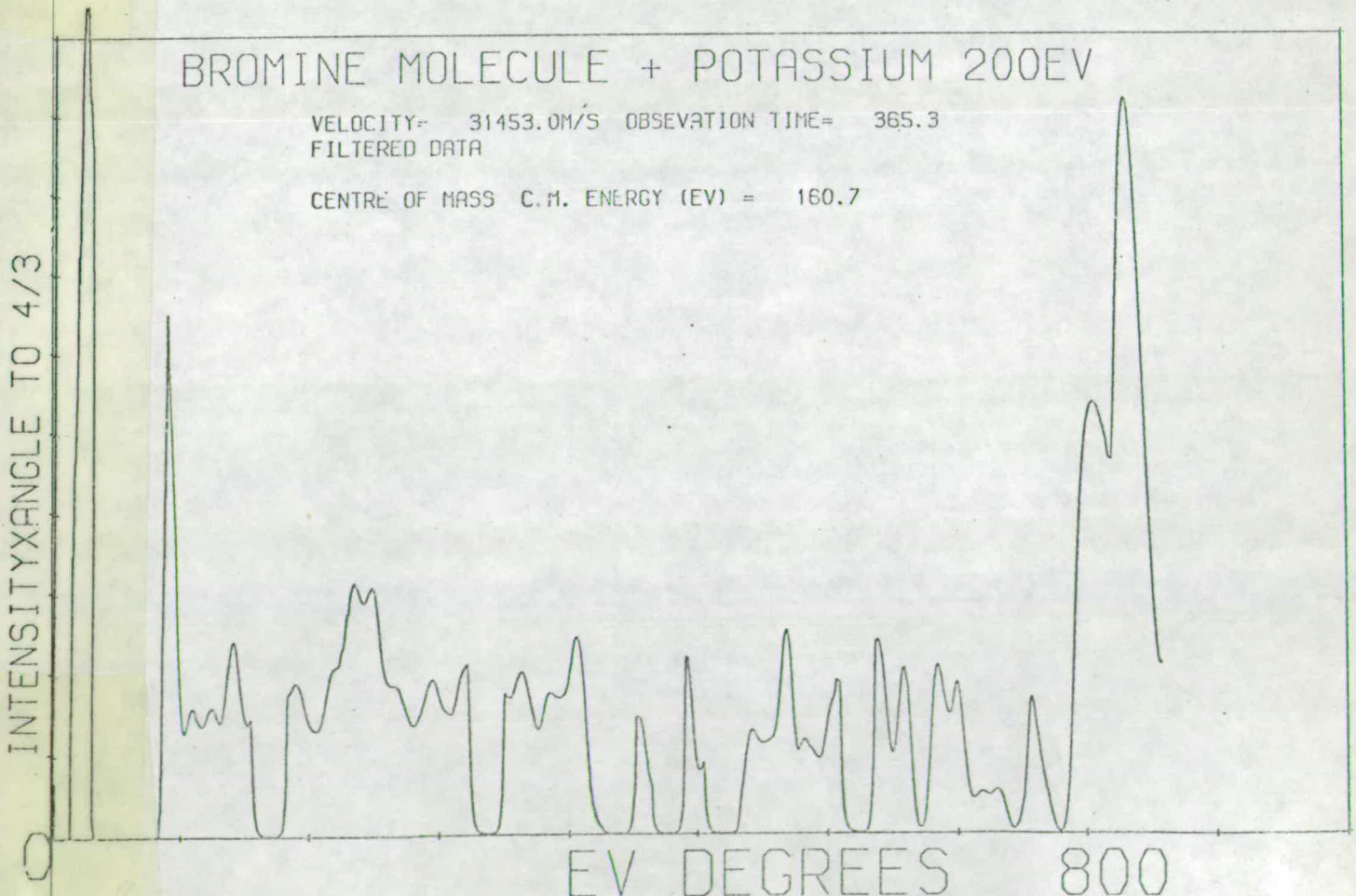

FIGURE 6.5 Neutral Differential Cross Section at 200eV for K/Br_2.

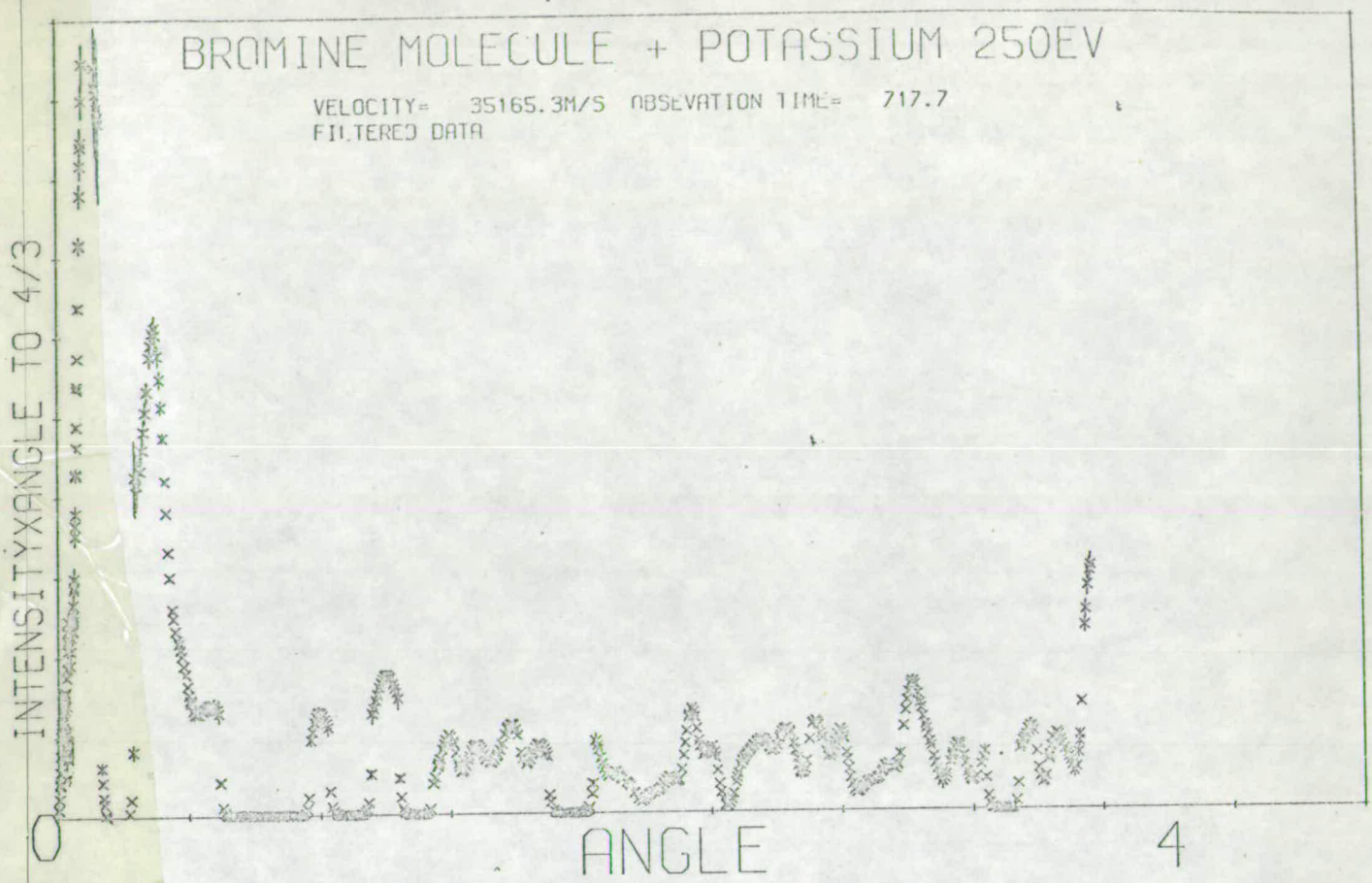

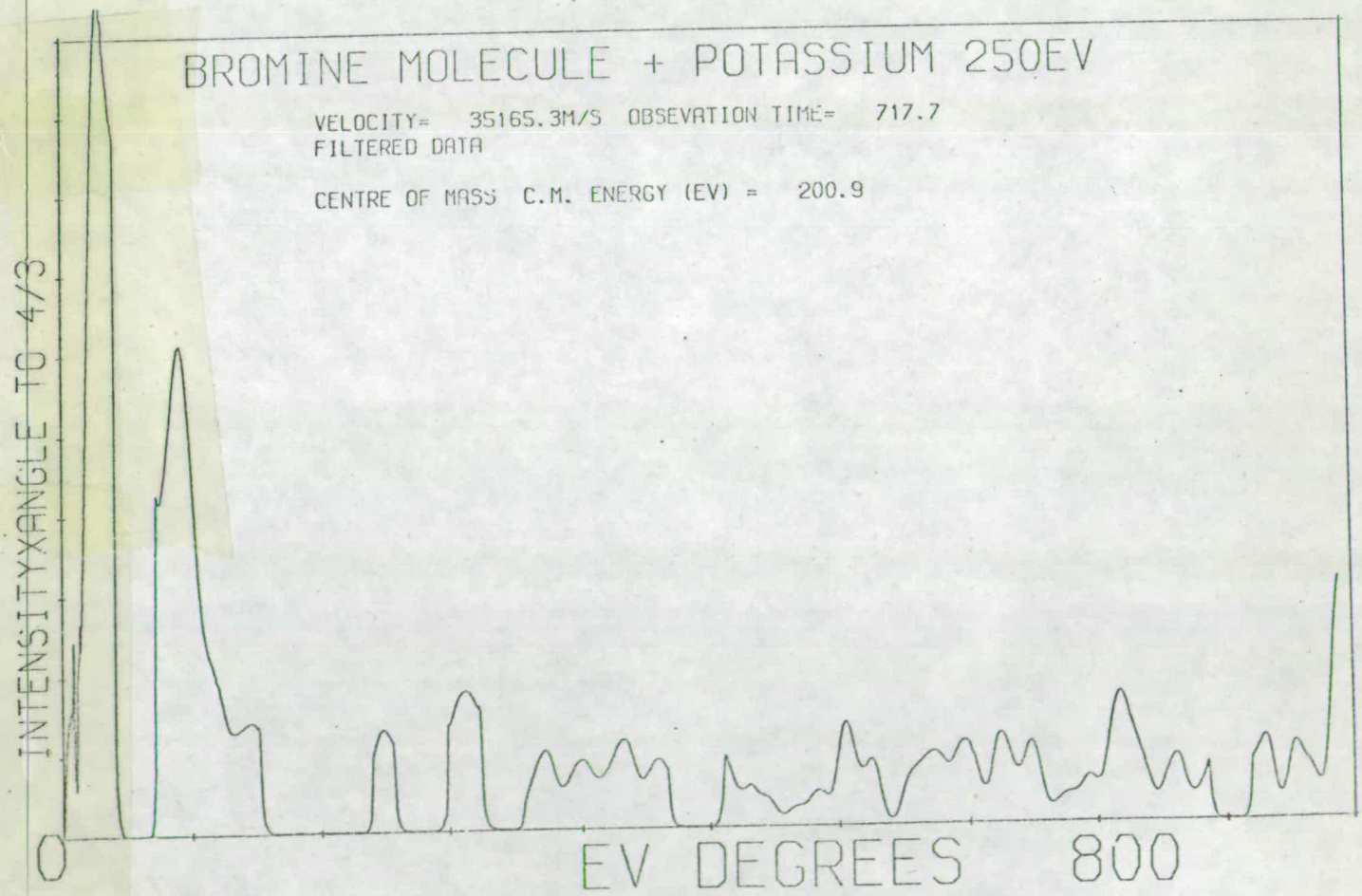

FIGURE 6.6 Neutral Differential Cross Section at 250eV for K/Br_2.

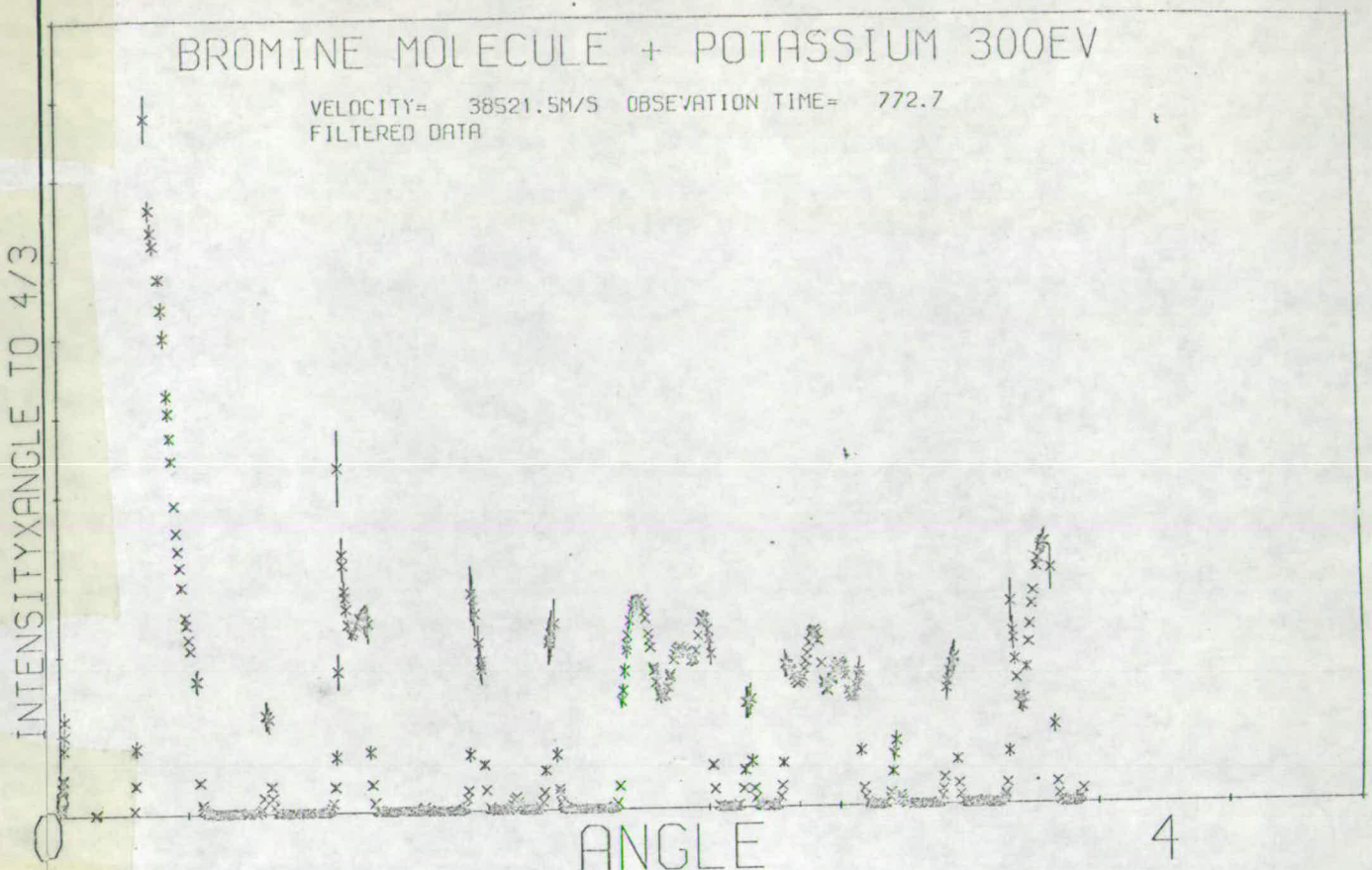

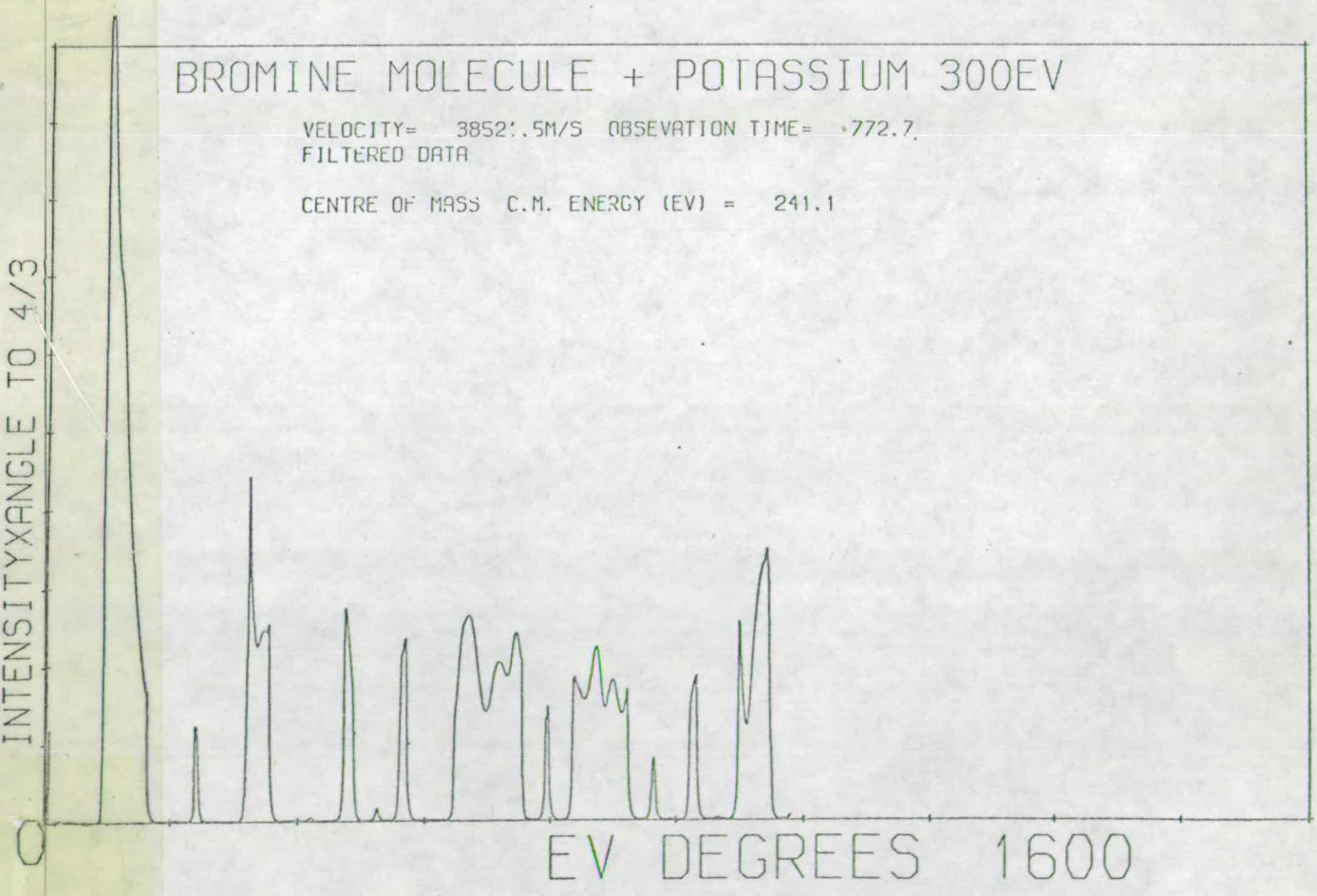

FIGURE 6.7 Neutral Differential Cross Section at 300eV for K/Br_2.

$H_{12}(R_x)$ was estimated as 4.5×10^{-2}eV. From these figures it is obvious that there should be a great deal of mixing between the two states, and this system should be very similar to K/I_2 where $R_x = 13.4a_o$ and $H_{12}(R_x) = 4.0 \times 10^{-2}$eV (taken from Chapter 2).

The envelope of the K/Br_2 and K/I_2 differential cross section plots are 100eV are very similar, although obviously not exact due to dissimilarities in the actual potential functions $H_{11}(R)$ and $H_{22}(R)$ and the reduced masses of the two systems.

Time did not permit a theoretical model, such as the eikonal approach described in Chapter 2, to be applied to the K/Br_2 system. However, such work will be done in this laboratory in the near future.

In their work, Delvigne and Los found the deep well rainbow appearing at 180eV^o. Assuming that this is a correct estimate, it can be seen that there is a large amount of neutral scattering in the 100eV plot at angles greater than 180eV^o due to interference between the scattering by the repulsive branches of the two potentials.

For their theoretical model of K/Br_2, Delvigne and Los used the method for the Na/I system described in Chapter 2. This employed the Landau - Zener theory for the evaluation of the scattered wave amplitudes and classical scattering theory for the deflection angles in order to compute the classical differential

cross sections. The comparison of experimental and theoretical predictions for the differential cross sections shows very poor agreement. The positions for the shallow and deep well rainbows predicted by the theoretical model, namely 80eV^{o} and 270eV^{o} respectively, are greatly different from those obtained experimentally being 32eV^{o} and 180eV^{o}. Further, the envelopes of the theoretical and experimental plots bear very little similarity.

The Collision System K/CH_3I

The scattering of neutral potassium atoms for the collision system K/CH_3I was measured for laboratory energies of 100eV, 200eV, 250eV, 300eV and 400eV. These are shown in Figures 6.8 to 6.12 respectively.

Most of the work done on alkali-methyl halide collisions has been performed in the thermal energy range, and a recent paper [89] (and the references quoted therein) reviews the experimental differential cross sections obtained and the theoretical models used to interpret the data.

Collisions at much higher energies such as 100eV and above will reveal the repulsive forces involved in the system. Figure 6.13 shows that there is a very good energy correspondence between the differential cross sections obtained at several very high energies. There appears a great deal of periodic structure involved in all of these high energy plots at angles of more than 100eV^{o}. This can

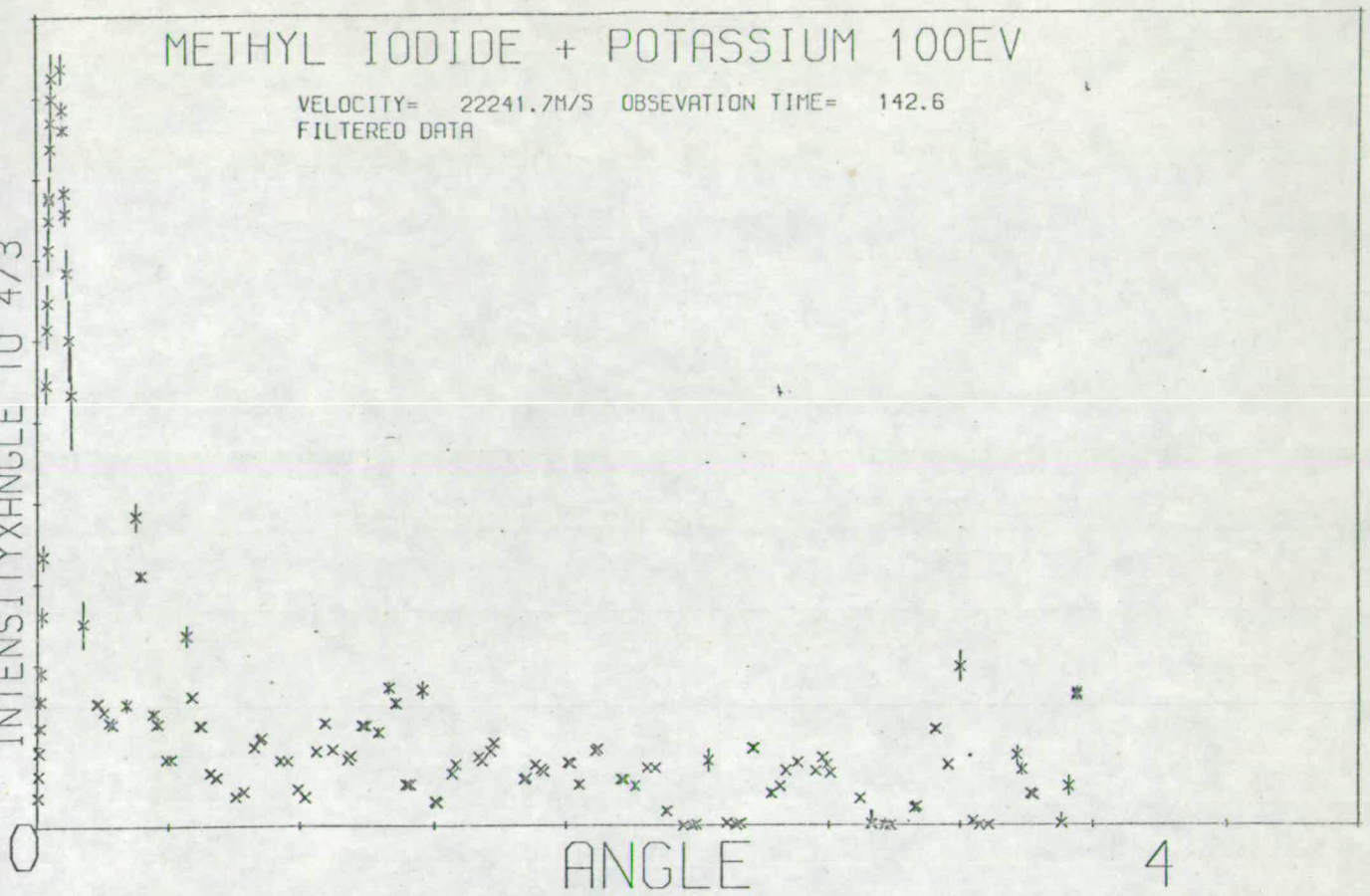

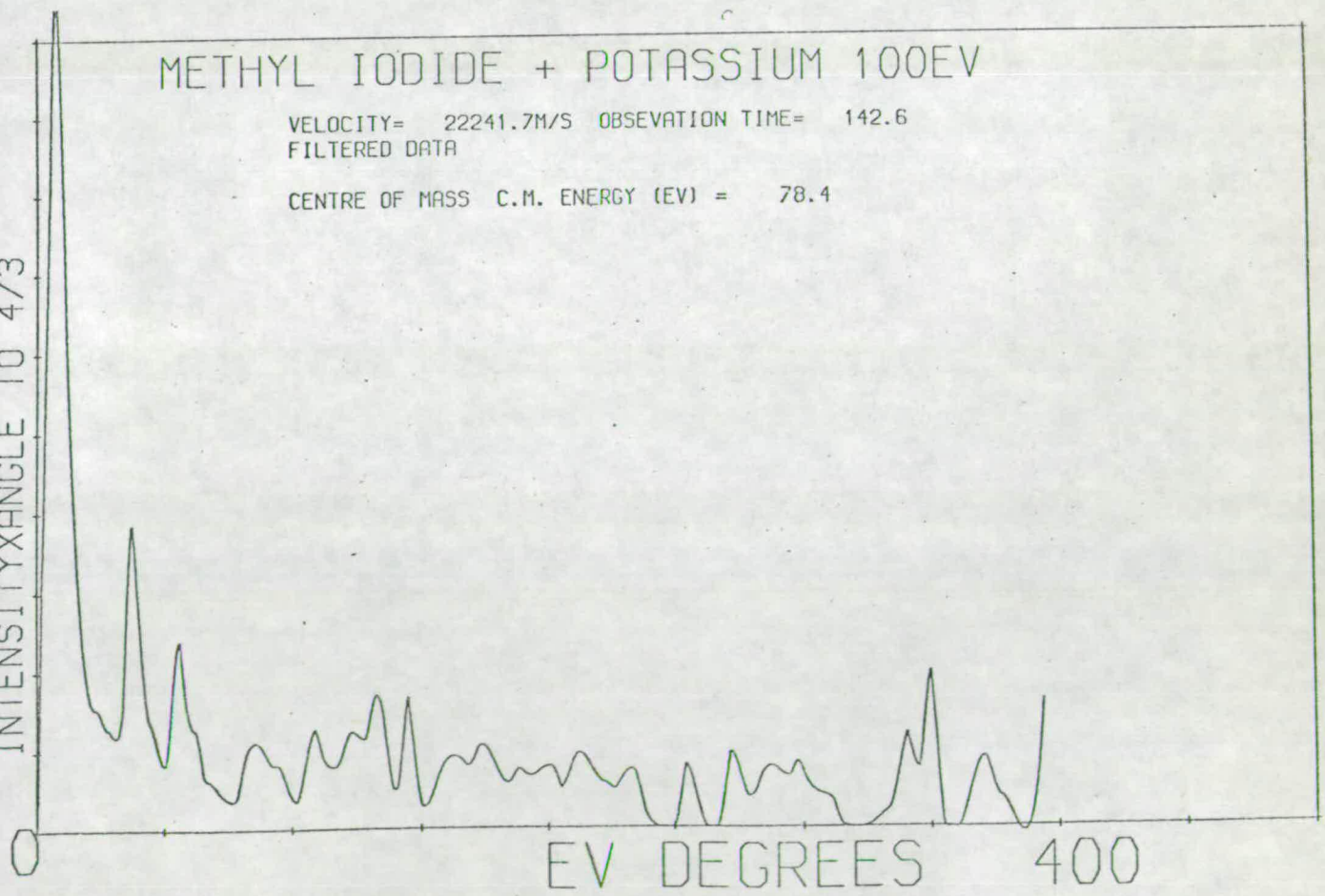

FIGURE 6.8 Differential Cross Section for neutral scattering for the system K/CH$_3$I at 100eV.

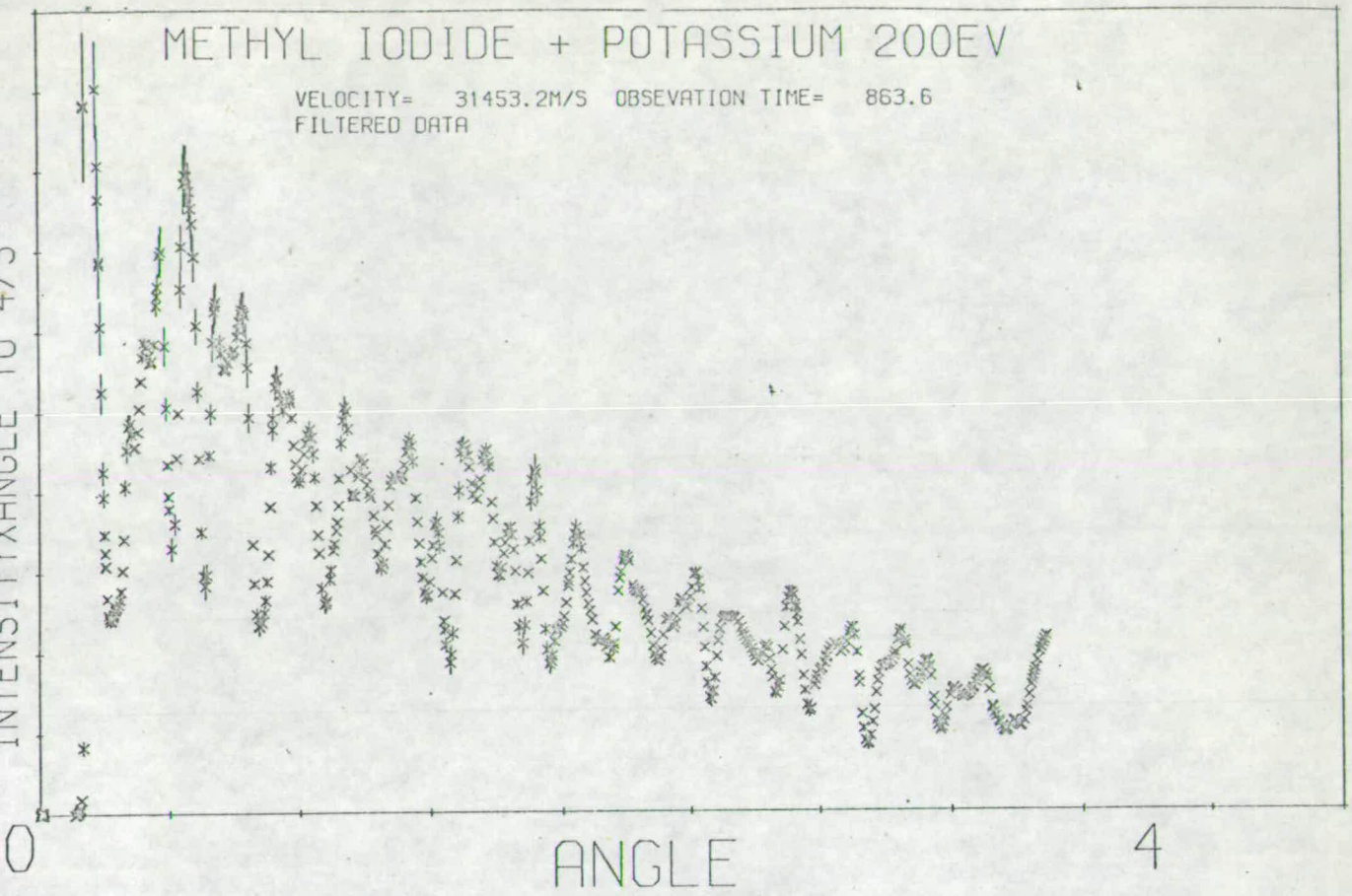

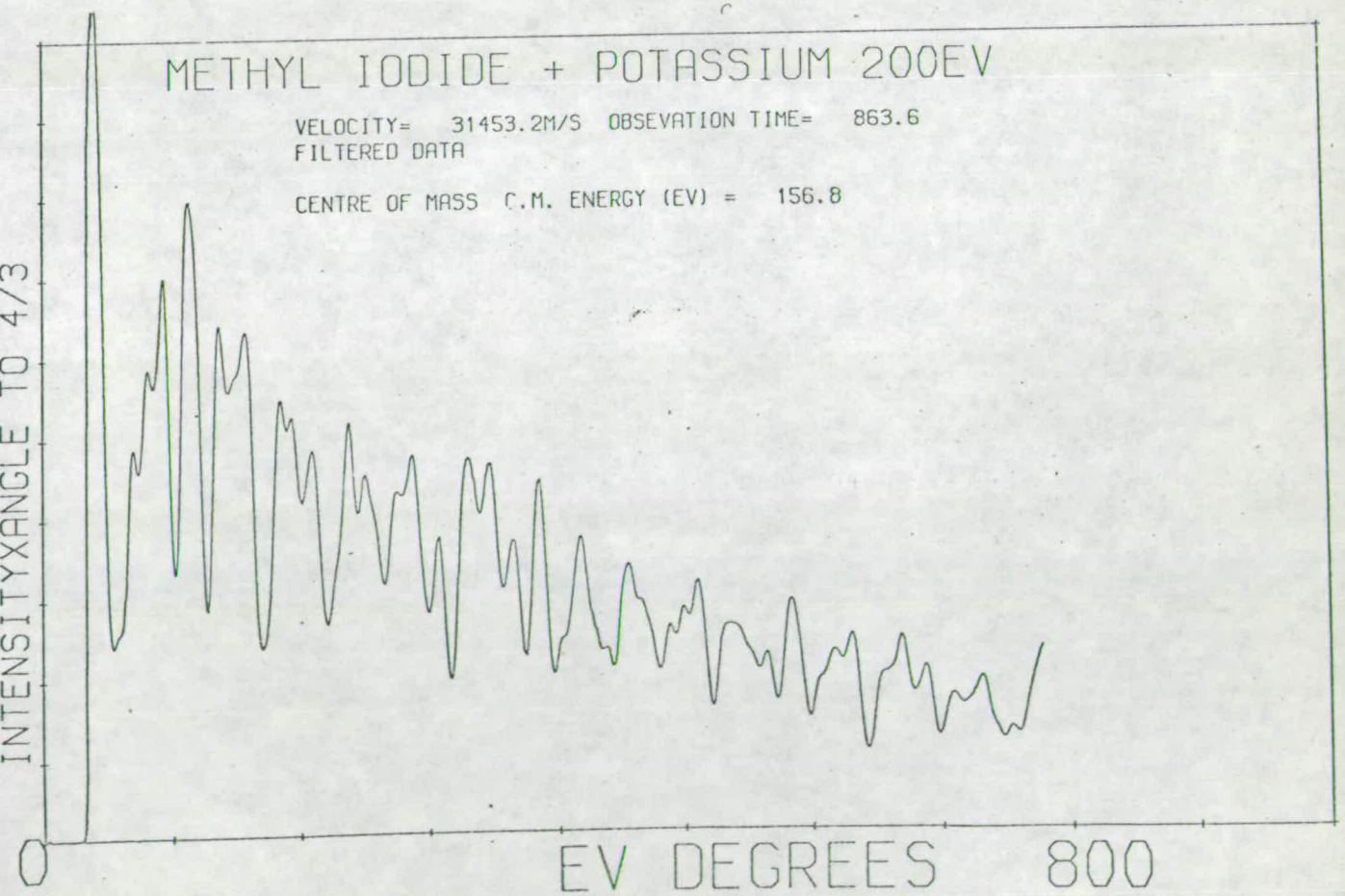

FIGURE 6.9 Differential Cross Section for neutral scattering for the system K/CH_3I at 200eV.

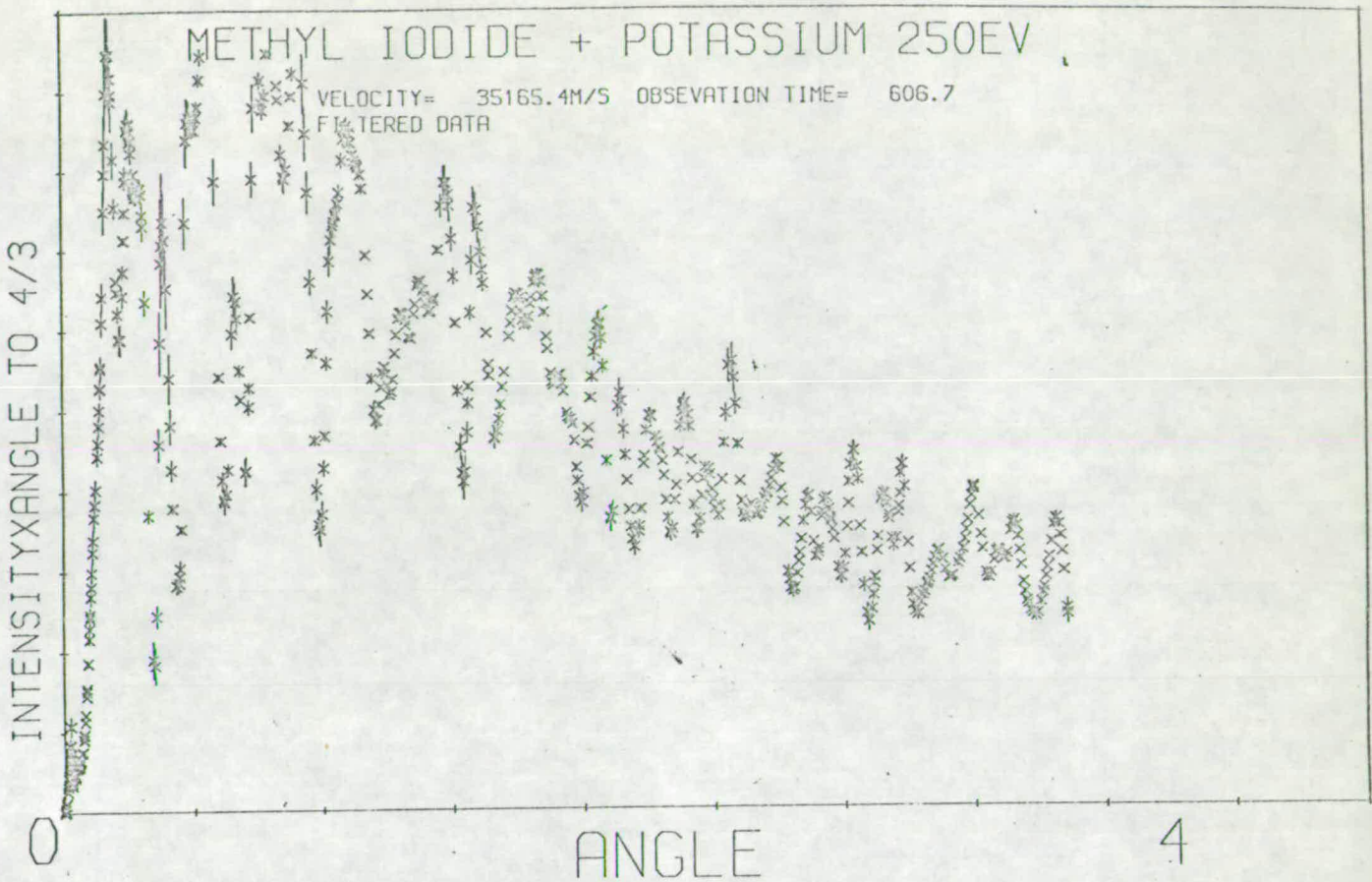

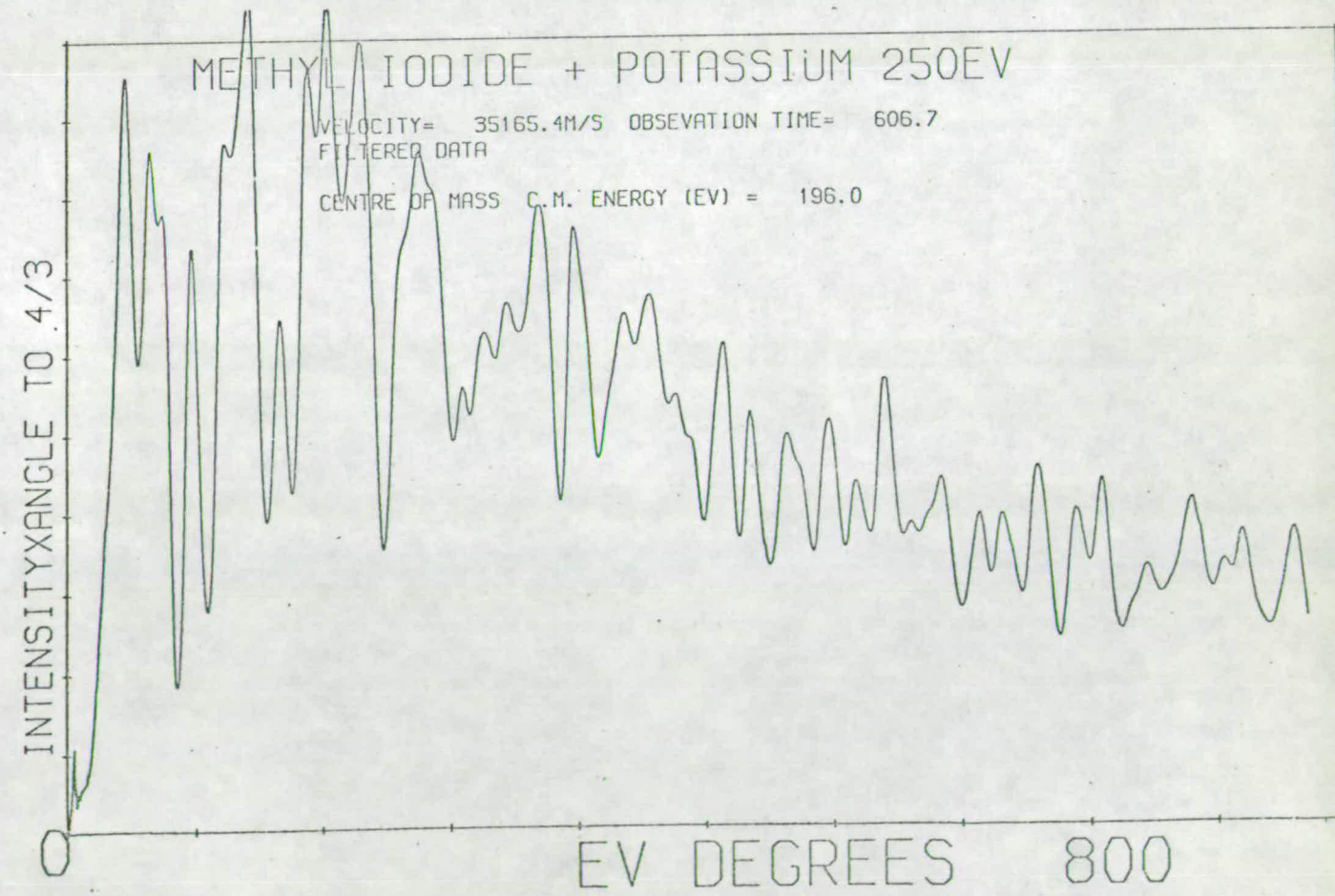

FIGURE 6.10 Differential Cross Section for neutral scattering for the system K/CH_3I at 250eV.

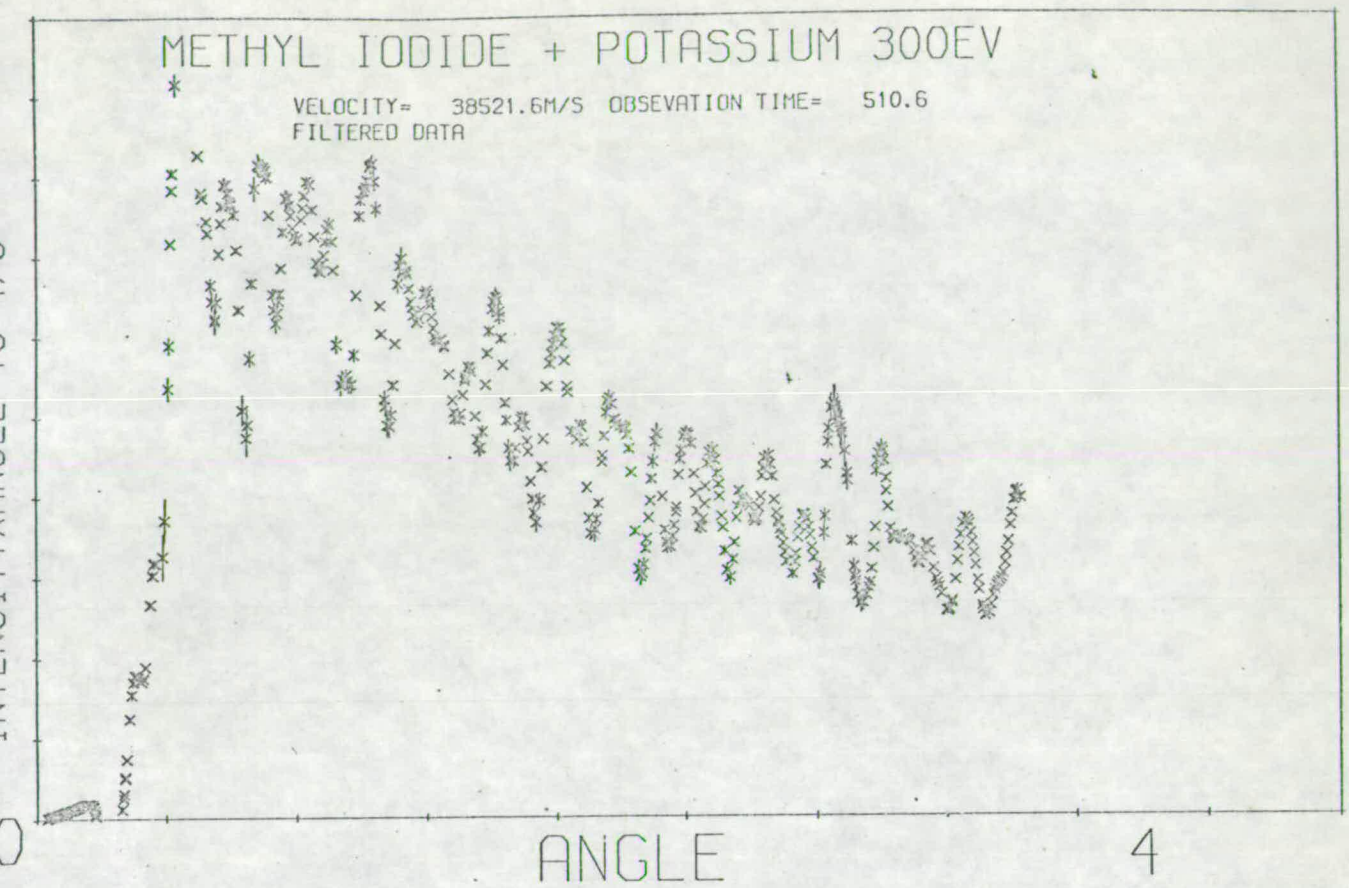

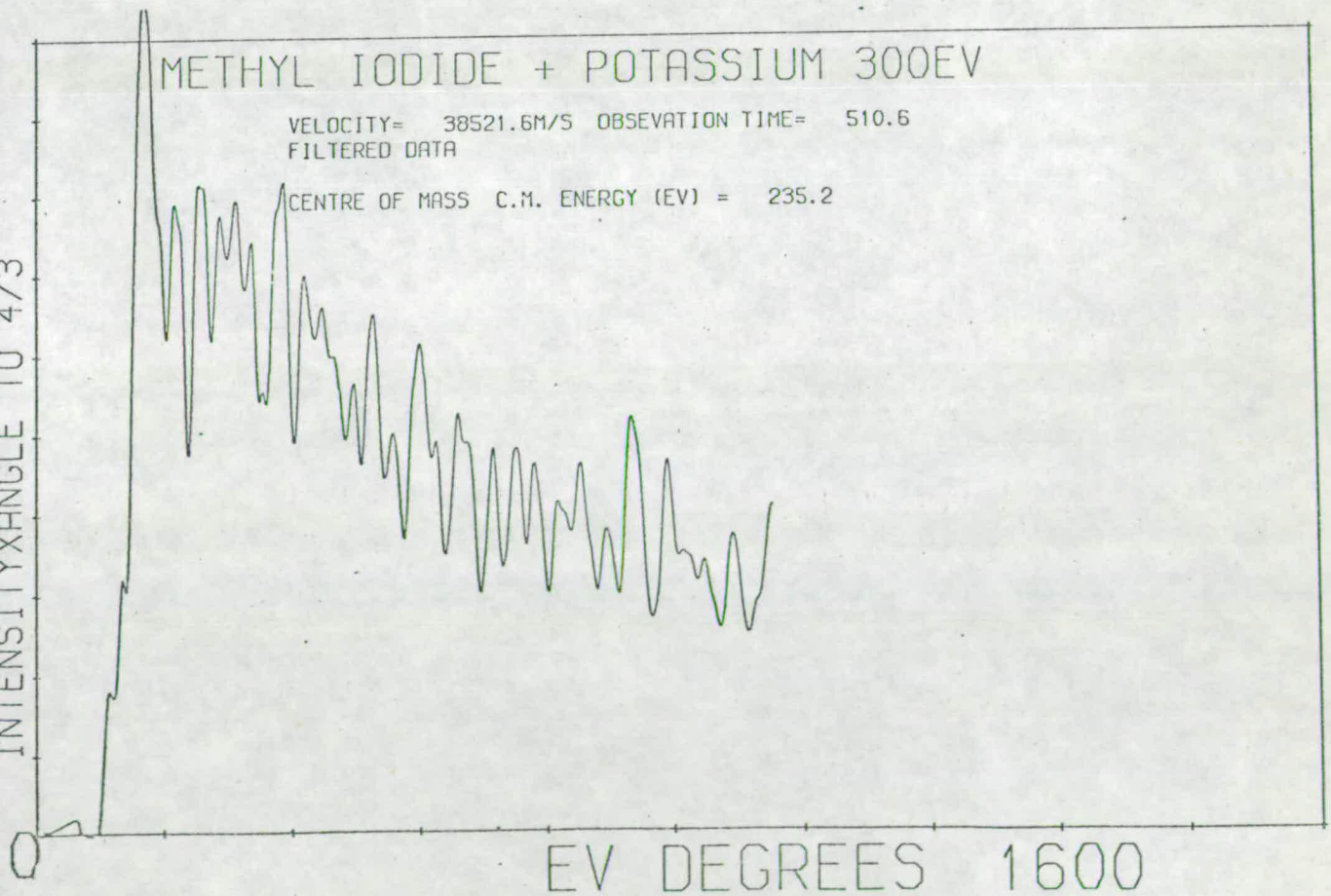

FIGURE 6.11 Differential Cross Section for neutral scattering for the system K/CH_3I at 300eV.

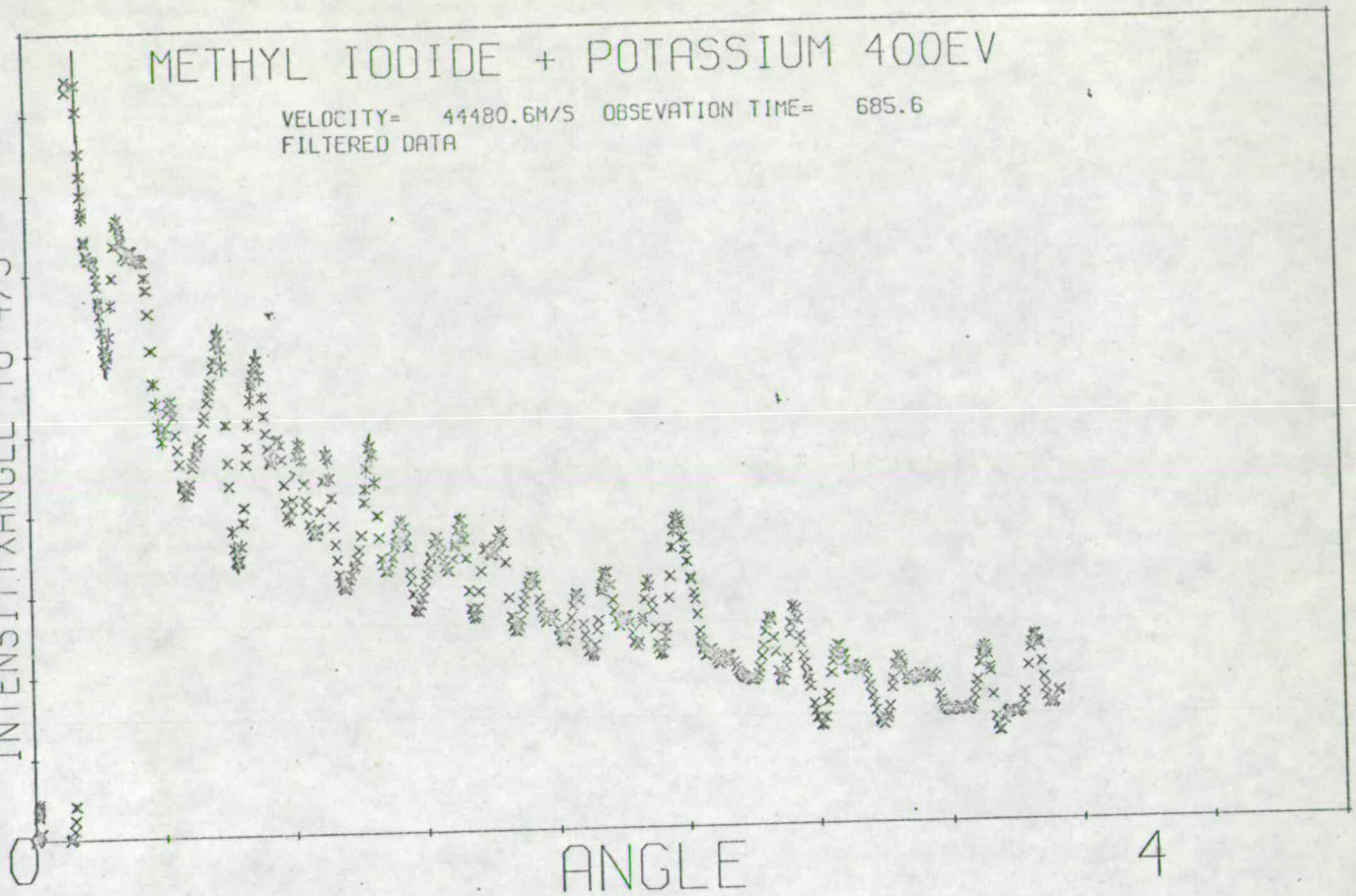

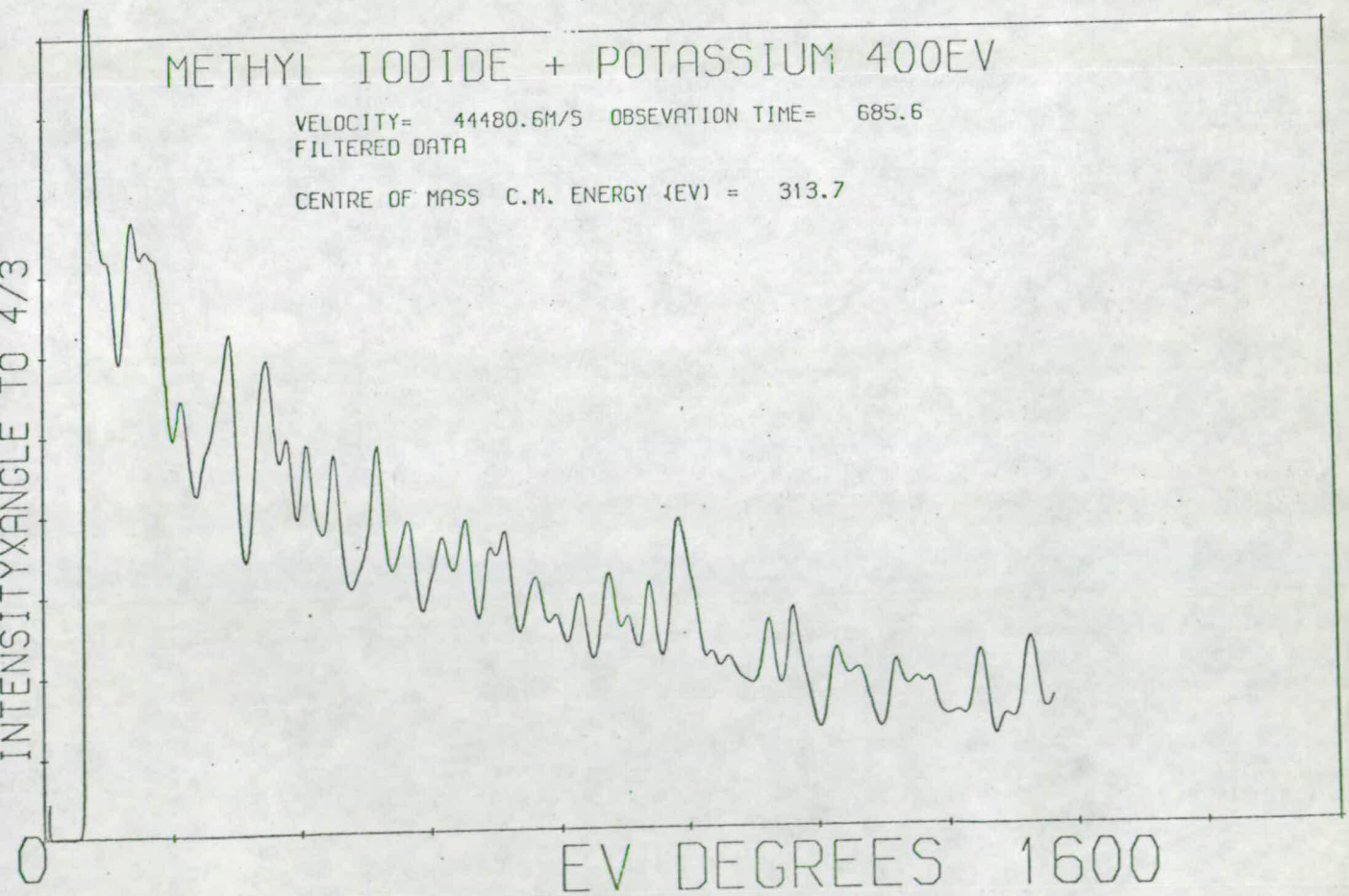

FIGURE 6.12 Differential Cross Section for neutral scattering for the system K/CH_3I at 400eV.

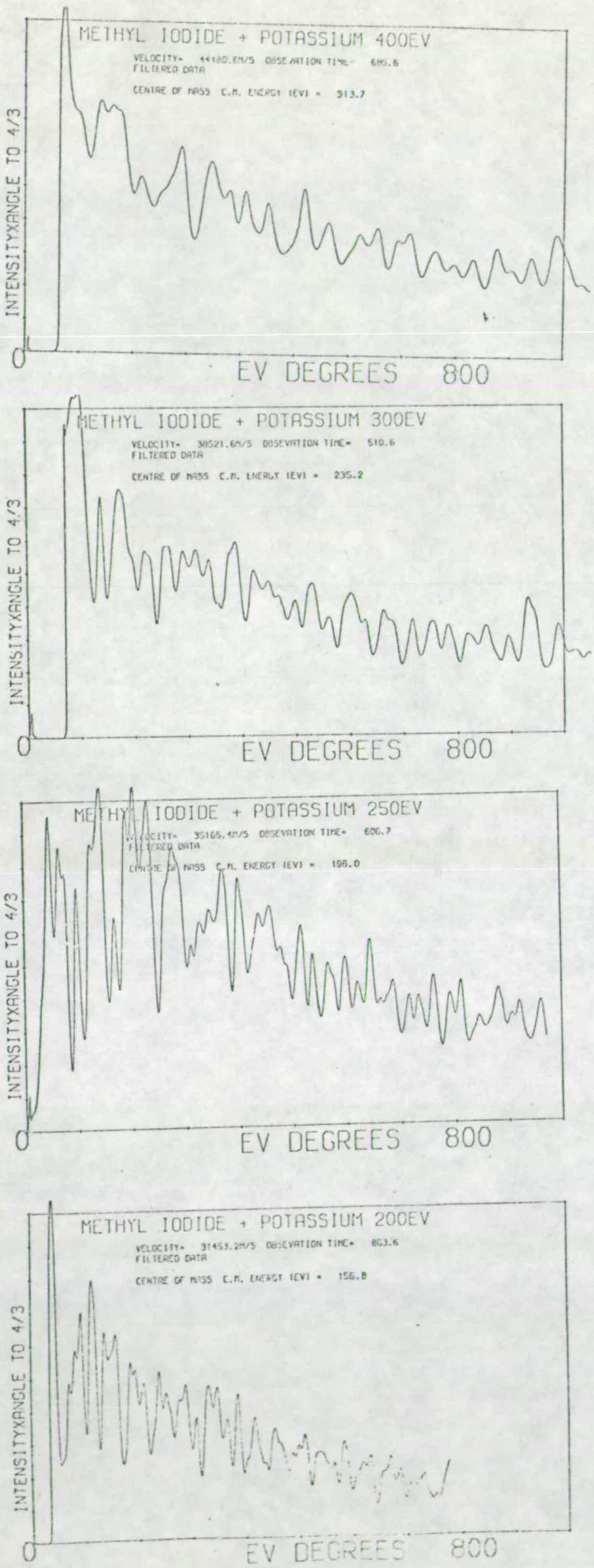

FIGURE 6.13 Summary of the K/CH_3I differential cross sections for neutral scattering.

only be possible if there are two or more states of the system involved, as only one state would yield the usual smooth scattering pattern peculiar to a monotonic potential.

Assuming for the sake of simplicity that only two states are present, oscillations will appear due to interference between the contributing branches of the two relevant deflection functions. Also there will be an amplitude modulation on the scattering function produced due to the switching of the system from one state to the other.

If the two states present are labelled 0 and 1, where 0 is the dominant state, and their respective contributions to the cross section are given by σ_o and σ_1 respectively, then, by the semiclassical approach, the combined cross section σ will be given by

$$\sigma = \sigma_o + \sigma_1 + 2(\sigma_o\sigma_1)^{\frac{1}{2}} \cos\beta \qquad 6.2$$

where β is the phase difference between the two contributing branches. If σ_o and σ_1 are assumed to be slowly varying, then maxima in the cross section occur when

$$\cos\beta = +1$$

and minima when

$$\cos\beta = -1$$

The mean of the cross section curve will be

$$\bar{\sigma} = \sigma_o + \sigma_1$$

Now if measurements of $\bar{\sigma}$ and ρ are made at each extrema in the combined cross section curve, where ρ is the displacement of the curve from its mean value, then by simple algebra

$$2\sigma_o = \bar{\sigma} + (\bar{\sigma}^2 - p^2)^{\frac{1}{2}}$$

$$2\sigma_1 = \bar{\sigma} - (\bar{\sigma}^2 - p^2)^{\frac{1}{2}} \qquad 6.3$$

Using the classical formula for the differential cross section $\sigma_o(\theta)$

$$\sigma_o(\theta) = \frac{b_o \left| \frac{db_o}{d\theta} \right| P_o(b_o)}{\sin\theta} \qquad 6.4$$

where $P_o(b_o)$ is the probability for a given impact parameter of exciting being in the state O, the relationship unfolds for a particular scattering angle θ^1

$$\int_{b_o(\theta=\theta^1)}^{o} b\,db = \int_{\theta^1}^{\pi} \sigma_o(\theta) \sin\theta\, d\theta \qquad 6.5$$

This assumes that to the first approximation $P_o(b_o) = 1$.

This can be split up into two regions of deflection, namely θ^1 to θ_{max}, the maximum angle of scattering observed experimentally, and θ_{max} to π. Hence

$$\frac{b_o^2}{2}(\theta^1) = \int_{\theta^1}^{\theta_{max}} \sigma_o(\theta)\sin\theta d\theta + \int_{\theta_{max}}^{\pi} \sigma_o(\theta)\sin\theta d\theta \qquad 6.6$$

As a first approximation, the second term on the right hand side of the above expression can be taken as half the square of the hard sphere radius for the collision.

Unfortunately in this treatment, the absolute values for $\sigma_o(\theta)$ are not measured and the above calculation cannot be performed without introducing scaling factors. However, using the experimental values obtained in arbitrary units, values of b_o for deflection angles of θ can be found. The optimistic feature is that a smooth almost straight line deflection function is obtained.

The position of the deflection function for the state 1 can be determined by the semiclassical relationship

$$k \int_{b_o}^{b_1} \theta db = \pi \qquad 6.7$$

where k is the wave number, and b_o and b_1 are the impact parameters for

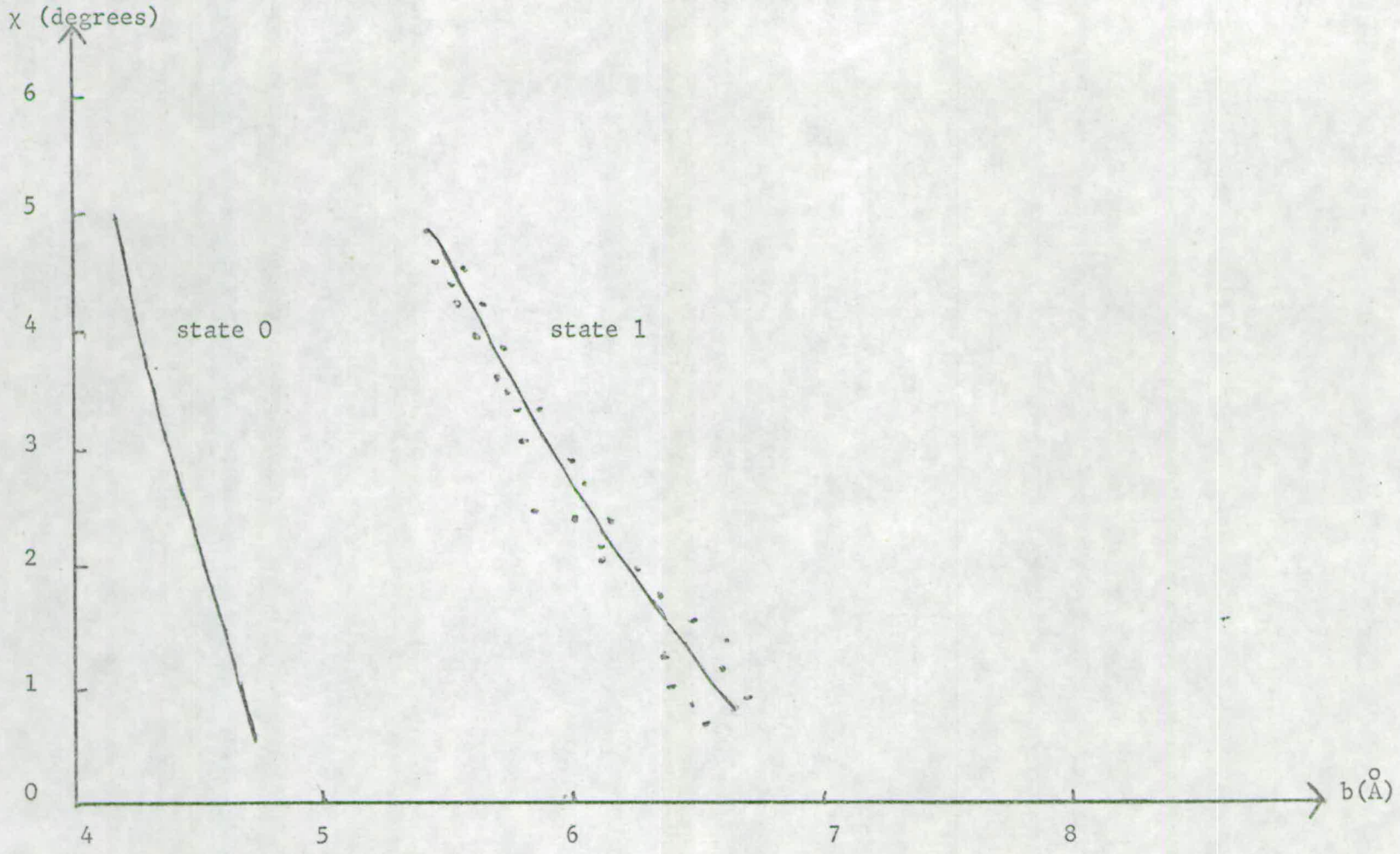

FIGURE 6.14 Plot of Deflection Functions against impact parameter for K/CH_3I at 250eV. The limitations of these curves are explained in the text.

the two states when an extrema arises in the cross section at an angle θ. This deflection appears to oscillate badly. (See Figure 6.14).

The value of $P_1(b_1)$, the probability of being in state 1 for a given impact parameter b_1, can be found using an equation similar to 6.4. Using such values to perform successive iterations of equations (6.4) to (6.7) should eventually yield smooth deflection functions and consistent values of $P_o(b)$ and $P_1(b)$.

There are unfortunately two very serious limitations. As mentioned before, very little can be done in a quantitative manner until the differential cross sections are found in absolute values. Just as important is that β, σ_o and σ_1 in equation (6.2) vary, and the interference of these oscillatory structures often covers up extrema due to each effect in the final differential cross section plot.

If these difficulties are overcome, then this model could yield good results. Unfortunately, time did not permit further investigation into this part of the work.

APPENDIX

As explained in Chapter 2, the value of $H_{12}(R)$ is at first calculated theoretically using equation (2.16). The following pages list these values to six places of decimals.

In the case of K/I, these values are further scaled to meet Moutinho's value of $H_{12}(R_x) = 1.4 \times 10^{-3}$eV at $R_x = 11.3$ Å.

In the case of K/I_2, however, they are scaled to meet Moutinho's value of 0.04eV at a value of $R_x = 13.4\ a_o$.

Internuclear Separation (a_o)	$H_{12}(R)$ (a.u. of energy) (theoretically calculated)
0.0	0.000000
1.0	- 0.032192
2.0	- 0.057247
3.0	0.001428
4.0	0.049605
5.0	0.051420
6.0	0.056732
7.0	0.048810
8.0	0.025572
9.0	0.014096
10.0	0.008603
11.0	0.005800
12.0	0.004145
13.0	0.002994
14.0	0.002204
15.0	0.001590
16.0	0.001130
17.0	0.000791
18.0	0.000546
19.0	0.000372
20.0	0.000251
21.0	0.000167
22.0	0.000111
23.0	0.000072
24.0	0.000047
25.0	0.000030

REFERENCES

1. FLUENDY, M.A.D., LAWLEY, K.P.

"Chemical Applications of Molecular Beam Scattering",
Chapman - Hall (1973).

2. MOTT, N.F., MASSEY, H.S.W.

"The Theory of Atomic Collisions",
Oxford Univ. Press (1965).

3. RAMSAY, N.F.

"Molecular Beams"
Oxford Univ. Press (1956).

4. PAULY, H., TOENNIES, J.P.

Adv. At. Mol. Phys. 1, 195 (1965)

5. MARGENAU, H., KESTNER, N.R.

"Theory of Intermolecular Forces"
Pergamon Press (1969).

6. HIRSCHFELDER, J.O., CURTISS, C.F., BIRD, R.B.

"Molecular Theory of Gases and Liquids"
Wiley (1954).

7. HIRSCHFELDER, J.O.

Adv. Chem. Phys., 12 (1967)

8. GREENE, E.F. MOURSUND, A.L., ROSS, J.

Adv. Chem. Phys., 10, 135 (1966).

9. BERNSTEIN, R.B.,

Adv. Chem. Phys., 10, 75 (1966).

10. ANDERSON, J.B., ANDRES, R.P., FENN, J.B.

Adv. At. Mol. Phys. 1, 345 (1965).

11. AMDUR, I., JORDAN, J.E.

Adv. Chem. Phys., 10, 29 (1966).

12. LASSETTRE, SKERBELE, DILLON, ROSS

J.C.P. 48, 5066 (1968).

13. BENNEWITZ, H.G., KRAMER, K.H., PAUL, W., TOENNIES, J.P.

Z. Physik 177, 84 (1964).

14. TAYLOR, E.H., DATZ, S.

J.C.P. 23 (9), 1711 (1955).

15. BULL, T.H., MOON, P.B.

Disc. Farad. Soc. 17, 54 (1954).

16. HERSCHBACH, D.R.

Adv. Chem. Phys., 10, 319 (1966).

17. HERSCHBACH, D.R., KWEI, G.H., NORRIS, J.A.

J.C.P. 34 (5), 1842 (1961).

18. STEBBINGS, R.F.,

Adv. Chem. Phys., 10, 195 (1966).

19. GIESE, C.F.

Adv. Chem. Phys., 10, 247 (1966).

20. GERSING, E. PAULY, H., SCHADLICH, E. VONDERSCHEN, M.

Faraday Discussion 55.

21. Van Den BERGH, H.E., FAUBEL, M., TOENNIES, J.P.

Faraday Discussion 55.

22. MAYLOTTE, D.H., POLANYI, J.C., WOODHALL, K.B.

J.C.P. 57, 1547 (1972).

23. SCHULTZ, A., CRUSE, H.W., ZARE, R.N.

J.C.P. 57, 1354 (1972).

24. BROOKS, P.R., JONES, E.M.

J.C.P. 45 (9), 3449 (1966).

25. BROOKS, P.R.

Faraday Discussion 55.

26. REDDINGTON, J.F., FLUENDY, M.A.D., LAWLEY, K.P.

Proc. IVth Int. Conf. Mol. Beams (Cannes 1973).

27. DELVIGNE, G.A.L., LOS, J.

To be published in Physica.

28. FORD, K.W., WHEELER, J.A.

Annals of Physics, 7, 259 (1959).

29. BUCK, U.,

J.C.P. 54 (5), 1923 (1971).

30. RAFF, L.M., KARPLUS, M.

J.C.P. 44, 1212 (1966).

31. ANDERSON, P.W.,

Phys. Rev. 76 (5), 647 (1949).

32. BIRNBAUM, G.

Adv. Chem. Phys., 12, 487 (1967).

33. HERMAN, F., SKILLMAN, S.

"Atomic Structure Calculations",

Prentice - Hall (1963).

34. COULSON, C.A.

"Valence"

Oxford. Univ. Press (1952).

35. LANDAU, L.D.

Phys. Z. Sowjet, 2, 46 (1932).

36. ZENER, C.

Proc. Roy. Soc. A 137, 696 (1932).

37. STUECKELBERG, E.C.G.

Helv. Phys. Acta, 5, 369 (1932).

38. COULSON, C.A., ZALEWSKI, K.

Proc. Roy. Soc. A 268, 437 (1962).

39. BATES, D.R.

Proc. Roy. Soc. A 257, 22 (1960).

40. GURNEE, E.F., MAGEE, J.L.

J.C.P. 26 (5), 1237 (1957).

41. PENNER, A., WALLACE, R.

Phys. Rev. A, 5 (2), 639 (1972).

42. HANDBOOK OF PHYSICS (2nd EDITION) 7-35

Editors: Condon, Odishaw.

43. HANDBOOK OF CHEMISTRY AND PHYSICS (48th EDITION) E-68

Editor: Weast.

44. BREWER, L., BRACKETT, E.

Chem. Rev. 61, 425 (1961).

45. HONIG, A., MANDEL, M., STITCH, M.L., TOWNES, C.H.

Phys. Rev. 96 (1), 629 (1954).

46. ROACH, A.C., BAYBUTT.

Chem. Phys. Lett. 7 (1), 7 (1970).

47. BATES, D.R., DAMGAARD, A.

Phil. Trans. Roy. Soc. A242, 101 (1949).

48. MOUTINHO, A.M.C.

Post Doctoral Report (Amsterdam) (1971).

49. EISBERG, R.M.

"Fundamentals of Modern Physics"

Wiley (1967).

50. PERSON, W.B.

J.C.P. 38, 109 (1963).

51. KUPPERMAN, A.

Private Communication.

52. DELVIGNE, G.A.L., LOS, J.

To be published in Physica.

53. DUCHART, B.S.

Ph.D. Thesis, Edinburgh (1971).

54. ANDERSON, J.B., ANDRES, R.P., FENN, J.B.

Adv. Chem. Phys. 10, 275 (1966).

55. POLITIEK, J., ROL, P.K., LOS, J., IKELAAR, P.G.

Rev. Sci. Inst. 39 (8), 1147 (1968).

56. SKINNER, G.T.

Physics of Fluids 4, 1172 (1961).

57. SAHA, M.N.

Phil. Mag. 46 (1923).

58. HUSMANN, O.K.

Progressin Astronautics and Aeronautics, 9, 195 (1963).

59. SIMPSON, J.A., KUYATT, C.E.

Rev. Sci. Inst. 34 (3), 265 (1963).

60. SOA, E.A., JENAER JAHRBUCH 1, 115 (1959).

61. HASKELL, H.B., HEINZ, O., LORENTS, D.C.

Rev. Sci. Inst. 37 (5), 607 (1966).

62. HASTED, J.B.

"Atomic and Molecular Processes",

Editor: Bates, D.R. Academic Press (London).

63. GENTRY, W.R., LEE, Y., MAHAN, B.H.

J.C.P. 49 (4), 1758 (1968).

64. PAULY, M., HOLLSTEIN, M.

Z. Physik 196, 353 (1966).

65. FONER, S.N.

Adv. At. Mol. Phys. 2, 385 (1966).

66. KERR, I.H.

Ph.D. Thesis, Edinburgh (to be published).

67. MORSE, F.A., BERNSTEIN, R.B.

J.C.P. 37 (9), 2019 (1962).

68. COWLEY, L.T.

Ph.D. Thesis, Edinburgh (1968).

69. McBRIDE, I.H.

"The Solution to the Laplace and Poisson Equations for an Ion Lens",

Company Report for Shell Research, Thronton, U.K.

70. ROSE, T.L.

Ph.D. Thesis (Part A), Yale University (1967).

71. HERMAN, Z., KERSTETTER, J.D., ROSE, T.L., WOLFGANG, R.

Rev. Sci. Inst. 40 (4), 538 (1969)

72. WILLMORE, A.P.J.

Ph.D. Thesis, London (1955).

73. COSSLETT, V.E.

"Electron Optics",

Oxford Univ. Press.

74. LASSETTRE, SKERBELE, DILLON, ROSS

J.C.P. 40, 5066 (1968).

75. GENTRY, W.R., GISLASON, E.A., MAHAN, B.H., TSAO, C.W.

J.C.P. 47 (2), 1856 (1967).

76. MOORE, J.H., DOERING, J.P.

J.C.P. 52 (4) 1962 (1970).

77. DITTNER, P.F., DATZ, S.

J.C.P. 54 (10), 4228 (1971).

78. CONNOR, R.J.

Nucl. Inst. Meth. 11, 122 (1961).

79. MOBLEY, R.C.

Phys. Rev. 88 (2), 360 (1952).

80. SMITH, A.B., GUENTHER, P., LARSEN, R., NELSON, C., WALKER, P., WHALEN, J.F.

Nucl. Inst. Meth. 50, 277 (1967).

81. FERGUSON, A.T.G.

Contemporary Physics, 5, 270 (1964).

82. FLEROV, N.N., TAMANOV, E.A.

Journ. Nucl. Energy 8, 91 (1958).

83. LEFEVRE, H.W., BORCHERS, R.R., POPPE, C.H.

Rev. Sci. Inst. 33, 1231 (1962).

84. VISSER, C.A., WOLLESWINKEL, J., LOS, J.

Journal of Physics E 3, 483 (1970).

85. COOPER, L., STEINBERG, D.

"Introduction to Methods of Optimisation",

Philadelphia (1970).

86. JONES, A.

Computer Journal 13 (3), 301 (1970).

87. DAVIDSON, T.A.

Ph.D. Thesis, Edinburgh (1973).

88. DELVIGNE, G.A.L., LOS, J.

Physica 59, 61 (1972).

89. BUNKER, D.L., GORING-SIMPSON, E.A.

Faraday Discussion 55.

90 JANAF THERMOCHEMICAL DATA (1964)

A C K N O W L E D G E M E N T S

I wish to express my sincere thanks to Dr M.A.D. Fluendy and Dr K.P. Lawley for their help, enthusiasm and encouragement, especially in the days when 'eureka' was not the in-word.

I would also like to thank the other members of the group who have helped me in many ways, and in particular to Mr I. Kerr for his help on the experiment.

I am greatly indebted to our two technicians who helped maintain and improve the apparatus. Mr W. Stevenson still performs his legendary feats of workshop wizardry, whilst Mr. D. Munro, our electronics expert, ensures that the electrons flow in the manner desired.

My thanks also to the University of Edinburgh for the provision of laboratory, library and computing facilities, and to the S.R.C. for their financial support.

My sincere thanks are also due to Dr J.L.J. Rosenfeld, Dr L.T. Cowley and Mr N. Sailes for all their help and kindness when I visited the Shell Research Centre, Thornton, during my C.A.P.S. visits.

Finally, I would like to thank Mrs Vyvienne Hosie for the excellent work done in typing this thesis.